# CHARACTERIZATION AND PROCESS PARAMETER OPTIMIZATION OF FRICTION STIR WELDED AA6061-RUTILE COMPOSITES

Thesis

Submitted in partial fulfilment of the requirements for the degree of

DOCTOR OF PHILOSOPHY

by

SUBRAMANYA R PRABHU B


DEPARTMENT OF MECHANICAL ENGINEERING

NATIONAL INSTITUTE OF TECHNOLOGY KARNATAKA,

SURATHKAL, MANGALORE -575025

JANUARY 2024

# CHARACTERIZATION AND PROCESS PARAMETER OPTIMIZATION OF FRICTION STIR WELDED AA6061-RUTILE COMPOSITES

Thesis

Submitted in partial fulfillment of the requirements for the degree of

DOCTOR OF PHILOSOPHY

by

**SUBRAMANYA R PRABHU B**

(Registration No: ME16F20)

Under the Guidance of

**Dr. Mervin A. Herbert**

Associate Professor

and

**Prof. Shrikantha S. Rao**

Professor


DEPARTMENT OF MECHANICAL ENGINEERING

NATIONAL INSTITUTE OF TECHNOLOGY KARNATAKA

SURATHKAL, MANGALORE-575 025

JANUARY 2024

*Dedicated to*

*My Parents, Sisters,*

*Gurus,*

*Wife, Little Samanvi and*

*Samarth*

# DECLARATION

*By the Ph. D. Research Scholar*

I hereby declare that the Research Thesis entitled ***"CHARACTERIZATION AND PROCESS PARAMETER OPTIMIZATION OF FRICTION STIR WELDED AA6061-RUTILE COMPOSITES"*** which is being submitted to **National Institute of Technology Karnataka, Surathkal** in partial fulfillment of the requirements of award of the degree **Doctor of Philosophy** in **Department of Mechanical Engineering** *is a bonafide report of the research work carried out by me.* The material contained in this Research Thesis has not been submitted to any University or Institution for the award of any degree.

**Register Number** : **165128 ME16F20**

**Name of the Research Scholar** : **Subramanya R Prabhu B**

**Signature of the Research Scholar :**

**Department of Mechanical Engineering**

Place: NITK- Surathkal

Date: 22/1/24.

# CERTIFICATE

This is to certify that the Research Thesis entitled ***"CHARACTERIZATION AND PROCESS PARAMETER OPTIMIZATION OF FRICTION STIR WELDED AA6061-RUTILE COMPOSITES"*** submitted by **Mr. Subramanya R Prabhu B. (Reg. No. 165128 ME16F20)** as the record of the research work carried out by him, is accepted as the Research Thesis submission in partial fulfillment of the requirements for the award of the degree of **Doctor of Philosophy.**

Dr. Mervin A. Herbert
Date: 22/01/2024
Research Guide

Dr. Shrikantha S. Rao
Date: 22-01-2024
Research Guide

Chairman DRPC
Date: 25/1/2024

राष्ट्रीय प्रौद्योगिकी संस्थान, कर्नाटक
यांत्रिकी अभियांत्रिकी विभाग
Dept. of Mechanical Engineering
National Institute of Technology Karnataka

## Acknowledgement

It has been indeed a great honor for me to work under the guidance of my advisors **Dr. Mervin A. Herbert** and **Dr. Shrikantha S. Rao,** Department of Mechanical Engineering, NITK Surathkal. With deep sense of gratitude and humility, I express my sincere thanks to them for their valuable guidance, untiring perseverance and unending patience which made the research not merely educational but also enjoyable. I also take this opportunity to thank the Director, NITK Surathkal and Head of Mechanical Engineering Department, NITK Surathkal for allowing me to carry out my doctoral studies.

I sincerely thank the Research Progress Assessment Committee consisting of Dr. I Regupathi (Associate Professor, Department of Chemical engineering), Dr. Shivananda Nayaka H (Associate Professor, Department of Mechanical engineering) for their valuable comments and constructive criticism which have helped the enrichment of this doctoral work. My heartfelt thanks to Dr. Arun Kumar Shettigar for his valuable suggestions and constant support during my research work. I am indeed extremely indebted to all of them.

I would like to thank all the teaching and non-teaching staff members of the Department of Mechanical Engineering, of NITK Surathkal and Department of Mechatronics Engineering, MIT Manipal for their continuous help and support throughout the research work.

I am immensely indebted to the unending help and support I received from my co-research colleagues Dr. Subash Acharya, Dr. Austine D Dsouza, Dr. Charitha, Dr. Karthik Rao MC, Mr. Srivathsa T V, Mr. Karthik during the course of my research work. I fail in my duty if I forget to thank my younger friend Dr. Anarghya A Murthy for his constant encouragement, timely help and morale support.

I am indebted to my parents Mr. Ramachandra V Prabhu and Mrs. Sarojini for inculcating in me the right values and virtues. I am extremely grateful to my sisters Mrs. Sukanya and Mrs Sujatha for providing continuous encouragement. I would also like to share the happiest moment with my wife Mrs. Divyashree H L my daughter

Samanvi Prabhu and my son Samarth S Prabhu, their support and endeavor kept my moral high throughout the research. I feel happy to express my sincere appreciation to all my family members, for their understanding, care, support and encouragement.

The list goes on and there are many others I should mention. There are people who have helped me all the way and provided me support when I didn't even realize I needed it, or needed it now, or needed it constantly. Listing all of them would fill a book itself, so I merely will have to limit myself to a few words: I THANK YOU ALL……!

---

Subramanya R Prabhu B

## Abstract

Increased demand for sophisticated materials has revealed characteristics including low density, high strength-to-weight ratio, and outstanding mechanical capabilities for use in aircraft, shipbuilding, and railroad construction. Fusion welding, which is frequently used for such materials, might cause cracks to form. The Welding Institute in the United Kingdom developed and patented a revolutionary welding method called Friction Stir Welding (FSW), which is used to join similar/dissimilar metals and composites. As a solid-state welding method that doesn't use inert gases and doesn't release any harmful gases when welding, friction stir welding is also known as "green welding." FSW has several advantages over fusion welding, including a higher joint strength, a defect-free weld, a more uniform distribution of grain structure in the weld zone, and reduced power consumption.

The primary goal of the current study is to determine the optimal way to join aluminium matrix composites. Stir cast AA6061-3 (wt.%) Rutile composite has been used as the material for friction stir welding. With the help of a CNC vertical machining centre, the specimen is welded. A scanning electron microscope is used to perform a microstructural study of the weld area. Energy Dispersive X-ray Analysis (EDAX) of the weld zone is carried out to examine the chemical composition. Additionally, mechanical properties are evaluated by measuring the hardness and tensile strength of the welded composite.

Composites that undergo friction stir welding develop an equiaxed grain structure with a uniform distribution of reinforced particles at the weld zone. The size of the rutile particles shrank at Nugget Zone, and the particles were observed to be redistributed. The mechanical properties of the joint have therefore been enhanced. At the Heat Affected Zone, the heat effect of the welding process causes the development of coarse grain (HAZ). The obtained results were examined using a classical approach. The joint strength of composites is improved via friction stir welding. Due to the small grain and presence of rutile particles, the nugget zone experienced a significant hardness increase. Experimental investigation shows that friction stir welding of stir cast AA6061-3 (wt.%) rutile composites using a combined square and

threaded cylindrical profiled pin tool with a rotational speed of 1000 rpm and a welding speed of 75 mm/min results in welds that are defect-free and have the best strength.

According to the research carried out using Taguchi design of experiments, rotating speed, welding speed, and tool pin profile are the factors that contribute most to an improvement in mechanical strength. The Taguchi technique's optimal process parameters and the related predicted value are experimentally verified using the confirmation test.

The optimization of process parameters to get joints with superior mechanical properties was done using statistical techniques as well as an evolutionary algorithm. The usage of an optimization strategy can produce the best results for the given problems within the constraints. To establish the optimum optimization strategy, various multi-objective optimization strategies are compared, including Grey Relational Analysis (GRA), Desirability Approach, and Teaching-Learning Based Optimization (TLBO).

Additionally, a multilayer perception neural network model based on genetic algorithms is used to predict the mechanical properties of composite joints. It is renowned for its nonlinear mapping of intricate static data. The validation experiments were conducted to validate the trained model. It is discovered that the mechanical property predictions are accurate and within reasonable bounds.

**Keywords:** Friction Stir Welding, Aluminium Matrix Composite, Nugget Zone, TLBO, GA-MLPNN.

**Contents**


| | | Page No. |
|---|---|---|
| Declaration | | |
| Certificate | | |
| Acknowledgements | | |
| Abstract | | |
| Contents | | i |
| List of Figures | | ix |
| List of Tables | | xvi |
| Nomenclature | | xix |
| 1 | INTRODUCTION | 1 |
| | 1.1 GENERAL BACKGROUND | 1 |
| | 1.2 THE HISTORY OF FSW | 2 |
| | 1.3 TLBO AND ARTIFICIAL INTELLIGENCE | 3 |
| | 1.3.1 TLBO Algorithm | 3 |
| | 1.3.2 GA-MLPNN | 3 |
| | 1.4 PROPOSED WORK SUMMARY | 4 |
| | 1.5 ORGANIZATION OF THE THESIS | 5 |
| 2 | LITERATURE SURVEY | 7 |
| | 2.1 PROCESSING OF ALUMINIUM MATRIX COMPOSITES | 7 |
| | 2.1.1 Powder Metallurgy | 9 |
| | 2.1.2 Stir casting | 9 |
| | 2.1.3 Liquid metal forging or Squeeze casting | 9 |
| | 2.1.4 Semi-solid powder processing | 9 |
| | 2.1.5 Diffusion bonding | 10 |
| | 2.1.6 Rheo-casting or Compo-casting | 10 |
| | 2.1.7 Physical vapor deposition | 10 |
| | 2.1.8 Friction stir processing (FSP) | 10 |
| | 2.2 STIR CASTING | 11 |
| | 2.3 WELDING OF ALUMINIUM MATRIX COMPOSITES | 14 |

2.3.1 Key issues in welding of aluminium matrix composites. 16
2.3.1.1 Solidification effects 16
2.3.1.2 Chemical reactions 17
2.3.1.3 Joint preparation 17
2.4 CONCEPT OF FRICTION STIR WELDING 19
2.5 MATERIAL SELECTION 23
2.6 MATERIAL FLOW PATTERN 25
2.6.1 Realization Mechanism of Friction Stir Weld 27
2.6.2 Influence of FSW Tool on Material Flow 28
2.7 DEVELOPMENT OF MICROSTRUCTURE AT WELD REGION 32
2.7.1 Unaffected Base Material 33
2.7.2 Heat-Affected Zone 33
2.7.3 Thermo Mechanically Affected Zone (TMAZ) 34
2.7.4 Nugget Zone / Stir Zone 35
2.7.5 Influence of probe diameter on Nugget Size 36
2.7.6 Variation in grain size and its impact on joint properties 36
2.8 THE IMPACT OF PROCESS PARAMETERS ON WELD QUALITY 39
2.8.1 FSW tools 40
2.8.1.1 Tool Materials 40
2.8.1.2 Tool Geometry 42
2.8.1.3 Diameter of FSW tool shoulder 43
2.8.1.4 Tool Shoulder Surface 44
2.8.1.5 Tool Pin Geometry 45
2.8.1.6 Diameter of tool pin 47
2.8.2 Effect of tool rotational speed 50
2.8.3 Effect of tool traverse speed/ welding speed 50
2.8.4 Impact of Axial Force on joint properties 51
2.9 MECHANICAL PROPERTIES 52
2.9.1 Hardness 52

2.9.2 Tensile Properties 53
2.10 OPTIMIZATION AND PREDICTION TECHNIQUE 57
2.10.1 Statistical Model 57
2.10.2 Modelling of Neural Networks 59
2.11 DEFECTS IN FSW 61
2.12 APPLICATIONS OF FSW 64
2.12.1 Marine and Shipbuilding Industries 64
2.12.2 Aviation industry 64
2.12.3 Locomotive industry 65
2.12.4 Land transportation 65
2.12.5 Other industry sectors 66
2.13 SUMMARY AND KNOWLEDGE GAP 66
2.14 STATEMENT OF PROBLEM 67
2.15 OBJECTIVES OF THE CURRENT WORK 68
2.16 SCOPE 69
2.17 DIRECTION FOR PRESENT WORK 70
3 RESEARCH METHODOLOGY 71
3.1 PREPARATION OF COMPOSITE MATERIAL 72
3.2 WELDING MACHINE 75
3.3 EXPERIMENTAL WORK 76
3.4 TOOLS FOR FSW 77
3.5 DESIGN OF FSW FIXTURE 79
3.6 SECTIONING OF TEST SPECIMENS OF FRICTION STIR WELDED AA6061-3wt% RUTILE COMPOSITE JOINT 81
3.7 CHARACTERIZATION OF FRICTION STIR WELDED AA6061-3wt% RUTILE COMPOSITE JOINT 82
3.7.1 X-Ray Diffraction (XRD) Analysis 82
3.7.2 Analysis of Microstructure 82
3.7.3 Testing of Mechanical Properties 83
3.7.3.1 Hardness test 83
3.7.3.2 Tensile test 84

3.8 DESIGN OF EXPERIMENT AND ANALYSIS 85
3.8.1 Phases of Taguchi Experiment 86
3.8.2 Signal-to-noise (S/N) ratio 87
3.8.3 Analysis of Variances 87
3.8.4 Multi-Response Optimization by Statistical Technique 87
3.8.5 Response Surface Methodology 88
3.8.6 Desirability Approach 89
3.9 TLBO ALGORITHM 90
3.10 GENETIC ALGORITHM - MULTILAYER PERCEPTION NEURAL NETWORK (GA- MLPNN) 93
3.10.1 The architecture of Multilayer Perception Neural Network (MLPNN) 93
3.10.1.1 Input layer 93
3.10.1.2 Hidden layer 94
3.10.1.3 Output layer 94
3.10.2 Backpropagation Algorithm 95
3.10.3 MLPNN methodology 96
3.10.3.1 Data normalization 96
3.10.3.2 MLPNN Procedure 96
3.10.4 Genetic Algorithm (GA) 97
3.10.4.1 Initial population 97
3.10.4.2 Selection 97
3.10.4.3 Crossover 97
3.10.4.4 Mutation 98
3.10.4.5 Fitness Evaluation 99
3.10.5 GA-MLPNN 99
4 RESULTS AND DISCUSSION 101
4.1 AS-CAST AA6061-3(wt%) RUTILE COMPOSITES - MICROSTRUCTURAL AND MECHANICAL CHARACTERIZATION 101
4.1.1 X-ray Diffraction Analysis 101

4.1.2 Scanning Electron Microscopic (SEM) Analysis 102
4.1.3 Mechanical properties of AA6061-3(wt%) rutile composite 105
4.2 FRICTION STIR WELDING OF AA6061 -3(wt%) RUTILE COMPOSITES 107
4.2.1 Identifying the working range for various tool probe geometries 108
4.3 MACRO AND MICROSTRUCTURAL ANALYSIS OF AA6061-3(wt%) RUTILE COMPOSITE JOINTS FORMED USING TOOL WITH THREADED CYLINDRICAL (TC) PROBE 112
4.3.1 Macro Analysis of AA6061-3(wt%) rutile composites joints 112
4.3.2 Microstructural Analysis of AA6061-3(wt%) rutile composites. 113
4.3.2.1 Microstructural analysis of Interfacial area of TMAZ and NZ 114
4.3.2.2 Microstructure variation in the weld zone. 117
4.4 MACRO AND MICROSTRUCTURAL ANALYSIS OF AA6061-3(wt%) RUTILE COMPOSITE JOINTS FORMED USING TOOL WITH SQUARE (Sq) PROFILE PROBE 120
4.4.1 Macro Analysis of AA6061-3(wt%) rutile composites joints 120
4.4.2 Microstructure of AA6061-3(wt%) Rutile composite joint 121
4.5 MACRO AND MICROSTRUCTURAL ANALYSIS OF AA6061-3(wt%) RUTILE COMPOSITE JOINTS FORMED USING TOOL WITH COMBINED SQUARE AND THREADED CYLINDRICAL (CSTC) PROFILE PROBE 124
4.5.1 Macro analysis of AA6061-3(wt%) Rutile composites joint 124

4.5.2 Microstructure of AA6061-3(wt%) Rutile joint 125
4.6 FS welded AA6061-3(wt%) rutile composite joint – Mechanical properties 127
4.6.1 Measurement of Hardness at weld zone 128
4.6.1.1 Distribution of hardness at weld zone, FS welded using TC tool 128
4.6.1.2 Variation in the distribution of hardness across AA6061-3(wt%) Rutile composite joint FS welded using Combined of Square and Threaded Cylindrical (CSTC) probe tool. 131
4.6.1.3 Variation in hardness of NZ of AA6061-3(wt%) Rutile composite joints FS welded using Square Profile Pin tool 135
4.6.2 Measurement of tensile strength 138
4.6.2.1 Tensile properties of AA6061-3(wt%) Rutile composite joints Friction Stir Welded using TC tool. 138
4.6.2.2 Tensile properties of FS welded AA6061-3(wt%) Rutile composite joints produced using Combined Square and Threaded Profile probe tool 140
4.6.2.3 Tensile properties of AA6061-3(wt%) Rutile composite joints Friction Stir Welded using a Square tool 141
4.6.2.4 Effect of tool geometries on Tensile characteristics of AA6061-3(wt%) Rutile composite joints. 142
4.6.3 Tensile properties along the weld direction of AA6061-3(wt%) Rutile composite joints FS Welded using TC, CSTC, and Sq tool 143
4.7 REPEATABILITY TEST 145

4.8 ANALYSIS OF TENSILE TEST FRACTURED SURFACES OF FS WELDED COMPOSITES 146
4.8.1 Analysis of fractured surfaces of tensile test performed across the weld direction 146
4.8.2 Investigation of fractured surfaces of the composite, tensile tested in the direction of the weld 147
4.9 ANALYSIS OF THE RELATIONSHIP BETWEEN GRAIN SIZE AND HARDNESS 151
4.10 RELATIONSHIP BETWEEN THE NZ HARDNESS AND UTS OF FS WELDED COMPOSITE 153
4.11 TAGUCHI DESIGN OF EXPERIMENT 155
4.11.1 Experimental results 155
4.11.2 Effect of process parameters on output responses - ANOVA 157
4.12 RESPONSE SURFACE METHODOLOGY 160
4.12.1 RSM Modelling 160
4.12.2 Regression Analysis 163
4.12.3 Summary 164
4.13 GREY RELATIONAL ANALYSIS (GRA) 165
4.13 .1 Response Pre-processing 165
4.13 .2 Calculating Grey Relational Coefficient (GRC) and Grey Relational Grade (GRG) 166
4.13 .3 Validation Test 169
4.13 .4 Analysis of variance (ANOVA) 170
4.14 DESIRABILITY APPROACH FOR OPTIMIZATION 170
4.14.1 Validation Test 171
4.15 TLBO 172
4.15.1 Validation 173
4.15.2 Multi-objective optimization using TLBO 173
4.15.3 Summary of the optimization results 174
4.16 PREDICTION OF THE FSW PROCESS USING GA MLPNN 175

4.17 SUMMARY OF THE RESULTS 181
4.17.1 Characterization of as-cast AA6061-3(wt%) rutile composites 181
4.17.2 Friction stir welding of AA6061 -3(wt%) rutile composites 181
4.17.3 Process parameter analysis utilizing the Taguchi design of experiments method 186
4.17.4 Process parameter optimization using Grey Relational Analysis (GRA), Desirability Approach (DA), and Teaching Learning Based Optimization (TLBO) 187
4.17.5 Prediction of mechanical properties using GA-MLPNN model 188
5 CONCLUSIONS AND SCOPE FOR FUTURE WORK 189
5.1 CONCLUSIONS 189
5.2 IMPLICATIONS AND PURPOSE OF INCLUDING DIFFERENT SOFT COMPUTING TECHNIQUES 191
5.3 DIRECTIONS FOR FUTURE RESEARCH 192
REFERENCES 193
APPENDIX 219
LIST OF PUBLICATIONS 223
BIODATA 225

## List of Figures


| Figure No. | Figure Caption | Page No. |
|---|---|---|
| 2.1 | Classification of the welding process to join the MMCs. | 16 |
| 2.2 | Friction stir welding machine (Courtesy: ETA Technology Pvt. Ltd. India, Friction Stir Welding Machine) | 20 |
| 2.3 | Friction Stir Welding terminology (Lin et al. 2020) | 21 |
| 2.4 | Schematic representation of friction-stir welding process (Courtesy: NASA/TM--1999-209876) | 22 |
| 2.5 | Material flow pattern in FS weld one [ Hamilton et al. (2008)] (a) Nugget top region and (b) Nugget cross-section. | 26 |
| 2.6 | (a) Weld cavity formation due to tool insertion (b) material flow driven by a pin, (c) Merged material flow driven by both pin and shoulder and (d) Pulling of base material into NZ (Courtesy: Kumar and Kailas 2008b) | 27 |
| 2.7 | (a) Pattern of Material flow and (b) zones of mechanical processing created during friction stir welding (Courtesy: Mishra et al. 2005). | 28 |
| 2.8 | The material flow when u = 2 mm/s, ω = 390 rpm at a)Advancing side, b) Retreating side (Zhang et al. 2005) | 30 |
| 2.9 | Flow of material when the tool rotates in a clockwise direction (Fonda et al. 2004) | 31 |
| 2.10 | Helical pattern material flow around threaded probe (Fernandez and Murr 2004) | 31 |
| 2.11 | FSW Optical cross-section (Heidarzadeh et al. 2020) | 33 |
| 2.12 | SEM images of the (a) TMAZ - Advancing side (b) TMAZ - Retreating side (c) HAZ and (d) BM. (Courtesy: (Liu et al. 2011) | 34 |
| 2.13 | (a) Generalized butt joint profile (b) Other types of joint profiles (Terry Khaled 2005) | 36 |
| 2.14 | Influence of probe diameter on Nugget Size (Reynolds 2000) | 36 |

| | | |
|---|---|---|
| 2.15 | Correlation between yield strength and the grain size (H. Suzuki 1963, William 2007) | 38 |
| 2.16 | Grain size at various locations on the nugget region of FS welded Al7050. (Mahoney et al. 1998) | 39 |
| 2.17 | Measured and computed peak temperature v/s Shoulder diameter. (Mehta et al. 2011a) | 44 |
| 2.18 | Shoulder diameter versus torque (Courtesy: Arora et al. 2011) | 44 |
| 2.19 | Geometries of tool shoulder, which makes contact with workpiece surface, (Courtesy: (Mahakur et al. 2021) | 45 |
| 2.20 | Pin profile's impact on dynamic orbit and pulsing action | 46 |
| 2.21 | Typical pin geometries. (a) Threaded cylindrical (b) Three flat threaded (c.) Triangular (Courtesy: Sun et al. 2009) (d) Trivex (Courtesy: Colegrove et al. 2004) (e) Threaded conical (f) Triflute (Courtesy: Rowe and Wayne 2006) | 47 |
| 2.22 | FSW tools with different pin profiles (Vijay and Murugan 2010) | 48 |
| 2.23 | Friction Stir Welding defects (Zettler and Vugrin 2003) | 64 |
| 3.1 | Flowchart of the methodology followed | 72 |
| 3.2a | SEM image of rutile particles | 73 |
| 3.2b | Rutile particles as received condition | 73 |
| 3.3 | Schematic representation of the bi-stage stir casting process | 74 |
| 3.4 | Various phases of stir casting process | 75 |
| 3.5 | Vertical Milling Machine | 76 |
| 3.6 | Experimental Setup | 77 |
| 3.7 | Friction Stir Welding tool with a) Threaded cylindrical pin, b) Square pin, and c) Combination of Square and Threaded cylindrical pin. | 80 |
| 3.8 | Fabricated and heat treated Friction stir welding tool with a) Threaded cylindrical pin, b) Square pin, and c) Combination of Square and Threaded cylindrical pin | 80 |
| 3.9 | FS welding Fixture setup | 81 |
| 3.10 | Schematic representation of specimens used for characterization | 81 |

| | | |
|---|---|---|
| 3.11 | Image of FSW specimen, showing advancing and retreating side, Nugget zone with onion rings, Thermo mechanically affected zone (TMAZ), and Heat affected zone (HAZ) | 83 |
| 3.12 | Image of composite joint FS welded using CSTC tool, showing advancing and retreating side, Nugget zone, TMAZ, HAZ. | 83 |
| 3.13 | Machined tensile test specimens | 84 |
| 3.14 | Fixture setup for tensile test on the universal testing machine | 85 |
| 3.15 | General representation of a manufacturing process. | 86 |
| 3.16 | Flow chart of TLBO algorithm (Rao et al. 2011) | 92 |
| 3.17 | Schematic Diagram of MLPNN | 93 |
| 3.18 | Representation of individual neurons with sigmoid nonlinearity. 100 | 94 |
| 3.19 | Schematic diagram of the backpropagation algorithm used to compare the output of a multiplayer perception with a desired signal for supervised learning. | 95 |
| 3.20 | Schematic diagram of single and double point cross-over. | 98 |
| 3.21 | Change in one or more genes in the children's solutions by mutation operator after the crossover phase | 98 |
| 3.22 | Schematic Diagram of GA-MLPNN | 100 |
| 4.1 | X-Ray Diffraction form displaying s the peaks of Al, TiO2 in as-cast AA6061-3 (wt%) rutile composite | 102 |
| 4.2 | (a) Microstructure of as-cast AA6061-3(wt%) rutile composite, (b) EDX spectrum of the region of interest showing peaks of Al, Ti, O2, Si, and Mg | 104 |
| 4.3 | (a) SEM image of base material - AA6061-3(wt%) rutile composite, EDX maps of (b) aluminium, (c) Titanium, (d) Oxygen, (e) Magnesium and (f) Silicon | 105 |
| 4.4 | The fracture surface of AA6061-3(wt%) Rutile composite | 107 |
| 4.5 | Friction stir welded AA6061-3(wt%)rutile composite specimen | 107 |
| 4.6 | SEM image displaying four distinct zones of FS welded AA6061-3(wt%) Rutile Composite. | 114 |

| | | |
|---|---|---|
| 4.7 | SEM image of interfacial zone of TMAZ and NZ of FS welded composite | 114 |
| 4.8 | FS Welded AA6061-3(wt%)rutile composite joint; (a) SEM image of NZ; and EDX map of b) Mg, c) $O_2$ d) Al, e) Si and f) Ti elements | 115 |
| 4.9 | Friction Stir Welded AA6061-3(wt%)rutile composite joint; Showing region of interest, quantitative results, and EDX spectrum showing the existence of Al-Mg-Ti-O-Si peaks. | 115 |
| 4.10 | FS Welded AA6061-3 (wt%) rutile composite joint showing SEM image of NZ, quantitative analysis of the elements EDX spectrum with Ti and O peaks | 116 |
| 4.11 | FS Welded AA6061-3 (wt%) rutile composite joint showing SEM image of NZ, quantitative analysis of the particles, and EDX map displaying Al, Ti, and O peaks | 116 |
| 4.12 | SEM image of NZ displaying the breakage of Rutile particles | 117 |
| 4.13 | Scanning Electron Micrograph of AA6061-3(wt%)rutile composite friction stir welded using TC tool with the rotational speed of 1000 rpm and welding speed 75 mm/min, showing grain size distribution at a) Top of the NZ, b) Middle of the NZ, c) bottom of the NZ, d) Advancing side of TMAZ and e) Retreating side of TMAZ. | 118 |
| 4.14 | Size of the grains at the NZ of FS welded AA6061-3(wt%)rutile composite using TC tool | 119 |
| 4.15 | Scanning Electron Micrograph of AA6061-3(wt%) Rutile composite joint friction stir welded using SQ tool with the rotational speed of 1000 rpm and welding speed of 75 mm/min, showing grain distribution at a) Retreating side of TMAZ b) Top of the NZ, c) Middle of the NZ, d) bottom of the NZ and e) Advancing side of TMAZ. | 122 |
| 4.16 | Grain size at the NZ of FS welded AA6061-3(wt%) Rutile joint produced using SQ tool | 123 |
| 4.17 | Scanning Electron Micrograph of AA6061-3(wt%) Rutile composite joint friction stir welded using CTSP tool with the rotational speed of | 125 |

| | | |
|---|---|---|
| | 750 rpm and welding speed of 60 mm/min, showing grain size distribution at (a) Retreating side TMAZ, (b) nugget top region, (c) nugget middle region of the threaded cylindrical tool, (d) nugget middle region of square tool (e) nugget bottom region and (f) Advancing side TMAZ | |
| 4.18 | Size of the grains at NZ of FS welded AA6061-3(wt%) rutile composite joint produced using CSTC tool | 127 |
| 4.19 | Distribution of hardness at NZ of AA6061-3 (wt%) Rutile composite FS welded using a TC tool at rotational speeds of 750, 1000, and 1250 rpm, maintaining tool traverse speed constant at 60 mm/min. | 129 |
| 4.20 | Distribution of hardness at NZ of AA6061-3 (wt%) Rutile composite FS welded using a TC tool at rotational speeds of 750, 1000, and 1250 rpm, maintaining tool traverse speed constant at 75 mm/min. | 130 |
| 4.21 | Distribution of hardness at NZ of AA6061-3 (wt%) Rutile composite FS welded using a TC tool at rotational speeds of 750, 1000, and 1250 rpm, maintaining tool traverse speed constant at 90 mm/min. | 131 |
| 4.22 | Distribution of hardness at NZ of AA6061-3 (wt%) Rutile composite FS welded using a CSTC tool at rotational speeds of 750, 1000, and 1250 rpm, maintaining the tool traverse speed constant at 60 mm/min. | 133 |
| 4.23 | Distribution of hardness at NZ of AA6061-3 (wt%) Rutile composite FS welded using a CSTC tool at rotational speeds of 750, 1000, and 1250 rpm, maintaining tool traverse speed constant at 75 mm/min. | 134 |
| 4.24 | Distribution of hardness at NZ of AA6061-3 (wt%) Rutile composite FS welded using a CSTC tool at rotational speeds of 750, 1000, and 1250 rpm, maintaining tool traverse speed constant at 90 mm/min. | 135 |
| 4.25 | Distribution of hardness at NZ of AA6061-3 (wt%) Rutile composite FS was welded using the SQ tool at rotational speeds of 750, 1000, and 1250 rpm, holding the tool traverse speed constant at 60 mm/min. | 136 |
| 4.26 | Distribution of hardness at NZ of AA6061-3 (wt%) Rutile composite FS was welded at rotational speeds of 750, 1000, and 1250 rpm and a constant tool traverse speed of 75 mm/min using the SQ tool. | 137 |

| | | |
|---|---|---|
| 4.27 | Distribution of hardness at NZ of AA6061-3 (wt%) Rutile composite FS welded at rotational speeds of 750, 1000, and 1250 rpm and a constant tool traverse speed of 90 mm/min using the SQ tool | 138 |
| 4.28 | UTS of the FS welded AA6061-3% Rutile composite joints using Threaded, Combination of Square and Threaded Cylindrical and Square profiled probe. | 143 |
| 4.29 | Fractured tensile test specimen | 146 |
| 4.30 | SEM images of the fractured area of AA6061-3%Rutile composite joints friction stir welded at a rotational speed of 1000 rpm and welding speed of 75 mm/min using: a) Threaded profile pin, b) Combination of Square and Threaded Cylindrical Profile pin and c) Square profile pin | 147 |
| 4.31 | Fractured tensile specimen of FS Welded composite joint tested in the weld direction. | 147 |
| 4.32 | SEM image of a fractured surface of AA6061-3 (wt%) Rutile composite joints friction stir welded using TC tool (along the weld direction) at a constant rotational speed of 1000rpm and a) welding speed of 60 mm/min, b) welding speed of 75 mm/min, c) welding speed of 90 mm/min, d) higher magnification image showing the dimples, pullout, decohesion, and cracked rutile particles. | 148 |
| 4.33 | SEM image of a fractured surface of AA6061-3 (wt%) Rutile composite joints friction stir welded using CSTC tool (along the weld direction) at a constant rotational speed of 1000rpm and a) welding speed of 60 mm/min, b) welding speed of 75 mm/min, c) welding speed of 90 mm/min, and d) higher magnification image showing the dimples, pullout, decohesion, and cracked rutile particles. | 149 |
| 4.34 | SEM image of a fractured surface of AA6061-3 (wt%) Rutile composite joints friction stir welded using SQ tool (along the weld direction) at a constant rotational speed of 1000rpm and a) welding speed of 60 mm/min, b) welding speed of 75 mm/min, c) welding | 150 |

| | | |
|---|---|---|
| | speed of 90 mm/min, and d) higher magnification image showing the dimples and Rutile particles. | |
| 4.35 | Hardness and grain size variation at the NZ of the FS welded AA6061-3% Rutile composite joint, welded using TC tool | 151 |
| 4.36 | Variation of hardness and grain size at the NZ of the FS welded AA6061-3% Rutile composite joint welded using the CSTC tool | 152 |
| 4.37 | Variation of hardness and grain size at the NZ of the FS welded AA6061-3% Rutile composite joint welded using the SQ tool | 152 |
| 4.38 | Relationship between UTS and hardness at the NZ, FS welded AA6061-3(wt%) Rutile composite using TC tool | 153 |
| 4.39 | Relationship between UTS and hardness at the NZ, FS welded AA6061-3(wt%) Rutile composite using CSTC tool | 154 |
| 4.40 | Relationship between UTS and hardness at the NZ, FS welded AA6061-3(wt%) Rutile composite using SQ tool | 155 |
| 4.41 | Effect of process parameters on yield strength | 159 |
| 4.42 | Effect of process parameters on UTS | 159 |
| 4.43 | Effect of process parameters on Hardness | 160 |
| 4.44 | Effect of process parameters on % elongation | 160 |
| 4.45 | Main effect plot for grey relational grade | 169 |
| 4.46 | Desirability optimization for friction stir welded AA6061/Rutile composite. | 171 |
| 4.47 | Regression plot of GA-MLPNN | 176 |
| 4.48 | MSE plot of train, test, and validation data. | 176 |
| 4.49 | Time Series Plot of Yield strength experimental, Yield strength MLPNN, Yield strength GA-MLPNN | 180 |
| 4.50 | Time Series Plot of UTS experimental, UTS MLPNN, UTS GA-MLPNN | 180 |
| 4.51 | Time Series Plot of Hardness experimental, Hardness MLPNN, Hardness GA-MLPNN | 180 |
| 4.52 | Time Series Plot of %elongation experimental, % elongation MLPNN, % elongation GA-MLPNN | 181 |

## List of Tables


| Table No. | Table Caption | Page No. |
|---|---|---|
| 2.1 | Tool material, workpiece material, and reinforcement used for FSW of composites. | 41 |
| 2.2 | Friction stir welded Al-$TiB_2$ composite–joint properties (Courtesy: (Vijay and Murugan 2010) | 49 |
| 2.3 | FSW process variables and joint efficiency of AMC joints | 55 |
| 3.1 | Chemical composition of matrix material (in wt. %) | 73 |
| 3.2 | Experimental Process Parameters. | 77 |
| 3.3 | Schedule for tensile testing FSW composites | 85 |
| 4.1 | Macrographs of FS welded AA6061-3 (wt%)Rutile composite to find the working range of process variables for tools with TC, SQ, and CSTC probes. | 109 |
| 4.2 | Weld quality at different rotational and welding speed combinations for a) TC, b) SQ, and c) CSTC tool | 111 |
| 4.3 | Macro structural pictures of AA6061-3(wt%)Rutile composites FS welded using TC tool | 112 |
| 4.4 | Grain size at different locations of the NZ of FS welded AA6061-3(wt%) rutile composite joint obtained using TC tool | 120 |
| 4.5 | Macrostructural images of AA6061-3(wt%) rutile composites FS welded at different process parameter combinations using SQ tool | 121 |
| 4.6 | Size of the grains at the different locations of the NZ of AA6061-3(wt%) Rutile composite joint fabricated at different process parameter combinations, using SQ tool | 123 |
| 4.7 | Macrostructural images of AA6061-3(wt%) Rutile composites FS welded at different process parameter combinations, using CSTC tool | 124 |
| 4.8 | Measured size of the grains at the top, middle, and bottom of the NZ of AA-6061-3(wt%) Rutile composite weld fabricated at various | 126 |

process parameter combinations using CSTC tool
4.9 Tensile strength of FS welded AA6061-3 (wt%) Rutile composite joints Welded using TC tool 139
4.10 Tensile strength of FS welded AA6061-3 (wt%) Rutile composite joints Welded using a combined square and threaded profile pin. 140
4.11 Tensile strength of FS welded AA6061-3 (wt%) Rutile composite joints Welded using a square profile pin 141
4.12 Tensile properties of composites joints FS Welded using TC tool 144
4.13 Tensile properties of composites joints FS Welded using CSTC tool 144
4.14 Tensile properties of composites joints FS Welded using SQ tool 145
4.15 Comparison of Average values of experimental results and repeatability test results. 145
4.16 Experimental design using L9 orthogonal array 156
4.17 Experimental results for each response 156
4.18 Analysis of variance for Yield Strength (MPa) 157
4.19 Analysis of variance for UTS (MPa) 158
4.20 Analysis of variance for Hardness (VHN) 158
4.21 Analysis of variance for % Elongation 158
4.22 Analysis of Variance of YS 161
4.23 Analysis of Variance of UTS 161
4.24 Analysis of Variance of Hardness 162
4.25 Analysis of Variance of % Elongation 163
4.26 Comparison of experimentally determined yield strength, UTS, hardness, and %elongation values with the predicted values by the RSM Model for friction stir welded AA6061/3wt% rutile composite 164
4.27 Normalized Values of Responses 167
4.28 Deviation Sequence, Grey Relational coefficient, and Grey Relational Grade 168
4.29 Grey Relational Grade (GRG) Response 168
4.30 Response values of the joint at trial 5 and joint with optimal process variables 169

| | | |
|---|---|---|
| 4.31 | ANOVA of GRG | 170 |
| 4.32 | Response values of the joint at trial 5, joints using TGRA using DA | 171 |
| 4.33 | TLBO algorithm predictions and the experimental values | 172 |
| 4.34 | Comparison of Optimized process parameter and Output response values. | 174 |
| 4.35 | Experimental Data. | 177 |
| 4.36 | Predicted values and corresponding Error from MLPNN | 178 |
| 4.37 | Predicted values and corresponding Error from GA-MLPNN | 179 |

## Nomenclature

| | |
|---|---|
| % El | Percentage Elongation |
| ABC | Artificial Bee Colony |
| Adj SS | Adjusted Sum of square |
| AI | Artificial Intelligent |
| $Al_2O_3$ | Aluminium Oxide |
| $Al_4C_3$ | Aluminium Carbide |
| AMCs | Aluminium matrix composites |
| ANN | Artificial neural networks |
| ANOVA | Analysis of Variance |
| AS | Advancing Side |
| ASTM | American Society for Testing and Materials |
| $B_4C$ | Boron Carbide |
| BM | Base Material |
| CSTC | Combined Square and Threaded Cylindrical |
| D/d | Shoulder diameter to pin diameter |
| DA | Desirability Approach |
| DF | Degree of Freedom |
| DOE | Design of Experiments |
| EDM | Electro Discharge Machine |
| EDX | Energy Dispersive X-Ray Analysis |
| Expt | Experimental values |
| F | Fisher's ratio |
| FEA | Finite Element Analysis |
| FS | Friction stir |
| FSW | Friction Stir Welding |
| GA | Genetic Algorithm |
| GD | Gradient Decent |
| Gr | Graphite |

| | |
|---|---|
| GRA | Grey Relational Analysis |
| GRC | Grey Relational Coefficient |
| GRG | Grey Relational Grade |
| HAZ | Heat Affected Zone |
| $H_v$ | Vickers Hardness |
| LM | Levenberg-Marquardt |
| $Mg_2Si$ | Magnesium silicide |
| MIG | Metal Inert Gas |
| ML | Sliding Torque |
| MLPNN | Multilayer Perception Neural Network |
| MMC | Metal Matrix Composites |
| MSE | Mean squared error |
| MT | Sticking Torque |
| NZ | Nugget Zone or Stir Zone |
| OA | Orthogonal Array |
| P | Probability |
| Pred | Predicted |
| PSO | Particle Swarm Optimization |
| R Err | Relative Error |
| RS | Rotational Speed |
| RSM | Response Surface Methodology |
| SEM | Scanning Electron Microscope |
| Seq SS | Sequential Sum of Square |
| SiC | Silicon Carbide |
| SQ | Square |
| TC | Threaded Cylindrical |
| TG | Tool Geometry |
| TGRA | Taguchi based Grey Relational Analysis |
| TiB2 | Titanium Diboride |
| Tic | Titanium Carbide |

| | |
|---|---|
| TIG | Tungsten Inert Gas |
| $TiO_2$ | Titanium Dioxide |
| TLBO | Teaching Learning Based Optimization |
| TMAZ | Thermo-Mechanically Affected Zone |
| TOPSIS | Technique for Order of Preference by Similarity to Ideal Solution |
| UTS | Ultimate Tensile Strength |
| WS | Welding Speed |
| $x$ | De-normalised value of input data |
| $x_{max}$ | Maximum value in data range |
| $x_{min}$ | Minimum value in data range |
| $x_n$ | Normalised value of input data |
| YS | Yield Strength |
| $ZrB_2$ | Zirconium Diboride |
| $\omega/v$ | Ratio of rotational/ welding speed |

# CHAPTER 1

# INTRODUCTION

## 1.1 GENERAL BACKGROUND

Aluminium matrix composite (AMC) refers to the class of high-performance, lightweight aluminium-centric material with two constituent parts, aluminium being a matrix and metal, ceramic or organic compound being a reinforcing material (Surappa 2003). These AMCs are found in a variety of applications in the locomotive, automobile, marine, and aerospace industries due to their superior qualities over the base material. AMCs exhibit ameliorated properties in terms of specific mass ratio, abrasion resistance, corrosion resistance, wear resistance, etc. (Ramnath et al. 2014, Mavhungu et al. 2017). AMCs have already replaced aluminium alloys in several applications where the tribological behavior of the material plays a critical role (Ozben et al. 2008, Dasgupta 2012).

The reinforcing materials are the primary load-bearing components in the AMCs. Therefore, particles such as SiC, $B_4C$, TiC, $TiB_2$, $ZrB_2$, $Al_2O_3$, fly ash, etc., which have better mechanical properties than the matrix are selected while fabricating a composite (Moona et al. 2018). Nowadays, minerals are transpired as potential reinforcement materials due to their environmental facets. Rutile is a copiously available low-cost mineral, composed of titanium dioxide ($TiO_2$). Being a natural form of $TiO_2$, rutile exhibits more significant wear resistance, better electrical and mechanical properties, and a lower coefficient of thermal expansion, which makes it an apt reinforcement for the composites (Arora et al. 2015a).

Difficulties in joining these AMCs through conventional fusion welding processes limit the potential application of these composites in specific industries. Effective welds in terms of quality and strength cannot be achieved by the conventional fusion welding process due to the formation of defects like porosities, solidification shrinkage, liquation cracking, non-uniform distribution of reinforcements, formation of brittle secondary phases in the weld region due to the reaction between matrix and reinforcements (Avettand-Fènoël and Simar 2016).

Friction Stir Welding (FSW), a welding technique that is both energy and environmental friendly, can be used to effectively address these problems. Being a solid-state welding process, FSW eliminates all the issues allied with the traditional fusion welding process and provides sound-quality joints.

## 1.2 THE HISTORY OF FSW

The FSW process is developed and patented by The Welding Institute (TWI) in 1991, to weld aluminium alloys. The temperature reached in the weld zone during FSW is lower than the parent material's melting point. The absence of both filler rods and a stringent welding environment made this process simple, compared to the fusion welding process (Thomas et al. 1991). Although FSW was developed to weld aluminum alloys, the application of FSW is efficaciously extended to join copper, magnesium alloys, steel, metal matrix composites, dissimilar metals, and alloys. (Ma et al. 2018).

It has been observed from the study that during FSW of aluminium, its alloys, and AMCs, grain structure at the weld zone was altered, resulting in varied mechanical properties. The combined effect of frictional heat, and severe plastic strain involved during the FSW process can develop finer grain and uniform dispersion of the reinforcement particles in the weld zone (Mishra et al. 2005). Hence the joint strength will improve during the FSW process. In addition, its environment friendliness, energy efficiency, and adaptability, make FSW a green technology welding process.

The quality of the joint produced by the FSW technique is dependent on several process variables such as rotational speed, tool traverse speed, axial thrust, tool pin geometry, tool tilt angle, and tool material (Nandan et al. 2008). Identifying the optimal FSW process parameters to join aluminium matrix composites is a critical issue in realizing the process. Consequently, there is a requirement to formulate modeling and optimization strategies for joining composite by the FSW process. Such issues are solved by using an engineering strategy to create a mathematical model. To study, forecast, and optimize the process factors of FSW of aluminium alloys, several studies employed mathematical models. The downside of this strategy is that it results in a single objective optimization or prediction procedure, which again generates a

new model to optimize more responses. An evolutionary algorithm such as a genetic algorithm can overcome these limitations, but efficient usage of this technique depends on the size of the population and the diversity of each solution in the given problem. Other evolutionary algorithms such as ABC and PSO are adopted by researchers. But successful usage of these techniques needs a proper selection of specific parameters related to the algorithm such as scaling, crossover, and mutation probability (Rao et al. 2011). To eliminate these limitations, an algorithm-specific parameter-less algorithm is developed by Rao et al. 2011, known as the Teaching Learning Based Optimization (TLBO) algorithm. It employs only general controlling variables like the number of iterations and population size for its working.

Artificial Intelligent (AI) techniques are preferred for highly complicated and nonlinear systems to anticipate multiple output characteristics depending on input variables. Industries benefit from the use of AI approaches for multi-objective prediction and optimization.

## 1.3 TLBO AND ARTIFICIAL INTELLIGENCE

### 1.3.1 TLBO Algorithm

Inspired by the teaching and learning process, Rao et al. (2011) developed a TLBO algorithm for process optimization. TLBO follows the principle of "how the teacher influences and enhances the output of a learner in the class" (Pawar and Rao 2013). The algorithm consists of two vital components namely Teacher and Learner. TLBO is based on two types of learning, one is through the teacher, and the other is through interaction among the learner known as the teacher phase and learner phase respectively. Being a population-based technique, a bunch of students (i.e., learners) is taken as the population in TLBO, and the subjects offered to the students are considered independent process parameters of the optimization problem. The results of the students are taken as the fitness value of the problem, which must be optimized.

### 1.3.2 GA-MLPNN

Artificial neural networks (ANNs) or Neural Networks (NNs) are the heart of deep learning algorithms whose architecture is inspired by the neural structure of a human

brain. Artificial neural networks (ANNs) are extensively used in solving complex problems like image recognition, indoor localization, peak-to-average power reduction, radar waveform generation, cancerous tissue identification, etc. (Mumali 2022). There are several types of ANNs namely Modular Neural Network, Feedforward Neural Network, Radial Basis Neural Network, etc. A more advanced form of the feed-forward neural network using the backpropagation method is the multilayer perception neural network (MLPNN). Genetic Algorithm (GA) was inspired by Darwin's evolutionary theory, which attempts to mimic the mechanics of natural selection and genetics. Each parameter represents a gene, and each solution represents a chromosome. A fitness (objective) function is used by GA to assess the fitness of each member of the population.

Neural networks have various tools like high convergence rates, different learning rules, different training algorithms, alternate transfer functions, etc. to improve the results or to achieve some required properties of the trained networks. However, when it comes to model building, the neural network has issues with interpretability and complexity. Thus, as the network's training develops, several attempts have been made to keep the gradient descent algorithm from becoming stuck in local minima.

The GA can scan multiple areas at once and has no restrictions on network topology. GA also offers the ability to choose solutions and does not require a back propagation technique. Hence by combining these two GA and MLPNN, we can overcome the problem of MLPNN being stuck in local minima.

## 1.4 PROPOSED WORK SUMMARY

A wide range of AMCs are being used in structural applications because of their higher strength-to-weight ratio and excellent mechanical properties. These composites are widely used in automobile, locomotive, and spaceship applications. However, the fabrication of AMCs involving joining through a conventional welding process leads to the deterioration of the properties of AMCs. By using friction stir welding, these issues can be solved. Finding the process variables to carry out individual experiments to get the appropriate joint strength is highly challenging. To analyze the FSW parameters, the orthogonal array approach (OA) (Taguchi design of experiment) aids

in achieving the optimum results. FSW trials were performed based on response surface methodology-based face-centered central composite design and the correlational models between the input process parameters and output responses have been developed. Conventional optimization methods such as the desirability approach and Taguchi-based grey relational analysis technique and Population-based evolutionary optimization technique namely TLBO have been applied for optimization. Further work is done to develop a prediction model for composite joints fabricated with friction stir welding. The GA-MLPNN-based prediction technique is chosen because it is capable of correctly predicting the yield strength, ultimate tensile strength (UTS), and hardness of the joint for the specified tool traverse speed/welding speed, rotational speed, and tool pin geometries. Validation experiments are run to validate the predicted model.

## 1.5 ORGANIZATION OF THE THESIS

In the present study, the investigation is conducted to evaluate the characteristics of AA 6061- 3wt% Rutile composites welded by the FSW technique. The influence of operational parameters on the joint properties was studied. Additionally, a meticulous analysis of the experiment was done using the orthogonal array (OA) technique. Single and multi-objective optimization was done using statistical techniques and evolutionary algorithms. Finally, a prediction model is developed using GA-MLPNN Technique. Various stages of these investigations are presented in the following six chapters as described below.

Chapter 1 explains the background along with the hurdles encountered and the motivation to carry out the present study. The objectives and an overview of the present investigation are also stated here.

Chapter 2 elucidates a detailed survey of the literature on the FSW process and its relevance in the joining of aluminium matrix composites. The manufacturing process used to produce AMCs is described, emphasizing the stir-casting process. The FSW process was explained briefly along with the material flow during the process. The joint characteristics (such as metallurgical and mechanical) of the welded composite are briefly discussed. The influence of process variables on the joint properties is

presented. The mathematical model developed for the multi-response analysis and optimization of the welding process is highlighted. The application of the ANN technique in the field of FSW process to predict mechanical properties is also emphasized. The goals and objectives of the current thesis have been established in light of the gaps discovered during a thorough literature review. This chapter also covers the use of Taguchi DOE, ANOVA, RSM, Grey Relational Analysis, Desirability Approach, and TLBO as well as a synopsis of the literature review, problem statement, objectives of the study, scope, and work plan.

Chapter 3 provides a thorough overview of the chosen experimental and measurement procedures to obtain the results of AA-6061-3wt% rutile composites being joined by friction stir welding. The detailed process for stir casting of composites, welding these composites to achieve superior weld quality, preparing specimens for various studies, and testing specimens to measure hardness and tensile strength are also included.

Chapter 4, explicates the characterization of as cast composite, quality of FS welded joints, Taguchi technique analysis of FSW process variables, and use of MLPNN technique for prediction of composite joint strength and hardness. The mechanical and metallurgical characteristics of the composite have been thoroughly examined and described. In FSW, the rotational speed, welding speed, and tool pin profile are varied in an initial attempt to determine the operating range to get the defect-free joints. Defects and their sources have also been thoroughly addressed. On those specimens that were defect-free, more investigation was conducted, and even their metallurgical and mechanical characterizations were reviewed.

Further, it discusses the analysis of the operational parameters employed to carry out the FSW process and the effect of those parameters on output responses using the Taguchi design of experiments. Response surface methodology is used to develop a mathematical model (response equation) for the analysis and prediction of output responses. Further, Multi response optimization is performed using conventional Grey Relational Analysis (GRA) and Desirability Approach (DA) and using TLBO, Prediction of process response is carried out by using GA-MLPNN.

Chapter 5 offers the general conclusion derived from the current research along with suggestions for future research directions.

# CHAPTER 2

# LITERATURE SURVEY

The relevance of the present work on friction stir welding of AA6061-3(wt%) rutile composites has been emphasized in Chapter 1. The current chapter concentrates on the work of numerous researchers in the field of developing aluminium matrix composites, FSW of alloys, welding of composites, and optimization and prediction techniques used in the present study. This chapter conducts and presents a comprehensive, in-depth, and critical literature assessment. The survey results include statistics and recommendations for a rigorous approach to experimental work, as well as an overview of previous work. The following key categories constitute the survey:

- Processing of Aluminium Matrix Composites (AMCs)
- Stir casting
- Welding of AMCs
- Friction Stir Welding (FSW) concepts
- Material Selection
- Material flow
- Microstructural changes in the weld area
- Effect of operational parameters on joint quality and Strength
- Analysis, Optimization, and Prediction Technique
- Application of FSW
- Limitations of FSW

## 2.1 PROCESSING OF ALUMINIUM MATRIX COMPOSITES

The emerging trends and advanced technologies have put forward the need for novel materials that possess an excellent combination of properties like high strength-to-weight ratio, improved toughness, better thermal, wear, and corrosion resistance in comparison with conventional monolithic materials. Composite materials, a derivative of conventional materials, exhibit superior thermo-physical and mechanical properties, substituting monolithic materials such as aluminium alloys, ferrous alloys,

and titanium alloys in several applications. The composite materials are composed of continuous phase (matrix) and discrete phase (reinforcements) constituents. Based on the type of reinforcements, composites are categorized as continuous fiber, discontinuous fiber, and particulate reinforced composite. Similarly, based on the chemical and physical nature of the matrix, composites are classified as metal or ceramic, or polymer matrix composites along with newly emerged carbon matrix and intermetallic matrix composites.

Metal matrix composites (MMCs) are transpired as promising materials in various industries due to their excellent, customizable physical, mechanical, and electrical properties as per the requirement. These materials exhibit higher strength-to-weight ratio, stiffness, corrosion and creep resistance, and abrasion resistance, both at room temperature and at elevated temperatures. Out of different MMCs, composites with aluminium as a matrix have gained attention from various industries such as locomotive, marine, automotive and aerospace industries in a variety of applications. Depending on the reinforced materials, Aluminium Matrix Composites (AMCs) exhibit improved physical and thermo-mechanical properties which can be tailored as per the requirement (Mustansar et al. 2019). However, the potential application of these AMCs for a specific application is limited due to a few drawbacks of these AMCs. The industry-ready material must possess homogeneous distribution of reinforced particles in the composite, better wettability, no/minimum porosity, and be chemically inert. The ease of joining these composites through the welding process is also a deciding factor in employing these materials for industrial applications.

AMCs can be prepared using different processing techniques. These techniques are broadly classified into in-situ synthesis and ex-situ synthesis processes. In the in-situ process, the formation of reinforcements in the aluminium matrix takes place by a single-step chemical reaction, which results in clean interfaces, better wettability/bonding, and reduced safety-related issues. One of the in-situ synthesis techniques is the XD process where a mixture of metallic and ceramic powders is heated above the melting temperature of metals (Mitra et al. 1993). In another process, ceramic reinforcements ($TiB_2$) are formed in the aluminium matrix through a chemical reaction (Herbert et al. 2008) However, the in-situ synthesis process faces some limitations such as kinetic and thermodynamic restriction which limits the size,

shape, and volume fraction and nature of the reinforcement as well as composition achieved during specified chemical reaction conditions. Some of the ex-situ synthesis processes are mentioned hereunder.

### 2.1.1 Powder Metallurgy

In this technique, fine metallic material and reinforcements with specific compositions are blended, pressed into a required shape, and bonded together with the help of degassing, heating, and thermo-mechanical treatments (Ravichandran et al. 2015). As it is a solid-state technique to prepare the composite, defects related to solidification such as porosity and shrinkage can be avoided in this process and reinforcement can be distributed homogeneously in the matrix.

### 2.1.2 Stir casting

This method, often known as the vortex technique, is the most basic and widely applied technique in the industry. Here reinforcements in the form of discontinuous hard particles are introduced into the matrix melt, stirred using an impeller at an elevated temperature, and then poured into a mold to get solidified in the required shape (Surappa 2003). Stir casting is a technique that can be utilized for industrial-scale mass manufacturing as it is less costly than other techniques.

### 2.1.3 Liquid metal forging or Squeeze casting

In this method, molten metal is poured into a mold cavity which is prefilled with fibers of the required size, shape, orientation, and volume fraction and is then subjected to an extremely high pressure for a specific time to get a final shape (Lawrence W. Cisko 1993).

### 2.1.4 Semi-solid powder processing

The required quantity of metal powder and reinforcements are first mixed. Further, this mixture is preheated to transform into a semisolid state and subsequently subjected to high pressure to form the metal matrix composite (Guo and Tsao 2000).

### 2.1.5 Diffusion bonding

In this process, preforms or continuous fibers are sandwiched between the layers of matrix foils and high pressure is applied at elevated temperature to form a composite by establishing a bond between reinforcement and the matrix through inter-diffusion (James 1997).

### 2.1.6 Rheo-casting or Compo-casting

The preheated short fibers or particulates are added into a highly viscous slurry of the metal matrix which is partially solid, by vigorous stirring. By continuous agitation, the viscosity of slurry reduces, leading to the mutual interaction among the reinforcements and matrix thus improving wetting and bonding between them.

### 2.1.7 Physical vapor deposition

Here, fibers are continuously fed through the high-pressure region of matrix material to form a thick metal coating on the fiber after condensation. An array of coated fibers are then assembled and hot-pressed to get a metal matrix composite.

### 2.1.8 Friction stir processing (FSP)

In this method, surface composites are prepared by severe plastic deformation and stirring of the workpiece material induced by a non-consuming FSP tool. Composites prepared by FSP techniques are free from pores, particles are uniformly distributed and fine equiaxed grain structures are produced in the composite.

In the processing of AMCs, stir casting has emerged as one of the promising methods, currently employed commercially as it has many advantages like simplicity, flexibility, and capability to manufacture a large quantity of products. Stir casting is the most favorable technique among all the available methods, because, in principle, it allows traditional metal production methods to be utilized, and allows exceptionally large parts to be produced, resulting in the reduction of the final product cost. Composite preparation cost by stir casting technique is about one-third of that by the

other methods and it is projected to be one-tenth when used in high-volume production (Hashim et al. 1999).

## 2.2 STIR CASTING

In the processing of AMCs through the stir casting route, reinforcement particles are stirred intensively in the molten aluminium alloy. Stirring of particles enables the proper distribution of agglomerated particles in molten alloy ensuring homogeneous distribution of reinforcements in the molten matrix.

Stir casting process parameters and the amount of reinforcements in the composites decide the quality and mechanical properties of the composites (Hashim et al. 1999). The critical points to be considered during the stir casting process are, a) Wettability between the matrix and reinforcement, 2) uniform dispersion of reinforcements in the matrix, c) Negligible or minimum porosity, and d) chemical reaction during the process.

In the stir casting process, achieving homogeneous dispersion of reinforcements in the matrix is one of the critical factors, which has a direct impact on the properties of the prepared composites. Uniform dispersion of the particles strongly depends on stirring time and speed, slurry viscosity, wettability, temperature, amount of gas entrapment, and the rate of solidification. Some of the major factors which affect the microstructure of cast composites are nucleation of particles, pushing of particles by the liquid-solid interface, settling of the particles in the matrix melt, and the chemical reaction between matrix and reinforcements at elevated temperature. The most observed issue in the stir casting process is the settling of particles in the bottom of the molten matrix during melt holding and while casting due to gravity. The mechanical properties of the composite are impacted by the heterogeneous distribution of the reinforcements in the matrix caused by particle settling.

Wettability between reinforcements and the matrix, affects the bonding quality among the constituents of the composite, thereby, controlling its final properties (Soltani et al. 2017). Wettability depends on the surface tension of the liquid matrix, the reinforcement’s surface energy, and the interfacial energy between the matrix and reinforcements. By reducing the surface tension of the liquid metal matrix, increasing the surface energy of the reinforcement, and decreasing interfacial energy between

solid reinforcements and molten metal matrix, wettability can be improved (Ghandvar et al. 2015). To achieve enhanced wettability, different techniques are employed such as the addition of alloying elements to the molten matrix, coating of reinforcements, and treating the reinforcement particles (Suthar and Patel 2018).

The presence of porosity is one of the key issues in the cast AMCs. During the stir-casting process, porosity may occur at the interface of the matrix and reinforcement. The size, dispersion, and volume fraction of the reinforcements in cast AMCs play a critical role in controlling the mechanical behavior of the composites (Bhandare and Sonawane 2013). Porosity in the cast material results in some of the defects such as ductility reduction, fracture of particles in the matrix-reinforcement interface due to the voids coalescence, failures initiated at the places of pores in the matrix, reduced corrosion resistance, and poor surface finish. The factors which assist the formation of porosity are, a) Entrapment of gas during stirring and mixing, b) hydrogen evolution, c) process variables like stirring speed, holding time, position, and size of the impeller, and d) shrinkage of the cast during solidification. Porosity in the composite cannot be eliminated, but it can be reduced to the minimum level by several methods such as degassing the molten matrix, bubbling of inert gas through the molten material, proper selection of process variables such as stirring speed, impeller size and its position in the melt, holding time, casting under pressure and solid state post-processing of the cast composite like rolling the cast composite to close the pores (Yigezu et al. 2013).

During the stir-casting process, dissolution of reinforcement may take place when the molten matrix is heated beyond a certain limit. These particles react with the matrix to form a brittle, needle-like secondary phase which deteriorates the mechanical properties of the composite. Thus, the mechanical property of the composite depends on the processing parameters and methods used to synthesize the composite material.

Moses et al. (2016) investigated the impact of stirring time, stirring speed, blade angle, and casting temperature on the mechanical characteristics of an AL6061-TiC composite synthesized using the stir-casting process. To reduce porosity, prevent TiC particles from clustering and segregating at grain boundaries, and have these particles distributed uniformly throughout the matrix, optimal values of the aforesaid factors are required.

Pazhouhanfar and Eghbali (2018) have prepared $TiB_2$ reinforced AA6061 matrix composite and have revealed that an increase in the $TiB_2$ content (up to 9 %) increases the tensile strength of the composite without compromising on elongation. To improve the wettability, $K_2TiF_6$ was added and $TiB_2$ particles were preheated to 250$^oC$ before adding to molten AA6061.

Thiagarajan et al. (2015) have investigated aluminium matrix-based hybrid composite by incorporating $TiO_2$ and Graphite with varying compositions. Mechanical properties such as tensile strength and hardness were improved with an increase in reinforcement contents, but clustering and non-homogeneous dispersion of particles were observed at a higher volume fraction of these particles (15% $TiO_2$ and 3% of Gr) due to the settling of hard particles at the bottom of the melt.

Aigbodion and Hassan (2007)have concluded that the volume fraction of SiC particles in the composite will have a direct relationship with the porosity level. As the amount of reinforcement in the composite rises, the porosity level rises as well, lowering the mechanical properties of the composite. Bhandare and Sonawane (2013) have reported that in SiC reinforced AA6061 matrix composite, wettability was achieved by keeping the matrix at a semisolid state. Further, it was observed that getting uniform distribution of particles in the liquid state was difficult to achieve. Preheating the mold drastically reduced the porosity level in the composite, which in turn enhanced the mechanical properties as reported by Bhandare and Sonawane (2013).

Bharath et al. (2019) incorporated two stage stir casting process to produce AA2014-$Al_2O_3$ composite. Adding reinforcement in two stages with a small interval in between and stirring the molten material before and after adding, drastically reduced the agglomeration of the particles in the matrix. Composites with higher volume fractions of reinforcements were prepared successfully with uniform distribution of particles without clustering.

Inegbenebor et al. (2018) worked on SiC reinforced AA6061 composite by varying SiC grit size and concluded that smaller grit size enables proper mixing and uniform dispersion, thereby enhancing the mechanical properties of the composite.

Li et al. (2016) developed an aluminium matrix composite with a high volume fraction of $B_4C$ by adopting a modified stir-casting process. Progressively adding

$B_4C$, Vacuum stirring, bottom pouring, vacuum casting, and in-air ingot cooling techniques were used to get high-quality composites in their study.

Soltani et al. (2017) have reported that shorter stirring periods and higher stirring temperature assist in incorporating SiC particles into the molten aluminium matrix and form a strong bond with it. But with higher temperatures, defects such as shrinkage, and porosity components, increased deteriorating mechanical properties.

## 2.3 WELDING OF ALUMINIUM MATRIX COMPOSITES

The promising properties of AMCs, make them employed in various industries such as automotive, marine, aeronautical, nuclear energy, etc. Various welding techniques were used to join metal matrix composites and are depicted in Figure 2.1.

Zhang et al. (1999) employed the vacuum brazing technique to join Al/SiCp MMC and found that the bonding quality in SiCp/ SiCp interface or Al/SiCp interface was poor and for the same process parameter, the joint strength reduces as the volume of the reinforcement-SiCp increases. Also, the results showed that, as the particle size increases, the joint strength decreases.

The vacuum diffusion bonding technique was adopted by Zhang et al. (1999a) to join SiC reinforced AMCs and observed that the strength of the diffusion joint varies inversely with the volume fraction of SiC particles. In addition, it was observed that achieving satisfactory joining quality in the dissimilar Al/SiCp diffusion joint is much more difficult.

Lei et al. (2011) studied plasma arc welding of SiCp/Al MMCs using Ar-$N_2$ mixture as plasma gas and Ti as filler material and showed that harmful $Al_4C_3$ needle-like phases are eliminated in the weld zone but other defects were still present in the joint such as slender, needle-like AlN phase, bulky $Al_3Ti$ phase, and segregation of particles. Further, the maximum joint strength achieved was 70% of that of the base material.

Ureña et al. (2000) adopted TIG welding to join AA2014/SiC composite and observed that severe microstructural changes happened along the depth of the weld. The top region of the weld area consists of completely dissolved SiC particles and brittle $Al_4C_3$ flakes. The middle region had partially dissolved SiC particles and smaller $Al_4C3$ flakes whereas the bottom region had $Al_4C_3$ crystals. Further, it was observed

that joint strength was about 50 % of the base material. Xi-he et al. (2009) performed TIG welding of Al-SiCp composites using Al-Si filler and Argon-Helium shielding gas. The use of gas helps in arc stability and the addition of filler assists in depressing harmful reactions at the matrix-particle interface, thus improving the quality of the joint. However, the non-uniform distribution of particles could not be avoided in the weld region.

Salazar and Barrena (2003) have carried out metal inert gas welding of AA7020/$Al_2O_3$ using Al-Si and Al-Mg fillers. It has been observed that the mechanical properties of joints deteriorate as a result of hardening precipitates dissolving at higher temperatures. The joint strength was reduced to 60% of that of the base material.

Wang et al. (2000) have utilized a modified laser beam welding process to weld Al6061/SiCp composite by adding Ti as an alloying element. The formation of harmful needles like $Al_4C_3$ is eliminated and superior quality weld was formed but some large pores were found in the partly melted zone. Storjohann et al. (2005) reported that during laser welding of $Al_2O_3$ reinforced AA6061 matrix composite using laser welding, clustering of $Al_2O_3$ particles and porosities was observed in the weld region, which drastically reduced the mechanical properties of the joint.

Bassani et al. (2007) worked on laser welding of A359/SiC composite using a $CO_2$ Diode laser source. Welding with $CO_2$ laser results in the dissolution of SiC particles and the formation of $Al_4C_3$ which makes the weld zone harder compromising the toughness of the joint. Whereas the use of a Diode laser reduces the formation of brittle $Al_4C_3$, the laser has limited penetration. Guo et al. (2012a) studied laser welding of AA1100/$B_4C$ composite with and without Ti filler. Needle-like $AlB_2$ and $Al_3BC$ phases were observed in the weld zone joined without filler. The addition of Ti foil reduces the formation of harmful phases, instead, TiC, $TiB_2$, and $Al_3Ti$ phases formed in the weld which improved the joint strength. Meng et al. (2013) used a laser welding technique to join $TiB_2$-reinforced metal matrix composite and reported that as the volume fraction of $TiB_2$ increases, the weld quality deteriorates.

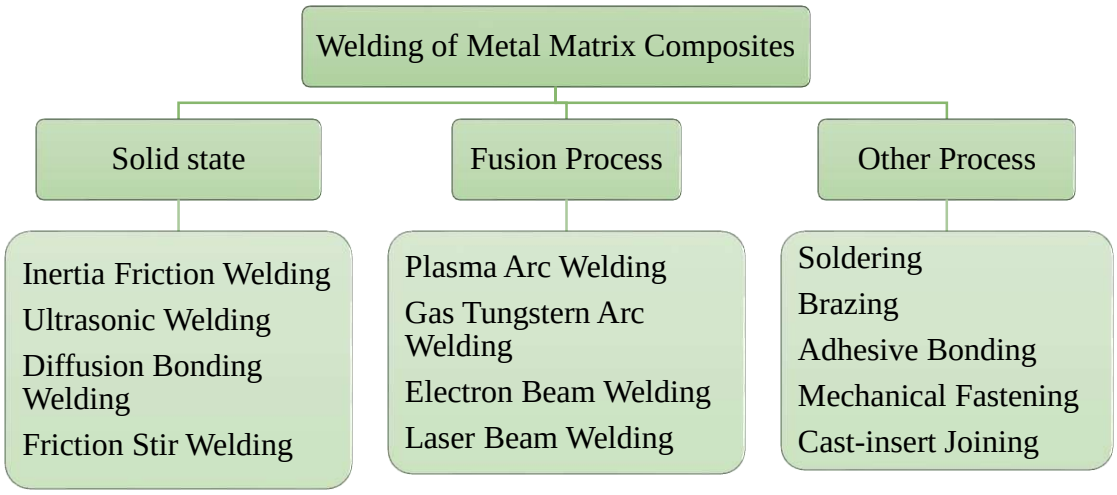


**Figure 2.1** Classification of the welding process to join the MMCs.

Chen et al. (2006) have studied the electron beam welding of $LD_2$/SiCp composite and reported that an interfacial reaction occurs forming $Al_4C_3$ precipitates. The size and quantity of $Al_4C_3$ are less in lower heat input and both are increased at higher heat input. Mechanical properties of the joint degrade at higher heat input due to the formation of brittle phases.

### 2.3.1 Key issues in welding of aluminium matrix composites.

AMCs are composed of aluminium. An aluminium alloy as matrix and hard reinforcement with the volume fraction varying from 0.1% to 60 %. AMCs are considered ideal, lightweight with high strength and new generation material. However, the use of this material in specific industrial applications has been limited due to the difficulties involved in joining these materials by conventional welding methods. There are several key issues associated with the welding of AMCs.

#### 2.3.1.1 Solidification effects

Particulate aluminium matrix composites are reinforced with non-metallic reinforcements such as $Al_2O_3$, SiC, TiC, $TiB_2$, $B_4C$, $YiO_2$, etc. In comparison with the matrix material, these reinforcements have different weights which results in segregation and settling at the bottom of the matrix when it is in a molten state.

In a molten state, the weld pool of composite is more viscous than the pure aluminium or alloy weld pool. The higher viscosity of the weld pool restricts the flow of material and reduces the heat transfer by the convective method. This greatly affects the grain structure and stress formation in composite during solidification. This type of solidification effect is commonly found in the fusion welding process and also these are difficult to control. While joining composites, it is necessary to select the welding technique carefully to prevent the dissolution of reinforcements and the heterogeneous packing density of the particles resulting from the transfer of reinforcements into the weld zone.

#### 2.3.1.2 Chemical reactions

From the literature, it is observed that some conventional fusion welding methods are used to weld a few particular AMCs. It is necessary to control the temperature during welding to prevent the dissolution of reinforcement particles, interdiffusion, and the development of hard, brittle harmful secondary phases in the weld zone. For example, in welding of SiC reinforced AMCs, SiC reacts with the molten aluminium alloy at elevated temperature and forms needle-like $Al_4C_3$ and thus increases the silicon content in the weld zone during solidification. Likewise, graphite or carbon particles react with the molten matrix to form detrimental phases. The presence of moisture affects the welding process as the metal carbides decompose releasing hydrocarbon gases, which enhance the weld susceptibility to corrosion and degradation of joint strength. The chemical compatibility of reinforcement and matrix for a given welding technique largely depends on the material and the type of process.

Most of the fusion welding processes work on higher thermal energy, which cannot be applied to join AMCs. For instance, most of the laser energy used in the welding process is absorbed by the reinforcements in comparison with the matrix, in the narrow weld zone of high heat flux. So, to minimize the detrimental reaction between the reinforcement particles and the molten metal, it is required to automate the fusion welding process by carefully controlling welding speed and temperature.

#### 2.3.1.3 Joint preparation

Before welding, joint preparation is necessary for some of the welding processes. As composites are reinforced with hard particles, these composites exhibit low ductility,

and high wear resistance and are difficult to machine using standard cutting tools of steel. AMCs with a high volume percentage of reinforcements (40-60%) behave like hard ceramic material which makes them hard to machine. While preparing the AMC joint before the specific welding, the operational parameters such as speed, feed, and force must be carefully selected and controlled to prevent the tearing of the composite panel or to avoid cracking. The use of diamond or diamond-coated tools is necessary to machine AMCs during joint preparation.

According to the literature, it is found that the joining of composite by conventional welding process has several drawbacks such as

- Formation of porosities and inclusion of impurities due to high solubility of gases in the molten matrix
- Non-uniform dispersion of reinforcement in the weld region, and dissolution of particles
- The production of needle-like, brittle secondary phases is due to the detrimental interaction between reinforcement and matrix.
- Clustering of particles when they are of nano size, or on account of poor wettability
- Defects related to solidification like, shrinkage, porosity, and cracking
- Extremely high residual stress and distortion as a result of the matrix's and the reinforcement's different thermal expansion coefficients.

These defects affect the weld's quality and degrade the AMCs' mechanical qualities. Solid-state welding has emerged as a viable technology for joining AMCs to produce joints of excellent quality. The temperature reached during solid-state welding is lower than the work piece melting point. As a result, all defects related to the material solidification are removed.

The friction stir welding method for joining aluminium alloys was developed and patented by The Welding Institute (TWI) in 1991 (Threadgilll et al. 2009). The precipitation-hardening aluminium alloys such as 7XXX and 2XXX series, are successfully joined by the FSW process, which is otherwise difficult to weld using the traditional fusion welding process (Cavaliere 2013). Further attempts are made to successfully join Cu, Mg, Ti alloys, aluminium, magnesium, steel-based metal matrix composites reinforced by carbides (SiC, TiC or $B_4C$), oxides ($Al_2O_3$ or $Y_2O_3$), nitride

(AlN), borides ($ZrB_2$, $TiB_2$) or silicide precipitates ($M_2Si$) (Heidarzadeh et al. 2020). Prolific literature has shown FSW can successfully be used to join difficult-to-weld materials with enhanced mechanical qualities and no weld defects (Avettand-Fènoël and Simar 2016). However, in contrast to aluminium alloys, the presence of reinforcing components limits the range of welding conditions in AMCs.

In recent years several researchers have worked on FSW of aluminium matrix composites. The detailed study on FSW has inferred the following important aspects of the process. First, AMCs which are reinforced with up to 30 (vol %) of hard ceramic particles joined successfully and superior quality weld with superior mechanical properties and without any defects were obtained using the FSW process. Further metallurgical study of friction stir welded joint revealed that no chemical reaction between matrix and composite was observed in the weld zone (Parikh et al. 2019). Second, the distribution of reinforcement particles was homogeneous, and no clustering of particles was observed in the weld zone as revealed by the microstructural studies. In comparison with the base material, the size of the particles was drastically reduced in the weld zone due to the collision among the particles, abrasion, and fragmentation action of the tool (Li et al. 2018). Thirdly, FSW of AMCs resulted in better and enhanced mechanical properties in the joints in comparison with AMCs joined by tungsten inert gas welding (TIG) (Muñoz et al. 2008). These factors make FSW a potentially viable route to join AMCs. Further, its fundamental benefits such as enhancement in joint efficiency, high production accuracy, and cost reduction have resulted in FSW as one of the attractive welding solutions for difficult-to-weld aluminium series like AA2***, 6***, 7***, and their composites.

## 2.4 CONCEPT OF FRICTION STIR WELDING

Industrial application of the AMCs mainly depends on the successful and effective joining technique. The presence of reinforcement particles makes it difficult for fusion welding methods to satisfy the joining requirement of composites. Solid-state welding of AMCs has a greater advantage over traditional fusion welding. In the year 1991, “The Welding Institute”, Cambridge (Thomas WM et al. 1991), developed a welding technique to weld aluminium without melting it, named friction stir welding (FSW). The FSW process is similar to milling, except instead of removing material, it joins it.

The welding process can be performed on a dedicated FSW machine or by using a conventional milling machine. One type of FSW machine is shown in Figure 2.2, FSW process was found to be an environmentally friendly versatile, and energy-efficient process.

**Figure 2.2** Friction stir welding machine (Courtesy: ETA Technology Pvt. Ltd. India, Friction Stir Welding Machine)

The fundamental requirements of the FSW process are a constant heat source, regular workpiece motion concerning the tool, uniform deformation of the material, and consolidation in the weld zone. Figure 2.3 displays a schematic illustration of the FSW process. In this process, a non-consumable tool with a pin and shoulder constructed of a tougher material is utilized. The revolving FSW tool is inserted into the workpiece's adjacent edges until its shoulder meets the surface. The tool is made to travel along the weld line after a short dwell time. The friction between the rotating tool and stationary workpiece during the insertion of a rotating tool causes a significant amount of heat to be generated, which plasticizes the workpiece at the weld zone. Rotating shoulders also generate frictional heat at the tool-workpiece surface interface and help compaction of material below the shoulder. The solid joint is formed using frictional heat and heat caused by the severe deformation of material due to applied axial force (Buffa et al. 2008).

FSW tool serves three important purposes i.e., a) develop sufficient frictional heat in the parts to be welded by friction between the workpiece and revolving tool (Shoulder

and pin), b) Induce proper material flow in the weld region, c) Constrain and act as a reservoir for the heated material under the shoulder (Zhang et al. 2012). The heat is developed due to the friction of the revolving FSW tool probe and shoulder with the workpiece and by the deformation of the material in it. The workpiece material around the FSW tool probe gets softened due to the localized heat. Combined linear translation and rotational movement of the tool enable the transfer of the softened plasticized material from the front side along the perimeter of the tool probe to the rear end of the tool probe. Thus, the plasticized material fills the gap left by the tool for onward movement. The tool shoulder limits material movement away from its bottom surface and exerts an axial force on the plasticized material that has softened. Under the shoulder, the material solidifies and creates a solid joint.

The tool's combined rotation and translation motion separates the weld zone into two areas. The side where the tool translation direction is the opposite of the tool rotational direction is known as the retreating side, and the side where they are equal is considered the advancing side.

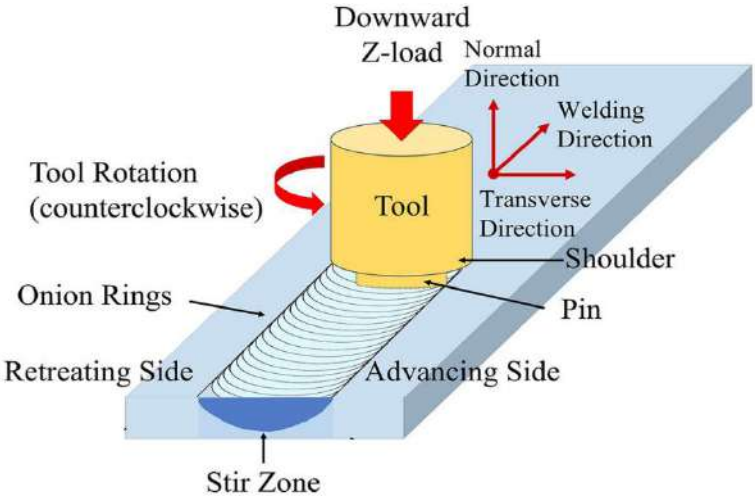


**Figure 2.3** Friction Stir Welding terminology (Lin et al. 2020)

The welding process variables are the key controlling features of the FSW process. These process variables influence the generation of frictional heat and flow of plasticized material and ultimately affect the microstructure, joint quality, and mechanical properties of the joint. The process variables are tool rotational speed, welding speed, tool pin geometry, tool tilt angle, and axial force. The relative angle between the workpiece and the axis of the tool is called the tool tilt angle.

The detailed procedure of the FSW technique is shown in Figure 2.4(a-f) along with the velocity vector values along all three axes as Vx, Vy, and Vz. The first step is to plunge the tool into the adjoining edges of the workpiece as shown in Figure 2.4a. The revolving tool approaches the workpiece at a constant speed (Vz) in this stage whereas the velocity vector along the other two axes is zero. The depth of plunging depends on the workpiece thickness, tool probe height, and axial force. The next step as shown in Figure 2.4b is dwell time where the tool is rotating at a constant speed, but the linear movement of the tool was absent hence all the velocity vectors become zero. In the next stage, the revolving tool is made to travel along the weld line at a predefined constant tool traverse/welding speed Vx as shown in Figure 2.4c, keeping the other two velocity vectors zero. The second dwell period is depicted in Figure 2.4d, where the tool traverse is stopped but the tool remains continuously revolving at a constant speed. Velocity vectors in all three axes are zero. Figure 2.4e shows the final stage of the process where the tool is retracted from the workpiece with a constant velocity of Vz and velocity along the other two directions is zero.

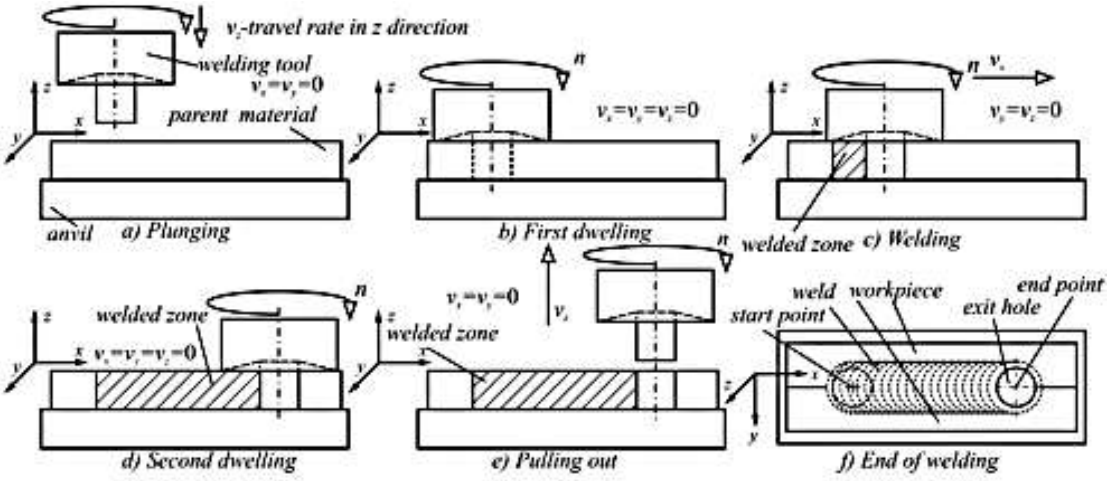


**Figure 2.4** Schematic representation of friction-stir welding process (Courtesy: NASA/TM--1999-209876)

Material flow in the weld zone is largely dependent on two criteria. One is a result of the extrusion process, in which the plasticized, softened material is forced outward by the combined action of the tool probe moving within the workpiece and the applied axial force. Another is due to the driving force developed due to the rotation of the

tool probe. The flow of material in the FSW process is discussed in detail in the following sections.

## 2.5 MATERIAL SELECTION

AA6061 is one of the most widely employed materials for structural application. The use of AA6061 in a variety of applications is mainly due to its few favorable properties such as easier formability, heat treatable, corrosion resistance, and good mechanical properties. These properties make AA6061 one of the important materials in aerospace, automotive, locomotive, and marine application.

One of the major inventions in the new material is the development of aluminium matrix composites (AMCs). They provide a profile of properties in such a way that existing monolithic materials are hard to offer it. AMCs are tested and employed in a lot of functional, structural, and non-structural applications in various industries.

The aerospace and automotive industries have a growing demand for inexpensive, lightweight materials. Also, due to environmental factors, research and development in mineral reinforced composites were started, which found their uses in the various parts of the automotive and defense industries. Minerals have emerged as a viable replacement for the ceramic reinforcements that are frequently employed in AMCs due to their low cost, availability, and environmentally benign behavior. Few natural minerals have great potential to be used as particulate reinforcements in composite manufacturing. Natural minerals like sillimanite, bauxite, corundum, talc, feldspar, etc. in the form of particles were used in the fabrication of aluminium alloy matrix composite for a variety of wear-resistant and structural applications. Rutile is one of the abundantly available, low-cost minerals, composed mainly of titanium dioxide ($TiO_2$). Being a natural form of $TiO_2$, rutile exhibits superior wear and corrosion resistance, better electrical and mechanical properties, lower coefficient of thermal expansion, higher thermal shock resistance, and thermal stability at elevated temperatures. Maity et al. (1995) processed Al-$TiO_2$ composite by stir casting method and studied the effect of volume fraction of reinforcement on particle distribution, void formation, and solidification process. It was reported that, though the wettability during stir casting was improved by the addition of magnesium into the melt, the addition of $TiO_2$ only up to 3% mixes properly with the melt. However, up to 20% of

$Al_2O_3$ and SiC can be incorporated into the molten aluminium. This is because $TiO_2$ has a much lower apparent density compared with SiC and $Al_2O_3$. The ratio of density to apparent density is much greater in the case of rutile particles, which probably leads to improper incorporation of particles in the matrix during the addition of $TiO_2$ beyond 3%. Ramesh et al. (2005) fabricated AA6061/$TiO_2$ composite through a liquid metallurgy route and evaluated its mechanical properties. The study revealed that $TiO_2$ was homogeneously distributed in the matrix when its volume percentage was less and as the volume fraction increases, the agglomeration of particles was observed. The composite exhibited a lower wear coefficient and higher hardness compared to the base aluminium alloy. Chaudhury and Panigrahi (2007) reinforced rutile particles with Al−2Mg using spray forming and sir casting techniques to evaluate the recrystallization kinetics of Al–2Mg–$TiO_2$ composites. The study revealed that faster recrystallization in cast condition occurred due to the thermal stresses induced into the composite owing to the thermal mismatch between the $TiO_2$ particle and Al matrix. Additionally, a significant improvement in the composites' mechanical properties was seen.

Elango and Raghunath (2013) investigated the tribological behavior of the stir-cast LM25+SiC+$TiO_2$. The study showed that increasing the volume content of $TiO_2$ in the composite reduces the wear rate due to the hardened nature and lubricating properties of the $TiO_2$. The composite also exhibited high strength and hardness.

Arora et al. (2015a) investigated the effect of $TiO_2$ particle size on the wear properties of LM13 aluminium alloy reinforced with $TiO_2$ composite. As the particle size becomes smaller and smaller, the wear resistance of the composite increases. Even at elevated temperatures, the composite exhibited better wear-resistant properties, making it an ideal material for IC engine parts and structural elements exposed to wear at higher temperatures. Kumar and Rajadurai (2016) studied the influence of natural rutile on the microhardness and wear properties of aluminium matrix-based hybrid composite. The addition of rutile enhanced both the density and microhardness of the composite compared to the base material. The composite showed better wear and mechanical properties. Yoganandam et al. (2016) evaluated the mechanical properties of $TiO_2$ reinforced AA6082 matrix composite prepared using a semi-solid

compo casting method. The study inferred that the addition of $TiO_2$ enhances the tensile strength of the composite significantly.

Gupta et al. (2019) used sillimanite and rutile minerals as reinforcement in the LM27 aluminium alloy matrix and evaluated their mechanical properties. The addition of rutile particles resulted in the refinement of the Si phase in the composite. The coefficient of friction was less in rutile reinforced composite due to its lubricating effect.

Abraham et al. (2019) worked on 6063/$TiO_2$ composite fabricated via friction stir processing (FSP) and evaluated microstructure and mechanical properties. Up to 18 (vol %) of rutile particles were successfully incorporated into the matrix element without clustering of the particles. A higher number of particles deteriorates the mechanical behavior of the composites due to the agglomeration of $TiO_2$ particles.

Rutile reinforced composite can find its application as wear-resistance components such as pistons, cylinder heads, and brake drums in the automobile sector and pump bodies in mineral processing industries Arora et al. (2015b). AA6061-Rutile composite is mainly proposed for automobile and avionics parts such as engine piston and connecting rods, valve and valve parts, brake pistons, hydraulic pistons various fittings used in marine, aircraft, etc., contactors, couplings, and structural parts such as bicycle hubs and bike frames (Sivasankaran and Alaboodi 2016).

## 2.6 MATERIAL FLOW PATTERN

The flow of material during the FSW process is complex and many mechanisms are presented to describe it. It involves plastic deformation during the process and complex material movement (Li et al. 1999). The geometry of the tool, the welding parameters, and the kind of joint design all have a significant role in the material flow pattern in FSW. During FSW, plunging the tool into the workpiece creates a cavity in the workpiece and the shape of it is dependent on tool pin geometry. Interaction between the rotating tool and the workpiece generates frictional heat which plasticizes the workpiece material around the rotating pin. The plasticized material is covered by the adjacent colder workpiece material and the bottom back plate. The material flow path is decided by this arrangement and the combined tool motion (both rotation and translation) along the weld direction. The material present at the leading side of the

workpiece can gradually plasticize and travel to the retreating side due to two distinct modes known as tool pin-driven and shoulder-driven flows. Further softened plasticized material flows through the retreating side of the weld zone and gets deposited at the rear side of the tool to form a solid joint (Colligan 1999a) (Seidel and Reynolds 2001). The typical flow pattern of materials in the FSW process is depicted in Figure 2.5. Colligan (1999b) experimented to evaluate the material flow pattern in dissimilar aluminium alloys namely AA6061 and AA7075. Grooves are made along the welding direction at different distances and small steel balls called tracers are inserted in these grooves to understand the material flow pattern. Radiographic examination of friction stir welded specimens revealed that distinct parts of the workpiece show different flow patterns. The threads or grooves on the FSW tool pin enable the forcing of stirred material into the downward direction. Similar to an extrusion operation, the softened material is transported around the tool probe's retreating side. It was noted that the pattern of material flow on the advancing and retreating sides differs (Seidel and Reynolds 2001). The shoulder of the tool rather than the tool probe threads affects the plasticized material flow at the top region of the weld zone, up to 1/3 thickness of the weld zone (Guerra et al. 2002). Due to the tool shoulder profile, a substantial amount of softened material flows to the advancing side from the retreating side at the top region of the weld zone. As a result, the flow of material in the weld region causes complex material movement along the weld line as well as vertical mixing of the material.

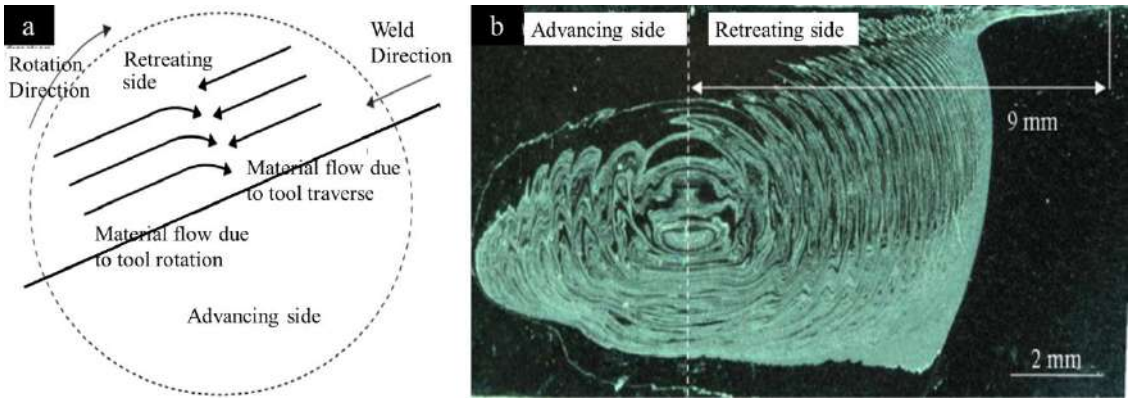


**Figure 2.5** Material flow pattern in FS weld one [ Hamilton et al. (2008)] (a) Nugget top region and (b) Nugget cross-section.

### 2.6.1 Realization Mechanism of Friction Stir Weld

There are two types of material flow during FSW known as pin driven and shoulder driven. During shoulder-driven flow, the softened material is transferred from the retreating side, through the shoulder surface. The transferred material gets deposited at the top of the advancing side with forging action caused by the tool. Whereas during pin-driven flow, the material moves around the periphery of the tool pin, layer by layer due to the extrusion process, and is stacked continuously along the weld line. As it is observed by Sinha et al. (2008), the extrusion of material around the pin and the shearing effect of the shoulder results in layer-by-layer material movement in the weld zone. Once the pin-driven and shoulder-driven materials interact at the retreating side, the softened material flows to the advancing side. As this interaction progresses, the merging of material driven by both pin and shoulder takes place. If there is sufficient temperature and hydrostatic pressure developed, then material flows and fills the weld cavity (Kumar and Kailas 2008a). Figure 2.6 shows a schematic representation of material flow driven by pin and shoulder during the FSW process.

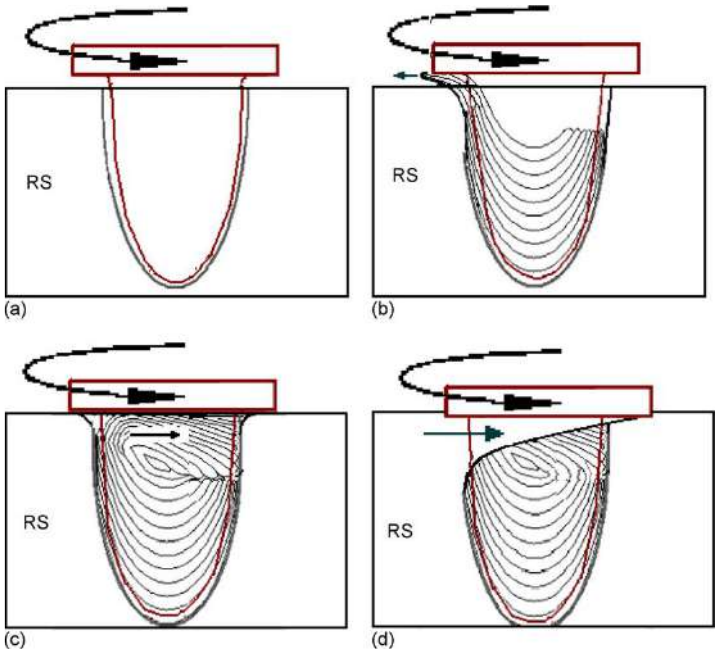


**Figure 2.6** (a) Weld cavity formation due to tool insertion (b) material flow driven by a pin, (c) Merged material flow driven by both pin and shoulder and (d) Pulling of base material into NZ (Courtesy: Kumar and Kailas 2008b)

### 2.6.2 Influence of FSW Tool on Material Flow

The microstructural features obtained after the friction stir welding process closely resembles the microstructures that resulted in hot worked (Extrusion and forging) aluminium alloys (Arbegast 2008). The different mechanical processing regions formed during the FSW process are depicted in Figures 2.7 (a-b). Conventional metal working models can be used to model the flow of material in the FSW process. The metal working model includes different zones such as preheating, initial deformation, extrusion followed by forging and finally cooling of the metal. Similarly, in FSW, the region in front of the tool pin is considered a preheating zone. As a result of mechanical deformational heat and frictional heat developed by the interaction between the hard rotating tool and the stationary workpiece, the temperature at the preheating zone steadily rises.

The thermal characteristics of the material and the welding speed affect the heat transfer rate during the FSW process. The heat generated at the tool-workpiece interface raises the temperature of the workpiece above a critical point, causing the material to soften and plasticize. Additionally, the induced stress is greater than the critical flow stress of the material, which causes the flow of material during the FSW process. As shown in Figure 2.7 (a-b), the material is forced both downward into the extrusion zone and upward into the shoulder zone.

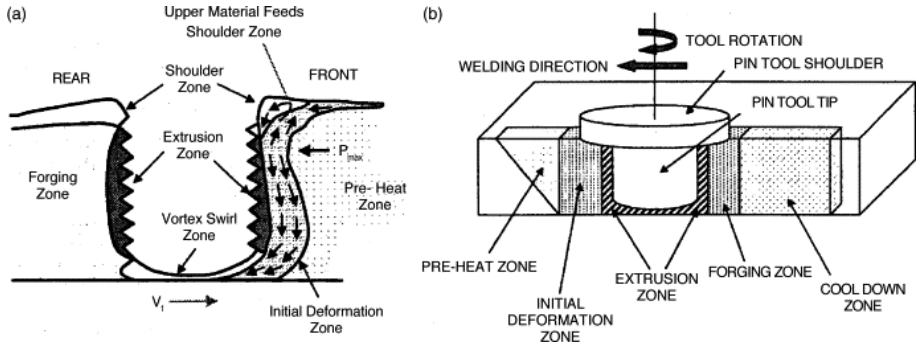


**Figure 2.7** (a) Pattern of Material flow and (b) zones of mechanical processing created during friction stir welding (Courtesy: Mishra et al. 2005).

As the tool probe rotates in the workpiece, a small vertex swirl zone is formed below the probe tip. The material captured in this zone experiences vortex flow patterns. In the extrusion zone having a fixed width, the material circulates the probe from leading

to the trailing edge. The critical isotherm on each side of the tool controls the extrusion zone width, where the attained temperature and the amount of stress are inadequate to let the flow of materials. The forging zone, where the cavity is generated by the tool moving forward, comes after the extrusion zone. Hydrostatic pressure forces the plasticized material from the tool front into the cavity. The tool shoulder both applies downward forging force and allows for the restriction of the softened material in the cavity. The material in the shoulder zone is dragged forcefully to the advancing side from the retreating. A post-heat or cool zone follows the forging zone, where the plasticized material cools either naturally or artificially.

The materials at the weld region go through three distinct types of flows during FSW. As the tool spins within the workpiece, the softened material is first transferred along the periphery of the tool. Next, the threads of the tool probe transmit the plasticized material in the downward direction in close vicinity to the tool, causing an equivalent quantity of material that is distant from the pin to travel upward. The workpiece and the tool also move relative to one another. A sound FSW joint is produced by the combined influence of these flows. The width of the flow area for recirculating plasticized material is determined by the rate of heat transfer, welding process parameters, and material qualities.

According to Zhang et al. (2005), the material flow on the retreating side differs from the advancing side. Figures 2.8 (a) through (b) and 2.9 show the flow of material during FSW. The material flow was simulated using finite element analysis. A study found that at the advancing side, softer material develops a fluidized bed, closer to the probe and moves around the probe. But on the retreating side, the material never moves into the rotational zone. Several revolutions later, the material on the advancing side begins to slough off behind the probe.

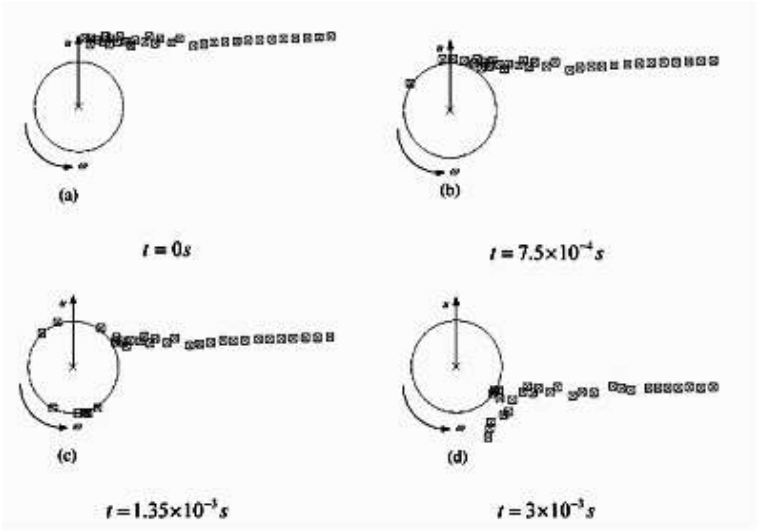


(a)

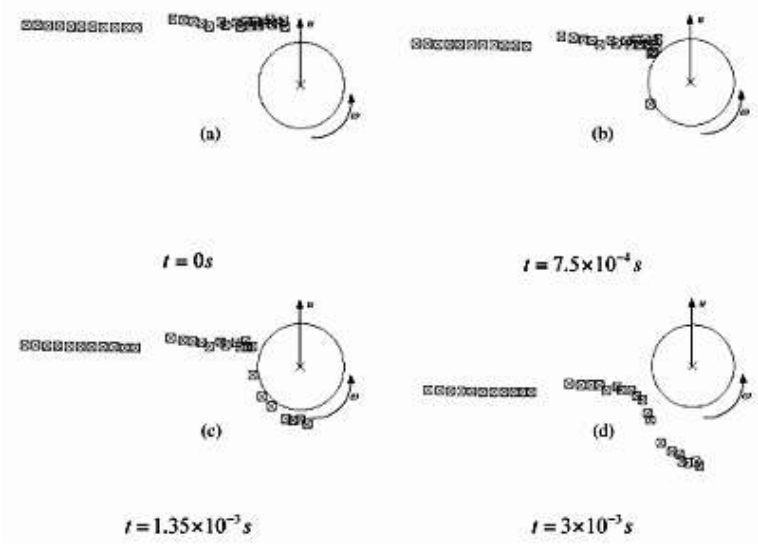


(b)

**Figure 2.8** The material flow when u = 2 mm/s, ω = 390 rpm at a) Advancing side, b) Retreating side (Zhang et al. 2005)

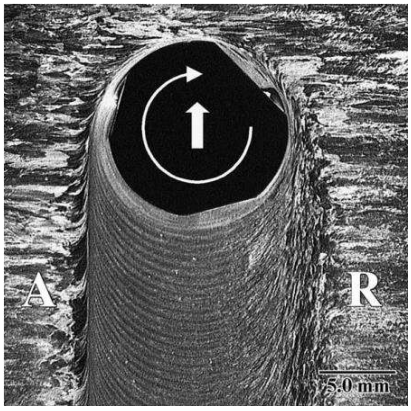


**Figure 2.9** Flow of material when the tool rotates in a clockwise direction (Fonda et al. 2004)

The material flow pattern in a threaded pin is depicted in Figure 2.10. A threaded profile pin aids in confirming that the plastically deformed material is evenly dispersed around the tool probe, as well as from the upper to lower weld portions and vice versa. According to Fernandez and Murr (2004), the threaded profile pin reduces mean particle size by 25% as opposed to the threadless pin, which reduces mean particle size by 7%. The thread pitch is another key factor in FSW. The pitch will behave more like a drill than a stirrer if it is between 1.40 and 2.0 mm. The workpiece material is pushed outward as a result of this impact, forming chips.

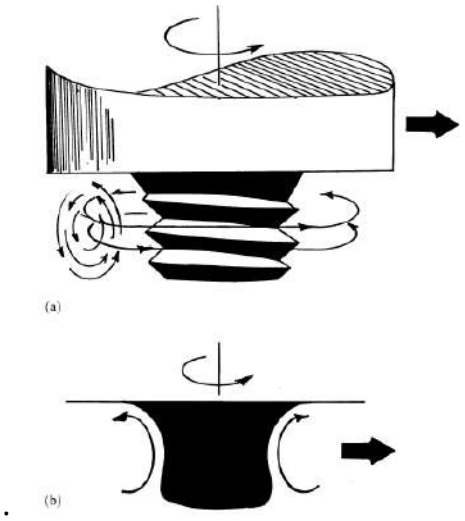


Figure 2.10 Helical pattern material flow around threaded probe (Fernandez and Murr 2004)

Similar mechanical and metallurgical characteristics were demonstrated when 0.85 mm and 1.10 mm thread profile pin pitch was employed by Boz and Kurt (2004). Hattingh et al. (2008), claim that an FSW tool having a threaded pin promotes plastic flow and assists the downward movement of material when the orientation of a thread is in the opposite direction of the spindle rotation.

According to Schneider et al. (2006), the maker tracer approach can be used to examine the flow of material that is plastically deformed in the FSW process at the weld region. The titanium and lead wire, which served as a marker, was positioned, below the material top region (approximately 1.3 mm) on the advancing side. Periodic trace patterns made up of segments with an arc form were seen on this side.

Chen and Cui (2008) used the pin-breaking approach to investigate the flow of material in threaded probes. It was observed that the sheared layer entirely detached from the pin with each tool rotation. A void is created rear of the tool on both sides as it moves forward. By forcing a separated layer to flow into this cavity, a nugget is created by the shear zone material.

## 2.7 DEVELOPMENT OF MICROSTRUCTURE AT WELD REGION

The investigation of the microstructural development of FS welded aluminium alloys has received considerable interest. The composition of the material and the heat treatment produce variations in the size and morphologies of the grain and crystallographic textures in aluminium alloys. Threadgill (1997)made the initial attempt to classify the weld zone depending on microstructures (Friction stir welds in aluminium alloys, Bulletin, March 1997). Figure 2.11 depicts the various microstructure zones that emerged at the weld site after welding. The weld zone is seen to be divided by the system into four distinct regions namely Nugget Zone or Stir Zone (NZ or SZ), Thermo-Mechanically Affected Zone (TMAZ), Heat Affected Zone (HAZ), and Unchanged Base Material (BM).

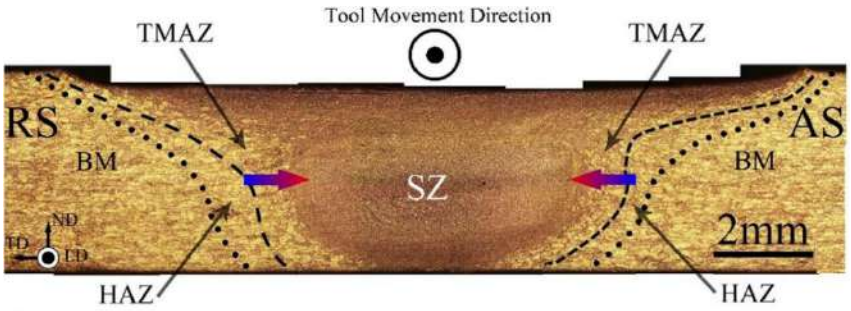


**Figure 2.11** FSW Optical cross-section (Heidarzadeh et al. 2020)

### 2.7.1 Unaffected Base Material

This material, which is located distant from the weld site and has not been distorted, might have gone through a negligible thermal cycle during the welding. The thermal cycle has no impact on the material's mechanical characteristics or microstructure.

### 2.7.2 Heat-Affected Zone

No plastic deformation has been observed in this region. However, this region experiences thermal energy, which facilitates it to reform the grain at HAZ. As a result, the grains in this zone are a little bit bigger than those in the base material. Thermal energy contributes to the over-aging of precipitates in precipitation-strengthening alloys, which deteriorates their mechanical properties ((Zhang et al. 1999a) (Jata et al. 2000), (Schubert et al. 2001),(Meng et al. 2021). The welding parameters determine how much heat is supplied to the workpiece at HAZ. According to the research so far, welding parameters greatly rely on the nature and purpose of the operation. As a result, the size and characteristics of the HAZ vary significantly. ((Mishra et al. 2005), (Heidarzadeh et al. 2020)).

Figure 2.12(a-d) depicts the Scanning Electron Microscopy (SEM) images of the various weld zones of friction stir welded materials as examined by Liu et al. (2011). TMAZ depicts the elongated and highly extruded grains on the advancing side (Figure 2.12(a)). However, on the retreating side (Figure 2.12(b), it has been observed that the boundary between the TMAZ and the nugget zone is unclear. The HAZ displays a grain structure (Figure 2.12(c)) comparable to the parent material as shown in Figure 2.12(d) since it does not experience any heating cycle or plastic deformation. (Liu et al. 2011).

### 2.7.3 Thermo Mechanically Affected Zone (TMAZ)

The grain's plastic deformation is a defining feature of TMAZ. Due to its vicinity to the NZ, the area is more susceptible to high temperatures. The shearing of grains, which results from the combined force of tool translation and rotating movement, is what causes the plastic deformation in TMAZ. The weld depth and proximity to the nugget zone affect the plastic deformation in the TMAZ.

The grains nearer to the weld center and towards the tool shoulder experience a higher deformation. The deformation of the grains decreases as one moves away from the weld center ((Kwon et al. 2002), (Mishra et al. 2005). The line separating the TMAZ and HAZ is not always clear. However, a technique based on angular distortion has been created to define the TMAZ's outer boundary (Woo et al. 2006). The strengthening precipitates near the nugget zone dissolve due to the substantially higher temperature in the TMAZ, and the strengthening precipitates near the HAZ coarsen, which results in a significant loss of strength.

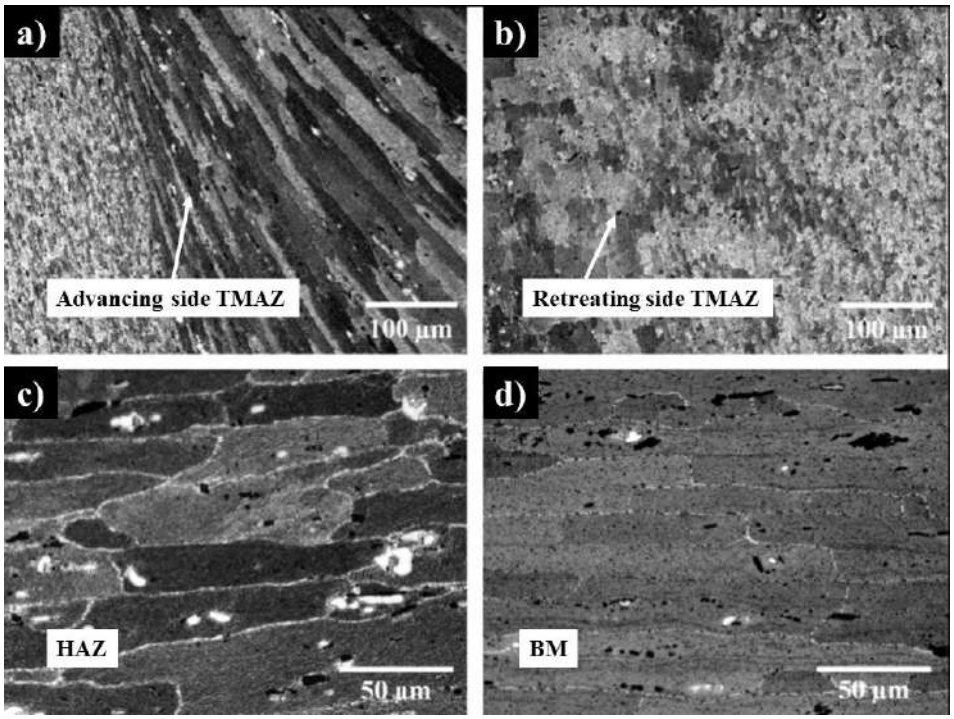


**Figure 2.12** SEM images of the (a) TMAZ - Advancing side (b) TMAZ - Retreating side (c) HAZ and (d) BM. (Courtesy: (Liu et al. 2011)

The welding conditions have a significant impact on the precise boundary between the dissolved and coarsened particles. As a result, the eventual distribution of precipitation depends on the zone's time-temperature history (Woo et al.2006, Mishra R.S et al. 2005). In the TMAZ, a zone between the base metal and NZ, elongated grains with upward orientation were observed around the nugget zone (Jata et al. 2000)ata K.V.et al.2000, Mishra R.S et al. 2005). On the advancing side, this transition zone is sharp but it appears to be rather dispersed on the retreating side. Higher local shear arising from the opposite direction of workpiece motion and the tool rotation results in a sharp transition in the advancing side (Khalilabad et al. 2022).

### 2.7.4 Nugget Zone / Stir Zone

A nugget zone, also known as a stir zone, is characterized by a recrystallized region (Mishra et al. 2005, Sato et al.1999, Rhodes et al.1997, Mahoney et al.1998, and Ma et al. 2003). It also describes the area that the tool pin had previously occupied. Depending on the welding process parameters, the material's heat conductivity, the built temperature, and the tool shape affect the size of the nugget zone. According to Mishra et al. (2005), the nugget shape can be further divided into elliptical and basin-shaped subcategories. According to Sato et al. (1999), the nugget's basin shape is generated in the FSW of the AA6063-T5 plate. Due to the exceptionally high heat produced at the interface of the workpiece and the tool shoulder, the broader nugget region was produced on the upper surface of the weld zone.

Meanwhile, in the FSW of AA7075-T6 plates, the elliptical nugget shape was developed as reported by Rhodes et al. (1997) and Mahoney et al. (1998). Ma et al. (2003) looked at the nugget morphology at various process parameters. The researchers concluded that lower rotating speeds produce basin-shaped objects, while higher rotational speeds produce elliptical objects. How the material flows in the different regions of the weld such as top, middle, and bottom was distinguished by Zhang et al. (2009), resulting in a weld nugget with an inverse trapezoidal form. Figures 2.13 (a) and (b), respectively, show the generic butt joint profile and different joint profiles with typical nuggets.

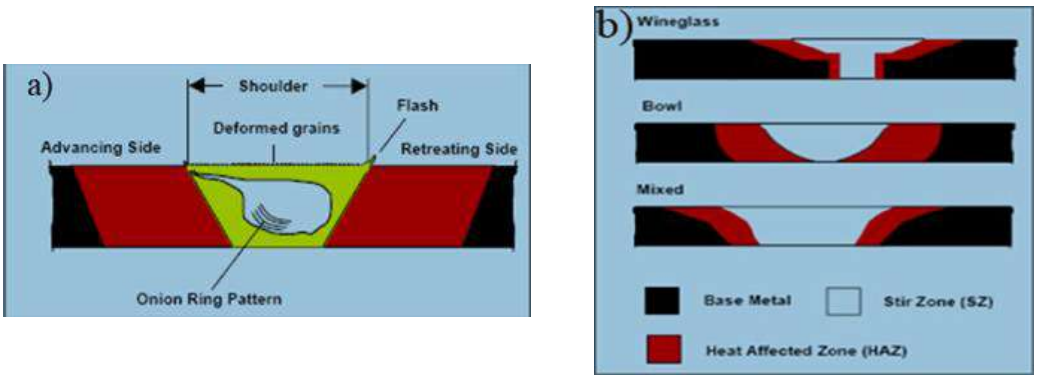


**Figure 2.13** (a) Generalized butt joint profile (b) Other types of joint profiles (Terry Khaled 2005)

### 2.7.5 Influence of probe diameter on Nugget Size

The correlation between nugget size and probe size was discovered by Reynolds (2000) The impact of probe diameter on nugget size is seen in Figure 2.14. The nugget's size is said to be somewhat greater than the probe's diameter, except where the probe tapers to a hemispherical termination at the bottom of the weld. Additionally, it was seen that the NZ takes a circular shape with a bigger diameter near the weld's midsection.

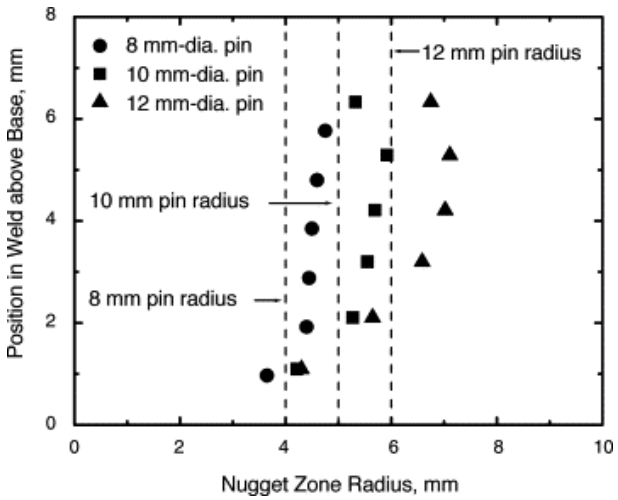


**Figure 2.14** Influence of probe diameter on Nugget Size (Reynolds 2000)

### 2.7.6 Variation in grain size and its impact on joint properties

According to the principle of strengthening, limiting or obstructing the motion of dislocation makes a material stronger as well as harder. The FSW process results in

slip or dislocation motion since it is connected to plastic deformation. For the following two reasons, the grain boundary functions as a barrier to dislocation motion:

- The rise in crystallographic misorientation is what causes the dislocation of grains with various orientations.
- The irregularity at the grain boundary causes he slip planes of grains to be out of alignment.

Compared to coarse grains, the material with fine grains is harder and stronger. The Hall-Petch equation states that the yield strength changes depending on the grain size (Sato et al. 2003)**.**

$$\sigma_y = \sigma_0 + k_y d^{-1/2} \quad (2.1)$$

Here "d" represents the average diameter of the grain, $\sigma_0$ is the "friction stress" which is the total resistance of the crystal lattice against the dislocation movement and $k_y$is a constant known as the "locking parameter" that represents the relative hardening contribution of borders of the grain which acts as the barriers to slip across the boundaries of the grain.

Grain size has an impact on yield strength (H. Suzuki et al. 1963), as seen in Figure 2.15, where yield strength is calculated as a function of the $d^{-1/2}$ of FS welded joints created with various welding conditions. It demonstrates the relationship between grain size and yield strength. As grain size reduces, the yield strength increases. The size of the grain is controlled by synchronizing the solidification rate from the liquid state and plastic deformation rate and by appropriate heat treatment methods.

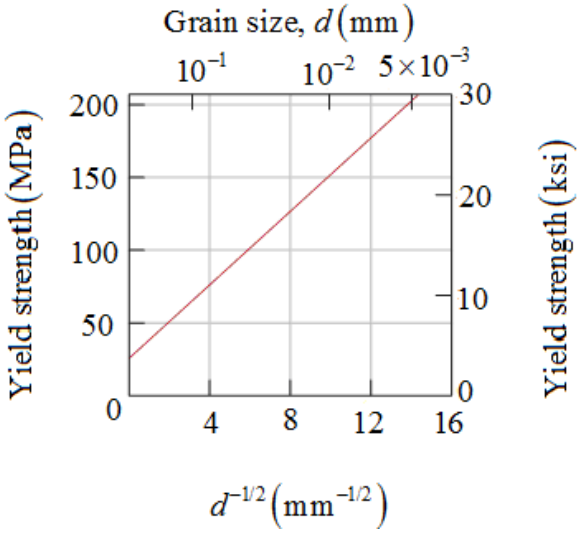


**Figure 2.15** Correlation between yield strength and the grain size (H. Suzuki 1963, William 2007)

Figure 2.16 displays the grain size distribution within the nugget zone of the friction stir welded AA7050 at various points. At the nugget zone's top, the grain size tends to be larger, and as one proceeds toward the nugget zone's bottom, the grain size tends to be smaller. (Mahoney et al. 1998) studied FSW of a 6.35mm thick plate and found that the grain size differs between the advancing and retreating sides. It was observed that the size of the grains varied from 5.3 microns at the top to 3.2 microns at the bottom of the weld zone. Similar to this, the difference in grain size between the advancing and retreating sides is 5.1 microns to 3.5 microns. The variable temperatures and heat dissipation in the nugget zone are the causes of the variance in grain size.

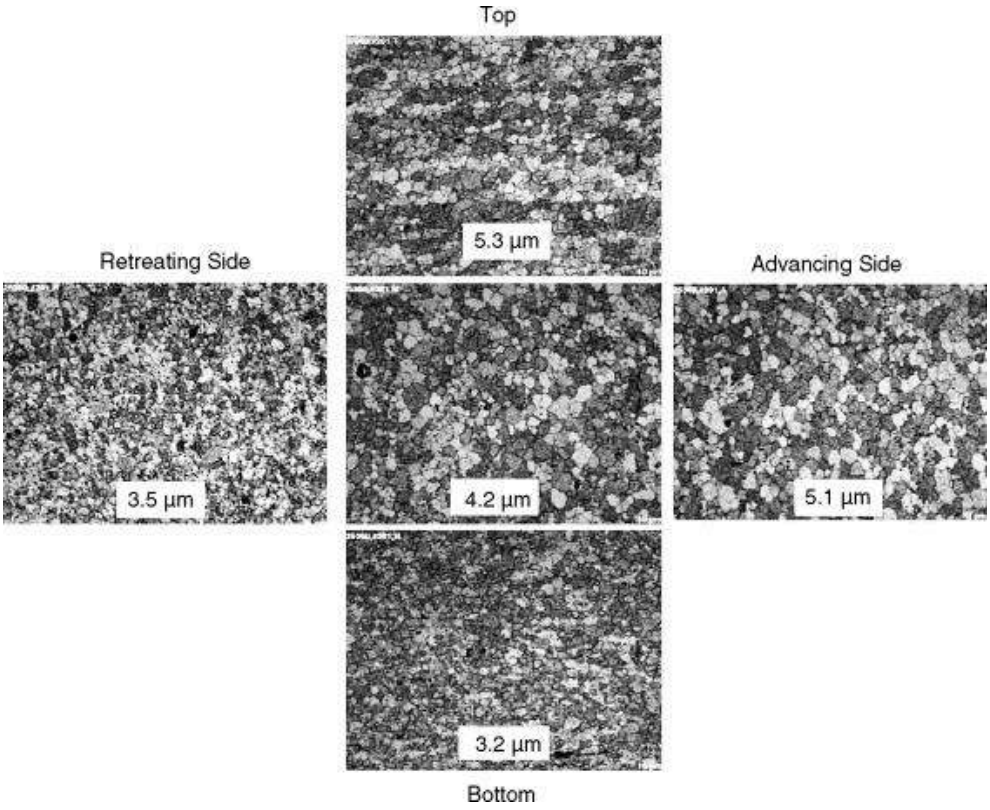


**Figure 2.16** Grain size at various locations on the nugget region of FS welded Al7050 (Mahoney et al. 1998).

Because the workpiece is in contact with the back plate, which acts as a heat sink, the peak temperature and thermal cycle are lower at the bottom of the nugget zone than at the top. The nugget bottom experiences a lesser temperature and reduced path of heat flow, the growth of the grains effectively slows down, producing larger grains during recrystallization. It is evident that as plate thickness rises, the temperature difference between the weld nugget's bottom and top widens, producing a larger range of grain sizes.

## 2.8 THE IMPACT OF PROCESS PARAMETERS ON WELD QUALITY

The friction stir welding process used to join aluminium alloy and AMC is affected by the tool's geometry, material, and operational parameters. Tool rotational speed, tool traverse/welding speed, and axial/thrust force are common operational parameters in the FSW process. These parameters play an important factor in producing high-

quality weldments as they aid in producing the frictional heat required for solid-state welding and encourage fine grains at the weld zone.

### 2.8.1 FSW tools

An FSW tool is one of the crucial elements in the welding process and is essential for its success. A rotating non-consumable tool typically has a probe with a variety of forms and a round shoulder. Frictional heating and deformation of the material, which are primary purposes of the FSW tool, is followed by the transport of the softened material from the front of the tool to the rear side to establish the joint, as the tool moves ahead. The probe is regarded as the weakest component in the process because of the intense strains and high temperatures that are created during welding (DebRoy et al. 2012). Inappropriate tool material and form selection result in tool wear, which affects both the weld properties and the life of the FSW tool. (Zeng et al. 2006).

The FSW tool life when joining aluminium alloys was investigated by DebRoy et al. (2012). Tool wear and life are influenced by the material of the tool and workpiece, operation parameters, the thickness of the workpiece, and tool shape. Using AISI 1080 steel on one side and soft metal aluminium on the other, Chen et al. (2004) tested the FSW of dissimilar metals. Weld zones have been seen to have multiple porosities and tool breakage. Due to a worn-out tool, inter-metallic compounds were also seen in the nugget region.

The joint characteristics of AA6061, FS welded with a tool having a threaded probe, were investigated by (Zeng et al. 2006). The tensile test revealed that the joint strength of the welded composites is considerably impacted by tool wear. Thus, it is essential to describe the properties of tool materials and shapes.

#### 2.8.1.1 Tool Materials

The choice of tool material has been covered in several publications. Before choosing the material for the tool, it is crucial to ensure that the tool has a basic manufacturing shape that will save production costs and produce a suitable stirring effect (Padmanaban et al. 2009). Friction stir welding was initially used to join soft metals, such as aluminium alloys, that can be simply deformed by tool steel. (Steuwer et al. 2006) (Leitão et al. 2009)(Tarasov et al. 2014). Steel is a material that is inexpensive

to process into the required shape and size, is widely accessible, and whose properties can be established. However, when welding composites, the presence of hard particles increases the rate of tool wear (Prado et al. 2001). Prado et al. (2001) attempted to investigate tool wear during the welding of the composite material AA6061-20% $Al_2O_3$. According to the study, tool wear increases as rotational speed increases.

Based on the research conducted thus far on the selection of the tool material and self-optimized tool wear, it seems that the tool has improved in terms of both stirring effect and wear.(Shindo et al. 2002) (Prado et al. 2003) (Fernandez and Murr 2004). The threaded probe of steel material was used by (Shindo et al. 2002) on the welding of Al359-20%SiC. A self-optimized form (without threads) produced an excellent, uniform weld without adding any more tool wear on the pin.

After some testing with the FSW tool having a featureless plain probe (without threads/sharp edges), a self-optimized tool shape was achieved. A superior quality weld with this optimum shape is produced without any tool wear. Most of the time, poor process parameter selection results in tool wear. Rapid tool wear results from slow welding speed and high rotational speed. A self-optimized tool shape's process parameters were described by (Fernandez and Murr 2004). The study discovered that, because the threads are loaded with work material, tool wear initially decreases as rotation speed drops and welding speed increases. Due to the tool's self-optimized shape, there will not be any wear after it has traveled over three meters. Table 2.1 summarizes research on the types of tool materials and workpiece materials used in the FSW of MMCs.

**Table 2.1** Tool material, workpiece material, and reinforcement used for FSW of composites.

| **Base Material** | **Reinforcement (Vol. %/ Wt. %)** | **Tool material** | **Author** |
|---|---|---|---|
| AA 6061 | $Al_2O_3$ (20) | Tool Steel | rado et al. (2003) |
| A359 | SiC (20) | Steel | Fernandez et al. (2004) |
| AA 6063 | $B_4C$ (6 and 10.4) | 4340 steel | Chena et al. (2004) |
| AA6061 | $Al_2O_3$ (20) | Ultra-hard | Marzoli et al. (2006) |
| AZ91 | SiC (10) | Tool steel | Won-Bae Lee et al. (2006) |

| | | | |
|---|---|---|---|
| AA2124 | SiC (25) | HSS Steel | Huseyin et al (2007) |
| AA7005 | $Al_2O_3$ (10) | Ferro–Titanite | Ceschini et al. (2007) |
| AA2009 | SiC (15) | Steel | Feng et al. (2007) |
| AA2009 | SiC (15) | Steel | Feng et al. (2008) |
| A356 | SiC (15) | D2 tool steel | Amirizad et al. (2008) |
| AA7005 | $Al_2O_3$ (10) | Steel | Cavaliere et al. (2008) |
| AA6061 | $Al_2O_3$ (20) | Ferro-Titanite | Pirondi et al. (2008) |
| AC4A | SiC (30) | WC–Co hard alloy | (Liu et al. 2015) |
| Al | $B_4C$ (2) | H13 Hot work steel | (Moradi Faradonbeh et al. 2018) |
| AA6061 | SiC/ Fly ash | H13 Tool steel | (Sachin et al. 2018) |
| AA6061 | $B_4C$ (15- 30 wt%) | Cermet (Ni-TiC) | (Li et al. 2018) |
| AA6092 | SiC/17.5p-T6 | AISI H13 | (Salih et al. 2019) |

#### 2.8.1.2 Tool Geometry

The FSW method relies heavily on tool geometry to transfer the softened material and control the traverse rate. Heat is created when the rotating FSW tool is inserted into the workpiece due to friction between the workpiece and the tool pin. The deformation of the material results in the production of heat as well. The area of contact between the two expands immediately after the tool shoulder comes into touch with the workpiece surface. Due to this friction between the workpiece and the shoulder increases, causing a greater quantity of heat to be produced. In thin sheets, the shoulder produces most of the heat. The pin, however, generates most of the heat in thick sheets. The ratio of the shoulder-to-pin dimension is crucial from a heating perspective. According to a study carried out by Padmanaban and Balasubramanian (2009), the shoulder limits the soft, plasticized material. This material extrudes from the tool's retreating side to its advancing side during the welding operation. The shoulder traps these materials, which are then consolidated behind the traversing tool to create a smooth surface finish. The second function of the tool is to mix and transfer the material.

Mishra et al. (2005) assert that the homogeneity of the microstructure and the joint properties are influenced by the tool geometries, tool traverse speed or welding speed,

and rotational speed. According to Lorrain et al. (2010), the ratio of shoulder to pin diameter, the surface angle of the shoulder, pin size, and shape are the most crucial characteristics. The following discussion covers the numerous tool geometry factors that impact weld quality.

#### 2.8.1.3 Diameter of FSW tool shoulder

The impact of the FSW tool shoulder diameter has received a lot of attention. Most of the heat is produced by the tool shoulder (Mehta et al. 2011b) (Elangovan and Balasubramanian 2008a), and the material flow field is mostly established by its control over the plasticized material (Kumar and Kailas 2008b). The effect of shoulder size on peak temperature, thermal cycle, torque, and power needs during FSW of AA7074-T6 was investigated by (Mehta et al. 2011b). The relationship between peak temperature and shoulder diameter is seen in Figure 2.17. The study found that when shoulder diameter grows, so does the temperature. During the welding operation, the tool shoulder must inhibit the soft material from escaping, and neither the traverse force nor the total torque should be excessive. According to (Elangovan and Balasubramanian 2007) the contact area expands with increasing tool shoulder diameter. resulting in generating more frictional heat which broadens the TMAZ and HAZ (Kumar and Kailas 2008b). As a result, it has been assumed that the quantity of frictional heat created decreases as the diameter does. Because there is less friction, there is less weld merging, which lowers the quality of the weld. Therefore, the highest strength is only achieved by a tool with the ideal shoulder diameter. Arora et al. (2011) proposed a method to control the ideal shoulder diameter by considering the two torque components namely sticking torque (MT) and sliding torque (ML). The relationship between the total torque and the diameter of the shoulder is shown in Figure 2.18. The targeted torques are determined by the axial pressure, tool geometry, and flow stresses in the workpiece. They claimed that by examining the relationship between sticking torque and shoulder diameter, the ideal diameter of the tool could be determined.

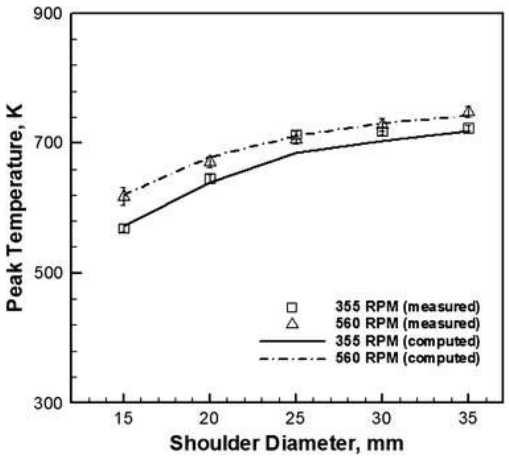


**Figure 2.17** Measured and computed peak temperature v/s Shoulder diameter. (Mehta et al. 2011a)

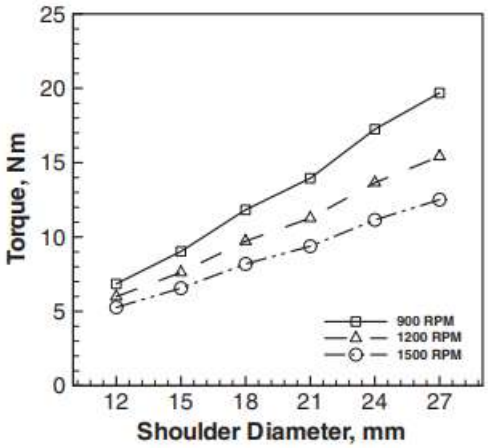


**Figure 2.18** Shoulder diameter versus torque (Courtesy: Arora et al. 2011)

### 2.8.1.4 Tool Shoulder Surface

The workpiece contact surface of the shoulder is also a crucial component of the tool design, according to a literature review. To promote material deformation, to provide correct material mixing, and to serve as a reservoir for the forging action to achieve a better surface finish, several features were used in the surface (Mishra et al. 2005) (Venkateshkannan et al. 2014). Figure 2.19 displays features of the probes that are frequently used. Concave-shaped tools provide high-quality welds, and their design and manufacturing are simple. The tool has a slight angle (6 to 10$^{o}$) from the pin base to the shoulder edge (Mishra et al. 2005).

During the tool's final stage of plunging, a little amount of material is driven into the cavity formed by the concave shoulder. The stored material in this cavity undergoes the tool shoulder's forging action. While the tool moves forward in its forward traverse motion, fresh softened material is pushed into this cavity, replacing the material that was previously stored in the flow of the pin. Using a concave-shaped shoulder, (Vilaça et al. 2007) examined friction stir welding of AA5083-H1 alloy. The shoulder's concave shape generated a clean surface finish. Further investigation into the impact of surface concavity on mechanical properties was conducted by Venkateswaralu et al. (2013).

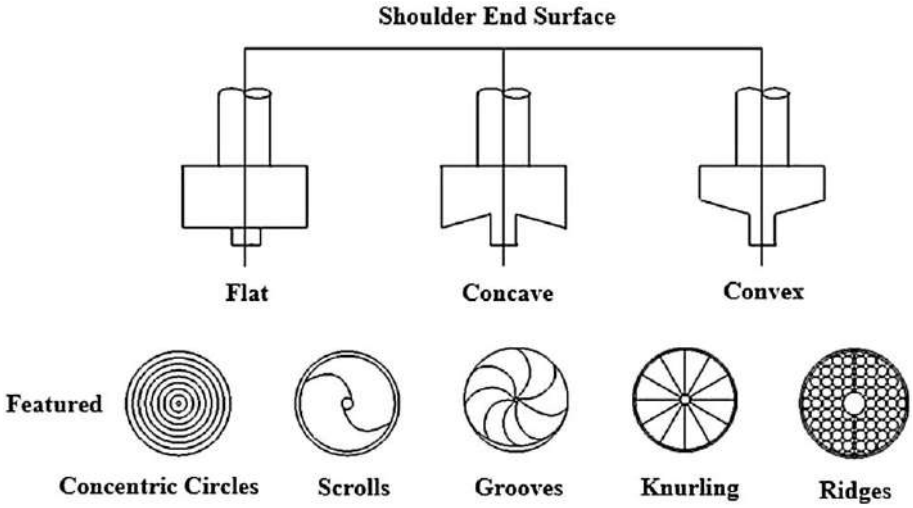


**Figure 2.19** Geometries of tool shoulder, which makes contact with workpiece surface, (Courtesy: (Mahakur et al. 2021)

The study entailed adding a flat surface to the shoulder's perimeter to change the surface concavity. The results showed that 2-mm flat shoulder surfaces followed by 7-degree concavities had higher tensile strength, which was thought to be more suitable for generating adequate tensile strength.

### 2.8.1.5 Tool Pin Geometry

To achieve better mechanical properties, a variety of tool pin shapes have been published in the literature (Sued et al. 2014) (Raturi et al. 2019). The pin profile must be designed to keep the most plasticized material in the weld cavity (Kumar and Kailas 2008a). The most common shapes used in the FSW process were cylindrical or

tapered with or without threads, including square, triangular, Flared-Triflute, and Skew-stir. (Thomas et al. 2003).

Additional heat is produced in the case of a tool having a threaded probe and encourages material to flow vertically in the threading direction. (Sued et al. 2014) . Left-hand threaded tools are typically rotated clockwise, while right-hand tools are rotated anticlockwise. According to (Boz and Kurt 2004) study, high-pitch threaded profile pins behave more like drills than stirrers, with material coming out in the shape of chips (Fernandez and Murr 2004). According to (Seidel and Reynolds 2001), joints with improved mechanical properties were obtained using a threaded profile pin having a pitch in the range of 0.8-1.1 mm (Elangovan and Balasubramanian 2008b) processed AA2219 using various tool geometries.

Figure 2.20 depicts different tool geometries employed in the FSW process and their dynamic orbits. The eccentricity of the triangle and square-shaped tool pins permits incompressible material to travel around the pin profile (Thomas and Nicholas 1997). The dynamic orbit and eccentricity of the pin are related. The dynamic orbit is linked to the eccentricity of the spinning softened material. The flow direction of softened material is regulated by the static-to-dynamic volume ratio of the FSW tool. The presence of a flat surface assists in a pulsating stirring action of softened plasticized material.

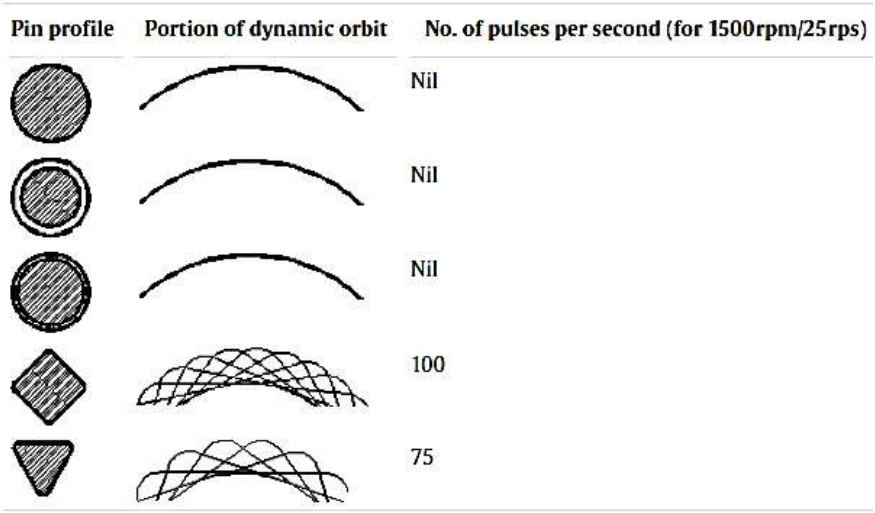


**Figure 2.20** Pin profile's impact on dynamic orbit and pulsing action (Elangovan and Balasubramanian 2008c)

### 2.8.1.6 Diameter of tool pin

In their study, Rajakumar et al. (2011) emphasized the significance of the diameter of the tool pin in achieving high-quality FSW joints. The pin diameter determines the volume of material being stirred. The amount of material stirred will likewise be smaller if the tool's diameter is smaller, and vice versa. A smaller volume of material is heated more effectively when a smaller pin diameter, a slower welding speed, and a faster rotational speed are combined. This causes turbulence in the flow of material and the formation of coarse grain structure. On the other hand, a bigger volume of material receives less heat input due to low welding and rotational speeds and large pin sizes. This results in inadequate material flow and plasticization.

For a given shoulder diameter, a tool with a higher pin diameter results in inadequate heat generation because of the broader contact area, which leads to defects in the TMAZ's advancing side (Rajakumar et al. 2011). The pin profile affects the flow of plasticized soft material, which also impacts the weld characteristics (Choi et al. 2010). The shapes of the few most popular tool pins are depicted in Figure 2.21. Compared to a cylindrical pin, a triangular or "trifluted" tool pin improves the flow of material. (Mahakur et al. 2021).

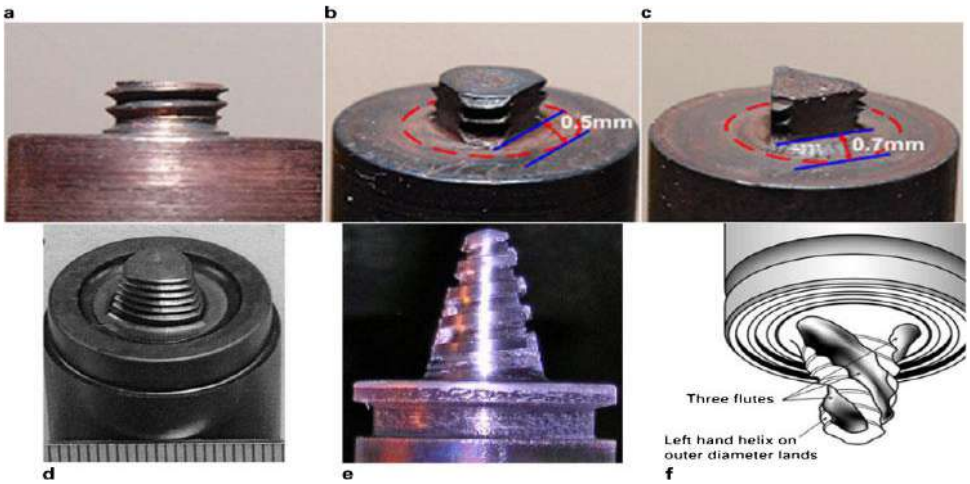


**Figure 2.21** Typical pin geometries. (a) Threaded cylindrical (b) Three flat threaded (c.) Triangular (Courtesy: Sun et al. 2009) (d) Trivex (Courtesy: Colegrove et al. 2004) (e) Threaded conical (f) Triflute (Courtesy: Rowe and Wayne 2006)

To examine the impact of tool geometries on the joint strength and grain structure of Al-$TiB_2$ MMCs, Vijay and Murugan (2010) used 18 different FSW tools. They changed the tool pin contour as well as the shoulder-to-pin diameter ratio (D/d). When compared to joints prepared using tools with straight pins, welds made with taper profile pin tools exhibit coarser grains. The tool pin profile affects the tensile strength of the friction stir welded specimen as well. The joints made using square tools showed better tensile strength than joints made with conventional tools because of the pulsating stirring action of the square flat surfaces.

Joints prepared with tapered square pins exhibited reduced tensile characteristics as tapered tools sweep less material than the straight square pin tool does. Due to its similarity to a straight cylindrical pin at high rotational speeds, octagonal profiled tool pins do not show any pulsating activity. Figure 2.22 displays the various tool pin profiles that were employed for the investigation.


**Figure 2.22** FSW tools with different pin profiles (Vijay and Murugan 2010)

The change in dynamic orbit caused by the rotating tool improves the tensile characteristics of the joints created by tools with square probes (Elangovan and Balasubramanian 2008b). In most cases, the FSW tool's static-to-dynamic volume ratio dictates the direction of material flow to the trailing side of the tool probe from the leading side. The impact of the profile of the tool pin on the percentage of elongation of the FS welded AMCs is shown in Table 2.2. The table demonstrates that, except for the octagon pin tool, the tool pin profile does not affect the percentage elongation. This is due to the parent metal's inclusion of ceramic particles, which greatly lowers the material's elongation. Like its effect on tensile strength, tool geometry also affects joint efficiency. When the AMC is welded with a square probe tool, the joint efficiency is good; however, when the AMC is welded with a tapered square probe tool, the joint efficiency is low.

**Table 2.2** Friction stir welded Al-$TiB_2$ composite–joint properties (Courtesy: (Vijay and Murugan 2010)

| Tool pin profile | Average (%) elongation | Average tensile strength (MPa) | Joint efficiency (%) |
|---|---|---|---|
| Octagon | 3.39 | 240.00 | 84.81 |
| Hexagon | 5.83 | 262.29 | 92.68 |
| Square | 6.37 | 281.51 | 99.47 |
| Octagon Tapered | 6.22 | 245.27 | 86.67 |
| Hexagon Tapered | 6.67 | 247.89 | 87.59 |
| Square Tapered | 5.32 | 223.33 | 78.92 |

Tool pins with threads and flutes help to improve material flow, increase heat production rate, and affect axial and transverse forces because of the increased interfacial surface. Mahmoud et al. (2009) assessed the friction stir processing of SiC reinforced aluminium matrix composite using four tool geometries: circular without thread, circular with thread, triangular, and square. While the circular tool had significantly less wear than the flat facing tools, the square probe produced a more evenly distributed distribution of SiC particles than the other tools. Elangovan and Balasubramanian (2008) investigated five tool profiles for the welding of AA6061

alloy: cylindrical (straight tapered and threaded), triangular, and Square. They found that for the set axial forces, the square pin-shaped tools produced welds free of defects.

### 2.8.2 Effect of tool rotational speed

The investigation on the impact of the rotational speed of the FSW tool on weld property revealed that the rotational speed affects the proper mixing of material and sufficient heat generation (Rajakumar et al. 2011) (Kumar and Murugan 2014). Regardless of the welding speed, less heat is produced at lower rotational speeds which results in improper material mixing. Rajkumar et al. (2011) investigated the impact of rotational speed on the ultimate tensile strength (UTS). The outcome showed that the amount of heat developed by friction is primarily influenced by speed. If less heat is produced, less heat will also be provided to the base material, which will affect the formation of softened plasticized material and its flow in the weld region. As a result, FSW has a lower value than UTS. Heat generation is more at high rotational speeds, hence heat supplied to the workpiece is also more. As a result, NZ has softer plasticized material, which causes turbulence in the flow of material and the formation of coarse grains in the region. Ashok et al. (2014) studied the impact of tool rotational speed on UTS and reported that the UTS rises with rotational speed up to a certain point before declining as rotational speed goes up further (Palanivel et al. 2012, Periyasamy 2012).

### 2.8.3 Effect of tool traverse speed/ welding speed

The tool traverse speed or the welding speed controls the heat exposure time, thereby governing the amount of heat delivered to the workpiece during the FSW process. (Rajakumar et al. 2010) (Kumar and Murugan 2014). A smaller amount of heat will be delivered if less heat is created. The joint properties are affected by the nature of material flow and the distribution of the temperature across the FSW joint. The pin/shoulder shape and operational parameters majorly influence the flow of material and thermal distribution. Nandan et al. (2008) and Sharma et al. (2012) found that as welding speed increases, percentage elongation (% El), joint efficiency, and ultimate tensile strength (UTS) decreases.

Furthermore, as welding speed is increased and tool rotational speed is decreased, the minimum hardness region moves towards the weld nugget zone from the initial HAZ. As welding speeds increase, stirring is no longer sufficient. The material does not move enough from the tool's advancing side to its retreating side. The softened area decreases due to the increased welding speed since there is less heat generated and the plasticized material cools faster. According to Mohsen et al. (2011), higher levels of SiC particle segregation in the NZ produce lower traverse speeds to minimize grain size in specimens with SiC particles.

On the other hand, increased traversal speed results in SiC particle accumulation and lower microhardness values. The effect of the rotational/welding speed ratio (ω/v) in FSW was studied by Abbasi et al. (2006). A modest decline in the effective tensile characteristics was seen when (ω/v) is increased, due to increased softening of the material resulting from the higher heat input. In addition, raising the (ω/v) ratio caused a larger weld nugget to form as a result of a rise in heat input and a simpler flow of material. Therefore, when the (ω/v) ratio grows, the likelihood of developing an "incomplete root penetration" fault decrease. According to Peng Dong et al. (2013), the tensile characteristics of the weld grow together with the welding speed. This is because less heat input at faster welding speeds weakens θ' precipitate development and transformation. As a result, the softened region is reduced in size and the weakest spot is moved to the TMAZ, which is next to the NZ, with minimal loss of strength during the measurement of the tensile strength (Liu et al. 2011, Rajamanickam et al.2008, Rajamanickam et al 2014)

### 2.8.4 Impact of Axial Force on joint properties

Axial force is another factor that must be considered during FSW. Only a little amount of data is currently accessible to realize the influence of axial force on the UTS (Krishna et al. 2002, Kumar et.al. 2008, Elangovan et al 2008 Jayaraman et al. 2009) According to Krishna et al. (2002), an axial force is the key factor influencing the pattern of material flow. Due to the lower axial force, a poorly plasticized material is produced at the weld's top. According to Kumar et al. (2008), bonding happens when two surfaces are brought close to interatomic tensions. The softened material in the weld zone is propelled to the end of the extrusion process by axial force.

The depth to which the pin plunges is also a function of axial force. Whenever the axial force is less, a tunnel fault exists at the base of the weld region. If the axial force is too high, the material will move as a flash on both the advancing and retreating sides of the weld zone. This causes thinning of the weld and lowers the weld's strength. The axial force has been shown to increase the tensile strength of AA6061 alloy joints made by FSW, according to Elangovan et al. (2008). At an axial force of 6kN, coarser grains with clustered strengthening precipitates were produced. A coarse grain with finely dispersed strengthening precipitates was generated with an axial force of 8 kN. According to Jayaraman et al. (2009), the strength of joints rises with increasing axial force up to a point before they start to fall.. Lower axial forces caused by improper material flow result in a defect in the weld region. The UTS decreases at higher axial force due to the thinning effect and the heterogeneous distribution of Si particles.

## 2.9 MECHANICAL PROPERTIES

### 2.9.1 Hardness

The information found in the literature on the mechanical properties of FS welded metal matrix composites is discussed in this section. Marzoli et al. (2006) stated that there was a loss of hardness in the nugget zone and noted that it was highly unusual based on their research on FSW of AA6061/20% $Al_2O_3$ composite. For an A356/15%SiC composite, Amirizad et al. (2006) reported that the weld zone's hardness (Nugget and TMAZ) is higher than the base material (Shettigar et al. 2013, Shettigar et al. 2014, Lee et al. 2006, Khodabakhshi et al. 2013). While welding an AA6061/$B_4C$ (3-7wt%) composite, Kalaiselven (2014) made similar observations.

The nugget zone's size shrank while the quantity of SiC particles increased because of particle fragmentation (Murugan and Ashok Kumar, 2013). The increase in hardness was caused by the homogenous distribution of these broken particles. After conducting a hardness test on friction stir-welded, heat-treated (T4) AA2124 alloy reinforced with a 25% SiC particle composite, (Uzun 2007) concluded that the low hardness value achieved at HAZ was caused by the annealing effect in the weld zone. It was determined that the second phase particle dissolution caused the increased hardness at TMAZ on both sides of the weld zone.

Ceschini et al. (2007) examined the impact of FSW on the evolution of the grain structure and joint characteristics in extruded AA7005-10% $Al_2O_3$ composite. According to their analysis, TMAZ had the highest level of hardness when compared to NZ, HAZ, and parent material. Friction stir welding of AA2009/15%SiC heat-treated (T6) composite was carried out by Feng et al. (2008) who observed that the hardness of the weld zone is affected by the distribution of strengthening precipitates, grain, and dislocation density. During FSW, the coarse precipitates partially dissolve and then re-precipitate due to natural aging. The hardness rises because of this phenomenon.

The increase in hardness at NZ was subsequently attributed to the recrystallization of grains (Murugan and Ashok Kumar 2013), (Yang et al. 2019) and the fragmentation of hard particles (Morisada et al. 2006a). According to (Chen et al. 2009), the hardness of friction stir welded AA6063 – (0-10.5%) $B_4C$ composite was reduced after heat treatment in the nugget one. (Nami et al. 2011) have worked on the FSW of the Al-Mg2Si composite and studied the influence of several tool pass in the weld region. Due to an increase in the number of passes of the FSW tool, the nugget zone width increased while hardness decreased. Higher heat input and slower cooling rate enable grain growth, thereby decreasing the width of the weld zone.

According to (Dinaharan and Murugan 2012a), NZ in AA6061-(5/10) $ZrB_2$ composite shows an improvement in hardness value compared to the base material. (Ni et al. 2013) observed the W shape hardness profile during FSW of AA2009-17 (vol.) % SiC composite. Yigezu et al. (2014) studied the impact of tool shoulder diameter on hardness. They concluded that hardness increases as the rotational speed and shoulder diameter increase. ((Vijayavel et al. 2014) (Murugan and Ashok Kumar 2013).

### 2.9.2 Tensile Properties

In contrast to the FS welded aluminium alloys, very few publications have been made about the evolution of the tensile characteristics of MMCs. The mechanical characteristics of the friction stir welded AA2009 -15(Vol%) SiCp composite were studied by Feng et al. in 2008. Precipitation strengthening, which is the outcome of the FSW thermal cycle, increased the tensile and yield strength. The strength of the composite is also increased by fine grain and hard tiny particles (Xu et al. 2009;

Murugan and Ashok Kumar 2013; Feng et al. 2008; Xie, Ma, & Geng, 2008; Park et 2010) (Morisada et al., 2006, Vijayavel et al. 2014). Both the longitudinal and transverse direction tensile strengths are lower than the basic material after heat treatment at the T4 condition. According to Minak et al. (2010), friction stir welding AA6061 reinforced with 22(Vol.) % $Al_2O_3$ composite results in joints with joint strengths of up to 99%.

The impact of tool pin profile on the joint strength of an Al reinforced with 10 (wt.) % $TiB_2$ composite has been studied by Vijay et al. (2010). Table 2.2 lists the strengths obtained using various pin profiles. Joints made using square tools demonstrated more tensile strength than joints made with other tool profiles, while tapered square tools had the lowest strength. According to Nami et al. (2011), the rotating speed of a friction stir-welded Al-15 (wt.) % $Mg_2Si$ composite affects its tensile strength (Khodabakhshi et al. 2013). Up to a certain point, an increase in rotational speed enhances the joint's tensile strength. Void and tunnel defects were seen as the rotating speed was increased further. Thus, tensile strength is consequently reduced. According to Gopalakrishnan and Murugan (2011), an increase in the Ti % results in an increase in the joint's UTS (Dinaharan 2012). UTS increases when the welding speed decreases. The FS welded composite's UTS rises as axial force increases up to a limit of 9 kN. before declining with increasing axial force after that point.

The weldability of composite (AA1100-16(Vol.) % $B_4C$ with alloy (AA6063) was examined by (Guo et al. 2012b). The failure occurs at the base material and the UTS of the welded joint strength is comparable to the UTS of the base material. According to (Wang et al. 2013), friction stir welded joints of the same material, AA2009 augmented with 15(Vol.) % SiC composite, demonstrated a considerable increase in strength when compared to as-FSW joints of the same material. According to Ni et al. (2013), the heat generated during FSW causes the strength and ductility to decrease due to softening at the HAZ.

The FSW of Al reinforced with nanoparticles of $Al_2O_3$ (2 Vol.%) composite, manufactured by powder metallurgy process, has been reported by Khodabakhshi et al. (2013). Strength and percentage of elongation increase as the heat input factor rises. The mechanical characteristics of friction stir welded composites are shown in Table 2.3.

**Table 2.3** FSW process variables and joint efficiency of AMC joints

| Base Material | Tool Material | Tool Geometry | Tool Rotational Speed RPM | Welding Speed mm/min | Axial force (kN) | Joint Efficiency | Ref. |
|---|---|---|---|---|---|---|---|
| AA6061/ 4.5Cu/ 5SiC | Tool Steel (60 HRC) | Combined Square and Threaded 15-6-5.7 | 710-1400 | 50-80 | - | 90 % | (Prabhu et al. 2016) |
| AA 2124/ 25SiC | - | Cylinder thread | 1120 | 40 | - | 81 | (Bozkurt and Boumerzoug 2018) |
| 6061/20 $Al_2O_3$ 7005/10 $Al_2O_3$ | - | - | 800 | 56 | - | 83.87 | (Cavaliere et al. 2004) |
| AA 2124/ 25SiC | H13 Steel 48 HRC | Cylinder thread 20-7.95 to 6.35-7.62 | 550 | 75 | 8.5 | 86.5 | (Cioffi et al. 2013) |
| AA 6061/10 SiC | High-Speed steel | Cylinder thread 18-6-5.7 | 1100 | 45 | 6 | 74 | (Periyasamy et al. 2013) |
| AA2009/ 17 SiC | Cermet | Cylindrical with Triangular tip 14-5-2.7 | 1000 | 50 | - | 77 | (Ni et al. 2013) |
| AA6061/ 12 $B_4C$ | High carbon high chromium steel (62 HRC) | Square 18-6-5.7 | 997 | 78 | 9.3 | 96.83 | (Kalaiselvan et al. 2014) |
| Al/$Mg_2Si$ | H13 Steel | Tapered (7°) Cylindrical Threaded 18-6-5.7 | 710-1400 | 125 | - | ~100 | (Nami et al. 2011) |
| AA 6061/20 $Al_2O_3$ | Ultra-hard material | Cylindrical 20-8-? | 700 | 300 | - | 70 | (Marzoli et al. 2006) |
| AA 6061/ 22 $Al_2O_3$ | Wear resistant steel 64 HRC | Cylindrical 15-4-? | 880 | 260 | - | 99 | (Minak et al. 2010) |

| | | | | | | | |
|---|---|---|---|---|---|---|---|
| Al/4.5Cu /$TiB_2$ | M2 Steel(62 HRC) | Cylindrical Threaded 18-6-5 | 710-1400 | 63 | - | - | (Peddavarapu et al. 2017) |
| AA 2009/15 SiC | Steel | Cylindrical Threaded 24-8-? | 600 | 5 | - | 95 | (Feng et al. 2008) |
| AA 2009/ 15 SiC | Ultra hard Cermet | Conical 20-8-5.8 | 800 | 100 | | 82 | (Wang et al. 2014) |
| LM25/5 SiC | HSS Coated with TiAlN | 19.5-6/4-5.7 Tapered | 1200-1800 | 20-60 | 6/7/8 | | (Devanathan and Babu 2014) |
| AA6061/ $ZrB_2$ | High carbon high chromium steel (62 HRC) | Square 18-6-5.7 | 1150 | 50 | 6 | 94-95 | (Dinaharan and Murugan 2012a) |
| Al/4.5Cu /10TiC | Steel Shoulder Titanium pin | Threaded 18-7-4.8 | 500 | 20 | 6 | 89 | (Kumar et al. 2014a) |
| AA6061-T6/AlNp | High carbon high chromium steel (62 HRC) | Square 18-6-5.7 | 1000-1400 | 25-85 | 3-7 | 93.42 | (Murugan and Ashok Kumar 2013) |
| AA6061/ 4.5Cu/ 10SiC | Tool Steel (60 HRC) | Combined Square and Threaded 15-6-5.7 | 710-1400 | 50-80 | - | 90 % | (Shettigar et al. 2013) |
| AA6061/ AlNp | High carbon high chromium steel (62 HRC) | Square 18-6-5.7 | 1200 | 55 | 5 | 93.42 | (Ashok Kumar and Murugan 2014) |
| Al/12Si/ 10 TiC | Steel Shoulder Titanium pin | Threaded 18/20/22-7-5.8 | 710-100 | 20-40 | - | - | (Yigezu et al. 2014) |
| AA6061/ 12 $B_4C$ | high carbon high chromium steel (62 HRC) | Square 18-6-5.7 | 997 | 78 | 9.3 | 96.83 | (Kalaiselvan and Murugan 2013) |
| Al/10 Ti $B_2$ | High carbon high chromium steel | Various tool pin profile | 2000 | 30 | 19.6 | 99.47 | (Vijay and Murugan 2010) |

## 2.10 OPTIMIZATION AND PREDICTION TECHNIQUE

Modeling and analyzing the relationship between input and output variables is the most crucial step in solving engineering challenges. Generally, two key modeling methods are used. These models are classified as analytical and empirical. Statistical models and neural network models are the further divisions of empirical models.

### 2.10.1 Statistical Model

A statistical model employs parameterization (fixed in parametric form) and determined form (polynomial form). In data collection, this technique seeks to measure both complicity and a specific fact. To attain the required joint strength, researchers have proposed several techniques to enhance the weld efficiency of the materials. In the case of FSW of composite, the process parameters, the tool geometry, and the tool shape all affect the joint strength. (Gopalakrishnan and Murugan 2011, Dinaharan and Murugan 2011, Kalaiselven 2012, Kalaiselvan et al. 2013, Murugun et al. 2013, Periyasamy et al. 2013, Anand Kumar et al. 2014, Ashok Kumar et al. 2014). Nowadays, emphasis is placed on finding ways to improve joint efficiency by adapting prediction and optimization algorithms. To anticipate and analyze the impact of process parameters on UTS of the AA6061 (3-7)%TiC composite joined, utilizing friction stir welding,(Gopalakrishnan and Murugan 2011) devised a second-order polynomial equation. According to their findings, the tool pin profile and welding speed are the two most important variables in the prediction model, but tool rotational speed plays a minimal role in predicting UTS. (Dinaharan and Murugan 2012b) (AA6061/$ZrB_2$) and (Kalaiselvan and Murugan 2012) (AA6061/$B_4C$) stated that the generalized reduced gradient method can be used to optimize process parameters. The selected process parameters are axial force, welding speed, and rotational speed particle percentage. According to the report, the optimization technique was successfully used to automate the FSW process. Using a mathematical model, (Kalaiselvan and Murugan 2013) also investigated the impact of process variables on the UTS of friction stir-welded AA6061/$B_4C$ composite. Rotational speed, welding speed, axial force, and reinforcing percentage are all the input process variables considered. They discovered that the UTS increased as the

percentage of reinforcement increased. As the thrust force welding speed and rotational speed were raised, the UTS displayed an increasing pattern to a certain extent. A reduction in the UTS was seen as these process parameters were increased further. The investigation of friction stir welded joints of AA6061-(0 to 20 Vol.) % AlNp composite by (Murugan and Ashok Kumar 2013) supports the same finding.

Periyasamy et al. (2013) et al. reported employing a desirability approach to multi-criterion optimization of FSW parameters for welding of AA6061 matrix reinforced with 20 (Vol.) % SiC (Silicon carbide). (Kumar et al. 2014b) claim that a full quadratic multiple regression equation was employed to examine the correlation between the output responses and input parameters. The link between the response control factor and the response parameters is linear and square. To forecast and optimize the process variables during FSW of an AA6061-T6/AlNp composite, Ashok Kumar and Murugan (2014) used a central composite design matrix.

High-quality welds with superior properties can be obtained by choosing the relevant process variables with their optimum values. Several techniques exist to predict the optimum process parameters. Bhushan and Sharma (2019) espoused Taguchi techniques and mathematical models to evaluate the interrelationship among the FSW process variables and different mechanical properties of the FS welded joints. Taguchi-based Grey Relational Analysis (TGRA) technique was adopted by (Kasman 2013) for multi-response optimization of FSW parameters to join dissimilar aluminum alloys. The robustness of the GRA technique was tested by conducting the confirmation trials using optimum process variables. The TOPSIS technique was used by (Prabhu et al. 2018) for the optimization of multiple responses of FSW process parameters to join AMCs. The study revealed that the process parameter values obtained from this technique provided better closeness coefficient values. (Palanivel et al. 2013) employed the Analysis of Variance (ANOVA) technique to find the significant factors and used Response Surface Methodology (RSM) to understand the interactions of various FSW process parameters. (Sreenivasan et al. 2019) optimized FSW of AA7075-SiC composite through genetic algorithm by using fitness function and predicted maximum value of hardness and tensile strength. Recently, (Parida and Pal 2015) proposed a fuzzy-assisted Taguchi approach for optimizing parameters of the FSW process with multiple responses such as tensile strength, tensile elongation,

and hardness. Multi-objective problems are converted into single-objective optimization problems using a fuzzy inference system. ANN with a backpropagation algorithm was developed by (Shojaeefard et al. 2013) for FSW of dissimilar alloys and performed multi-response optimization using the Particle Swarm Optimization (PSO) method. (Prasanth and Hans Raj 2018) applied the Artificial Bee Colony (ABC) algorithm to evaluate the optimal combination of process variables to attain better joint characteristics of FS welded dissimilar aluminium alloys.

From the available literature, it is learned that several traditional methods were used for the optimization of the FSW process, but these methods do not work well over a wider range of problems and often they offer a local optimum solution. Evolutionary algorithms such as GA can overcome these limitations, but efficient usage of this technique depends on the size of the population and the diversity of each solution in the given problem. Other evolutionary algorithms such as ABC and PSO are adopted by researchers. But successful usage of these techniques needs a proper selection of specific parameters related to the algorithm such as scaling, crossover, and mutation probability (Rao et al. 2011). Choosing suitable algorithm-specific variables for a given problem is itself a major task in these optimization techniques. To eliminate these limitations, an algorithm-specific parameter-less algorithm developed by (Rao and Patel 2013) is known as Teaching–Learning-Based Optimization (TLBO algorithm). It employs only general controlling variables like the size of the population and the number of iterations for its working.

### 2.10.2 Modelling of Neural Networks

Minsky from MIT formulated an Artificial Neural Network (ANN), which is widely employed by researchers in numerous institutions, professions, and government organizations to solve a variety of issues, including signal/image processing, process control, and automation, the prediction of system failure or malfunction, and production process optimization (Isaac et al. 2018). Due to ANN's ability in addressing nonlinear problems without an association between input and output parameters, it has gained widespread attention and use.

An artificial neural network (ANN) is a data processing network that finds unidentified dependencies between input and output variables. Many interconnected

information processing units make up the ANN network. This technique allows for better prediction of the behavior of very large, complicated, nonlinear systems with a lot of input and output variables. The network's design and learning techniques, which were utilized to build the network using experimental input and output data, are the only sources of mapping capabilities employed by the prediction system. The network learns by examining the patterns in the input and output data it receives during training. The network can then apply this knowledge to forecast how unknown input parameters would behave. ANNs are categorized as single-layer feed-forward neural networks (SLFFNN), multilayer feed-forward neural networks (MLFFNN), and recurrent neural networks (RNN) based on their architecture. (Sharkawy 2020).

The manufacturing process is highly nonlinear and complex. The process is comprised of various input data, with no relationship between input and output data. that can represent the process's behavior mathematically. Only a few studies utilizing ANN to forecast the mechanical characteristics of FS welded alloys have been published. (Okuyucu et al. 2007) used an ANN model to try and predict the mechanical characteristics of FS welded aluminium alloy. An SLFFNN using a back propagation learning technique was utilized to train, test, and predict the joint properties. Considered output characteristics are hardness at the nugget zone, yield strength, percentage elongation, and tensile strength. Rotational and welding speed are considered input elements. The measured values and the projected values showed a strong connection with each other. The effectiveness of neural networks utilizing the Gradient Decent (GD) and Levenberg-Marquardt (LM) learning methods has been studied by Yousif et al. (2008). The GD learning algorithm uses a 1st order approximation, while the LM learning method uses a 2nd order Taylor series performance metric. As a result, LM learning performed better than GD. Response Surface Method (RSM) and ANN models have been compared by Lakshminarayanan et al. (2009) in estimating the tensile strength of FS welded AA7039 alloy. The use of ANN and FEM to forecast the average grain size during the FSW process was studied by Livan Fratini et al. (2009). The ANN model was fed the FEM model's output values in order to forecast the outcome. Plastic strain, Strain rate, temperature, and Zener Hollowmon parameters are the network's input parameters. The precise prediction of grain size was made using the feed_forward with back_propagation

model. Additionally, the predictability of the same model for the lap joint and T joints was examined, and good predictability was discovered.

By employing rotating speed, welding speed, and tool probe geometry as input variables, the Multilayer Perception Neural Network (MLPNN) model, according to Kudzanayi Chiteka (2014), was able to forecast tensile strength with accuracy. MLPNN is an enhanced version of a feed-forward neural network employing a backpropagation algorithm. The neural network has various tools like high convergence rates, different learning rules, different training algorithms, alternate transfer functions, etc. to improve the results or to achieve some required properties of the trained networks. However, when it comes to model building, the neural network has issues with interpretability and complexity. Thus, numerous attempts have been made to prevent the gradient descent method from being stuck in local minima as the network's training progresses. The genetic algorithm (GA) has no limits on network structure and can simultaneously scan various areas. In addition to allowing for solution selection, GA does not necessitate the employment of a back propagation method. Thus, by combining these two GA and MLPNN, we may be able to resolve the problem of MLPNN becoming stuck in local minima.

## 2.11 DEFECTS IN FSW

Any kind of defect compromises a component's functionality. In FSW the defects related to the melting of the workpiece and solidification, such as porosity, cracks, destructive phases, intermetallic phases, etc. are entirely eradicated as the material does not undergo melting. However, due to improper process parameter selection, defects such as pin/worm/tunnel holes, less penetration depth, piping defects, and kissing bonds are discovered in the weld zone (Elangovan and Balasubramanian (2007), Elangovan and Balasubramanian (2008a), Lakshminarayanan and Balasubramanian (2009), Mehta and Badheka (2016), Langari and Kolahan (2019), Soni et al. (2017). Both material flow and energy balance were attained under ideal process conditions. The amount of heat produced during the hot working procedure was sufficient to lower the material's resistance to deformation. Heat also impacts microstructural changes including coarse grain, recrystallization, grain reorientation, and dissolving of strengthening precipitate. Material resistance to deformation and

changes in its microstructure are both greatly influenced by the chemical composition of the substance. At extremely low temperatures, some materials experience metallurgical characteristic changes, while others do not experience any changes until higher temperatures are reached. Nonbonding and void formation are symptoms of too-cold processing conditions. A hot processing condition is one where there is an excessive flow of material, which causes undesirable mechanical property degradation and material expulsion like a flash.

Two approaches were used to create hot processing conditions. 1) The produced temperature is above the material's solidus temperature. 2) Although the temperature developed is getting close to the solidus, the direct deformation zone's heat loss is being adequately reduced to cause unintended thermal softening of the workpiece. But the welded materials' mechanical qualities deteriorated. (Daniela Lohwasser and Zhan Chen 2010). The FSW method generates a lot of heat, which causes the surface to have blisters or surface galling (Leal et al. 2008, Arbegast, 2008). Thermal softening of the workpiece occurs away from the tool shoulder's border with further heat increase. After that, the tool shoulder initiates throwing out/ ejecting material in the form of a flash rather than constraining it. (Arbegast 2008, Singh et al. 2011, Leitão et al. 2012, Palanivel et al. 2012, Cioffi et al. 2013,) As a result, there is not enough material in the weld zone, which causes defects at the weld region's surface. Sometimes, when FSW is performed using thrust force rather than a tool position control system, severe thermal softening renders the material immediately beneath the shoulder incapable of withstanding the axial thrust force pressing on it. Due to this, the material thins, resulting in a reduction in thickness. The pin can scrape against the back plate, rupturing the workpiece at the weld's root and causing extra material to flash out of the weld zone because of the fixed probe length and the thinning impact on the material. This is depicted in Figure 2.25, titled "Excessive Flash". Nugget collapse occurs when there is an excessive soft material flow from the shoulder to the pin-driven region (William J. Arbegast 2008). According to J. Adamowsk et al. (2007), Tunnel or worm faults originate from incorrect material mixing due to insufficient or overly high rotational speed combined with an inadequate thrust force. According to Chionopoulos et al. (2008), the tool's poor design may potentially contribute to defects. When opposed to a conical type of tool, a screw-type tool can

only join a small number of components. Ayad et al. (2012) showed that the emergence of a tunnel hole at the junction of TMAZ and NZ was caused by high rotational speed and welding speed. According to Zhang et al. (2012), a tunnel defect developed in the weld zone at higher and lower welding speeds with higher rotating speeds.

According to Oosterkamp et al. (2004), due to the breakdown of the oxide layer during the welding, a kissing bond was developed in the weld zone. Insufficient stretching of the contact surfaces surrounding the welding pin causes the oxide layer to break up. In an Al alloy that had been FS-welded, Sato et al. (2004) and Sato et al. (2005) used TEM to study the microstructure near the zigzag line. The oxide coating on the butt surface is broken up into particles and spread throughout the zigzag line's cross-section during the FSW process. Hua-Bin Chen et al. (2006) researched FSW defects. According to the study, insufficient heat production and frictional force led to the formation of the kissing bond. Finding a kissing bond using a non-destructive method is exceedingly challenging. According to Sato et al. (2005), kissing bonds encourage cracks. Insufficient penetration depth or a short tool length are the two causes of lack of penetration depth. A shorter tool's length could be the result of tool wear. The increase in welding speed while maintaining constant rotational speed is what causes the wormhole to start near the bottom of the weld. Tools constructed of brittle materials will cause heated holes to appear at low processing temperatures. Due to insufficient material flow towards the bottom of the NZ, the wormhole grows with the welding speed. There are signs that the creation of the wormhole defect depends on the relationship between rotation speed and welding speed (Adamowski 2007, Dinaharan 2012, Kalaiselvan and Murugan, 2013, Murugan and Kumar, 2013). As seen in Figure 2.23, Daniela Lohwasser and Zhan Chen, (2010) and Chaitanya Sharma et al. (2012) detected several defects in the FSW process. They observed that the square tool pin profile had a greater eccentricity and generated the least amount of weld defects. The ratio of the tool's static volume to its dynamic volume is used to characterize the eccentricity. The flat faces produced a pulsing movement that enhanced the stirring process.

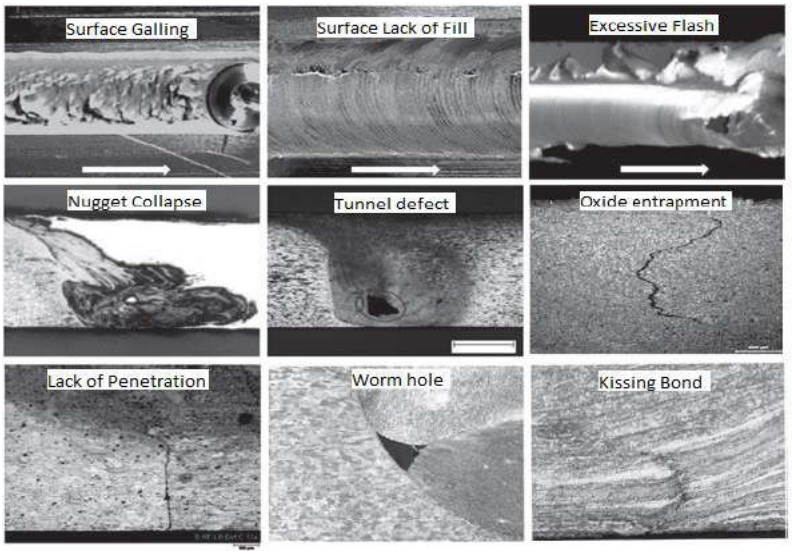


**Figure 2.23** Friction Stir Welding defects (Zettler and Vugrin 2003)

## 2.12 APPLICATIONS OF FSW (Courtesy: Mishra et al. 2005)

### 2.12.1 Marine and Shipbuilding Industries

The Marine and Shipbuilding industries were the first to select and utilize the FSW technology for commercial purposes. The following applications are appropriate for the process::

- Panels for decks, sides, bulkheads, and floors
- Marine and transport structures
- Offshore accommodation
- Refrigeration plant
- Aluminium extrusions
- Masts and booms, e.g., for sailing boats.
- Helicopter landing platforms

### 2.12.2 Aviation industry

Friction stir welding is being used in the aerospace sector to create prototype and production parts. For use in military and civilian aircraft, there are opportunities to weld ribs, skins to spars, and stringers. Friction stir welding has been used to replace almost 60% of the rivets in the Eclipse 500 airplane. When compared to fabrication

and machining from solid, this has many benefits, including lower manufacturing costs and weight savings. Friction stir welding has been utilized to complete longitudinal butt welds in fuel tanks made of aluminium alloys for spacecraft. By welding the sheets before forming, The procedure could potentially be used to expand the size of sheets that are sold commercially. Therefore, the FSW procedure can be used for:

- Space vehicle's Cryogenic fuel tanks
- Wings, fuselages, empennages
- External throw-away tanks for military aircraft
- Aviation fuel tanks
- Various structural components
- Scientific and military rockets
- Repair of faulty MIG welds

### 2.12.3 Locomotive industry

The bullet train components, made from aluminium extrusions, may be FS welded, such as freight wagons, railroad tankers, rolling stock, underground carriages, and trolley cars.

### 2.12.4 Land transportation

Automotive businesses are choosing the FSW method for their industrial applications. The following are the applications:

- Wheel rims
- Truck bodies
- Space frames
- Chassis cradles
- Mobile cranes
- Armour plate vehicles
- Tail lifts for truck

### 2.12.5 Other industry sectors

In addition, FSW can be used for:

- Refrigeration panels
- Electric motor housings (in production)
- Gas tanks and gas cylinders
- Cooking equipment and kitchens etc.

## 2.13 SUMMARY AND KNOWLEDGE GAP

This assessment of the literature concludes that ceramic and mineral-reinforced aluminium alloys are superior to conventional aluminium alloys in applications demanding strength and increased stiffness. Rutile particles can be used to strengthen the AA6061 alloy, which is very beneficial to the aerospace and automotive industries. Due to the development of dangerous intermetallic phases and the segregation of mineral and ceramic particles, fusion welding of these composites presents significant challenges. Friction Stir welding is a solid-state joining process used for welding aluminium metal matrix composites (MMCs). In the aircraft sector, the FSW of aluminium alloys and MMCs is in great demand due to its low cost and high efficiency, in turn substituting the traditional joining technologies. According to research, the most promising tools for friction stir welding of mineral reinforced aluminium metal matrix composites are a square profile probe and a threaded profile probe tool. It has been noted that there hasn't been much research done on rutile particle reinforced aluminium MMCs, and there hasn't been much discussion on friction stir welding of AA6061-3(wt%) rutile composites. As a result, this composite is used as the subject of an investigation to examine how well FSW joins them and to connect the correlations between structure and properties. To create strong welds, tool geometry is crucial. A cylindrical threaded probe and concave shoulder are well-known features of the welding tool, even though there isn't much information available in the existing literature due to the proprietary character of tool designs. Furthermore, because the FSW process is dynamic, a recurrent neural model will work well as a prediction model. The application of MLPNN or any of its derivatives in the FSW process has not received much attention.

The investigation of the effects of the FSW technique and welding parameters on the mechanical characteristics and microstructural alterations of AA6061-3 (wt%) rutile composites is explained in the current work.

## 2.14 STATEMENT OF PROBLEM

An aerospace engineer is interested in the materials and methods used to build vehicles for transportation. The prospects and opportunities in the transportation and aerospace sectors have substantially grown because of improvements in the materials utilized in these sectors. But these developments also necessitate complex technology, including the right joining method. Critical structural components frequently need joints, which must be as strong and durable as possible under high-intensity static and dynamic stresses.

The FSW process has many benefits over traditional welding processes as it is a totally solid state. Traditional arc welding methods locally liquefy the workpiece, leaving behind large grains and high residual stresses that, when the workpiece cools, significantly deteriorate the material's characteristics. Additionally, arc welding frequently calls for the employment of a filler material, which alters the composition of the joint and adds the filler's weight to it. When riveting, mechanical fasteners must be added, and pieces may need to be thicker at fastening points to boost strength, both of which add weight to the component. in comparison to standard plates, it could potentially lead to decreased tensile characteristics and fatigue life. The aerospace and transportation industry must address the issue of strength loss and weight gain. A thorough study of the characteristics of friction stir welds under static and dynamic loads is required to apply FSW in critical components. The AA6061 alloy used in the transportation sector is one very popular aluminium alloy that could profit from using FSW joints. This alloy is reasonably priced, has excellent strength, and is ductile. The alloy does, however, have some disadvantages. As a result, the use of composites based on the AA6061 alloy and reinforced with the appropriate ceramic particles has grown recently. These alloy-based composites are typically MIG (Metal Inert Gas) welded, laser welded, or riveted in industrial settings. These procedures could, however, be costly and unreliable, impair macroscopic qualities, or add weight and

reduce strength. If the required research is done on FSW joints of AA6061 alloy-based composite, FSW offers a financially advantageous alternative.

Joints are subjected to a wide range of environmental conditions, compound pressures, and moments in industrial applications. Friction stir welded joints contain highly varied microstructures and residual stresses that have an impact on the performance of the material in addition to complex loading scenarios. Finally, the inherent material characteristics along with static and dynamic loads may result in the joint failing sooner than anticipated. It would be challenging to isolate the factors that cause failure if all loads and environmental factors were integrated into a single test. Tests for static and dynamic loads were conducted to simulate the friction stir welds behavior in real applications. In this manner, information on the joint's performance for the two main types of loading was gathered. This knowledge improves comprehension of the behavior of FS welded components.

The current work describes the typical welding procedures, points out the issues they raise, goes into great detail about FSW, and outlines its development. For the FSW study, AA6061-3(wt%) rutile composite was chosen since it is difficult to weld using traditional welding techniques.

## 2.15 OBJECTIVES OF THE CURRENT WORK

The primary objective of the study is to understand the relationship among the FSW operating variables namely tool rotation speed, tool traverse/welding speed, tool probe geometry, and the FSW process responses using the Taguchi technique. The microstructural changes in the weld zone and the mechanical properties of the welded composites were considered FSW process responses. The evolution of the microstructure at the composite weld zone for various combinations of rotating speed, welding speed, and tool pin profile is examined. The optimization of the process variable and prediction of these variables which give better joint properties are performed using statistical and evolutionary techniques. The following goals have been established after taking into consideration the current advances in the field of FSW:

1. Carry out Friction Stir Welding of Al6061-3%Rutile composites to investigate the role of tool geometry, tool rotational speed, and welding speed in obtaining defect-free welds.
2. Microstructural study of composites welded through FSW technique, to analyze the grain refinement and redistribution of reinforced particles at welded zone.
3. Assess the mechanical properties of the welded composite like tensile strength, hardness, and % elongation.
4. Analyze the impact of process variables on friction stir welding of composites through the Design of Experiments and optimization of the process using statistical techniques.
5. Use of an appropriate evolutionary method to simulate the correlation between FSW process variables and their impact on the mechanical properties of the joints.

## 2.16 SCOPE

Based on the targeted objective, the investigation's scope includes;

a. Experimentally investigate the impact of process variables on the joint efficiency of the FS welded composites.
b. Explore the possibility of analyzing the impact of tool geometries on the microstructure and mechanical behavior of composites.
c. Analyzing the effect of process parameters and tool pin profile on the ultimate tensile strength of the composite.
d. Use suitable optimization techniques to optimize the process parameters which yields superior mechanical properties.
e. The modeling of GA-MLPNN correlates the friction stir welding variables with the ultimate tensile strength, hardness, and percentage elongation of the composites.

## 2.17 DIRECTION FOR PRESENT WORK

The main objective of this study is to increase our understanding of the static and dynamic behavior of friction stir-welded AA6061-3(wt%) rutile composite joints. Reducing manufacturing costs and improving component strength over conventional joining techniques employed with the AA6061-3(wt%) rutile composite, would help the transportation industry to find the viability of the FSW process to join this composite. The secondary goal of this study is to identify correlations between the microstructural properties arising from various sets of FSW process factors and the static and dynamic performance of butt joints in the AA6061-3(wt%) rutile composite.

# Chapter 3

## RESEARCH METHODOLOGY

According to the literature study presented in the previous chapter, there is a lot of research being done in the field of friction stir welding (FSW) of hard-to-weld materials. As observed in the survey, much research is done on the joining of particulate aluminium matrix composite by the solid-state welding process. The current work emphasizes on FSW of rutile reinforced AA6061 composite, the formation of grain structure at the weld region, and the effect of operational variables on the joint properties. The mechanical properties of the FSW joints were studied for various combinations of process parameters such as tool rotational speed, tool traverse speed, and tool profiles, by conducting experiments at a few specific points, providing a glimpse of the possible FSW of the said material. However, the industrial application needs more information so that the process may be successfully employed and optimized based on either controlling input factors or output reactions. Therefore, the issue at hand is the market acceptance of technological advances. The end user, or the industry, will benefit more by expanding the data by including more combinations of input factors and associated output responses. The GA-MLPNN model, which provides a correlation between process parameters and output responses, will offer the necessary solution for improving the database. The following is an outline of the research:

- Preparation of rutile reinforced 3(wt %), AA 6061 matrix composite, followed by characterization using Scanning Electron Microscope (SEM).
- Performing friction stir welding of composites to identify the range of operational variables which gives defect-less joints for different tool pin profiles.
- Determining the modification in microstructural and mechanical properties of the composites through Scanning Electron Microscopy, tensile test, and hardness test.
- Using the Taguchi approach to assess the impact of operational variables on the joint properties.
- Performing multi-response optimization of FSW process using both conventional statistical technique as well as with nature-inspired evolutionary algorithm.

- Developing the empirical model using soft computing techniques to predict the mechanical properties of the composite joints.

In the beginning composite material is prepared and tools with different probe profiles were designed. Experiments were planned and conducted which covered all the aspects mentioned above. Figure 3.1 depicts the overall methodology followed in the study.

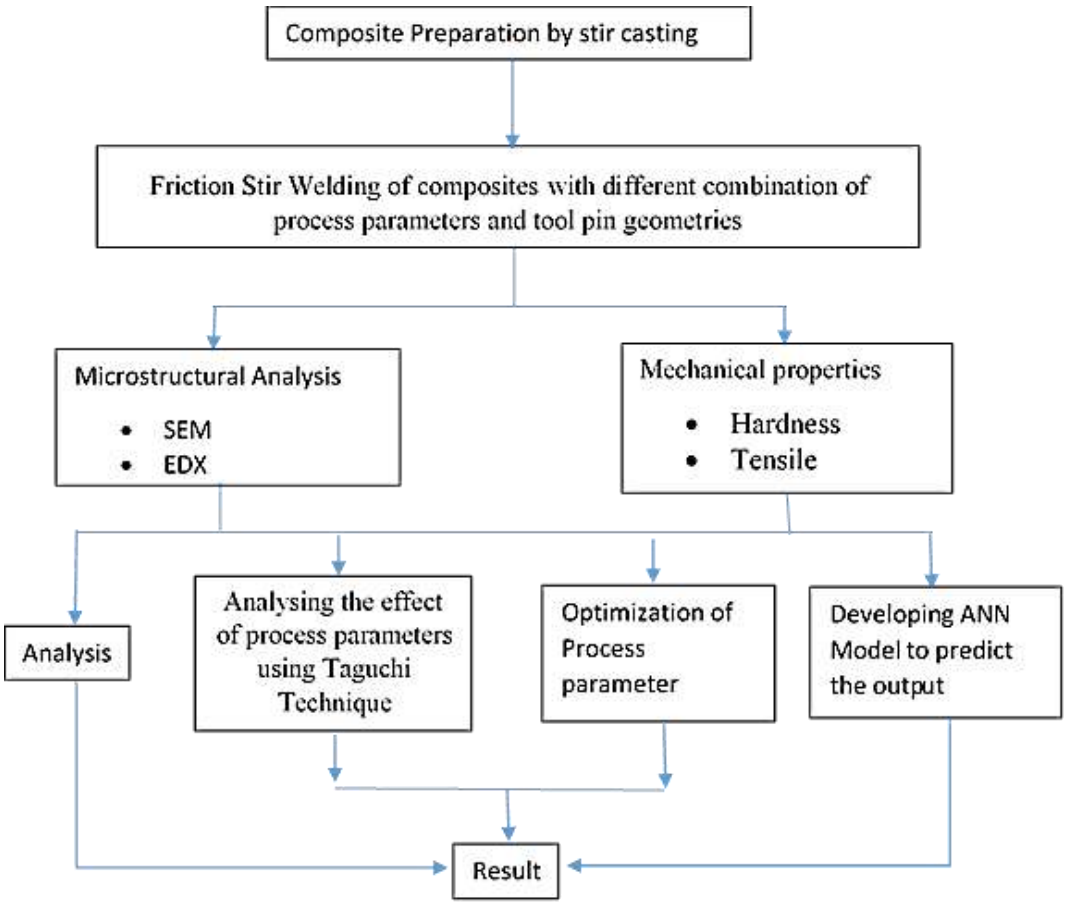


**Figure 3.1** Flowchart of the methodology followed

## 3.1 PREPARATION OF COMPOSITE MATERIAL

Depending on the kind of reinforcing elements, shape, size, and morphology, the composites were prepared by various techniques such as squeeze casting, stir casting, liquid infiltration, spray deposition, vacuum hot pressing, powder metallurgy, and friction stir processing (FSP) (Lloyd 1994)(Mustansar et al. 2019). Among various processing methods, stir casting is one of the promising, commercially viable methods to process AMCs (Hashim et al. 1999). In the present study, a modified stir casting

technique was used to fabricate AMCs using AA6061 alloy as matrix and rutile with an average size of 10 μm as reinforcement particulate. Table 1 lists the chemical composition of AA6061 matrix material. Figure 3.2a and figure 3.2b show the rutile particle's SEM image and Rutile particles as received condition respectively.

**Table 3.1** Chemical composition of matrix material (in wt. %)

| Copper | Magnesium | Silicon (wt. | Iron | Manganese | Aluminium |
|---|---|---|---|---|---|
| 4.5 | 0.8 – 1.2 | 0.4 – 0.8 | 0.7 | 0.15 | Remaining |

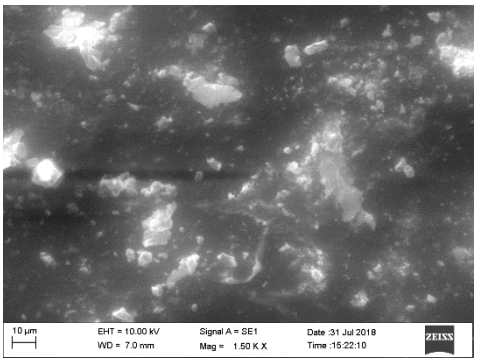


**Figure 3.2a** SEM image of rutile particles

**Figure 3.2b** Rutile particles as received condition

Figure 3.3 shows the flowchart of the bi-stage stir casting process. A 3.0 kg ingot of AA6061 Al alloy was melted at 800 °C in a ceramic crucible using an electric furnace. The setup was covered to avoid the absorption of gases. Hexachloroethane tablets were added to the molten metal for degassing the melt. To enhance the wettability of reinforcement with the molten metal, 1 wt.% Mg was added to the molten AA6061 matrix. The addition of Mg improved the wettability of the reinforcement by reducing the surface tension of the molten metal. Adding beyond 1 wt.% Mg into the melt altered the viscosity of the melt and thereby imperiled the proper distribution of the particles (Taylor et al. 2013).

Simultaneously, rutile particles of given quantities were preheated at 700 °C for 1 h to remove any moisture content from the particle. Preheating also enhanced the wettability of the particle by forming a layer of oxide on its surface. Before adding particles, the melt was stirred using a graphite-coated steel stirrer to form the vortex. The stirrer was immersed at 1/3 vortex from the top surface and operated at a speed of 300 r/min.

Preheated particles were added to the melt at a constant temperature of 800 °C, in two steps to avoid the agglomeration of rutile particles in the molten metal. The addition of particles into the melt in a single step severely altered the viscosity of the melt, thereby affecting the proper mixing of particles in the matrix. The addition of particles into the melt in two steps separated by a small-time interval greatly enhanced the proper dispersion of particles in the matrix. Stirring continued for 5 minutes after the addition of the particles. Nitrogen gas was purged on the surface of the melt during stirring to reduce oxidation. Finally, the composite was poured into the die and preheated at a temperature of 450 °C. Preheating the die prevented molten metal from suddenly dropping in temperature as it encountered the die and kept the slurry molten throughout the pouring process.

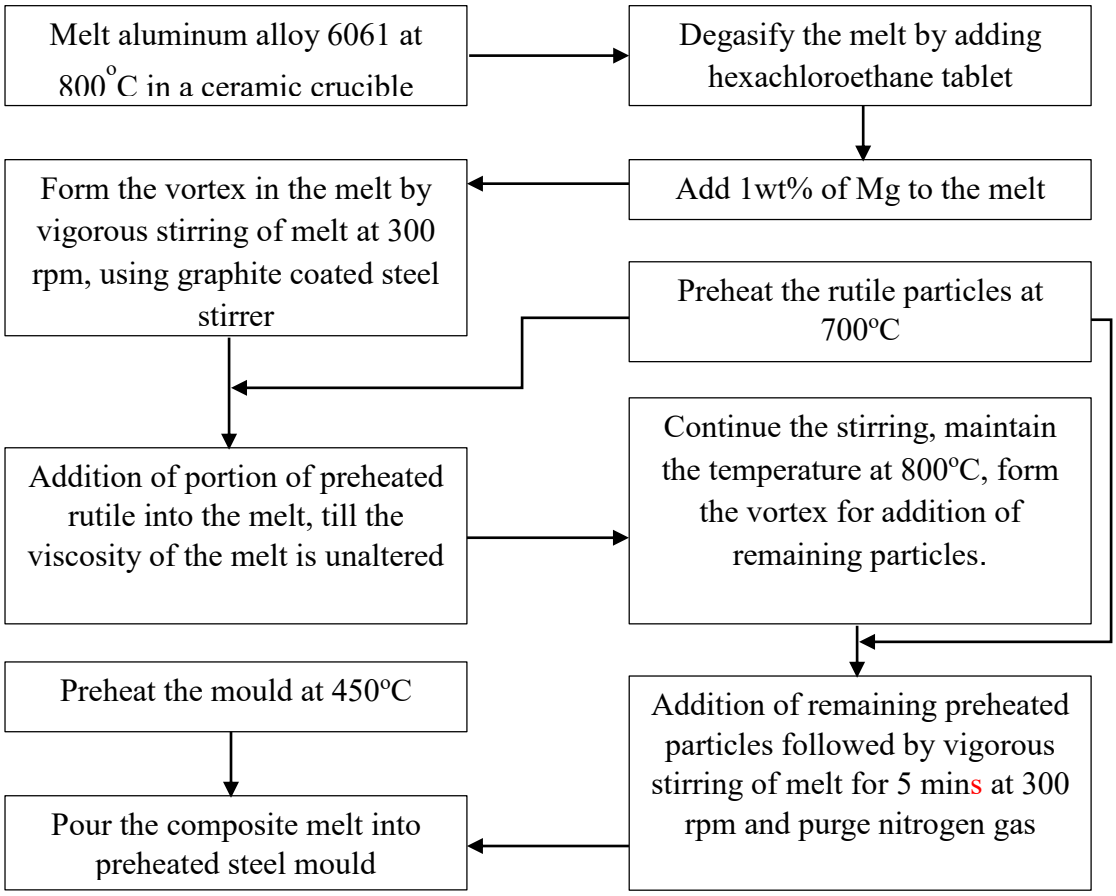


**Figure 3.3** Schematic representation of the bi-stage stir casting process

Figure 3.4 represents a step-by-step process of stir casting. With the use of a milling machine, the cast composite is machined to obtain the desired shape and dimension to perform the FSW of the composite.

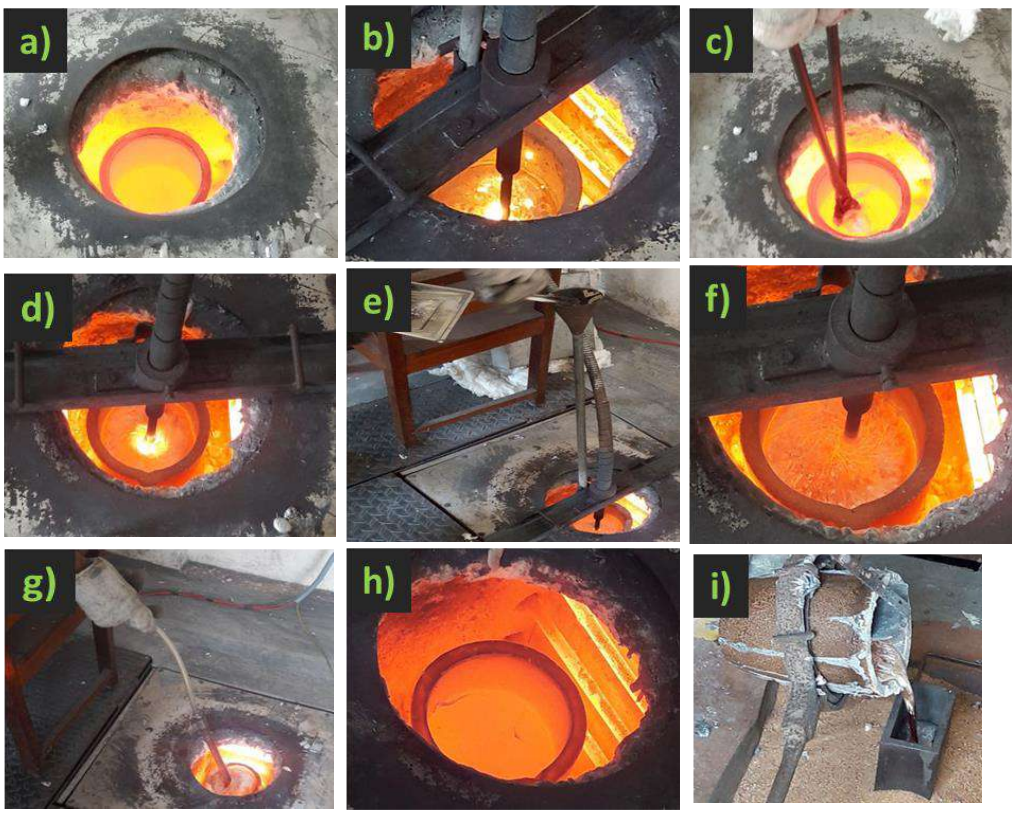


Figure 3.4 Various phases of stir casting process: a) Molten AA6061 in the crucible, temperature 800$^{o}$C, b) Addition of Hexachloroethane tablets to molten metal followed by slag removal, c) Addition of Magnesium d) Stirring of melt to form vortex e) Addition of Rutile particle to molten metal during stir condition, f) Stirring of molten metal for 10 mins to obtain uniform distribution of Rutile particles g) Nitrogen purging h) Composite before pouring and i) Pouring of composite into a die.

## 3.2 WELDING MACHINE

Readymade FSW machines are available to perform welding operations. However, the cost of this equipment is high. A CNC vertical machining center can also be utilized as an FSW machine. The main challenges in using a machining center as an FSW machine are designing an appropriate fixture to hold the workpiece, placing it accurately with

the FSW tool, and supporting it throughout the welding operation. Based on the requirement, DTC 250 (Drilling, Tapping, and Machining Centre) 3-axis Computer Numerical Control machine (SPARK) supplied by ACE Manufacturing system has been chosen. A vertical milling machine depicted in Figure 3.5 is used for FSW.


**Figure 3.5** Vertical Milling Machine

## 3.3 EXPERIMENTAL WORK

The cast composite AA6061- 3wt% Rutile is machined to obtain the required shape and size (100mm in length, 50mm in width, and 5mm in thickness) using a milling machine. To avoid the abutting joint faces being driven apart, the welding plates were set on a steel support plate and secured tightly. The backing plate must be able to withstand the normal forces brought on by FSW. Figure 3.6 depicts the experimental setup used to perform the FSW process. The fixture was tilted to an angle of 2°in the direction of the tool travel path (Krishna et al. 2014). The rotating FSW tool was inserted into the workpiece's adjoining edges until its shoulder made contact with the surface with sufficient axial force. The tool was kept at the initial inserted location with the shoulder touching the work surface for a dwell period of 20 seconds to achieve the necessary frictional heating. The machine table was then set to a predetermined welding speed.

After a dwell time of 20 seconds, the rotating tool was lifted as it approached the farthest point of the joint.

**Figure 3.6** Experimental Setup

The weld that had just been made would be hot, thus a cooling period of 30 minutes was allowed to pass while it was clamped. The welded workpiece was then taken out, and a fresh set of work parts was clamped for more welding. The same procedure was repeated for all other experiments. The FSW process parameters and their values are shown in Table 3.2.

**Table 3.2** Experimental Process Parameters.

| | | Tool Rotational Speed (rpm) | | |
|---|---|---|---|---|
| | | 750 | 1000 | 1250 |
| Welding speed (mm/min) | 60 | T1 | T4 | T7 |
| | 75 | T2 | T5 | T8 |
| | 90 | T3 | T6 | T9 |

### 3.4 TOOLS FOR FSW

For the joining procedure to be successful, the FSW tool is crucial. A rotating non-consumable tool typically has a probe with a range of shapes and a circular shoulder. The fundamental function of the tool is to heat the workpiece by producing friction and distortion and directing the flexible softened material around the tool probe to create a solid joint. Cylindrical or tapered probe profiles, either with or without threads, are the most often used probe profiles.(Thomas et al. 2005). Complex probe profiles such as

triangular, square, Skew-stir, and Flared-Triflute also have been used as added features to the tool probe which improves the flow path of plasticized material (Rai et al. 2011). The mixing capacity of the tool probe is mainly dependent on the ratio of swept volume to the static volume of the probe. The plain cylindrical probe has a ratio of one, whereas the addition of features such as flat edges, threads, and flutes in the probe increases the ratio. Based on the available literature, the two most common types of tool probe profiles were selected for the study namely threaded cylindrical and square probes. A threaded cylindrical probe (Diameter 6mm and 1 mm pitch) used in the present study has a ratio of 1.01, whereas a square probe has a ratio of 1.57. The threaded cylindrical probe has a left-hand thread, that pushes the material downwards along the probe surface when it is rotating in a clockwise direction. This phenomenon assists in improved mixing action (Zhang et al. 2012). AMCs welded with the square probe have displayed the excellent quality of weld with improved UTS. Pulsating effects produced by the sharp edges of the square probe enable fragmentation and homogeneous distribution of reinforced particles and reduction in grain size (Hassan et al. 2012).

A new type of tool probe was also designed to evaluate the combined effect of threaded cylindrical and square probes. The pin is a combination of thread and square shape. The threaded profile is made at the base of the tool probe towards the shoulder, followed by a square section at the tip of the probe. The pin's height must be only a little bit less than the depth of the workpiece or the weld. The work piece has a 5 mm depth. Therefore, the pin's height is taken as 4.7 mm. (BIST et al. 2016). The range of shoulder diameters that are most frequently employed is 2.5 to 3 times the probe diameter. Maintaining a shoulder to pin diameter ratio of less than 4 and greater than 2 will prevent overheating and underheating. (Vijayavel et al. 2014)**.** The shoulder-to-pin diameter ratio in the current investigation is maintained at 3. To accomplish welding operations, a CNC vertical milling center is utilized. The shoulder is manufactured with a concave shape at the bottom, and a 7° inclination is given perpendicular to the tool's vertical axis. It functions as an accumulator and produces enough heat for welding. To dissipate heat more quickly both before and after welding, the shoulder's height should be greater than its diameter. The tool's other end needs to have a suitable gripping mechanism. The tool material must have qualities like the ability to sustain impact load during plunging, resistance to high temperatures, resistance to wear, and compressive

load. Since tool steel M2 has the majority of the qualities mentioned above, it has been chosen. The hardness of the FSW tool has a significant impact on the friction_coefficient ('μ'). The amount of friction that happened between the stationary workpiece and the revolving tool, and the coefficient of friction, "μ" are directly proportional to one another. Therefore, it can be inferred that the tool hardness will determine how much heat is produced during the FSW process as well as how resistant the material is to wear (Rajakumar et al. 2010). The joint's strength depends on the amount of heat produced at the weld zone. The strength of the joints would deteriorate if the heat generated at the weld zone is insufficient. The Thermo Mechanical Affected Zone (TMAZ) may develop defects on the retreating side as a result of the increased heat produced at the weld zone, which will promote grain growth and severely cluster the precipitates at the NZ. Lower hardness is generated in NZ as a result of this. The higher strength of the joints was achieved, according to Rajakumar et al. (2011), when they were formed using tools with hardness ranging from 45 HRC to 55 HRC.

In this study, three distinct types of tools were manufactured and heat-treated to a tool hardness of 62 HRC. Schematic representations of FSW tools are shown in Figure 3.7. (Threaded cylindrical, square, and combination of square and threaded cylindrical pin profiled tool). Hereafter, the tool with the Threaded Cylindrical probe is represented by TC, the Square Profile probe by Sq, and the Combination of Square and Threaded Cylindrical probe tool by CSTC. Figure 3.8 depicts the FSW tools with different probe geometries used in the study.

## 3.5 DESIGN OF FSW FIXTURE

Fixture's main goal is to shorten the specimen's operating-process setting time. The fixture was made with the need that it holds the specimen firmly and allows for rapid part switching. Butt joints are the most common kind of weld joint. There is no restriction on the specimen's length, but the width of the workpiece after the weld must be 100mm (two butting plate width is 100 mm). A groove, of 14mm depth and width of 100mm with press fit tolerance was made on the fixture base to hold the specimen rigidly. The depth includes backing plate thickness and 60% to 80% of the workpiece thickness. The backing plate's primary role during welding is to support the workpiece.

The upward supporting plate is provided to avoid lifting the plate during welding. The material of the fixture must have less thermal conductivity. The base fixture material is made of chromium steel. The backing plate and supporting plate are made of mild steel. Figure 3.9 shows the FSW fixture setup.

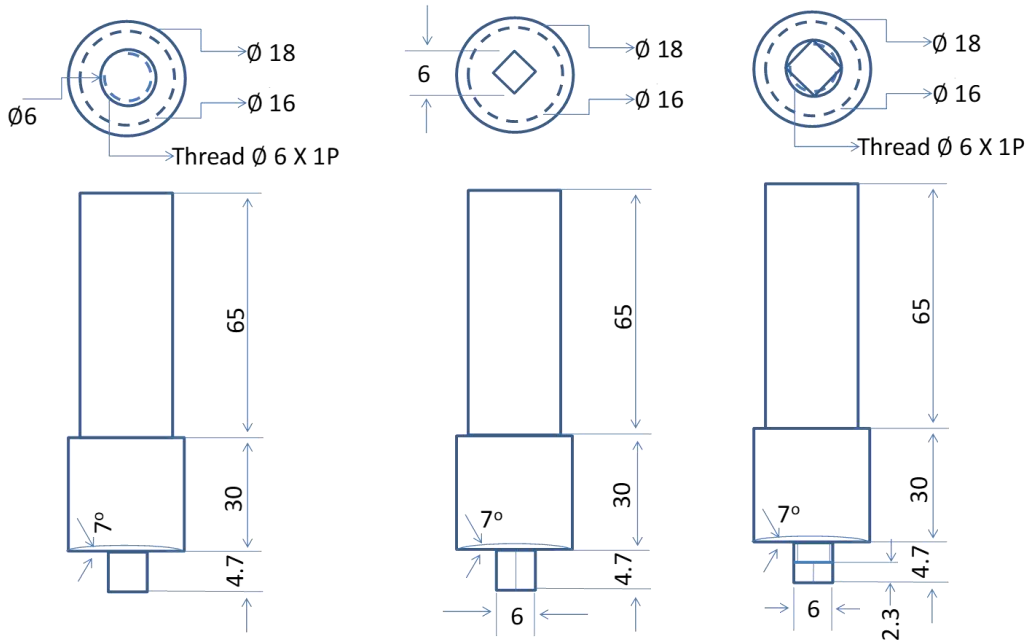


**Figure 3.7** Friction Stir Welding tool with a) Threaded cylindrical pin, b) Square pin, and c) Combination of Square and Threaded cylindrical pin.

**Figure 3.8** Fabricated and heat treated Friction stir welding tool with a) Threaded cylindrical pin, b) Square pin, and c) Combination of Square and Threaded cylindrical pin

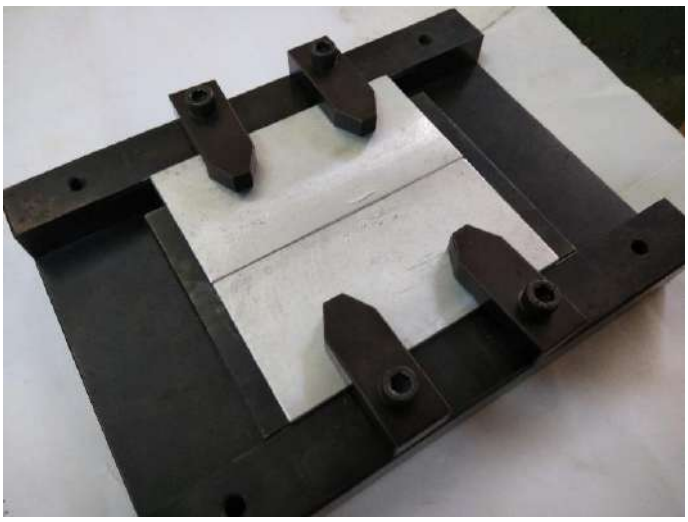

**Figure 3.9** FS welding Fixture setup

## 3.6 SECTIONING OF TEST SPECIMENS OF FRICTION STIR WELDED AA6061-3wt% RUTILE COMPOSITE JOINT

To prepare the specimens for microstructural analysis, hardness tests, and tensile testing friction stir welded AA6061 – 3(wt%) Rutile composite plates were sectioned and formed as shown in Figure 3.10. Surfaces that were across the joint and perpendicular to the welding direction were chosen for the microstructural analysis and hardness measurements. Wire EDM (Electro Discharge Machine) was used to section the samples.

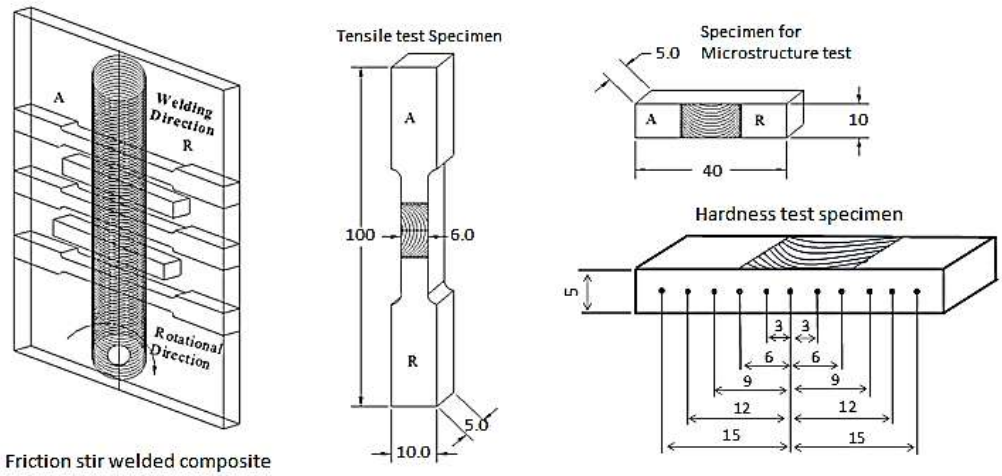


**Figure 3.10** Schematic representation of specimens used for characterization

## 3.7 CHARACTERIZATION OF FRICTION STIR WELDED AA6061-3wt% RUTILE COMPOSITE JOINT

### 3.7.1 X-Ray Diffraction (XRD) Analysis

XRD analysis of friction stir welded AA6061- 3(wt%) Rutile composite was performed using an X-ray diffractometer (JEOL made - DX-GE-2PModel), operated with Cu-Kα at 20 mA and 40KV, to detect the various phases existing in the as-cast as well as in the FS welded composites. For all composite specimens, the 2θ range is set between 20° and 80° to cover all of the phases' significant intensity peaks. The NZ samples were chosen for the analysis since NZ experiences maximum temperature during FSW. The dimensions chosen for this are 6 mm by 5 mm by 3 mm. JCPDF data files were used to analyze the diffracted data and find peaks associated with different constituent phases.

### 3.7.2 Analysis of Microstructure

An incredibly helpful investigation instrument for displaying the surface details of the specimen is the scanning electron microscope (SEM). Secondary electron imaging modes of the SEM (Model: JSM-6380LA, JEOL) observations have been used, along with Energy Dispersive X-Ray Analysis (EDX) on the welded composite to disclose the microstructure at various areas. 20kV is the working voltage. For joints that were constructed using the TC tool, the regions where microstructural pictures have been obtained are shown in Figure 3.11. Joints formed with the Sq tool also exhibit a similar type of weld region. Images have been captured at the top region of the nugget, Middle region of the nugget, Bottom region of the nugget, advancing side of the TMAZ region, and the retreating side of the TMAZ region. According to the American Society for Testing and Materials standard (ASTM) E112-10, the line intercept method was used to determine the average grain size.

Figure 3.12 shows the SEM image of NZ of composite FS welded using the CSTC tool. The nugget zone is slightly different than the one shown in Figure 3.11, as this weld is performed with a tool having a combination of threaded cylindrical and square pins. Each pin develops a different type of material flow, which alters the nugget region as shown in Figure 3.12. A threaded pin offers a uniform flow of materials from top to

bottom of the pin, whereas a square pin offers proper mixing of the material, fragmentation, and homogeneous dispersion of reinforcement and enables grain refinement.

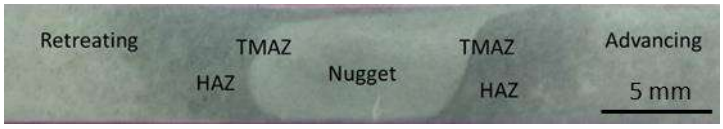


**Figure 3.11** Image of FSW specimen, showing advancing and retreating side, Nugget zone with onion rings, Thermo mechanically affected zone (TMAZ), and Heat affected zone (HAZ)


**Figure 3.12** Image of composite joint FS welded using CSTC tool, showing advancing and retreating side, Nugget zone, TMAZ, HAZ.

### 3.7.3 Testing of Mechanical Properties

#### 3.7.3.1 Hardness test

Testing has been done on the friction stir welded components for hardness, tensile strength, yield strength, and percentage elongation. The material's hardness is measured using a Vickers macro hardness tester with a 5 kg indentation load applied for 15 seconds. The area for the hardness test was selected on the same plane as the microstructural studies. The hardness of the specimens is checked at the central axis of the specimen. The measurement is taken at 3mm intervals to a span of 15 mm on either side of the nugget region. Figure 3.10 illustrates the specimen dimensions and measuring distances for the hardness test. Following the hardness test, the diagonal length of indentation in each sample was accurately measured. Equation 3.1 is used to calculate the Vickers Hardness Number:

$$H_v = 1.854 \frac{P}{d^2} \qquad (3.1)$$

Where P stands for the indentation load in kgs, and d for the mean diagonal length in mm. When determining a specimen's hardness, it's crucial to make sure that the distance

between the indentation marks is at least three times the diagonal distance. This is employed to prevent elastic deformations from affecting the accuracy of the hardness readings and to reduce measurement errors for diagonal length.

### 3.7.3.2 Tensile test

The specimens considered for performing the tensile test were machined as per ASTM E8M-04 standard. Utilizing SEM, microstructural analysis was performed on the specimens' broken surfaces after being subjected to tensile testing. The tensile test was performed on as-cast composites and the specimens were welded at different process parameter combinations. Table 3.3 displays the schedule for the tensile tests. A universal testing machine was used for the test. The tensile test will be conducted at a cross-slide speed of 0.5 mm/min. Three samples from each case were taken into account for the tensile test. For further examination, the average tensile strength of these samples was used. Figure 3.10 depicts the schematic representation of the tensile test specimen. The machined test specimens for tensile strength are shown in Figure 3.13. The fixture arrangement in the universal testing machine used for the test was shown in Figure 3.14.

The joint efficiency (%) (Joint strength) of each FS welded joint is calculated by using equation 3.2 (GENG et al. 2019)

$$\text{Joint efficiency (\%)} = \frac{\boldsymbol{Average\ strength\ of\ the\ joint}}{\boldsymbol{Base\ material\ Strength}} \times \mathbf{100} \quad (3.2)$$

Equation 3.3 is used to represent the relative error in terms of a percentage, which refers to the inaccuracy in predicting each process parameter (Ghetiya et al. 2016)

$$\text{Relative error (\%)} = \frac{Experimental\ UTS - Predicted\ UTS}{Experimental\ UTS} \times 100 \quad (3.3)$$

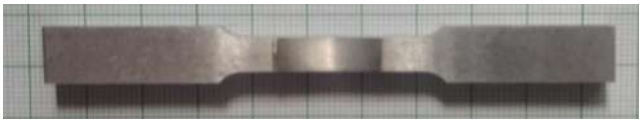

**Figure 3.13** Machined tensile test specimens

**Figure 3.14** Fixture setup for tensile test on the universal testing machine

**Table 3.3** Schedule for tensile testing FSW composites

| Across the joint | | | Along the joint | | |
|---|---|---|---|---|---|
| Tool Rotational Speed (rpm) | Welding Speed (mm/min) | Tool probe profile | Tool Rotational Speed (rpm) | Welding Speed (mm/min) | Tool probe profile |
| 750, 1000, 1250 | 60, 75, 90 | TC, SQ, and CSTC | 1000 | 60, 75, 90 | TC, SQ, and CSTC |

## 3.8 DESIGN OF EXPERIMENT AND ANALYSIS

By predicting which parameters have an impact on the process performance, the main goal of the design of the experiment and analysis is to give a succinct explanation of how to successfully decrease and regulate process variance. By appropriately changing the process parameter values, variation in the result can be reduced. The tests in this study effort are carried out using an orthogonal array (OA). OA is one approach that is most adaptable to a range of circumstances. The design of the experiment includes two or more parameters with different levels. Every level of statistical variation exists. To identify the contributing factors, the results of the test combinations are monitored, and the entire collection of findings is examined. The trials were carried out to evaluate how well the technique worked. Experiments can be made to take less time and cost less

money by using better designs. Figure 3.15 depicts a general representation of a process that has some variables (X) that can be controlled and some variables (Y) that cannot.

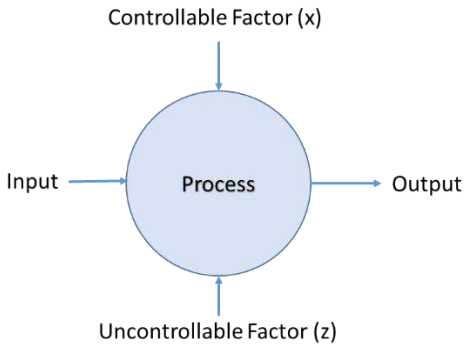


**Figure 3.15** General representation of a manufacturing process.

The experiments' goals are as follows:

1. Determining the variable that has the greatest influence on the result of Y.
2. Y must be defined and set so that it always approaches the desired nominal value.
3. X affects Y in some way. Since a change in X will cause Y to vary, the amount of Y's variability should be less.
4. Determining and adjusting the influential X to minimize the impact of Z variables.

### 3.8.1 Phases of Taguchi Experiment

In Table 3.2, the controlling variables for welding composites are listed. The welding process uses three control factors: rotational speed, welding speed, and tool pin profile. The following factors were taken into consideration when designing experiments based on Taguchi's OA. 1. The number of factors and how they interact, 2. Process varying levels. Three factors, each with three levels, were taken into consideration in the current study. It was ultimately decided to disregard the second-order interaction between the variables to save time and resource usage. Each variable with three levels has two DOFs, giving the process a total of six DOFs. Using Taguchi's method, the experiment's DOF should be lower than or equal to the chosen OA. Hence in this analysis, L9 OA with 8 DOF was chosen. The implications of the OA design will result in a reduction of the experiments from 27 to 9.

### 3.8.2 Signal-to-noise (S/N) ratio

To keep the variance at an ideal level, the best suitable control factor can be chosen based on the output behavior. The variance in the output can be calculated by applying the Taguchi technique to change the repetition data into a distinct value. The transition can be seen in the signal-to-noise ratio (S/N). There are three S/N ratios available depending on the characteristics. In that, to analyze the response, the "larger is better" equation is used (Delir Nazarlou et al. 2021)

Larger is better:

$$\delta_n = -10 \log\left(\frac{1}{n}\sum Y_{klm}^2\right) \quad (3.4)$$

$Y_{klm}$ is the output response of $k^{th}$ quality behavior in the $l^{th}$ trial, at the $m^{th}$ test.

### 3.8.3 Analysis of Variances

The statistical method known as analysis of variance (ANOVA) is employed to predict how the process variables and how they interact with one another will impact the quality attributes (Bhushan and Sharma 2019). To assess whether there are any significant differences between the means of a variety of observational groups, each of which has a normal distribution, ANOVA employs tests based on variance ratios. The significant parameter that influences the performance characteristics can be identified using the percentage contribution. Furthermore, based on a 95% confidence level, the F-test, which bears Fisher's name (1925), can be used to pinpoint the parameter that significantly affects the quality features. Usually, the parameter has a bigger impact on performance if F has a greater value. To ascertain the design parameters and their interaction, which have a substantial impact on the performance characteristics, an ANOVA is conducted using Minitab 17 software (2015).

### 3.8.4 Multi-Response Optimization by Statistical Technique

To determine a system or a process that incorporates unknown information, numerous statistical optimization techniques are applied. The Taguchi method is one of the most widely utilized optimization strategies for engineering issues. For the optimization of a problem with many responses, the Taguchi is insufficient. The Taguchi method combined with grey relational analysis is thought to be an efficient method for solving

and analyzing a problem with various responses. This technique examines a process where the impact of parameters on the responses is unclear or lacking.

The GRA technique uses the following steps:

- ✓ Normalizing the initial data. This is also called the grey relational generation.
- ✓ The grey relational coefficient calculation.
- ✓ The grey relational grade calculation.
- ✓ Finding the ideal combination.
- ✓ Carrying out an analysis of variance (ANOVA).
- ✓ Prediction of the optimal grey relational grade (GRG) value.
- ✓ Performing the confirmation experiment.

### 3.8.5 Response Surface Methodology

Central composite design (CCD) is adopted in this study for fitting a second-order response surface. CCD contains a set of trail experiments, a set of trail experiments at axial points, and a set of trail experiments at center points. In CCD, axial points are used to provide an estimation of the curvature of the response surface while center points (essentially random replicates of experimental runs at the center point) are included to reduce the model prediction error and provide uniform precision, which ensures the equal variance of prediction in the design space or response surface. Such uniform precision in the design space protects against bias because of the presence of higher-order terms in the response surface (Karthikeyan and Balasubramanian 2010). The center points in CCD provide a check for uniform precision, process stability, variance of prediction, and protection against bias. A uniform precision design offers more protection against bias in the regression coefficients [Montgomery 1991]. In CCD the total number of experiments required to be conducted is determined by a formula ($2^k$ + 2k +c) where k is the number of factors in the study, $2^k$ is the number of trial experiments, 2k is the number of axial and c is the number of central points. The suggested number of central points for three factors varies from five to six [https://onlinecourses.science.psu.edu/stat503/node/59]. Many researchers have considered six random test trials at a center point, as a trade-off between the suggested value of c and available resources, in their experimental studies (Rajakumar et al.

2010)(Krishna et al. 2014). Accordingly, in this study central composite design matrix with three factors at three levels that consists of 20 sets of coded experimental conditions ($2^3$ = 8 sets of trail experiments, 6 sets of experimental trails at axial or star points, and 6 sets of experimental runs at center points), are considered to estimate the linear, quadratic two-way interactions of the FSW three process variables (tool rotational speed, tool traverse speed, and tool geometry) on the four response variables (yield strength, ultimate tensile strength, hardness, and % elongation).

### 3.8.6 Desirability Approach

Several statistical methods were used to solve multi-response tasks such as constrained optimization problems, contour plot overlaying for responses, and desirability approach. The latter is desired as it is simple to adopt, and it offers flexibility in prioritizing and giving prominence to each response. In the desirability approach, multiple responses were combined into a dimensionless number, as a performance measure called as desirability function. In this technique, each measured response is converted into a unit-less entity in an interval of (0, 1) where a higher value represents that the response is more desirable whereas a low value represents response is highly undesirable. Based on the requirement, three types of criteria can be adopted to solve the problems, i.e., maximization of the response, minimization of the response, or response equal to the target value. In the present study, for all the responses, maximization of the response criteria is selected as a higher value of these responses represents better joint performance. The desirability of each response is calculated using the following equation 3.5 (Periyasamy et al. 2013).

$$di = \left(\frac{Yi-Li}{Hi-Li}\right)^{w} \qquad 3.5$$

Where Li<Yi<Hi

The nature of the desirability function for each objective can be altered using weights. These weights help in emphasizing the lower or upper bounds or the target value. Weights can be varied between 0 and 1, and when weight is equal to 1, $d_i$ will vary from 0 to 1 in linear mode. In the desirability function, an importance r can be assigned to each response with other responses and it can vary from 1 to 5 where value 5 is the

most important value represented as (+++++) and 1 represents the least important value and shown as (+).

When the various levels of significance were assigned to various responses, then the overall objective function is given by (Periyasamy et al. 2013).

$$D = \left(\prod_{i=1}^{n} d_i^{r_i}\right)^{1/\sum r_i} \qquad 3.6$$

### 3.9 TLBO ALGORITHM

Inspired by the teaching and learning process, Rao et al. (2011) developed a TLBO algorithm for process optimization. TLBO follows the principle of "how the teacher influences and enhances the output of a learner in the class" [Rao et al. 2012]. The algorithm consists of two vital components namely Teacher and Learner. TLBO is based on two types of learning: one through the teacher, and the other through interaction among the learners, known as the teacher and learner phases. Being a population-based technique, a bunch of students (i.e., learners) is taken as the population in TLBO, and the subjects offered to the students are considered independent process parameters of the optimization problem. The results of the students are taken as the fitness value of the problem, which has to be optimized. Fig. 3.16 depicts the flowchart of the working of the TLBO algorithm.

*Level I - Teacher Level:*

At this level, the teacher tries to enhance the average results of the class in his subject. Assume there are 'n' learners and 'm' subjects. Let the learner be denoted by k, varying from 1 to n, and the subject is denoted by j, varying from 1 to m, and iteration be denoted by 'i'. At any iteration, the average result of the learner in a subject is represented by $M_{ji}$. By considering all the subjects from the total learner population, the best overall results (i.e., $A_{\text{total-kbest, i}}$) are taken as the output/result of the best learner, denoted by $k_{best.}$ The best learner is then renamed as a teacher in the algorithm, as a teacher is usually a better-learned person. The difference between the average result of a learner in each subject and the value corresponding to the best learner (i.e., teacher) is presented as (Rao et al. 2011),

$$Mean\ Diff_{j,k,i} = r_i(A_{j,kbest,i} - T_F M_{j,i}) \quad 3.7$$

where $A_{j,kbest,i}$ is the result of the best learner in the subject/variable 'j', $r_i$ represents random number within the interval of 0 and 1 and $T_F$ is the teaching factor and it takes values either 1 or 2. Value of the $T_F$ is calculated by (Rao et al. 2011)

$$T_F = round[1 + rand(0,1)\{2 - 1\}] \quad 3.8$$

The prevailing solution is revised based on the $Mean\ Diff_{j,k,i}$ in the teacher phase as per the below equation (Rao et al. 2011)

$$A'_{j,k,i} = A_{j,k,i} + Mean\ Diff_{j,k,i} \quad 3.9$$

Here $A'_{j,k,i}$ is the revised value of $A_{j,k,i}$. Finally, accept $A'_{j,k,i}$ if it provides a higher function value. All these values are maintained and transferred to the learner level as input values at the end of the teacher level.

*Learner level:*

Usually, by interacting among themselves, learners enhance their knowledge. For the given size of population 'n', the learning process at this level is formulated as follows:

Choose any two learners F and G randomly, such that $A'_{total-F,i} \neq A'_{total-G,i}$ (Where $A'_{total-F,i}$ and $A'_{total-G,i}$ are the revised values of $A_{total-G,i}$ and $A_{total-G,i}$ respectively at the end of the previous level) (Rao et al. 2011)

$$A''_{j,F,i} = A'_{j,F,i} + r_i(A'_{j,F,i} - A'_{j,G,i}), \quad \text{if } A'_{total-F,i} < A'_{total-G,i} \quad 3.10$$

$$A''_{j,F,i} = A'_{j,F,i} + r_i(A'_{j,G,i} - A'_{j,F,i}), \quad \text{if } A'_{total-F,i} > A'_{total-G,i} \quad 3.11$$

Accept $A''_{j,F,i}$ if the function value provided by this is better than the previous condition.

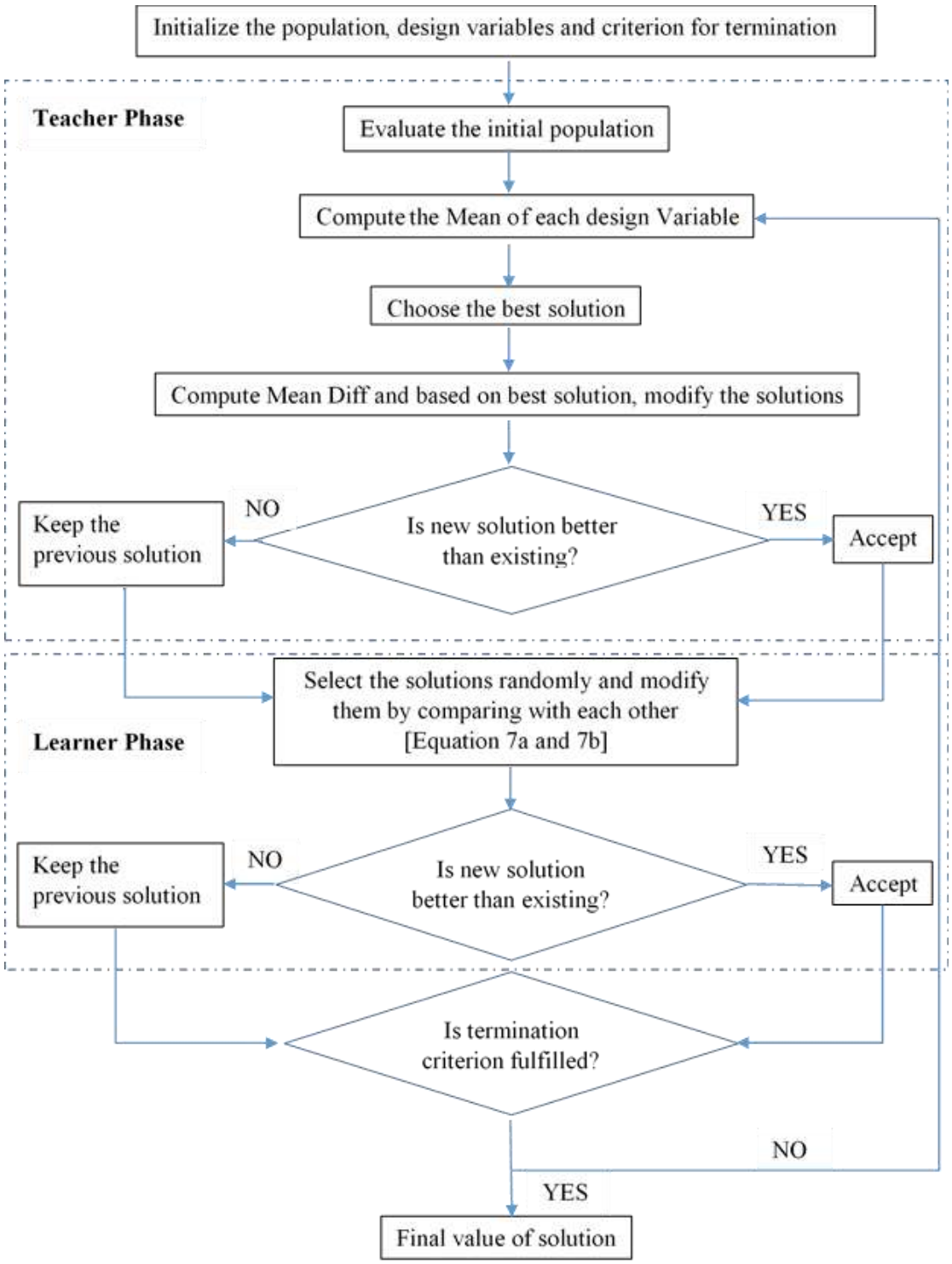


**Figure 3.16** Flow chart of TLBO algorithm (Rao et al. 2011)

## 3.10 GENETIC ALGORITHM - MULTILAYER PERCEPTION NEURAL NETWORK (GA- MLPNN)

### 3.10.1 The architecture of Multilayer Perception Neural Network (MLPNN):

MLPNN is an enhanced version of a feed-forward neural network employing a back propagation algorithm. It consists of three layers – input, hidden and output layer. The schematic arrangement of MLPNN is shown in Figure 3.17.

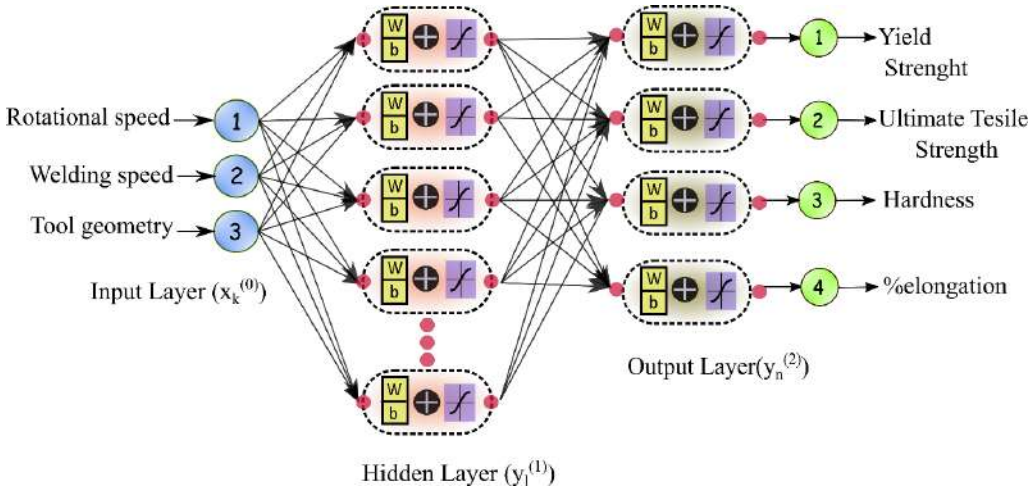


**Figure 3.17** Schematic Diagram of MLPNN

#### 3.10.1.1 Input layer:

The input layer is the first layer which receives the data that must be processed further to the next hidden layer. The input layer consists of a set of signals $x_k^{(0)}$ that is $x_1^{(0)} \ldots\ldots, x_k^{(0)}$ are called artificial neurons. The output of these neurons is sent to hidden layers for further processing.

The equation of the output can be written as (Jin et al. 2022):

$$y_l^{(1)} = f\left(x_l^{(1)}\right), \qquad 3.12$$

$x_l^{(1)}$ is the weighted or the total sum of the input signals,

$$x_l^{(1)} = \sum_{k=0}^{k} w_{kl}^{(1)}\, x_k^{(0)} \qquad 3.13$$

$f\left(x_l^{(1)}\right)$, is a nonlinear function. $w_{kl}^{(1)}$ are the weights that act as the coefficients in the nodal summation of neural networks.

Summation of each neuron also includes a dc bias term. The dc bias term adjusts the operating point during the calculations. For example, in equation 3.13 if we set $x_0^{(0)} = 1$, $w_{0l}^{(0)}$ would be the biased term for this neuron.

### 3.10.1.2 Hidden layer:

The hidden layer consists of an activation function that helps in the smooth adaptation of the network's weights and biases. Hidden layers can have many numbers of layers like the first hidden layer, second hidden layer, etc., and for each hidden layer the number of neurons can be specified. The nonlinear function generally used in neural networks from the signal processing application is the sigmoid or tanh function, as shown in Figure 3.20, equation 3.14 (Jin et al. 2022)

$$y = f(x) = \tanh(x) = \frac{e^{x} - e^{-x}}{e^{x} + e^{-x}} \qquad 3.14$$

The output of the hidden layer passes the neurons to the output layer which is given by equations 3.15 and 3.16 (Anarghya et al. 2018)

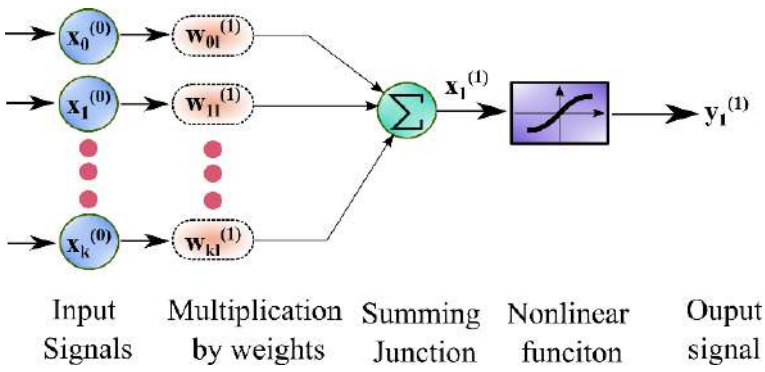


**Figure 3.18** Representation of individual neurons with sigmoid nonlinearity**.**

$$y_n^{(2)} = f\left(x_n^{(2)}\right), \qquad 3.15$$

$$x_n^{(2)} = \sum_{m=0}^{m} w_{nm}^{(2)}\, x_m^{(1)} \qquad 3.16$$

### 3.10.1.3 Output layer

The output layer consists of linear summation to ease the calculation of high-density nonlinear data/neurons from the hidden layer.

### 3.10.2 Back propagation Algorithm

The back propagation algorithm is a supervised learning method used during the learning phase of neural networks to adapt coefficients smoothly. A known intended signal is compared to the network's output in this supervised learning technique to provide a gauge of the network's performance during the learning phase. Back propagation is a steepest-descent procedure in which the error signal first modifies the output layer weights, then travels on to the hidden layer weights, and finally returns to the input layer. The discrepancy between the neural network's current output signal and the desired output signal is known as the error signal. Feed-forward networks operate in such a way that the input signals are passed to the output signal but there is no error generation. The back propagation algorithm has error generation in the learning phase which is propagated from the output back to the input to adjust the weights as shown in Figure 3.19. Equation 3.17 gives the error between the desired signal and the output of this network (Anarghya et al. 2018)

$$e = d - y^{(2)} \qquad 3.17$$

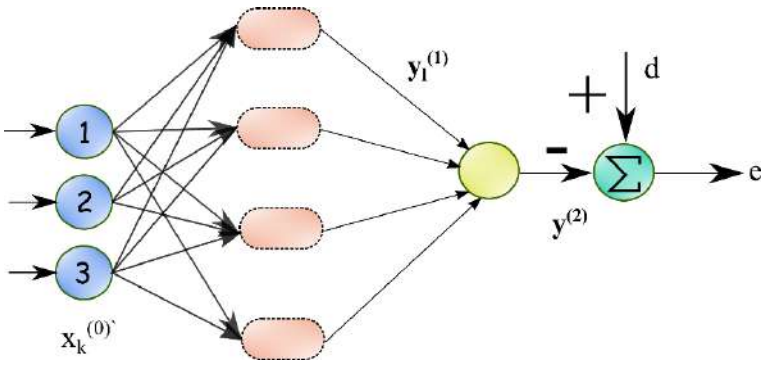


**Figure 3.19** Schematic diagram of the back propagation algorithm used to compare the output of a multiplayer perception with a desired signal for supervised learning.

The back propagation algorithm uses can use various adaptation functions to adjust the weights in neurons. Here the $ij - th$ weight in each neuron is adjusted in proportion to the gradient of the squared error to the weight of $h - th$ layer, (Madhiarasan 2022)

$$w_{ij}^{(h)}(new) = w_{ij}^{(h)}(old) - \mu \frac{\partial e^2}{\partial w_{ij}^{(h)}}(old) \quad 3.18$$

where $\mu$ is a convergence factor, and it might be different for each weight.

For the output layer with weights in Figure 3.19. $w_l^{(2)}$ , this gradient is (Madhiarasan 2022)

$$\frac{\partial e^2}{\partial w_l^{(2)}} = 2e \frac{\partial e^2}{\partial w_l^{(2)}} = -2e \frac{\partial y^2}{\partial w_l^{(2)}} \quad 3.19$$

### 3.10.3 MLPNN methodology

#### 3.10.3.1 Data normalization

The ability of a neural network to learn and generalize is enhanced by data variety, which can be achieved by reducing data similarity. As a result, both input and output data were normalized within the range of [0, 1] using equation 3.20 (Anarghya et al. 2018)

$$x_n = \frac{y_{max} - y_{min}}{x_{max} - x_{min}} (x - x_{min}) + y_{min} \quad 3.20$$

#### 3.10.3.2 MLPNN Procedure

In this experiment, rotational speed, welding speed, and tool geometry is chosen as the neurons for the input layer. The output layer consists of yield strength, ultimate tensile strength, hardness, and %elongation. The network type of the MLPNN is a backpropagation algorithm with a training function in the hidden layer as gradient descent with momentum and adaptive learning rate backpropagation (GDX). The intermediate transfer function or the processing function was chosen as the sigmoidal or tanh function. In GDX there are factors like learning rate and momentum rate that can be adjusted to control the pace of the learning algorithm. MLPNN also depends on the number of neurons in the hidden layer and the momentum rate. In this experiment neural network analysis was done using MATLAB.

### 3.10.4 Genetic Algorithm (GA)

Darwin's evolutionary theory served as an inspiration for GA, which tries to replicate the workings of genetics and natural selection. Each solution stands in for a chromosome, whereas each parameter represents a gene. GA evaluates each population member's fitness using an objective fitness function. To enhance unacceptable results, the best solutions are picked at random using a selection (for instance, roulette wheel) mechanism. Since GA tends to select subpar answers, locally imprisoned good solutions can be extracted using other solutions.

#### 3.10.4.1 Initial population:

The GA method begins with either produced population or a population chosen at random. The diversity of this population can be increased by using specific functions, such as the Gaussian random distribution. Each chromosome has a set of variables that correspond to the genes. To increase population variety and increase the likelihood of finding acceptable regions, the initialization process' main objective is to distribute the solutions as evenly as possible across the search area.

#### 3.10.4.2 Selection:

The primary source of inspiration for this element of the GA algorithm is natural selection. In the natural selection process, the strongest or the fittest individual has a better chance of survival. The same concept is applied here in GA fittest chromosome genes contribute more to the future generation of the same species. There are many methods for creating the next generation like a roulette wheel, Boltzmann selection, steady state selection, single point cross-over, double point cross-over, truncation selection, etc.

#### 3.10.4.3 Crossover:

After the fittest chromosomes are selected a new generation should be created. In nature, the chromosomes of male and female genes are merged to form a new chromosome. Here also in the genetic algorithm, two-parent chromosomes or solutions are merged by the operator to produce new chromosomes (children/solution). The various operators that perform this operation are single-point crossover, double-point

crossover, heuristic crossover, multi-point crossover, etc. Single- and double-point crossover is shown in Figure 3.20. (Sreenivasan et al. 2019)

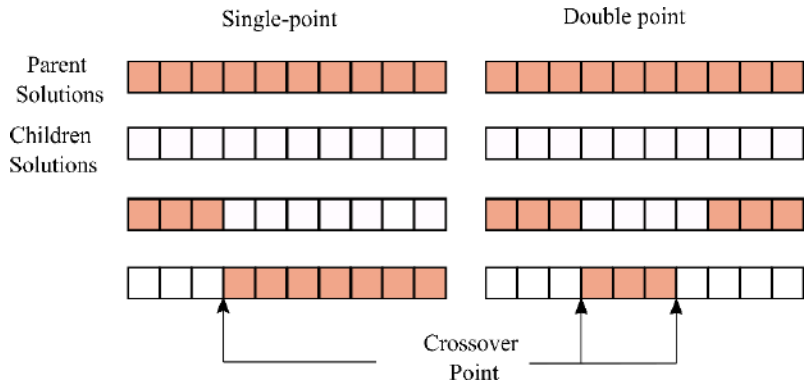


**Figure 3.20** Schematic diagram of single and double point cross-over.

### 3.10.4.4 Mutation:

The mutation is a process where the newly obtained genes from crossover are altered. This is shown in Figure 3.21. Because a large mutation rate would turn GA into a primitive random search, the mutation rate is always kept low in GA. The mutation operator maintains the population diversity by introducing an additional level of randomization. This operator increases the likelihood of avoiding local solutions while preventing solutions from becoming identical in the GA algorithm. Some of the mutation methods are Gaussian, Supervised mutation, Power mutation, etc. (Falco et al. 2002)

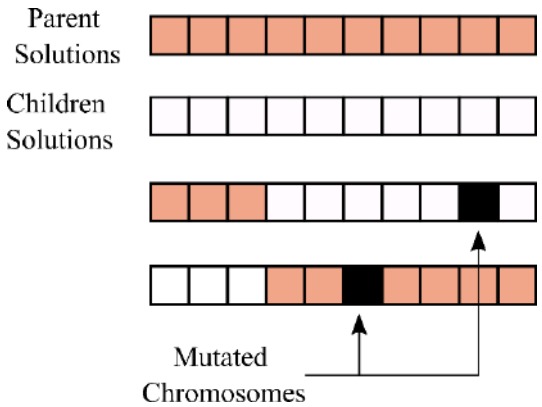


**Figure 3.21** Change in one or more genes in the children's solutions by mutation operator after the crossover phase

#### 3.10.4.5 Fitness Evaluation:

In this method altered genes are subject to fitness evaluation function like mean square error. A minimum threshold value is kept as a criterion for the evaluation of fitness depending on the experiment.

If the values of genes are within the threshold limit, they are accepted as new genes. If the values of genes are not within the threshold limit, then they are sent as the initial population. This evaluation is done to reduce the over-fit population.

### 3.10.5 GA-MLPNN

The neural network has various tools like high convergence rates, different learning rules, different training algorithms, alternate transfer functions, etc. to improve the results or to achieve some required properties of the trained networks. However, when it comes to model building, the neural network has issues with interpretability and complexity. Thus, as the network's training develops, several attempts have been made to keep the gradient descent algorithm from becoming stuck in local minima.

The genetic algorithm (GA) can scan multiple areas at once and has no restrictions on network topology (Katoch et al. 2021). GA also offers the ability to choose solutions and does not require a back propagation technique. Hence by combining these two GA and MLPNN, we can overcome the problem of MLPNN being stuck in local minima (Isaac et al. 2018). MLPNN is given the initial data and the initial weights and biases of the neural network are the required population for GA. After the initial population is given GA undergoes selection, crossover, mutation, and fitness evaluation. The fitness function here is a mean square error (MSE). Only if the MSE value is less than 0.005 then the population is considered as the fittest. This population is again sent to the neural network as updated weights and biases for further processing. The GA's altered initial weights and biases are being used to train a backpropagation algorithm as shown in Figure 3.22. This is how MLPNN's local search may be transformed into a global search. The GA population size value of 25, mutation rate value of 0.3, and crossover rate value of 0.6 were chosen for operating GA in this experiment.

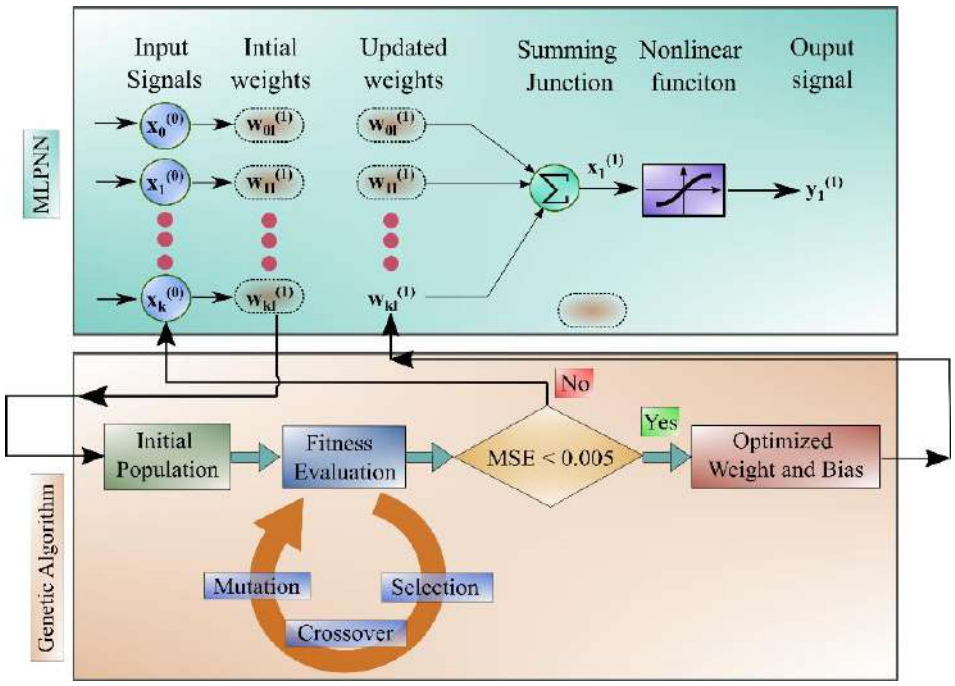


**Figure 3.22** Schematic Diagram of GA-MLPNN

# Chapter 4

# RESULTS AND DISCUSSION

The current chapter deals with the systematic characterization of the as-cast AA6061 matrix reinforced with 3(wt%) rutile particles using XRD, SEM/EDX microanalysis. The mechanical properties of the composites, such as hardness and tensile strength, are also evaluated. An orthogonal array has been utilized to investigate the relationship between the input process variables and the output responses of FSW. Multi-objective optimization of the FSW process is done using statistical methods and evolutionary algorithms. Based on input process data, GA-MLPNN models have bee`n constructed to forecast the hardness, yield strength, ultimate tensile strength, and % elongation of the welded composites. The findings of the study are presented and extensively discussed in the following parts:

## 4.1 AS-CAST AA6061-3(wt%) RUTILE COMPOSITES - MICROSTRUCTURAL AND MECHANICAL CHARACTERIZATION

The phases of the as-cast composite have been evaluated, and the grain structure has been examined. The results are presented in the following parts:

### 4.1.1 X-ray Diffraction Analysis

X-Ray diffraction (XRD) [Rigaku Miniflex 600 (5th gen), Make Rigaku] was used in the scanning range of $10° \leq 2\theta \leq 80°$ with an increment of $0.05°$ to determine the details about various elements present in the prepared composites (Mahto et al. 2019). XRD also provides information about the existence of any other phases in the cast composites. XRD images shown in Figure 4.1 indicate the existence of $TiO_2$ particulates within the matrix. XRD images indicate that Aluminium and $TiO_2$ are the primary constitutional phases existing in the prepared composite and also imply the absence of intermetallic phases and impurities in the composite.

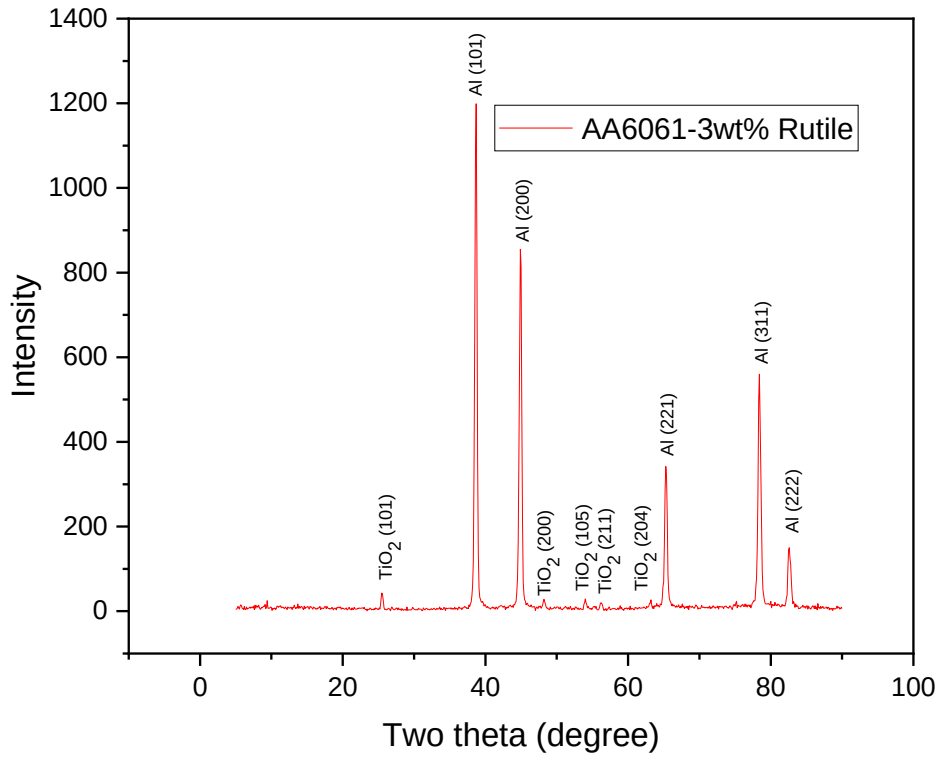


**Figure 4.1** X-Ray Diffraction form displaying s the peaks of Al, $TiO_2$ in as-cast AA6061-3 (wt%) rutile composite.

### 4.1.2 Scanning Electron Microscopic (SEM) Analysis

The SEM image of the as-cast AA6061-3(wt%) rutile composite is shown in Figure 4.2(a), displaying a typical dendritic structure (Arora et al. 2015). When the nucleation is poor and the liquid is not inoculated, it must be undercooled before the solid forms. A small solid protuberance called a dendrite that forms at the interface is encouraged to grow in these conditions due to the undercooling of the liquid before solidification. As the solid dendrite expands, the latent heat of fusion is transferred into the inadequately cooled liquid, pushing its temperature toward the freezing point. The duration and speed of stirring have an impact on grain size. Faster stirring and shorter processing times ought to produce smaller grains (Bhushan and Kumar 2011).

The typical grain size of the as-cast AA6061-3(wt%) rutile composite was found to be 78±4μm. It was found that the rutile particles were distributed rather uniformly throughout the matrix without clustering together. The addition of magnesium into the melt during the fabrication of the composite produces a transitory layer between the

matrix and the reinforcements which greatly enhances the wettability (Yigezu et al. 2013). The low wetting angle of the transitory layer reduces the surface tension of the liquid matrix resulting in the surrounding of particles with a similar structure of matrix alloy and the particles (Singh et al. 2017). The proper wetting of rutile particles results in uniform distribution of the particles.

The aggregation of hard reinforcing particles, which frequently reduces the composite's toughness, is the most important defect of AMCs that has been seen in the past. The stir-cast composite does not include this kind of defect. The reason for better dispersion of rutile particles in the matrix without agglomeration of particles could be due to the bi-stage addition of the particles into the melt. The improved bi-stage addition of particles into the melt probably controls the viscosity of the molten matrix. When preheated reinforced particles were added all at once to the molten alloy, the viscosity of the melt increased, which creates a problem in the proper stirring of the melt. Possibly bi-stage addition of particles eliminates the difficulty in stirring thereby avoiding agglomeration of particles (PRABHU et al. 2019). This results in a fairly uniform dispersion of reinforcing particles in the AA6061 matrix.

Spot EDX was done at the region of interest to find out the presence of elements and peaks of the elements present in that location are shown in Figure 4.2 (b). During the stir-casting process, the rutile particles are mixed within the solution and are trapped by converging dendrites in the intercellular regions. The rutile particles influence the recrystallization creating nucleation sites during solidification (Sajjadi et al. 2012) (Karbalaei Akbari et al. 2015).

**Related Article: PRABHU, S. R., SHETTIGAR, A. K., HERBERT, M. A., and RAO, S. S.** (2019). "Microstructure and mechanical properties of rutile-reinforced AA6061 matrix composites produced via stir casting process." *Trans. Nonferrous Met. Soc. China (English Ed.*, 29(11), 2229–2236.

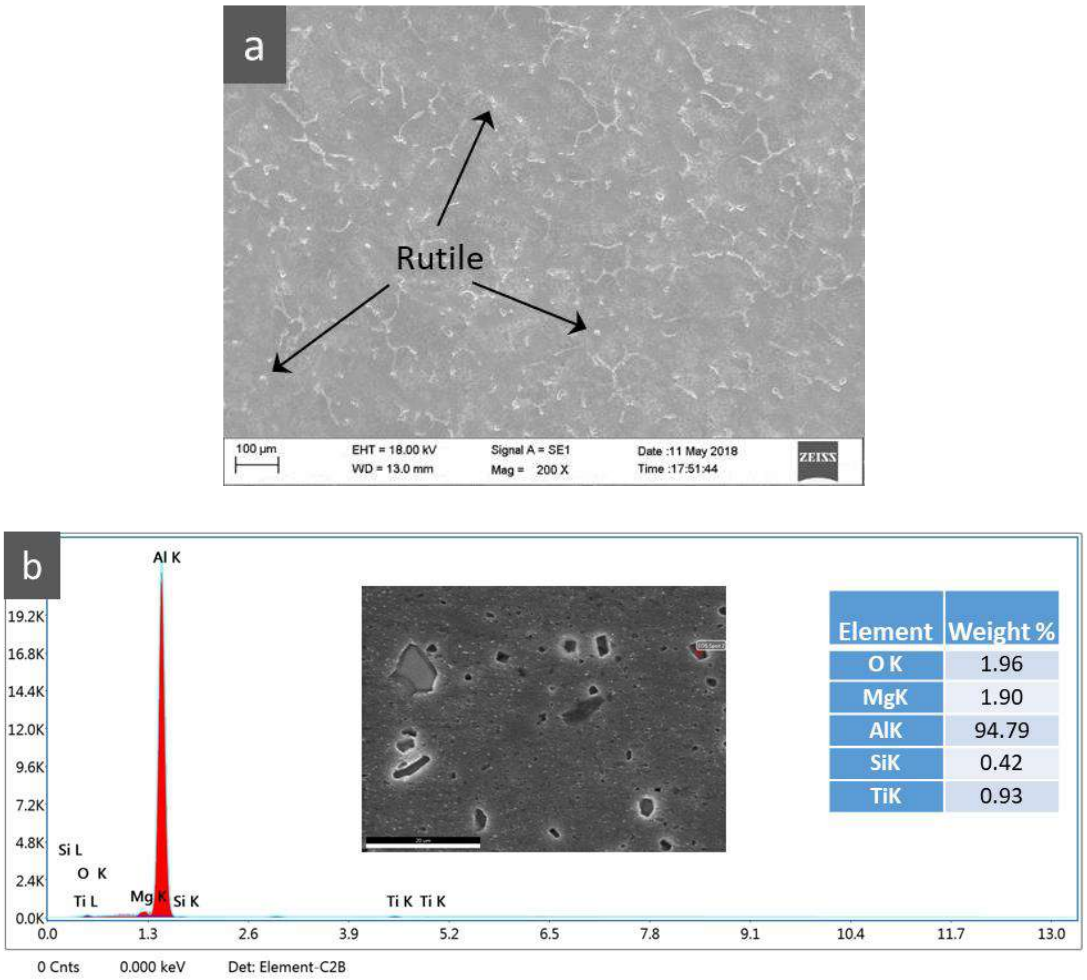


**Figure 4.2** (a) Microstructure of as-cast AA6061-3(wt%) rutile composite, (b) EDX spectrum of the region of interest showing peaks of Al, Ti, O2, Si, and Mg

Figures 4.3 (a to f) show the SEM/EDX mapping (area) of the prepared composite showing the elements Al, Ti, $O_2$, Mg, and Si, respectively. The EDX map of the Ti element in Figure 4.3 (c) and the appearance of the peak which belongs to the $TiO_2$ phase in the XRD pattern, confirm the presence of $TiO_2$ particles in the composites.

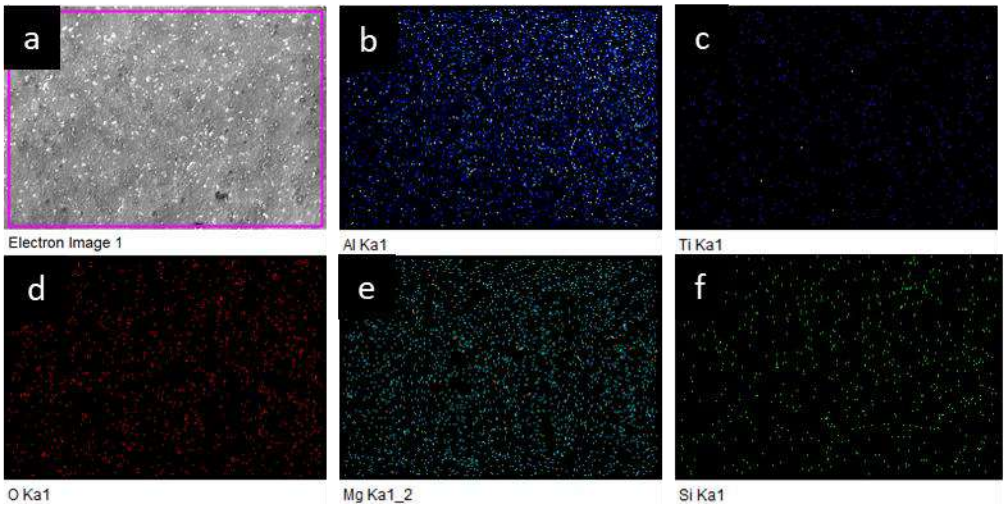


**Figure 4.3** (a) SEM image of base material - AA6061-3(wt%) rutile composite, EDX maps of (b) aluminium, (c) Titanium, (d) Oxygen, (e) Magnesium and (f) Silicon

### 4.1.3 Mechanical properties of AA6061-3(wt%) rutile composite

The degree to which a substance is resistant to plastic deformation brought on by indentation depends on its hardness. The Vickers hardness value of AA6061-3(wt%) Rutile composite was found to be 84±3 VHN. With the presence of rutile particles, the hardness of specimens increased up to 50% compared to that of the base matrix alloy. The inclusion of hard particles into the less hard ductile matrix enhances the hardness by various mechanisms (Pazhouhanfar and Eghbali 2018). Harder reinforced particles act as hurdles for the movement of dislocation. The presence of small individual hard reinforcements in the matrix can hamper the motion of dislocations, provided these reinforcements are stronger than the base material in which they are reinforced. Compared to the matrix, rutile particles have higher stiffness and hardness and enhance the matrix's resistance to plastic deformation. Hence, the hardness of the composites also increases. Also, the reinforced particles improve the hardness of the composites by reducing the grain size of the matrix material (Nwobi-okoye et al. 2019). In stir casting, hard particles are added to the molten matrix and these particles offer preferred heterogeneous nucleation sites for matrix grains. Matrix microstructure gets refined by the inclusion of rutile particles. This leads to an increase in the hardness of composites.

In general, tensile characteristics depend on microstructure, distribution of reinforcements, and precipitates. The Ultimate Tensile Strength (UTS), yield strength (YS), and percentage elongation (% El) are calculated based on load-displacement graphs generated from the tensile test. It was observed that the YS and UTS of the composite remarkably increased with the addition of rutile particles, at the expense of ductility. The addition of hard particles into the ductile matrix improves the load-bearing capacity and results in higher yield strength. Grain refinement due to the addition of rutile particles also contributes to the increase of yield strength (Sharma et al. 2015). Grain boundaries act as obstacles to the movement of dislocation, increasing yield stress. Also, as per the Orowan mechanism, uniformly dispersed, high-volume, finer and stable particles act as obstacles to the movement of dislocations (Shin et al. 2014). Hence the dislocation loops developed surrounding the particles increase the stress required for deformation resulting in higher strength. On the contrary, the brittle nature of rutile particles reduces the ductility of AMC. This could be due to the existence of Rutile which leads to strain hardening during deformation, thereby reducing its ductility (Rajesh et al. 2016).

To understand the mechanism of failure, the fracture surface produced from the tensile test is studied. The measured values of YS, UTS and % Elongation of AA6061-3(wt%) rutile composite are 130 ± 4 MPa, 190 ± 6 MPa and 9.5% ± 0.2, respectively. Particle-Matrix interfacial bonding strength plays a vital role in evaluating the fracture mode of the AMCs. During deformation, particle fracture will occur if the interfacial bonding strength is high. On the other hand, if the bonding strength is poor, decohesion between the rutile and the aluminium matrix will occur before the particle fracture (Ceschini et al. 2007a). Fig. 4.4 depicts the particle fracture mode for the AMCs having strong interfacial bonds. The presence of tear ridges and dimples on the fracture surface indicates a ductile fracture. The reinforcements (rutile particles) were visible at the bottom of the dimples. The voids begin at the matrix-particle interface because there are particles present inside the dimples. Another indication that the fracture spreads by inter-dendritic separation is the presence of dendritic nodules on the fracture surface.

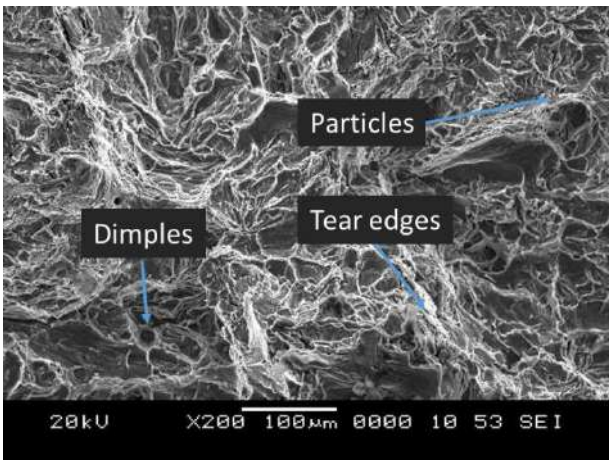


**Figure 4.4** The fracture surface of AA6061-3(wt%) Rutile composite

## 4.2 FRICTION STIR WELDING OF AA6061 -3(wt%) RUTILE COMPOSITES

The friction stir welding technique was successfully used to join the AA6061-3(wt%) rutile composite material under a variety of process parameters. Figure 4.5 displays the specimen after welding. The side of the half plate which faces the clockwise rotation of the tool along the welding direction is known as Advancing Side of the welded composite. The other side where the rotation of the tool and weld directions are opposite is the retreating side. Investigation and correlation with process parameters have been made about the structural characteristics and the hardness change at the weld zone of friction stir welded AA6061-3(wt%) rutile composite material. On the surface of the weld, a semicircular shape has been achieved that is identical to that created during the milling process (see Figure 4.5).

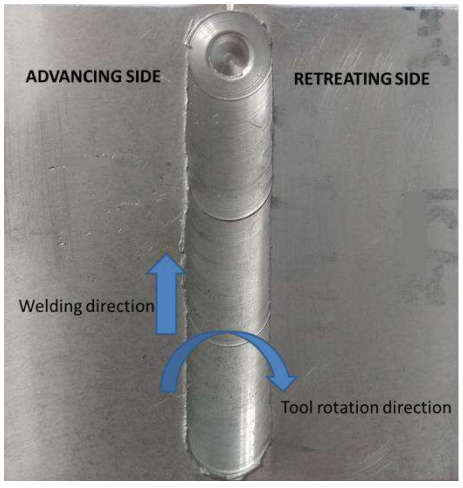


**Figure 4.5** Friction stir welded AA6061-3(wt%)rutile composite specimen

The wake effect during FSW was created by the friction between the tool shoulder and the horizontal movement on the surface of the plate (Ceschini t al. 2007a) (Salih et al. 2019). All joints provide the uniform appearance of semicircular geometry. On the surface of the weld, there weren't any noticeable voids or excessive flashes. The tool probe creates a keyhole at the end of the weld as a tool retracts from the weld.

### 4.2.1 Identifying the working range for various tool probe geometries

The initial phase of the work involved the identification of the range for process variables to obtain defectless weld using different tool probe geometries. Sound joints are obtained when the perfect combination of process variables is selected. It is crucial to establish and select the ideal welding parameters to achieve effective joint strength. The parameters considered in this work are the- rotation of the tool, speed of the welding and profiles of the pin. Table 4.1 tabulates the nature of the defect that occurred during the welding of composites. By carrying out FSW at a tool traverse speed of 100 mm/min and rotational speed of 500 rpm using a tool with Threaded Cylindrical (TC) pin, a less amount of heat is generated. At the same time, higher heat generation is observed at a tool traverse speed of 50 mm/min and rotational speed of 1500 rpm. Pinhole, wormhole, and tunnel defects have been observed in a few process parameter combinations as listed in Table 4.1. In the case of the tool with a Combined Square and Threaded Cylindrical (CSTC) pin, the lesser heat input was seen at a tool traverse speed of 100 mm/min and rotational speed of 750 rpm. And, higher heat input was seen at tool traverse speed of 50 mm/min and rotational speed of 1250 rpm. The Square (SQ) probe tool demonstrated a defect-less working range comparable to the CSTC tool. The amount of heat developed during welding is mainly dependent on rotational speed irrespective of tool traverse speed. The tool traverse speed determines only the quantity of heat supplied to the weld region (Salih et al. 2019). While the tool traverse speed controls the heat exposure period and subsequent cooling rate, the rotational speed has a greater impact on the generated peak temperature. Low tool rotational speed inhibits material temperature from rising sufficiently, preventing the deformed material from absorbing enough heat thereby increasing the resistance to material flow. Because the material cannot adequately undergo the hot forging process that the tool generates, some imperfections, such as pin holes and wormholes, persist in the weld region

(Rezaei et al. 2011). Increased frictional heat results in higher heat induced in the NZ at higher rotating speeds. This causes the components to be mixed and stirred more vigorously which causes turbulence in the material flow (Rajakumar et al. 2011). Tunnel defects arise from excessive turbulence in the material flow. It has been seen that the size of the tunnel hole likewise grows as the welding speed rises. (Tutunchilar 2012). Higher welding speed leads to a lower heat supply to the weld region, causing a lack of bonding and the formation of defects (Yang et al. 2019).

By examining the weld zone for micro and macro-level flaws like tunnel defects, wormholes, and pinholes, the viable working ranges for rotating speed, tool traverse/welding speed, and tool probe geometries were determined after completing numerous trial operations. Table 4.2 lists the quality of the weld obtained for different rotational speed and welding speed combinations. In Table 4.2 '×' mark indicates a joint with welding defects whereas '✓' indicates a defect-free welded joint. For various kinds of tools, there are different feasible working ranges. In comparison to SQ and CSTC tools, the TC tool's workable operating range is wider. The FSW tool's threads aid and direct the flow of material around the pin and from top to bottom, which reduces the formation of flaws. Due to their lower ductility, AMCs have smaller practical working ranges than aluminium alloys. (Pandiyarajan et al. 2019). The upper and lower limitations for each parameter level are listed in Chapter 3. Additional investigation was conducted for the parameters that lead to joints free of flaws for three different FSW tool probe geometries.

**Table 4.1** Macrographs of FS welded AA6061-3 (wt%)Rutile composite to find the working range of process variables for tools with TC, SQ, and CSTC probes.

| **Tool Probe Profile** | **Rotational speed (rpm)** | **Welding speed (mm/min)** | **Macro image** | **Type of Defect** | **Causes of Defect** |
|---|---|---|---|---|---|
| | 500 | 50 |  | Pin hole | Inadequate heat generation |

| | | | | | |
|---|---|---|---|---|---|
| Threaded Cylindrical (TC) | 500 | 100 |  | Worm hole | Insufficient heat generation and metal transportation |
| | 1500 | 50 |  | Worm hole | Excessive heat generation |
| | 1500 | 100 |  | Tunnel hole | Increase in the turbulence of the plasticized metal |
| Square (SQ) | 750 | 50 |  | Pin hole | Inadequate heat generation |
| | 750 | 100 |  | Worm hole | Insufficient heat generation and metal transportation |
| | 1250 | 50 |  | Tunnel hole | Excess heat input per unit length |
| | 1250 | 100 |  | Tunnel hole | Excess heat input per unit length |
| Combined square and threaded cylindrical (CSTC) | 500 | 50 |  | Pin hole | Inadequate heat generation |
| | 750 | 100 |  | Pin and worm hole | Insufficient heat generation and metal transportation |
| | 1500 | 50 |  | Pin hole & tunnel hole | Excess heat input per unit length and no vertical movement of the metal |
| | 1250 | 100 |  | Worm hole & tunnel hole | Excess heat input per unit length and no vertical movement of the metal |

**Table 4.2** Weld quality at different rotational and welding speed combinations for a) TC, b) SQ, and c) CSTC tool

| a) Threaded Cylindrical pin | | Rotational Speed(rpm) | | | | |
|---|---|---|---|---|---|---|
| | | 500 | 750 | 1000 | 1250 | 1500 |
| Welding Speed (mm/min) | 50 | × | ✓ | ✓ | ✓ | × |
| | 60 | ✓ | ✓ | ✓ | ✓ | ✓ |
| | 75 | ✓ | ✓ | ✓ | ✓ | ✓ |
| | 90 | × | ✓ | ✓ | ✓ | ✓ |
| | 100 | × | ✓ | ✓ | × | × |

| b) Square Pin | | Rotational Speed(rpm) | | | | |
|---|---|---|---|---|---|---|
| | | 500 | 750 | 1000 | 1250 | 1500 |
| Welding Speed (mm/min) | 50 | × | × | ✓ | × | × |
| | 60 | ✓ | ✓ | ✓ | ✓ | × |
| | 75 | ✓ | ✓ | ✓ | ✓ | ✓ |
| | 90 | × | ✓ | ✓ | ✓ | ✓ |
| | 100 | × | × | ✓ | × | × |

| c) Combined square and a threaded cylindrical pin | | Rotational Speed (rpm) | | | | |
|---|---|---|---|---|---|---|
| | | 500 | 750 | 1000 | 1250 | 1500 |
| Welding Speed (mm/min) | 50 | × | ✓ | ✓ | × | × |
| | 60 | ✓ | ✓ | ✓ | ✓ | ✓ |
| | 75 | ✓ | ✓ | ✓ | ✓ | ✓ |
| | 90 | × | ✓ | ✓ | ✓ | ✓ |
| | 100 | × | × | ✓ | × | × |

## 4.3 MACRO AND MICROSTRUCTURAL ANALYSIS OF AA6061-3(wt%) RUTILE COMPOSITE JOINTS FORMED USING TOOL WITH THREADED CYLINDRICAL (TC) PROBE

### 4.3.1 Macro Analysis of AA6061-3(wt%) rutile composites joints

The defect-free joint produced by a TC tool at various rotational speeds and tool traverse speeds is shown in Table 4.3. To achieve defect-free joints, it is important to generate enough heat and ensure adequate material flow through careful process parameter selection. Table 4.3 displays the defect-less joints that were seen in the weld area in addition to the cases described in Table 4.1. At lower rotational speeds, a basin-shaped nugget zone is seen; as the rotational speed increases, an elliptical-shaped nugget zone is seen (Mishra et al. 2005). The macro photographs in Table 4.3 support this observation.

**Table 4.3** Macro structural pictures of AA6061-3(wt%)Rutile composites FS welded using TC tool

| Expt. No | Rotational Speed (rpm) | Welding Speed (mm/min) | Macro image of FS welded composite |
|---|---|---|---|
| E1 | 750 | 60 |  |
| E2 | 750 | 75 |  |
| E3 | 750 | 90 |  |
| E4 | 1000 | 60 |  |
| E5 | 1000 | 75 |  |
| E6 | 1000 | 90 |  |
| E7 | 1250 | 60 |  |
| E8 | 1250 | 75 |  |
| E9 | 1250 | 90 |  |

### 4.3.2 Microstructural Analysis of AA6061-3(wt%) rutile composites.

Utilizing SEM, the microstructure of the friction stir-welded specimen was studied. The material is deformed plastically, and the grain is refined because of the tool's swirling action at the weld region. Compared to the base material, the microstructure of the weld zone showed a substantial alteration. Figure 4.6 displays the micro picture of one such sample. It demonstrates the steady transformation of the microstructure at the weld center from the initial coarse, undeformed base material grains to fine, equiaxed grains.

Based on the evolution of microstructure, (Threadgill 2007) has reported that the weld zone can be divided into four regions, which is confirmed in this work and Figure 4.6 shows these regions as follows.:

i) Nugget Zone (NZ) is the location where fine equiaxed grains were created, according to Fernández et al. (2017). Particles are rearranged from clustered and non-uniform dispersion in the parent material to uniform distribution in the weld NZ as a result of frictional heat caused by vigorous tool stirring in the workpiece (Mishra et al. 2003).

ii) Due to the vigorous swirling of the tool, the NZ is surrounded by grains that are severely distorted and elongated. (Meng et al. 2021). This region is referred to as the Thermo Mechanical Affected Zone (TMAZ). In contrast to the other zones, the TMAZ region's breadth is seen to be extremely small, which is consistent with research by (Dong et al. 2013). Incomplete recrystallization occurs in the TMAZ zone because there is less plastic deformation there than in the NZ region. TMAZ reveals that $TiO_2$ particles and grains are arranged at an angle. In the TMAZ an extended grain boundary with parallel band-like dispersion of particles is seen as a result of heat developed by friction and plastic deformation brought on by applied forces. (Kalaiselvan et al. 2014).

iii) Between TMAZ and parent material is a region known as the Heat Affected Zone (HAZ). At HAZ, the material is affected by the thermal cycle, but no plastic deformation was observed here. Due to this, the grains are bigger than the parent material at the HAZ. (Parikh et al. 2019).

iv) Parent Material (PM), whose microstructure and mechanical properties are unaltered during the FSW process (Mishra et al. 2003).

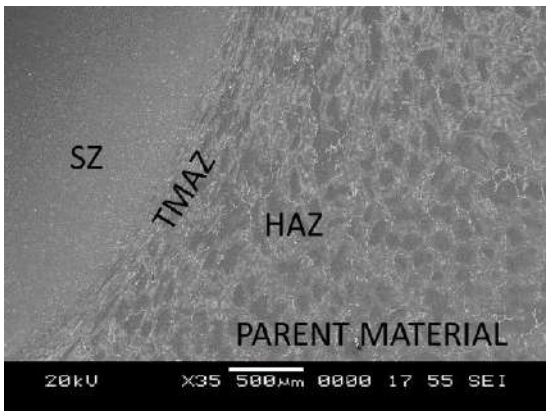


**Figure 4.6** SEM image displaying four distinct zones of FS welded AA6061-3(wt%) Rutile Composite.

#### 4.3.2.1 Microstructural analysis of Interfacial area of TMAZ and NZ

The SEM image of the interfacial area of TMAZ and NZ of FS welded composite is depicted in Figure 4.7 When compared to the TMAZ region, the NZ had a lot of tiny particles. This is because the abrasive action of the rotating tool along with the collision of hard reinforced particles creates a lot of tiny particles in NZ. The severe stirring of the tool uniformly disperses the tiny particles in the NZ. The uniformly distributed small particles lead to an increase in the load-bearing ability of the composite(Sharma et al. 2015).

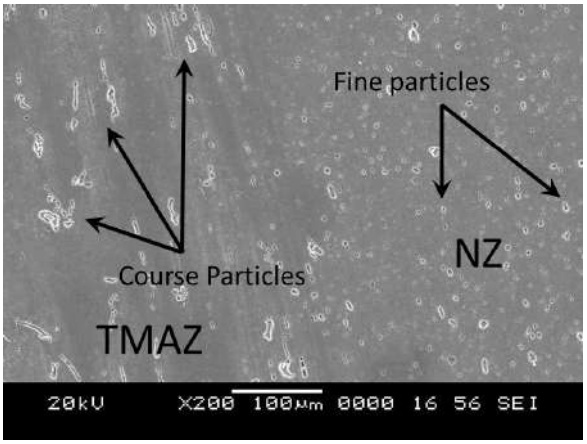


**Figure 4.7** SEM image of interfacial zone of TMAZ and NZ of FS welded composite

The dispersion of various elements in the NZ of FS welded composite is depicted in Figure 4.8 (a to f). In NZ, every element is equally distributed. Fine equiaxed grains are created by the vigorous swirling of the tool in NZ's center. When compared to other probes, the weld produced by the CSTC tool shows fine equiaxed grains. The

interaction of the tool with the workpiece develops frictional heat that plasticizes the material and the rotating tool pin facilitates severe stirring of the parent material resulting in dynamic recrystallization in the weld zone. (Jain et al. 2019). Through extreme plastic deformation, dynamic recrystallization (DRX) significantly accelerates grain refining. Hence fine grains and uniform distribution of particles were observed at NZ in comparison with the other zones.

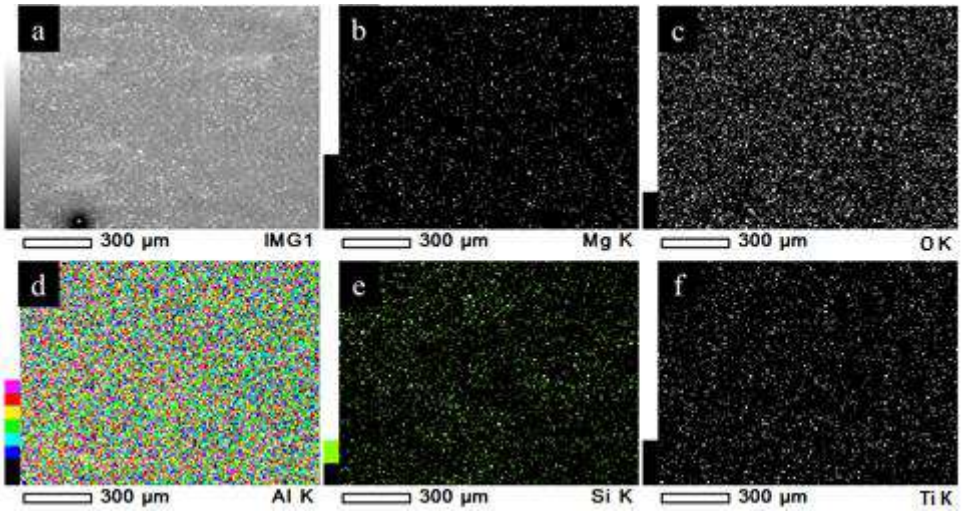


**Figure 4.8** FS Welded AA6061-3(wt%)rutile composite joint; (a) SEM image of NZ; and EDX map of b) Mg, c) $O_2$ d) Al, e) Si and f) Ti elements.

Figure 4.9 represents an SEM image of the region of interest at NZ, quantitative results and EDX spot analysis of FS welded AA6061-3(wt%) rutile composite joint. Area mapping of the nugget zone was done as shown in Figure 4.9 and is analyzed through EDX. As shown in Figure 4.9, peaks corresponding to Al, Si, Ti, Mg, and $O_2$ elements have been seen.

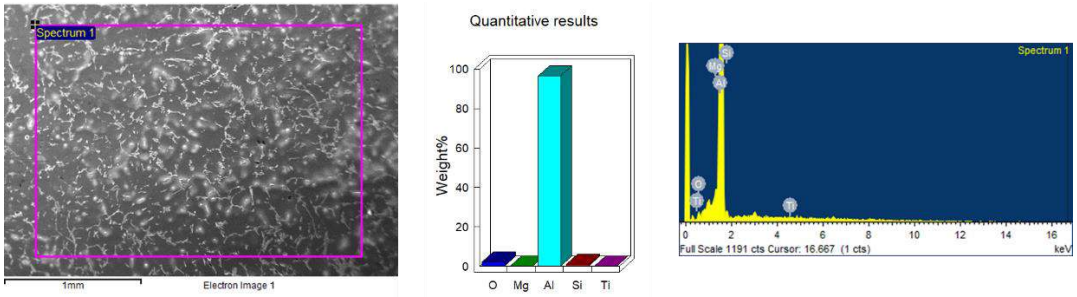


**Figure 4.9** Friction Stir Welded AA6061-3(wt%)rutile composite joint; Showing region of interest, quantitative results, and EDX spectrum showing the existence of Al-Mg-Ti-O-Si peaks.

SEM image of the NZ focusing on the quantitative analysis of the elements present and EDX spot analysis plots of FS welded AA6061-3(wt%)rutile composite joint is shown in figure 4.10. EDX confirmed that the circular-shaped objects in the SEM image are the rutile particle. EDX spot analysis revealed that the peaks corresponded to Ti and O. At the end of the rutile particles, tiny cracks have been seen, which served as proof that the rutile particles broke down in the NZ.

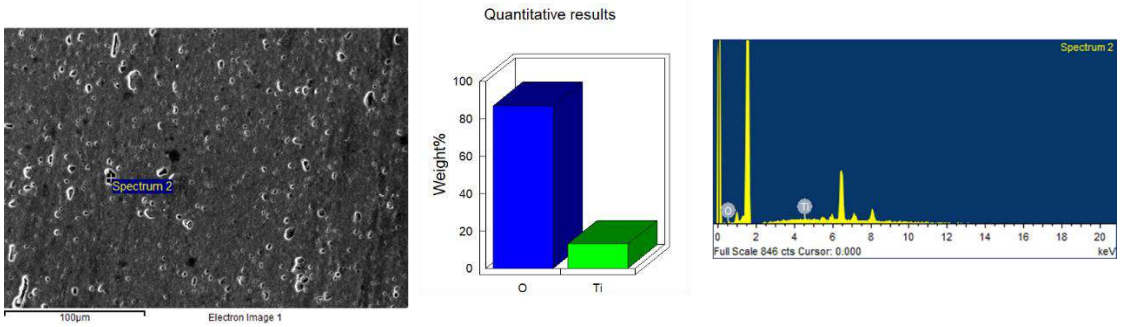


**Figure 4.10** FS Welded AA6061-3 (wt%) rutile composite joint showing SEM image of NZ, Quantitative analysis of the elements EDX spectrum with Ti and O peaks

SEM image of the NZ with particles, quantitative analysis of the elements, and EDX spot analysis plots of FS welded AA6061-3(wt%) rutile composite is shown in Figure 4.11. The bright spots present in the SEM image are Al elements surrounded by rutile particles, and the stir zone's EDX map confirms this with the associated peaks. The stirring movement of the FSW tool is responsible for the numerous tiny precipitates found in NZ. These precipitates, which were first found near the boundary of the grains in the parent material, are evenly dispersed throughout NZ.

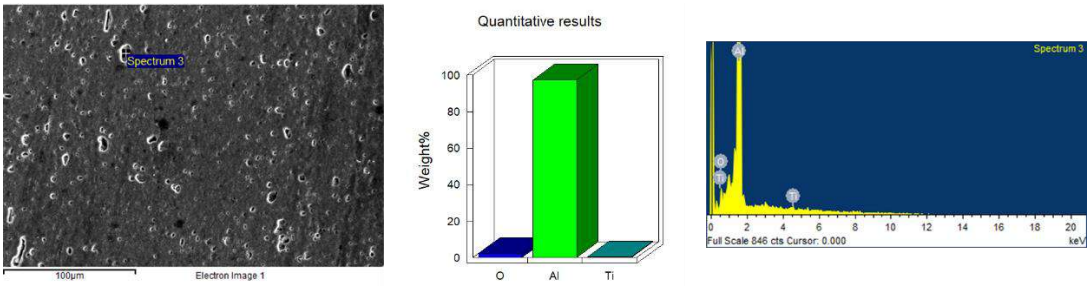


**Figure 4.11** FS Welded AA6061-3 (wt%) rutile composite joint showing SEM image of NZ, quantitative analysis of the particles, and EDX map displaying Al, Ti, and O peaks.

The SEM image shown in Figure 4.12 depicts the evidence for the breaking down of rutile particles. Due to the stirring effect of the FSW tool, the reinforcements with sharp edges strike one another and break into little particles. The breaking also happens as a result of the rotating tool's abrasive action. (Kumar and Murugan 2014).

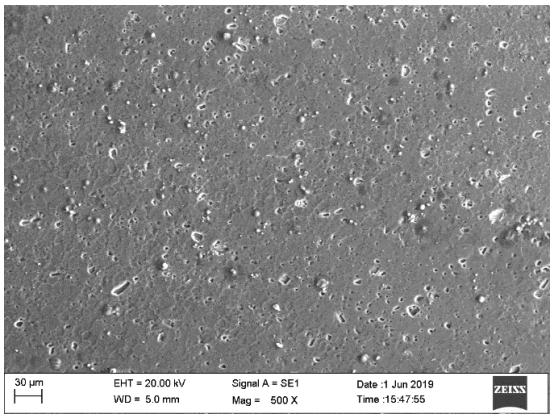


**Figure 4.12** SEM image of NZ displaying the breakage of Rutile particles

#### 4.3.2.2 Microstructure variation in the weld zone.

The SEM images of an FS welded AA6061-3(wt%) rutile composite that was joined using the TC tool at tool traverse speed and rotational speed of 75 mm/min 1000 rpm respectively are shown in Figure 4.13 (a to e). As shown in Figure 4.13(a-c), the average grain size at the top, middle, and bottom of the NZ is 4.8±0.13, 4.5±0.19, 3.9±0.11 µm, respectively. 4.13. Table 4.3 lists the measured grain size values at the NZ of the composite welded using different process parameter combinations. The grains are getting smaller from the top to the bottom surface of the weld zone (Mishra et al. 2005). The centrifugal force experienced by the top portion of the NZ is usually higher than the bottom region of NZ (Xu et al. 2009). The metal surface was subjected to a slight extrusion crushing force during recrystallization, which produced a larger crystal nucleus. The workpiece heats up in the meantime as a result of the shoulder rubbing motion. Higher temperatures and slower cooling rates at the shoulder-workpiece interface enable grain growth (Ahmed et al. 2021). The frictional heat generated at the tool pin-workpiece interface is lower because the tool pin's penetration depth is less than the thickness of the workpiece. As a result, there is insufficient plasticization and material flow in the bottom section of NZ. The back plate, on which the workpiece was kept, not only supports the workpiece against the axial force but also acts as a heat sink.

The heat generated at the weld region is transferred to the back plate by conduction thereby increasing the cooling rate. This suppresses grain growth, resulting in finer grains at the bottom of the NZ. This is in agreement with the conclusions reported by (Li and Liu 2013). Grain size variation has two main mechanisms affecting it: (1) Heat input results in annealing, which increases grain size; (2) Continuous dynamic recrystallization because of the tool pin's stirring action results in the formation of new nucleation sites, which results in a decrease in grain size. The fact that a fine structure is obtained in the stir zone of the specimens, as shown by these results, suggests that the second mechanism is prominent (Barmouz et al. 2011). The microstructure observed at the TMAZ (both sides of NZ) is depicted in Figure 4.13(d and e).

| | | |
|---|---|---|
| Rotational speed = 1000 rpm; Welding speed = 75 mm/min<br>(a) Top of NZ, grain size approx. = 4.8±0.13 μm | 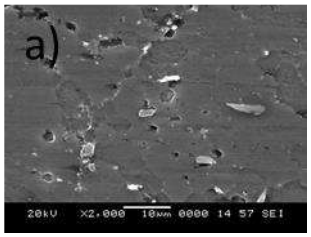 | (b) Middle of NZ, grain size approx. = 4.5±0.19 μm<br>(c) Bottom of NZ, grain size approx. = 3.9±0.11 μm |
| 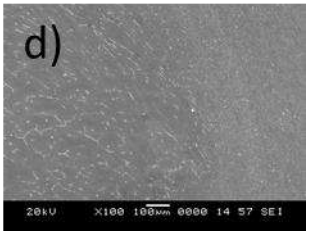 | 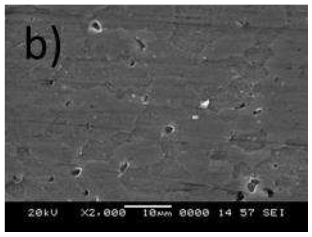 | 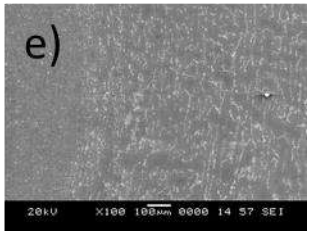 |
| (d) Advancing side of NZ and transition zone (TMAZ and HAZ) | 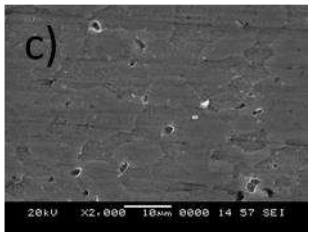 | (e) Retreating side of NZ and transition zone (TMAZ and HAZ) |

**Figure 4.13** Scanning Electron Micrograph of AA6061-3(wt%)rutile composite friction stir welded using TC tool with the rotational speed of 1000 rpm and welding speed 75 mm/min.

**Related Article: Prabhu, S. R. B., Shettigar, A. K., Herbert, M. A., and Rao, S. S.** (2019). "Microstructure evolution and mechanical properties of friction stir welded AA6061/rutile composite." *Mater. Res. Express*, 6(8).

At the TMAZ, non-homogeneous coarser grains that were severely distorted, elongated, and bent were seen. The weld generated at a lower rotational speed has slightly smaller grains than the weld produced at a greater rotational speed, as shown in Table 4.4. This phenomenon may be due to the specimen with the lower rotating speed producing slightly less heat than the specimen with the greater rotational speed, which inhibits the grains' ability to grow further. According to Table 4.4, the top of the NZ of the weld made at a tool traverse speed of 60 mm/min and rotational speed of 1250 rpm showed the largest average grain size of 6.5 microns. However, the sample welded at a traverse speed of 90 mm/min and a rotating speed of 1000 rpm has the smallest average grain size. It is obvious that higher rotational speed generates a large amount of heat and lower welding speed assists in transferring this heat to the material thereby decreasing the cooling rate. This phenomenon results in the grain growth and coarsening of grains. The quantity of heat produced is lesser at a low rotational speed. Also, the quicker tool traverse speed led to lesser heat transfer to the weld zone due to reduced frictional time. More strain was induced due to the prevailing low heat condition resulting in dynamic recrystallization. This phenomenon leads to the grain refinement and formation of finer grains. Additionally, the reinforced rutile particles at the grain borders inhibit grain growth due to a pinning effect, hence the size of the grains becomes smaller and finer (Abioye et al. 2019). Figure 4.14 depicts the microstructure of the weld region of the composite obtained through the FSW process using the TC tool.

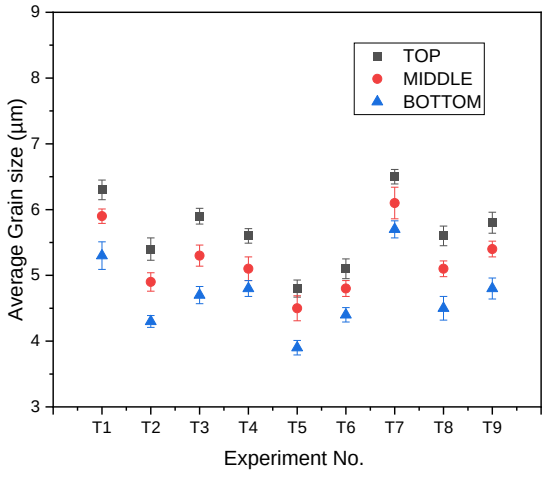


**Figure 4.14** Size of the grains at the NZ of FS welded AA6061-3(wt%)rutile composite using TC tool

**Table 4.4** Grain size at different locations of the NZ of FS welded AA6061-3(wt%) rutile composite joint obtained using TC tool

| Experiment No. | Rotational speed (rpm) | Welding speed (mm/min) | Average Grain size (µm) | | |
|---|---|---|---|---|---|
| | | | Top | Middle | Bottom |
| 1 | 750 | 60 | 6.3±0.15 | 5.9±0.11 | 5.3±0.21 |
| 2 | 750 | 75 | 5.4±0.17 | 4.9±0.14 | 4.3±0.09 |
| 3 | 750 | 90 | 5.9±0.12 | 5.3±0.16 | 4.7±0.13 |
| 4 | 1000 | 60 | 5.6±0.11 | 5.1±0.18 | 4.8±0.12 |
| 5 | 1000 | 75 | 4.8±0.13 | 4.5±0.19 | 3.9±0.11 |
| 6 | 1000 | 90 | 5.1±0.15 | 4.8±0.12 | 4.4±0.11 |
| 7 | 1250 | 60 | 6.5±0.11 | 6.1±0.24 | 5.7±0.13 |
| 8 | 1250 | 75 | 5.6±0.15 | 5.1±0.12 | 4.5±0.18 |
| 9 | 1250 | 90 | 5.8±0.16 | 5.4±0.12 | 4.8±0.16 |

## 4.4 MACRO AND MICROSTRUCTURAL ANALYSIS OF AA6061-3(wt%) RUTILE COMPOSITE JOINTS FORMED USING TOOL WITH SQUARE (SQ) PROFILE PROBE

### 4.4.1 Macro Analysis of AA6061-3(wt%) rutile composites joints

The macro images of the AA6061-3(wt%) Rutile composite FS welded with different combinations of welding speeds of 60, 75, and 90 mm/min and rotational speeds of 750, 1000, and 1250 rpm, using a tool with Square (SQ) probe is listed in table 4.5. For every instance of welding with an SQ tool, the NZ displayed a basin shape. The geometry of the tool is mostly responsible for the change in nugget shape. (Mishra et al. 2005) (Mohammadzadeh Jamalian et al. 2016). The softened material in the weld zone must be properly stirred and mixed for it to flow around the pin. The material that has been agitated is extruded from the front to the back of the pin by the tool as it moves forward. The material flow around the probe is dependent on its geometry. Tool probe geometries with flat faces are allied with eccentricity, which assists the incompressible material to move around the probe. The material is trapped in the flats and then released

behind the tool, promoting more effective mixing. The addition of the flats was also shown to increase the temperature and nugget area (Zhang et al. 2012). A flat surface on the tool probe changes the tool's dynamic to static volume ratio. For the SQ tool, this ratio is found to be 1.57. Compared to other tools studied in this work, the SQ tool sweeps more material. Additionally, the square tool's flat faces cause the flow of the plasticized material to agitate pulsatingly. For rotational speeds of 750, 1000, and 1250 rpm, respectively, the SQ tool generates 50, 66, and 83 pulses per second. When a weld junction is made with a TC tool, there is no pulsating effect.

**Table 4.5** Macrostructural images of AA6061-3(wt%) rutile composites FS welded at different process parameter combinations using SQ tool

| Experiment No | Rotational Speed (rpm) | Welding Speed (mm/min) | Macro image of composite with 3% Rutile |
|---|---|---|---|
| 1. | 750 | 60 |  |
| 2. | 750 | 75 |  |
| 3. | 750 | 90 |  |
| 4. | 1000 | 60 |  |
| 5. | 1000 | 75 |  |
| 6. | 1000 | 90 |  |
| 7. | 1250 | 60 |  |
| 8. | 1250 | 75 |  |
| 9. | 1250 | 90 |  |

### 4.4.2 Microstructure of AA6061-3(wt%) Rutile composite joint

The SEM images of AA6061-3(wt%) Rutile composite joint, FS welded using SQ tool, with tool traverse speed and rotational speed of 75 mm/min and 1000 rpm respectively, are shown in figure 4.15 (a - e). The distribution of grains at the different locations of the NZ is depicted in Figure 4.15 (a-c). Table 4.6 lists the measured average grain size

for different process parameter combinations. The average size of the grains is found to be 4±0.09 µm at the top, 3.3±0.15 µm at the middle, and 2.9±0.15 µm at the bottom of the NZ. Figure 4.15 (d) and (e) depicts the advancing and retreating side of the TMAZ where bent and elongated grains were observed.

Rotational speed = 1000 rpm: Welding speed = 90 mm/min

(a) Top weld NZ grain size approx. = 4±0.09 µm

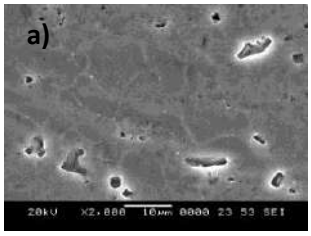


b) Middle weld NZ grain size approx. = 3.3±0.15µm

(c) Bottom weldNZ grain size approx. = 2.9±0.15µm

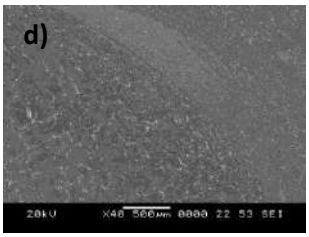


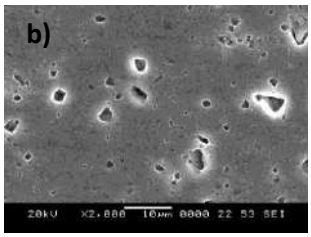


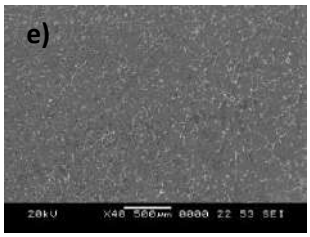


(d) Advancing side of NZ and transition region (TMAZ and HAZ)

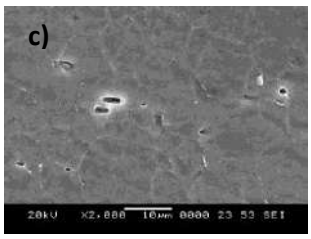


e) Retreating side of NZ and transition region (TMAZ and HAZ)

**Figure 4.15** Scanning Electron Micrograph of AA6061-3(wt%) Rutile composite joint friction stir welded using SQ tool with the rotational speed of 1000 rpm and welding speed of 75 mm/min.

The grain size at the nugget zone of the FS welded composite joined using the SQ tool is shown in Figure 4.16. It is obvious that for all joints, the grain size increases at the top of the nugget zone and decreases as one moves toward the nugget region's bottom. The joint fabricated at a rotational speed of 1250 rpm and welding speed of 60 mm/min exhibited a higher grain size of 5.9±0.12 microns. The weld zone's grains became coarser due to the higher heat conditions present at the lower welding speed (60 mm/min). On the other hand, the smaller average grain size of 4±0.09 microns is obtained in sample 5, which is FS welded with rotational speed and tool traverse speed of 1000 rpm and 75 mm/min respectively. The higher welding speed, which results in an optimal heat input due to a reduced friction period, is what causes the smaller average

grain size. The increased strain and strain rate brought on by the prevailing low heat situation is also responsible for the more dynamic re-crystallization. (Kumar et al. 2014) (Feng et al. 2008) which in turn contributes to grain refinement. Further, the pinning effect of rutile particles (Sivasankaran et al. 2011) which are mostly located at grain boundaries, inhibits the grain growth and resulting in smaller grains.

**Table 4.6** Size of the grains at different locations of the NZ of AA6061-3(wt%) Rutile composite joint fabricated using SQ tool

| Experiment No. | Tool Rotational speed (rpm) | Traverse speed (mm/min) | Average Grain size (µm) | | |
|---|---|---|---|---|---|
| | | | Top | Middle | Bottom |
| 1 | 750 | 60 | 5.7±0.13 | 4.8±0.15 | 4.3±0.1 |
| 2 | 750 | 75 | 4.7±0.12 | 4±0.21 | 3.2±0.08 |
| 3 | 750 | 90 | 5.4±0.09 | 4.7±0.13 | 4.1±0.14 |
| 4 | 1000 | 60 | 4.9±0.19 | 4±0.11 | 3.6±0.12 |
| 5 | 1000 | 75 | 4±0.09 | 3.3±0.15 | 2.9±0.15 |
| 6 | 1000 | 90 | 4.4±0.16 | 3.7±0.19 | 3.1±0.21 |
| 7 | 1250 | 60 | 5.9±0.12 | 5.3±0.21 | 4.6±0.21 |
| 8 | 1250 | 75 | 5.1±0.11 | 4.6±0.13 | 3.7±0.14 |
| 9 | 1250 | 90 | 5.5±0.19 | 4.8±0.18 | 4.3±0.22 |

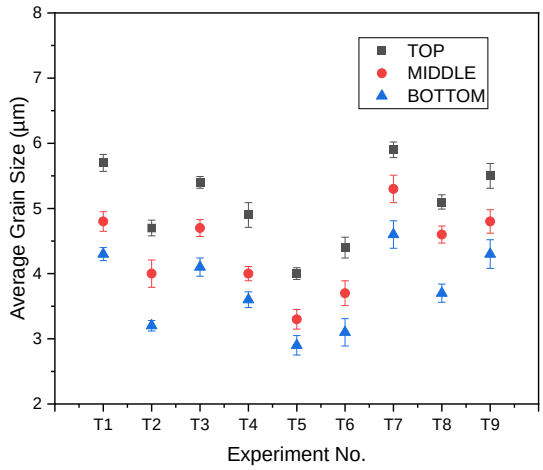


**Figure 4.16** Grain size at NZ of FS welded AA6061-3(wt%) Rutile joint produced using SQ tool

## 4.5 MACRO AND MICROSTRUCTURAL ANALYSIS OF AA6061-3(wt%) RUTILE COMPOSITE JOINTS FORMED USING TOOL WITH COMBINED SQUARE AND THREADED CYLINDRICAL (CSTC) PROFILE PROBE

### 4.5.1 Macro analysis of AA6061-3(wt%) Rutile composites joint

The macro images of the AA6061-3(wt%) Rutile composites FS welded, with different combinations of welding speeds of 60, 75, 90 mm/min and rotational speeds of 750, 1000, and 1250 rpm and by using CSTC tool, are shown in Table 4.7. In all instances where welding was done with the CSTC tool, the NZ displayed a mixed basin and elliptical shape. The geometry of the tool is mostly responsible for the change in the nugget's shape (Mishra et al. 2003). The relationship between dynamic and static volume determines how plasticized material flows from the front side of the rotating tool to back side. For the CSTC tool, this ratio is measured to be 1.28.

**Table 4.7** Macrostructural images of AA6061-3(wt%) Rutile composites FS welded at different process parameter combinations, using CSTC tool

| Experiment No | Rotational Speed (rpm) | Welding Speed (mm/min) | Macro image of composite with 3% Rutile |
|---|---|---|---|
| 1. | 750 | 60 |  |
| 2. | 750 | 75 |  |
| 3. | 750 | 90 |  |
| 4. | 1000 | 60 |  |
| 5. | 1000 | 75 |  |
| 6. | 1000 | 90 |  |
| 7. | 1250 | 60 |  |
| 8. | 1250 | 75 |  |
| 9. | 1250 | 90 |  |

### 4.5.2 Microstructure of AA6061-3(wt%) Rutile joint

Figure 4.17 (a - f) shows the SEM images of AA6061-3(wt%) Rutile composite FS welded using the CSTC tool with rotational speed and tool traverse speed of 1000 rpm and 75 mm/min respectively. Figure 4.17 (b-d) shows the measured size of the grains at four distinct locations of the NZ, i.e. near the top of the threaded cylindrical pin, just above and below the interfacial region of square and threaded probe, and near the bottom region of the square probe.

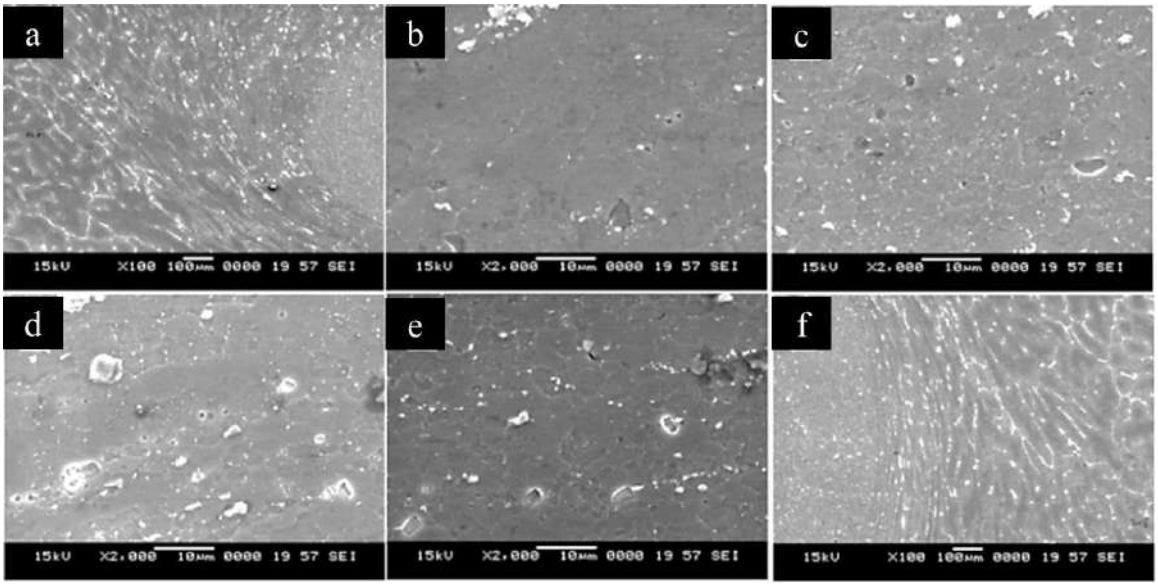


**Figure 4.17** Scanning Electron Micrograph of AA6061-3(wt%) Rutile composite joint friction stir welded using CTSP tool with the rotational speed of 750 rpm and welding speed of 60 mm/min, showing grain size distribution at (a) Retreating side TMAZ, (b) nugget top region, (c) nugget middle region of the specimen welded by threaded cylindrical tool, (d) nugget middle region of specimen welded by square tool (e) nugget bottom region and (f) Advancing side TMAZ

Table 4.8 lists the size of the grains measured at various regions of FS welded joints obtained using different process parameter combinations. The grain size measured near the top, just above the interfacial region, just below the interfacial region, and at the bottom region of the NZ are 3.4±0.12, 3.1±0.06, 3.1±0.22 and 2.8±0.11µm, respectively. The resultant grain size is significantly lower than the parent material. Additionally, for various combinations of process parameters, the grains in NZ for

samples welded by the CSTC tool are smaller than the TC tool samples. This is caused by the combined action of the tool pin's threaded section and flat, square faces, which affect the stirring effect and fragmentation of both grains and the reinforcing particles. The TMAZ's retreating and advancing sides are depicted in Figures 4.17(a) and (f), respectively. On both sides of the TMAZ, elongated and rotated grain formations have been seen.

**Table 4.8** Measured size of the grains at the top, middle, and bottom of the NZ of AA-6061-3(wt%) Rutile composite weld fabricated at various process parameter combinations using CSTC tool

| Expt No. | Rotational speed (rpm) | Welding speed (mm/min) | Average Grain size (µm) | | | |
|---|---|---|---|---|---|---|
| | | | Top | Above the interfacial region of TC and SQ | Below the interfacial region of TC and SQ | Bottom |
| 1 | 750 | 60 | 5.4±0.12 | 4.6±0.1 | 4.8±0.14 | 4.3±0.11 |
| 2 | 750 | 75 | 4.3±0.11 | 3.8±0.15 | 4±0.21 | 3.4±0.13 |
| 3 | 750 | 90 | 5±0.08 | 4.3±0.11 | 4.5±0.14 | 4.1±0.19 |
| 4 | 1000 | 60 | 4.5±0.17 | 3.8±0.09 | 4.1±0.18 | 3.5±0.21 |
| 5 | 1000 | 75 | 3.4±0.12 | 3.1±0.06 | 3.1±0.22 | 2.8±0.11 |
| 6 | 1000 | 90 | 4.1±0.09 | 3.5±0.07 | 3.7±0.17 | 3.4±0.19 |
| 7 | 1250 | 60 | 5.6±0.09 | 4.9±0.14 | 5.1±0.18 | 4.6±0.16 |
| 8 | 1250 | 75 | 4.9±0.13 | 4.3±0.11 | 4.5±0.19 | 3.9±0.11 |
| 9 | 1250 | 90 | 5.2±0.15 | 4.5±0.2 | 4.7±0.19 | 4.2±0.12 |

The plots for grain size distribution at the NZ of FS welded AA6061-3(wt%) Rutile composite using the CSTC tool are shown in Figure 4.18. It has been observed that the average grain size in the NZ of the joint fabricated using the CSTC tool is less than the samples obtained from the TC tool. FSW tool having square probe exhibits higher swept volume to static volume ratio. Therefore, it develops pulsating stirring action in the flowing material, resulting in greater amount of deformation, which through dynamic recrystallization leads to the formation of finer grains. On the other hand, the threaded pin

also ensures the enhanced mixing of the deformed material, assisted by the threads of the tool. The threaded pin also ensures that the plastically deformed workpiece material is transported from the top to the bottom of the pin (Fernandez and Murr 2004). The stirring effect and the material flow created by the tool pin profiles need to have both horizontal and vertical movement. The threads assist in the vertical flow of material whereas horizontal flow is driven by the 'flat' feature of the tool pin (Sued et al. 2014). As the CSTC tool has both features, it performs well and produces excellent quality welds. The primary barrier involved in restricting dislocation movement the grain boundaries, therefore materials with smaller grains were stronger because they would place greater limits on dislocation movement. (Chowdhury et al. 2010). Therefore, the strength of the joint fabricated by a combination of square and threaded tools is anticipated to be higher than the joint produced using a tool having a threaded probe.

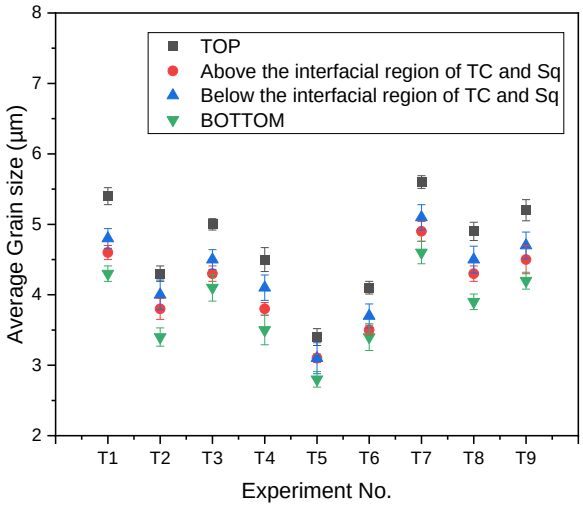


**Figure 4.18** Size of the grains at NZ of FS welded AA6061-3(wt%) rutile composite joint produced using CSTC tool

### 4.6 FS welded AA6061-3(wt%) rutile composite joint – Mechanical properties

The composition, weight proportion of hard reinforcements in the matrix, distribution of reinforcements in the matrix, and processing techniques all affect the mechanical properties of metal matrix composites. (Haghshenas 2016) (Moona et al. 2018). The tensile strength of the AA6061-3(wt%) Rutile composite joint is affected by various factors such as rutile particle and precipitate distributions at the weld zone, the morphology of the grains, processing temperature, and intermetallic phase formation

(Ramesh et al. 2005). Rutile particles are usually used in metal matrix composite preparation to enhance their mechanical and wear properties. Increased brittleness at the price of matrix ductility caused by a higher weight percentage of rutile particles in the matrix causes a decrease in strength. (Maity et al. 1995). To assess the joint's performance and broaden the potential applications of FSW for joining composites, mechanical tests have been carried out.

### 4.6.1 Measurement of Hardness at weld zone

#### 4.6.1.1 Distribution of hardness at weld zone, FS welded using TC tool

One of the key process parameters in the FSW process is the tool rotational speed. By creating frictional heat between the FSW tool's contact surfaces (Shoulder and probe) and the workpiece material, it transforms the material into a plastic state. The plasticized material surrounding the pin is mixed and stirred by it. (Kalaiselvan and Murugan 2013) The inclusion of reinforcement particles increases the nucleation sites, which causes the matrix's grain size to shrink. (Ceschini et al. 2007b). Plots are shown in Figure 4.19 for the FSW joints of the AA6061-3(wt%)rutile composite that was made using a TC tool at different speeds of rotation of 750, 1000, and 1250 rpm, respectively, while the speed of welding (transverse speed) was maintained at 60 mm/min. On both sides of the weld line, the hardness is determined. Finer grain size and work hardening due to higher dislocation density as a result of severe plastic deformation during the FSW process contributed to increase in hardness in the NZ than the base material (Ravindiran et al. 2016). A high plastic strain developed due to the severe stirring of the tool which results in the rearrangement of reinforcements from the clustered and non-uniform dispersion in the parent material to a uniform dispersion in the weld NZ (Prasad et al. 2021). This was evident in every sample that was welded using different process parameter combinations. On both sides of NZ, a decline in hardness was seen as the distance from the center increased. At a zone between the NZ and parent material, commonly referred to as the Heat Affected Zone (HAZ), a decreased hardness value has been seen. This is mainly due to the softening of grains brought on by the thermal cycle caused by the motion of the rotating tool in the workpiece material. When compared to the advancing side, a higher hardness value was noticed on the retreating side. This difference in hardness distribution results from an uneven field of plasticized

material flow on both sides of the welded joint, in which the retreating side faces less plastic strain than the advancing side. More deformation heat is produced as a result, raising the temperature on the advancing side close to the weld centre. According to Aval et al. (2011) higher peak temperatures on the advancing side result in greater grain coarsening and strengthening precipitate dissolution, because of which the advancing side is less hard than the receding side. NZ is more homogeneous at low welding speeds compared to high welding speeds because a higher heat input per unit weld produces a more uniform distribution of the temperature. The hardness value was found to decrease as the rotational speed rose from 1000 rpm to 1250 rpm at a constant tool traverse speed of 60 mm/min. This is mostly caused by an increase in heat intake. The weld material experiences higher temperature and strain rate as a result of the increased heat input (Murugan and Ashok Kumar 2013). If enough heat is produced during the FSW process, the work material plasticizes and is moved to the retreating side from the advancing side. The transferred material cools down and consolidates at the rear side of the tool by the forging process. (Bodaghi and Dehghani 2017). Refinement of the grains and strain hardening by deformation affect the hardness of the FSW joint. The joint manufactured at rotational speed and tool traverse speed of 1000 rpm and 60 mm/min, respectively, exhibits the highest hardness value of 106 VHN. The joint that was created at a rotational speed of 1250 rpm and a tool traversal speed of 60 mm/min had the lowest hardness value, which is 89 VHN.

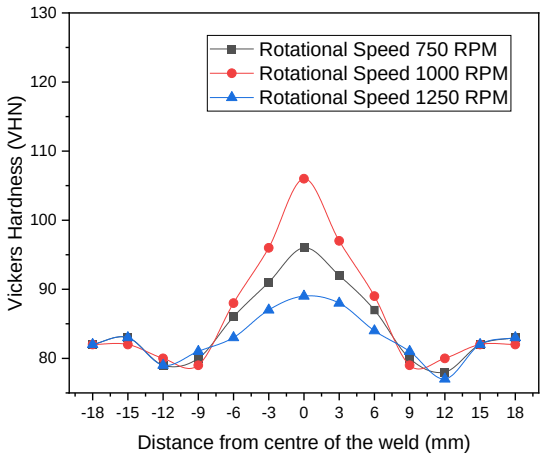


**Figure 4.19** Distribution of hardness at NZ of AA6061-3 (wt%) Rutile composite FS welded using a TC tool at rotational speeds of 750, 1000, and 1250 rpm, maintaining tool traverse speed constant at 60 mm/min.

Plots of the hardness variation across the FS welded joint of the AA6061-3(wt%) rutile composite, manufactured using a TC tool at varied rotating speeds of 750, 1000, and 1250 rpm, respectively, and constant tool traverse speed of 75 mm/min, are shown in figure 4.20. The stirred, plasticized material flows to the rear of the tool probe from the front side due to the rotation of the revolving tool. The heat transfer rate, which in turn impacts the time of exposure to frictional heat is determined by the welding speed. (Malopheyev et al. 2016). As a result, during FSW, the welding speed has a significant impact on the rate of heating and cooling in a thermal cycle. The heat per unit length reduces when the welding speed rises from 60 mm/min to 75 mm/min, increasing the hardness value. The hardness significantly decreased when the rotational speed was raised from 1000 to 1250 rpm while the welding speed was maintained at 75 mm/min. Large-sized grains occur as a result of the improved heat supply and slower cooling rate caused by the faster tool rotation.(Hassan et al. 2012). The joint that was constructed at a rotational speed of 1000 rpm and a welding speed of 75 mm/min exhibits the maximum hardness value of 118 VHN. The lowest hardness (100 VHN) is observed in a joint manufactured with a rotating speed of 1250 rpm and a tool traverse speed of 75 mm/min.

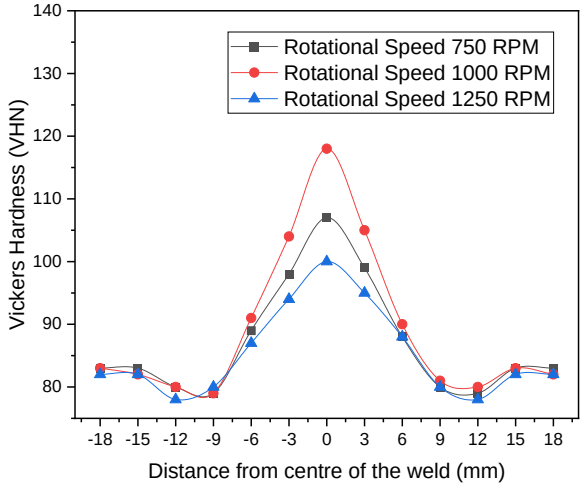


**Figure 4.20** Distribution of hardness at NZ of AA6061-3 (wt%) Rutile composite FS welded using a TC tool at rotational speeds of 750, 1000, and 1250 rpm, maintaining tool traverse speed constant at 75 mm/min.

The Distribution of hardness at NZ of AA6061-3(wt%) Rutile composite FS welded at rotational speeds of 750, 1000, and 1250 rpm and constant welding speed of 90mm/min

using the TC tool is shown in figure 4.21. Maximum hardness (110 VHN) is observed for a rotational speed and tool traverse speed of 1000 rpm and 90 mm/min, respectively. A lower hardness value of 96 VHN was achieved with a rotational speed of 1250 rpm and a welding speed of 90 mm/min. Similar to this, 750 rpm rotation and 90 mm/min welding yielded 99VHN hardness. However, when the rotational speed and welding speed increase, the stirring action of the FSW tool becomes noticeably weaker. As a result, at these speeds, the weld defects can be seen. The hardness value decreases with increased welding speed. High rotational speed and rapid welding speed have caused rutile particles to agglomerate and collect, which lowers the hardness of the material. Lower hardness readings are caused by the heterogeneous distribution of rutile particles in the region of measurement at higher rotating speeds (1250 rpm) and faster welding speeds (90 mm/min).

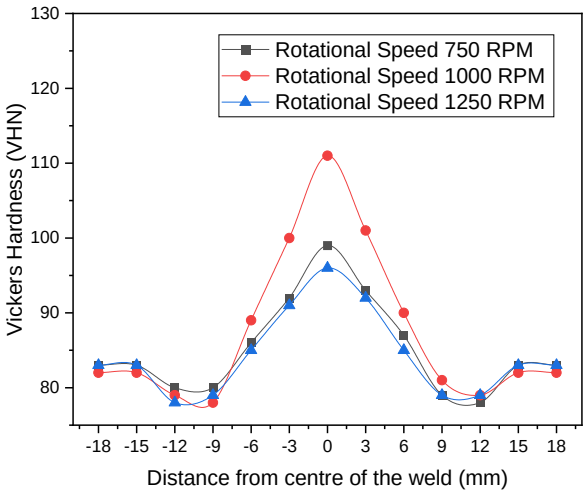


**Figure 4.21** Distribution of hardness at NZ of AA6061-3 (wt%) Rutile composite FS welded using a TC tool at rotational speeds of 750, 1000, and 1250 rpm, maintaining tool traverse speed constant at 90 mm/min.

### 4.6.1.2 Variation in the distribution of hardness across AA6061-3(wt%) Rutile composite joint FS welded using Combined of Square and Threaded Cylindrical (CSTC) probe tool.

The variation of the hardness across the FS welded AA6061-3(wt%) Rutile composite joint fabricated using a CSTC tool at different rotational speeds of 750, 1000, and 1250rpm with a constant tool traverse speed of 60 mm/min is depicted in Figure 4.22. It was found that regardless of the tool's rotational speed, the nugget zone's hardness is

significantly higher than that of the parent material. There are two main reasons for the higher hardness of the NZ:

(i) In comparison with the base material, the grains are smaller and finer in the nugget zone, and refinement of grains plays a major role in material strengthening. The Hall-Petch equation states that as the size of the grain decreases, the hardness increases.
(ii) The small particles of intermetallic compounds are also beneficial to hardness improvement, according to the Orowan hardening mechanism.

The swirling effect of the FSW tool results in significant plastic strain in the weld zone. Redistribution of the reinforcement from non-uniform and agglomerated conditions in the parent material to uniform dispersion in the NZ is responsible for the difference in hardness between the HAZ and NZ. The primary causes of property improvement in NZ are also due to the homogenous distribution of rutile particles and their dispersion throughout the matrix. There is a very apparent separation between the TMAZ and the NZ. The alignment of rutile grains and particles in the inclined direction is seen in TMAZ. Due to heat produced by friction and plastic deformation brought on by applied stresses in TMAZ, an extended grain boundary with the parallel band-like distribution of particles was observed (Figures 4.6 and 4.7) (Abraham et al. 2019). The lowest hardness was recorded in the HAZ for all the joints fabricated. The retreating side exhibits higher hardness than the advancing side. This variation in the hardness is brought on by the uneven plastic flow on two sides of the weld NZ. In comparison to the retreating side, the advancing side encounters larger plastic strains, which in turn causes more deformation heat. As a result, the temperature on the advancing side is higher than the temperature on the retreating side near the weld center. More coarsening and disintegration of stronger precipitates occur on the advancing side as a result of higher peak temperatures. As a result, the advancing side has lesser hardness than the retreating side. (Aval et al. 2011). It was discovered that the nugget region's hardness decreases when the rotational speed increased from 1000 to1250 rpm due to an increase in heat generation. The joint that was constructed with rotational speed and tool traverse speed of 1000 rpm and 60 mm/min, respectively, had the greatest hardness of 115 VHN. In contrast, the joint that was constructed at a rotating speed of 1250 rpm and a welding speed of 60mm/min had the lowest hardness measured at 97 VHN.

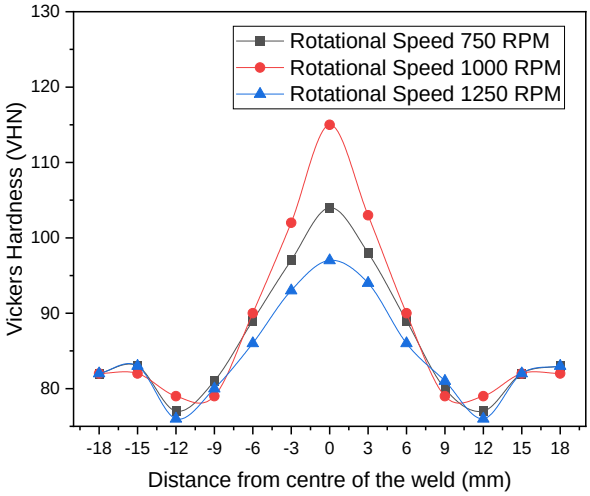


**Figure 4.22** Distribution of hardness at NZ of AA6061-3 (wt%) Rutile composite FS welded using a CSTC tool at rotational speeds of 750, 1000, and 1250 rpm, maintaining the tool traverse speed constant at 60 mm/min.

The distribution of hardness at NZ of AA6061-3(wt%) Rutile composite FS welded at rotational speeds of 750, 1000, and 1250 rpm maintaining tool traverse speed at 75 mm/min using the CSTC tool is depicted in figure 4.23. The joint specimen with the maximum hardness of 128 VHN was made using a tool traverse speed of 75 mm/min and a rotating speed of 1000 rpm. On the other hand, the joint that was created at a welding speed of 75mm/min and a rotating speed of 1250 rpm had the lowest hardness measured at 109 VHN. The lowest hardness is observed in the region represented as HAZ, where softening of grains may have occurred. The highest hardness was observed in the nugget zone. Hardness was improved as the tool traverse speed was raised from 60 to 75 mm/min. This is due to a decrease in the amount of heat exposed per unit length of the weld zone as welding speed increased from 60 to 75 mm/min. High plastic strain from the stirring of the FSW tool caused the particles to move from an agglomerated and non-uniform dispersion in the parent material to a homogenous dispersion in the NZ. (Li et al. 2018). On both sides of the NZ (referred to as TMAZ in the plot), where the material is thermally affected and plastically deformed, a somewhat increased hardness in contrast to the base material can be seen. Elongated grains were observed in the TMAZ. In all the samples, the hardness of TMAZ had slightly higher values than that of HAZ. The work hardening and second-phase particle dissolution

brought on by severe plastic deformation is responsible for the rise in hardness in the TMAZ. (Raturi et al. 2019).

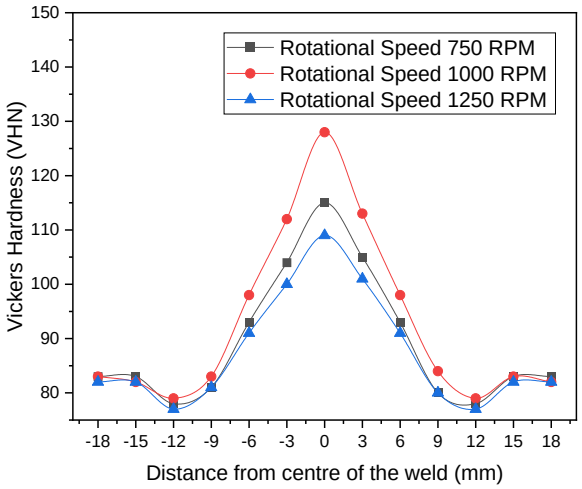


**Figure 4.23** Distribution of hardness at NZ of AA6061-3 (wt%) Rutile composite FS welded using a CSTC tool at rotational speeds of 750, 1000, and 1250 rpm, maintaining tool traverse speed constant at 75 mm/min.

The hardness variation across the FS welded joints of AA6061-3 (wt%) rutile composite fabricated using a CSTC tool at different rotational speeds of 750, 1000, and 1250 rpm while maintaining tool traverse speed at 90 mm/min, is shown in Figure 4.24. The joint that was constructed with a rotating speed of 1000 rpm and a welding speed of 90 mm/min exhibits the highest hardness value of 120 VHN at the nugget zone. The joint that was constructed with a rotational speed of 1250 rpm and a tool traverse speed of 90 mm/min has the lowest value, which is 105 VHN. The hardness obtained was significantly less at higher rotational speeds (1250 rpm) and faster welding speeds (90mm/min). The same causes that were mentioned in section 4.6.1.2 earlier also contribute to this phenomenon.

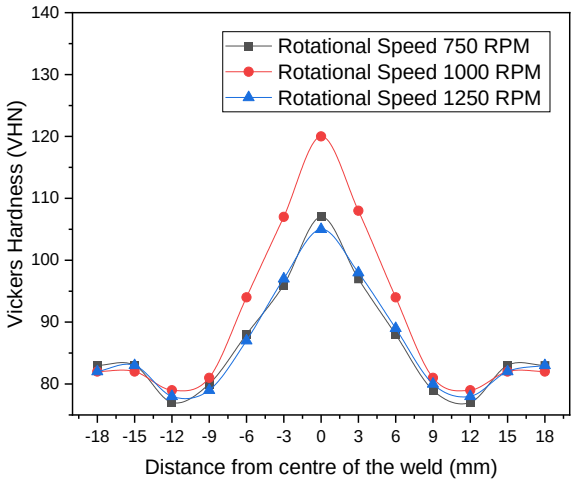


**Figure 4.24** Distribution of hardness at NZ of AA6061-3 (wt%) Rutile composite FS welded using a CSTC tool at rotational speeds of 750, 1000, and 1250 rpm, maintaining tool traverse speed constant at 90 mm/min.

### 4.6.1.3 Variation in hardness of NZ of AA6061-3(wt%) Rutile composite joints FS welded using Square Profile Pin tool

The plots in Figure 4.25 show the hardness distribution in the NZ of FS welded AA6061-3(wt%) Rutile composite joint, welded using an SQ tool at three different rotational speeds, 750, 1000, and 1250 rpm. The tool transverse speed was kept constant at 60 mm/min. The hardness was measured on both sides of the weld center. The rotational speed primarily affects the relative velocity between the stationary workpiece material and the rotating tool. As a result, the welding speed has little impact on the rate of heat creation. High welding speeds typically result in lower temperatures and heat input. (Çam and Mistikoglu 2014). Lower welding speed results in more heat being applied to the materials, which enhances plastic deformation of the material and the creation of an efficient weld joint. Because of the increased influence of dynamic recrystallization, the homogenous distribution of rutile particles, the abundance of small, rounded particles, and the reduced grain size, FS welded samples exhibit better hardness in the nugget zone compared to the base material. (Pratap et al. 2020) . Due to particle collisions, the small particles created by the tool's stirring action wear down the surface of the larger particles, giving them a spherical form. (Shettigar et al. 2013). The hardness reduced as the rotating speed rose from 1000 rpm to 1250 rpm. The heat

produced also rises as the rotational speed does, which causes the grain to become coarser and less hard. The hardness produced at TMAZ is less than the nugget region but greater than the parent material, as it is on either side of the weld nugget, i.e., on the retreating and advancing sides. The HAZ zone, which is in between the TMAZ and the base material, is subjected to the temperature cycle and there is no mechanical deformation. As a result, HAZ has been shown to include coarse grains, and as a result, the acquired hardness is lower than that of the base material. The joint that was constructed with a rotating speed of 1000 rpm and a welding speed of 60 mm/min exhibits a higher hardness value of 105 VHN. The joint was constructed at a rotational speed of 1250 rpm and a welding speed of 60 mm/min. has the lowest hardness value of 88 VHN.

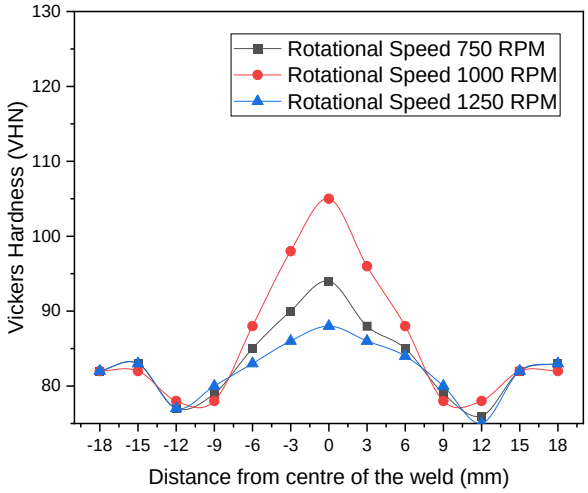


**Figure 4.25** Distribution of hardness at NZ of AA6061-3 (wt%) Rutile composite FS welded using the SQ tool at rotational speeds of 750, 1000, and 1250 rpm, holding the tool traverse speed constant at 60 mm/min.

Figure 4.26 shows the variation in the hardness of the composite FS welded with varied mixes of rotational speed and tool traverse speed. The plot of hardness distribution indicates that the NZ had a higher hardness value than the base composite regardless of tool rotating speed and welding speed. The following are the causes of the increase in hardness in NZ:

1) Grain size has been refined and reduced compared to the original material. The strength of the material is significantly influenced by the grain size. The Hall-Petch

equation states that the relationship between the material's hardness and grain size is inverse.

2) According to the Orowan hardness equation, the uniform distribution of rutile particles in the nugget zone contributes to the rise in hardness.

In NZ, the tool's swirling effect led to considerable plastic deformation, which created fine grains. Rutile particles rounded and broke when they were struck firmly against one another. In NZ, these rutile particles are uniformly dispersed, with a reduction in size and a rise in quantity. (Moradi Faradonbeh et al. 2018). In TMAZ, the material is thermally affected and plastically deformed, exhibiting a slightly lower hardness value than the NZ. Elongated grains were observed in TMAZ. All of the samples' hardness results showed that the TMAZ region had slightly greater hardness values than the HAZ zone. In HAZ, lower hardness is attained. The thermal cycle, which caused grain coarsening and softening, is the main cause of the decrease in hardness in the HAZ. The joint that was constructed with tool traverse and rotational speeds of 75 mm/min and 1000 rpm, respectively, exhibits the maximum hardness value of 116 VHN. The joint manufactured with a rotating speed of 1250 rpm and tool traverse speed of 75 mm/min has the lowest hardness value of 99 VHN.

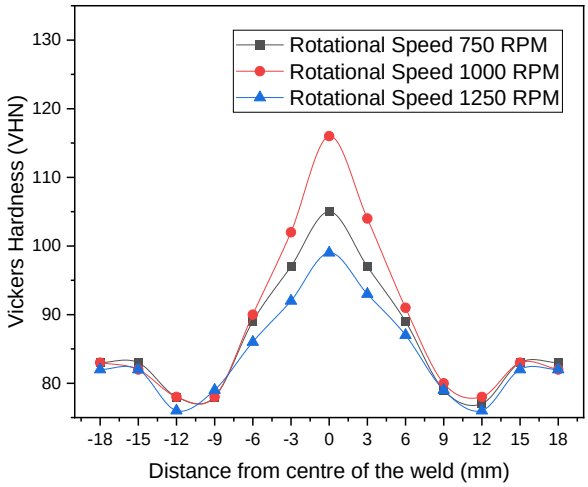


**Figure 4.26** Distribution of hardness at NZ of AA6061-3 (wt%) Rutile composite FS welded at rotational speeds of 750, 1000, and 1250 rpm and a constant tool traverse speed of 75 mm/min using the SQ tool.

The hardness variation in the NZ of FS welded AA6061-3(wt%) Rutile composite joint welded using SQ tool at different rotational speeds of 750, 1000, and 1250 rpm and

constant tool traverse speed of 90 mm/min is depicted in figure 4.27. The maximum hardness value is reached with a tool traverse speed of 90 mm/min and a rotational speed of 1000 rpm. The hardness value decreases between 1000 and 1250 rpm as a result of an increase in heat output. The hardness value decreases with increased welding speed. This may be mainly caused by the agglomeration or buildup of rutile particles in NZ as a result of fast rotating and welding speeds. Therefore, at higher rotational speeds (1250 rpm) and higher welding speeds (90mm/min), the heterogeneous distribution of rutile particles in the weld zone would lead to undesirable results. The joint that was constructed at a rotational speed of 1000 rpm and a tool traverse speed of 90 mm/min exhibits the highest hardness value of 109 VHN. The joint manufactured with a rotating speed of 1250 rpm and tool traverse speed of 90 mm/min has the lowest hardness value of 95 VHN.

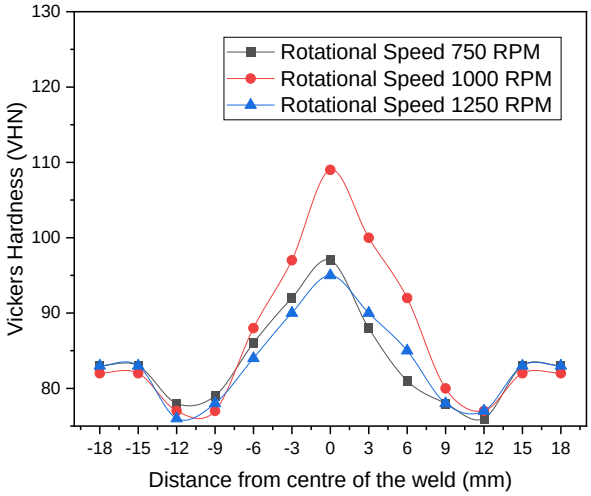


**Figure 4.27** Distribution of hardness at NZ of AA6061-3 (wt%) Rutile composite FS welded at rotational speeds of 750, 1000, and 1250 rpm and a constant tool traverse speed of 90 mm/min using the SQ tool

### 4.6.2 Measurement of tensile strength

#### 4.6.2.1 Tensile properties of AA6061-3(wt%) Rutile composite joints Friction Stir Welded using TC tool.

The tensile strengths of FS welded AA6061-3(wt%) Rutile composite joints using TC tool, at different tool traverse and rotational speeds combinations are listed in table 4.9. The UTS of joints increases as tool traverse speed is raised from 60 to 75 mm/min, and

the UTS decreases as welding speed is increased further. The workpiece fractures at the HAZ, close to the parent material, for samples welded at speeds less than 90 mm/min. Beyond 90 mm/min, welding speed increases cause pinhole, wormhole, and tunnel flaws to occur. Consequently, the specimens break at NZ (Shettigar et al. 2013). Tensile strength is reduced as a result of this. The material that has been stirred, traverses to the rear side from the front of the tool probe as the revolving tool advances. The welding speed affects the rate of heat input. (Padhy et al. 2018). The tool traverse speed controls the amount of time that frictional heat is exposed per unit weld length, affecting the rate of heat transfer and thereby assisting grain growth. When welding quickly, less heat is applied to the weld zone, which causes the material to cool more quickly. The UTS also rises when the rotating speed rises from 750 rpm to 1000 rpm. UTS decreases as rotational speed is increased further. The rotational speed and tool traverse speed that results in the highest joint efficiency are 1000 rpm and 75 mm/min, respectively. As the rotational speed is increased further, joint efficiency (defined in the section on research methodology) declines. The ideal process parameter values for FSW utilizing the TC tool are determined to be a tool traverse speed of 75 mm/min and a rotational speed of 1000 rpm.

**Table 4.9** Tensile strength of FS welded AA6061-3 (wt%) Rutile composite joints Welded using TC tool

| **Rotational Speed (rpm)** | **Welding Speed (mm/min)** | **Yield Strength (MPa)** | **Ultimate Tensile strength (MPa)** | **Elongation %** | **Joint efficiency (%)** |
|---|---|---|---|---|---|
| 750 | 60 | 80 ± 3 | 116 ± 2 | 8.2 ± 0.1 | 61.05 |
| 750 | 75 | 91 ± 2 | 130 ± 3 | 7.9 ± 0.1 | 68.42 |
| 750 | 90 | 84 ± 2 | 122 ± 2 | 7.7 ± 0.1 | 64.21 |
| 1000 | 60 | 95 ± 3 | 136 ± 3 | 7.6 ± 0.1 | 71.58 |
| 1000 | 75 | 106 ± 4 | 152 ± 3 | 7.3 ± 0.1 | 80.00 |
| 1000 | 90 | 101 ± 3 | 145 ± 3 | 7.1 ± 0.1 | 76.32 |
| 1250 | 60 | 88 ± 2 | 125 ± 2 | 8.3 ± 0.1 | 65.79 |
| 1250 | 75 | 99 ± 2 | 142 ± 4 | 8 ± 0.1 | 74.74 |
| 1250 | 90 | 94 ± 2 | 138 ± 3 | 7.6 ± 0.1 | 72.63 |

### 4.6.2.2 Tensile properties of FS welded AA6061-3(wt%) Rutile composite joints produced using Combined Square and Threaded Profile probe tool

Table 4.10 lists the results of the tensile tests performed on FS welded AA6061-3(wt%) Rutile composite joints, joined using the CSTC tool. At a welding speed of 75 mm/min and a rotational speed of 1000 rpm, the joint efficiency reached its maximum value of 92.63 %. At lower rotational speed (750 rpm) and higher rotational speed (1250 rpm), lesser joint efficiency was observed. When the rotational speed was raised to 1000 rpm from 750 rpm, an increase in the joint efficiency was observed and it reaches the maximum level. With subsequent increases in rotational speed, the joint efficiency deteriorated. Low rotational speeds result in poor stirring and low tool temperatures cause base material to not be properly consolidated. As a result, lesser joint efficacy was attained. A faster rotational speed improves the heat and stirring conditions, resulting in more uniform grain refinement thereby increasing the joint efficiency. A significant increase in the rotational speed produces excess stirring, high heat, and a lower cooling rate, leading to grain growth (Rezaei et al. 2011). Hence lower tensile properties were obtained at a higher rotational speed.

**Table 4.10** Tensile strength of FS welded AA6061-3 (wt%) Rutile composite joints Welded using a combined square and threaded profile pin.

| Rotational Speed (rpm) | Tool traverse (mm/min) | Yield Strength (MPa) | Ultimate Tensile Strength (MPa) | % Elongation | Joint efficiency (%) |
|---|---|---|---|---|---|
| 750 | 60 | 94 ± 3 | 135 ± 3 | 8.1 ± 0.1 | 71.05 |
| 750 | 75 | 106 ± 3 | 151 ± 3 | 7.7 ± 0.1 | 79.47 |
| 750 | 90 | 99 ± 2 | 142 ± 2 | 7.4 ± 0.1 | 74.74 |
| 1000 | 60 | 110 ± 4 | 158 ± 3 | 7.5 ± 0.1 | 83.16 |
| 1000 | 75 | 128 ± 4 | 176 ± 4 | 7.1 ± 0.1 | 92.63 |
| 1000 | 90 | 118 ± 3 | 168 ± 4 | 7 ± 0.1 | 88.42 |
| 1250 | 60 | 102 ± 3 | 145 ± 3 | 8.1 ± 0.1 | 76.32 |
| 1250 | 75 | 117 ± 3 | 165 ± 4 | 7.8 ± 0.1 | 86.84 |
| 1250 | 90 | 110 ± 2 | 160 ± 4 | 7.5 ± 0.1 | 84.21 |

#### 4.6.2.3 Tensile properties of AA6061-3(wt%) Rutile composite joints Friction Stir Welded using a Square tool

The measured tensile strength values of FS welded AA6061-3(wt%) Rutile composite joints using the SQ tool are listed in Table 4.11. Maximum joint efficiency was obtained at a tool traverse speed of 75 mm/min and rotational speed of 1000 rpm. When rotational speed is raised to 1000 rpm from 750 rpm, an increase in joint efficiency is observed and reaches a maximum value of 86%. With subsequent increases in rotational speed, the joint efficiency dropped. The composite joint that was FS welded with the SQ tool had a higher tensile property than joints that were FS welded using the TC tool. This might be a result of the tool's higher dynamic-to-static volume (DV to SV) ratio and the pulsating effect caused by the sharp edges of the tool. Higher DV to SV ratio and pulsating effect enables sweeping of large amount of material around the pin, generates higher temperature and assists in formation of finer grains (Mao et al. 2017; Sivaprasad and Muthupandi 2020)

**Table 4.11** Tensile strength of FS welded AA6061-3 (wt%) Rutile composite joints Welded using a square profile pin

| Rotational Speed (rpm) | Tool traverse (mm/min) | Yield Strength (MPa) | Ultimate Tensile Strength (MPa) | % Elongation | Joint efficiency (%) |
|---|---|---|---|---|---|
| 750 | 60 | 87 ± 2 | 124 ± 2 | 7.7 ± 0.1 | 65.26 |
| 750 | 75 | 99 ± 3 | 139 ± 2 | 7.3 ± 0.1 | 73.16 |
| 750 | 90 | 93 ± 2 | 130 ± 3 | 7 ± 0.1 | 68.42 |
| 1000 | 60 | 102 ± 3 | 145 ± 3 | 7.2 ± 0.1 | 76.32 |
| 1000 | 75 | 117 ± 3 | 163 ± 4 | 6.9 ± 0.1 | 85.79 |
| 1000 | 90 | 110 ± 3 | 155 ± 4 | 6.7 ± 0.1 | 81.58 |
| 1250 | 60 | 95 ± 2 | 133 ± 3 | 7.8 ± 0.1 | 70.00 |
| 1250 | 75 | 108 ± 2 | 151 ± 4 | 7.3 ± 0.1 | 79.47 |
| 1250 | 90 | 104 ± 2 | 147 ± 3 | 7.1 ± 0.1 | 77.37 |

#### 4.6.2.4 Effect of tool geometries on Tensile characteristics of AA6061-3(wt%) Rutile composite joints.

The bar chart in Figure 4.28 displays the UTS of the composite FS welded joints made using various combinations of the welding speed, tool profile, and tool rotational speed. The UTS of the FS welded composite joint grows and achieves a maximum value as the tool rotational speed is raised to 1000 rpm from 750 rpm. By increasing the rotating speed even more, from 1000 rpm to 1250 rpm, UTS is decreased. By generating enough heat from friction between the contact surfaces of the stationary workpiece and the rotating tool probe, the material gets plasticized in the vicinity of the rotating tool. The material around the tool is mixed as a result of the tool's spinning speed. Due to insufficient heat generation, plasticized material stirs less slowly at low rotational speeds. Since the relative velocity between the rotating tool probe and the material increases as rotational speed rises from 750 rpm to 1000 rpm, more heat is produced in the NZ. As a result, the material is properly mixed. The heat generation is also larger at higher tool rotational speeds, which causes turbulence in the material flow. While the tool rotation speed has a major influence on the amount of heat produced by the friction between the workpiece and the rotating tool, the welding speed affects the cooling rate. At constant rotational speed, samples produced with welding speeds that were either too low or too high displayed reduced tensile strength. At lower welding speed an increase in heat input and slower cooling rate results in coarse grains (grain growth). Due to slow welding speed, excessive stirring might lead to tunnel problems. Higher welding speeds, however, result in insufficient heat input into the joint, which in turn causes an insufficient stirring of softened material from the advancing to the retreating side, contributing to tunnel flaws. Also at higher welding speeds, the amount of heat supplied may not be sufficient to properly soften and flow the material because the rubbing of the tool shoulder and workpiece occurs for a shorter period, leading to defects in the welding joints and ultimately a reduction in joint strength. Therefore, both low and high traversal rates may lead to decreased tensile strength (Salih et al. 2015).

It is obvious that, among the various tools used in the study, the CSTC tool demonstrated maximum ultimate tensile strength at tool traverse speeds of 75 mm/min and tool rotational speed of 1000 rpm. The pulsating effect resulted from the square

faces of the tool probe and proper material flow guided by the tool thread, which leads to the proper mixing of the softened plasticized material in the weld zone. Hence, the joint strength may have increased. The joint that was constructed with a TC tool displayed a lower UTS.

It has been observed that there is an excessive amount of heat generated in the weld zone during experiments with extremely high rotation and high welding speed. Higher heat input causes material to soften excessively, which makes it more likely to experience turbulent flow. Additionally, it has been noted that there is "poor friction" in the weld zone, which leads to slipping and insufficient material transfer to the advancing side . These combined processes lead to the creation of defects and exceedingly weak joint strength.

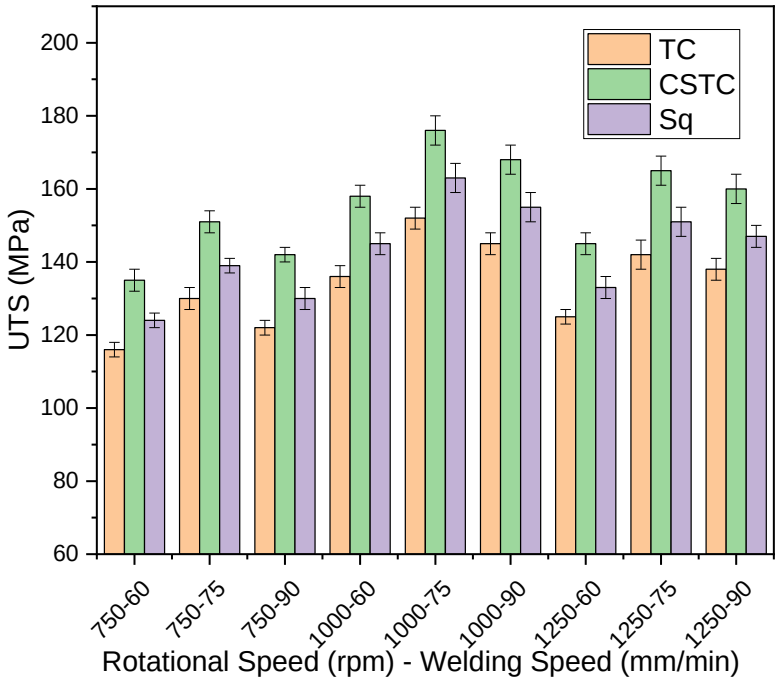


**Figure 4.28** UTS of the FS welded AA6061-3% Rutile composite joints using Threaded, Combination of Square and Threaded Cylindrical and Square profiled probe.

### 4.6.3 Tensile properties along the weld direction of AA6061-3(wt%) Rutile composite joints FS Welded using TC, CSTC, and SQ tool

The tensile characteristics of composite joints FS welded at various process parameter combinations are shown in Tables 4.12 to 4.14. Regardless of the tool pin profile and

process settings, the composite joint's ultimate tensile strength is greater than that of the parent material. The ultimate tensile strength for a threaded profile pin tool increased when the welding speed increased to 75 mm/min from 60 mm/min with a constant rotational speed of 1000 rpm, as shown in Table 4.12. The composite material's maximum tensile strength is 15% higher than the base material's. The ultimate tensile strength of a composite joint friction stir welded with a CSTC tool is displayed in Table 4.13. It is observed that as the tool traverse speed is raised to 75 mm/min from 60 mm/min, the ultimate tensile strength increases. In comparison to the base material, the composite has a 20% higher UTS, welded at rotational speed and tool traverse speed of 1000 rpm 75 mm/min respectively. The ultimate tensile strength for joints created with an SQ tool is displayed in Table 4.14. For composites FS welded at rotational speed and tool traverse speed of 1000 rpm and 75 mm/min respectively, the improvement of 16% in ultimate tensile strength above the base material UTS is observed. The production of tiny grains and the homogeneous distribution of rutile particles are what cause the UTS to grow.

**Table 4.12** Tensile properties of composites joints FS Welded using TC tool

| **Tool Rotational speed (rpm)** | **Tool traverse speed (mm/min)** | **UTS (MPa)** | **% Elongation** | **Increase in the strength (%)** |
|---|---|---|---|---|
| 1000 | 60 | 200±4 | 19.1±1 | 5.3 |
| 1000 | 75 | 218±4 | 16.6±1 | 14.7 |
| 1000 | 90 | 210±4 | 17.3±1 | 10.5 |

**Table 4.13** Tensile properties of composites joints FS Welded using CSTC tool

| **Tool Rotational speed (rpm)** | **Tool traverse speed (mm/min)** | **UTS (MPa)** | **% Elongation** | **Increase in the strength (%)** |
|---|---|---|---|---|
| 1000 | 60 | 208±3 | 18.3±1 | 9.5 |
| 1000 | 75 | 228±3 | 17.4±1 | 20 |
| 1000 | 90 | 217±3 | 18.1±1 | 14.2 |

**Table 4.14** Tensile properties of composites joints FS Welded using SQ tool

| Tool Rotational speed (rpm) | Tool traverse speed (mm/min) | UTS (MPa) | % Elongation | Increase in the strength (%) |
|---|---|---|---|---|
| 1000 | 60 | 204±4 | 18.3±1 | 7.4 |
| 1000 | 75 | 221±3 | 16.8±1 | 16.3 |
| 1000 | 90 | 215±3 | 17.8±1 | 13.2 |

## 4.7 REPEATABILITY TEST

The results of the repeatability test for the mechanical characteristics of the FS welded composites are reported in Table 4.15. The average values of the tests and the repeatability tests have been found to vary slightly. For every FS welded joint, the rotational speed is maintained at 1000 rpm.

**Table 4.15** Comparison of Average values of experimental results and repeatability test results.

| Sl. No. | Tool Profile | Welding speed mm/min | Hardness (VHN) | | UTS (MPa) | |
|---|---|---|---|---|---|---|
| | | | Average | repeatability | Average | repeatability |
| 1 | TC | 60 | 106±2 | 107 | 136 ± 3 | 138 |
| 2 | TC | 75 | 118±2 | 116 | 152 ± 3 | 151 |
| 3 | TC | 90 | 110±1 | 111 | 145 ± 3 | 147 |
| 7 | CSTC | 60 | 115±2 | 114 | 158 ± 3 | 156 |
| 8 | CSTC | 75 | 126±3 | 128 | 176 ± 4 | 174 |
| 9 | CSTC | 90 | 120±2 | 121 | 168 ± 4 | 169 |
| 13 | SQ | 60 | 105±1 | 105 | 145 ± 3 | 147 |
| 14 | SQ | 75 | 116±2 | 117 | 163 ± 4 | 161 |
| 15 | SQ | 90 | 109±2 | 109 | 155 ± 4 | 157 |

## 4.8 ANALYSIS OF TENSILE TEST FRACTURED SURFACES OF FS WELDED COMPOSITES

### 4.8.1 Analysis of fractured surfaces of tensile test performed across the weld direction

To interpret the microstructural impacts on the fracture properties and ductility of the composite, the analysis of fracture surfaces of tensile test specimens is useful. It is well recognized that three primary processes regulate fracture in MMCs.: (1) Breakage of the reinforcements, (2) voids form as a result of interfacial decohesion at the particle-matrix interface., (3) coalescence and growth of voids in the matrix (Bozkurt and Boumerzoug 2018). The fractured surfaces of tensile test specimens of FS welded composite joints fabricated with tool traverse speed and rotational speed of 90 mm/min, and 1000 rpm, respectively, using the CSTC tool are shown in Figure 4.29. The analysis of the fractured surface indicated that the fracture was ductile. It has been observed that all the samples were broken at HAZ, irrespective of the process variable and tool profile combination. In all the samples, HAZ exhibited the lowest hardness.

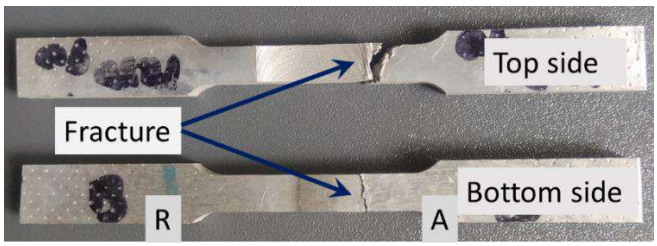


**Figure 4.29** Fractured tensile test specimen

Figure 4.30 (a-c) shows the fracture surface of composites FS welded using TC, CSTC, and SQ tools, respectively. Fracture surface of composite joint FS welded at rotational speed and tool traverse speed of 1000 rpm and 75 mm/min respectively using TC tool is shown in figure 4.30(a), indicated ductile fracture. Large, shallow dimples with tearing edges are its distinguishing feature. The fracture surface did not contain any broken fragments. Due to greater stress, particle cracking is more prevalent when there are clusters or agglomeration of particles. Due to the difference in the strain among the matrix and particles, the matrix particles decohere. Figure 4.30 (b) depicts the fractured area of composite joint FS welded at rotational speed and tool traverse speed of 1000

rpm and 75 mm/min respectively, using the CSTC tool. The tear edges, cracks, and dimples have been seen on the fracture surface. Figure 4.3 (c) depicts the fracture surface of the composite joint FS welded at rotational speed and tool traverse speed of 1000 rpm and 75 mm/min, respectively, using the SQ tool. There were dimples, tear edges, and cracks on the fracture surface. The welded composites are fractured at HAZ.

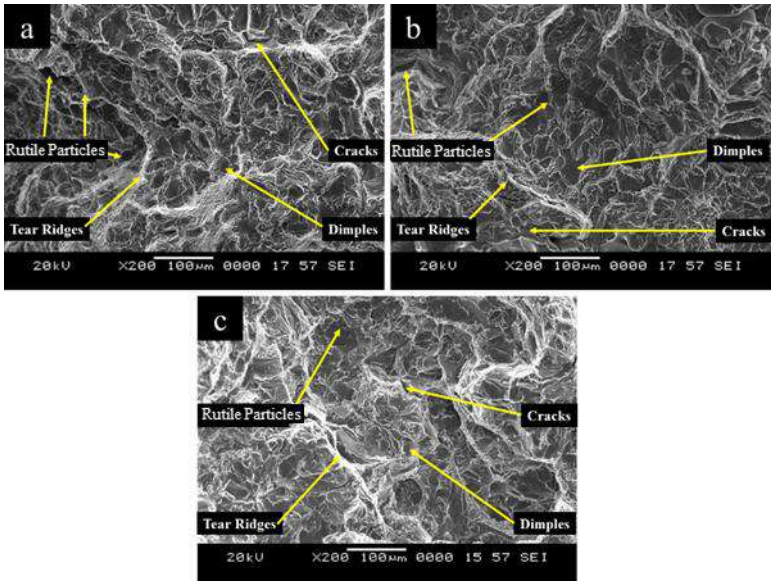


**Figure 4.30** SEM images of the fractured area of AA6061-3%Rutile composite joints friction stir welded at a rotational speed of 1000 rpm and welding speed of 75 mm/min using: a) Threaded profile pin, b) Combination of Square and Threaded Cylindrical Profile pin and c) Square profile pin

### 4.8.2 Investigation of fractured surfaces of the composite, tensile tested in the direction of the weld

Figure 4.31 depicts the macroscopic image of the fractured area of the FS welded composite, tested for tensile strength in the direction of the weld. Observations reveal that the crack is has expanded at a 45° angle {plane of maximum shear) to the tensile test axis. The shear fracture pattern typically exhibits this characteristic.


**Figure 4.31** Fractured tensile specimen of FS Welded composite joint tested in the weld direction.

Figure 4.32 (a - d) shows the tensile fractured surface of FS welded composite joint prepared using TC tool with different welding speeds of 60, 75, and 90 mm/min and with a constant rotational speed of 1000 rpm. Particle and matrix disintegration occurred in every instance. Consequently, two separate failure mechanisms are interacting. First, the surrounding matrix has been plastically deformed, causing a cracking of particles inside the large dimple. Rutile particles shatter as a result of stress being applied to them during the test, which causes interfacial shearing. Because of the high stress value, the cracks that initially formed in the particles grew and moved across the matrix, connecting with the nearby particulates. (Urena 2000). Second, thin tearing edges and small, shallow dimples dominate the fracture surface. Due to the weld nugget's finer grains, small dimples were visible. (Dinaharan et al. 2012). Cracked, broken particles and pull-out particles were observed. The failure mode was ductile. The welded composite's facture surfaces showed fine and equalized dimples when compared to those of the base material.

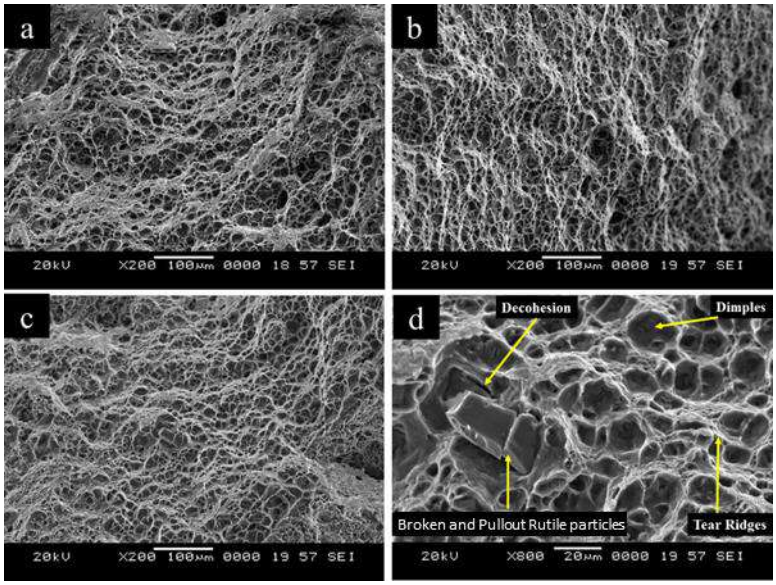


**Figure 4.32** SEM image of a fractured surface of AA6061-3 (wt%) Rutile composite joints friction stir welded using TC tool (along the weld direction) at a constant rotational speed of 1000rpm and a) welding speed of 60 mm/min, b) welding speed of 75 mm/min, c) welding speed of 90 mm/min, d) higher magnification image showing the dimples, pullout, decohesion, and cracked rutile particles.

The features of fractured areas of tensile specimens that were welded at speeds of 60 mm/min, 75 mm/min, and 90 mm/min, respectively, with a constant rotating speed of 1000 rpm are shown in Figure 4.32 (a-c). Dimple fracture is evident by the presence of dimples on the fracture surface. Due to the presence of fine, equiaxed grains in NZ, a network of tiny dimples can be seen on the fractured surface of the FS welded composite. Dimples, pullout, decohesion, and broken rutile particles are depicted in Figure 4.32 (d).

The fractured surface of composite joint FS welded using the CSTC tool at a constant rotational speed of 1000 rpm and different welding speeds of 60, 75, and 90 mm/min are shown in Figure 4.33 (a-d).

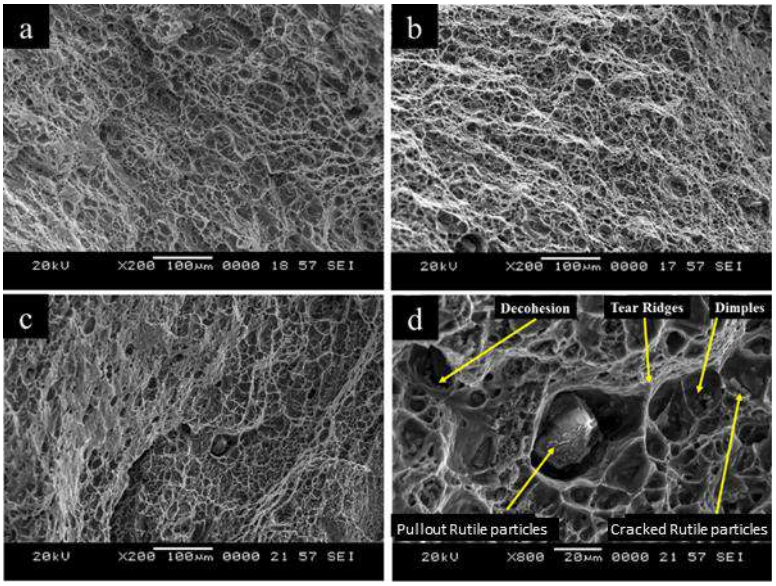


**Figure 4.33** SEM image of a fractured surface of AA6061-3 (wt%) Rutile composite joints friction stir welded using CSTC tool (along the weld direction) at a constant rotational speed of 1000rpm and a) welding speed of 60 mm/min, b) welding speed of 75 mm/min, c) welding speed of 90 mm/min, and d) higher magnification image showing the dimples, pullout, decohesion, and cracked rutile particles.

The fracture surface of the joint tensile specimen created with the CSTC tool and the joint tensile specimen created with the TC tool were both identical. The ductile fracture was the mode of fracture. Small particles can be found at the bottom of the fine dimples on the fractured surface. At the base of the dimple, there were also broken particles to

be seen. Due to the presence of fine, equiaxed grains, a network of tiny dimples can be seen on the fractured area of the FS welded composite. The magnified image of the fracture surface shown in Figure 4.33 (d) includes dimples, decohesion, pullout, and shattered rutile particles.

Figure 4.34 (a - d) shows the SEM images of a fractured surface of AA6061-3 (wt%) Rutile composite joints friction stir welded using an SQ tool (along the weld direction) at a constant rotational speed of 1000 rpm and different welding speeds of 60, 75 and 90 mm/min. The tensile fracture analysis revealed the existence of large voids associated with the particle-matrix decohesion, big dimples, rip ridges, and the appearance of little dimples inside the large dimples as a result of the matrix's ductile failure. Due to the presence of fine, equiaxed grains in NZ, a network of tiny dimples can be seen on the fractured area of the FS welded composite. The magnified image of the fracture surface shown in Figure 4.34 (d) includes dimples, pullout, decohesion, and shattered rutile particles. Deeper dimples are a sign of severe plastic deformation.

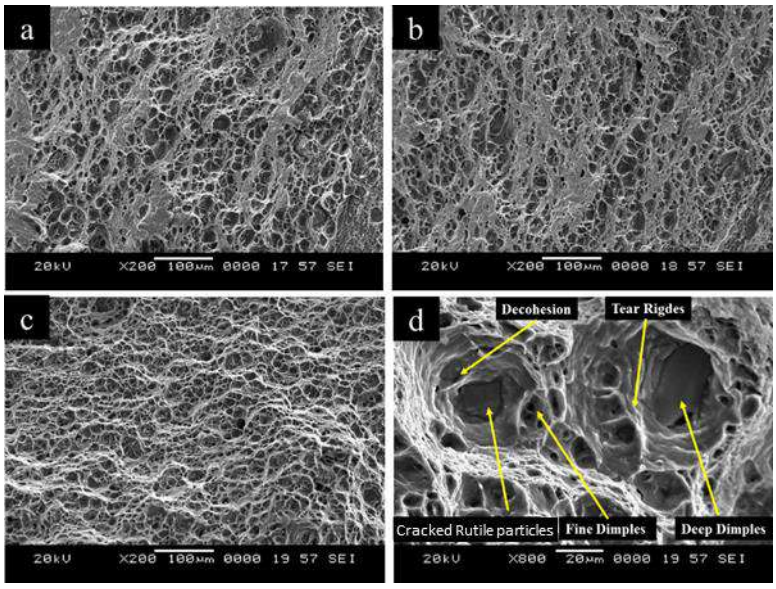


**Figure 4.34** SEM image of a fractured surface of AA6061-3 (wt%) Rutile composite joints friction stir welded using SQ tool (along the weld direction) at a constant rotational speed of 1000rpm and a) welding speed of 60 mm/min, b) welding speed of 75 mm/min, c) welding speed of 90 mm/min, and d) higher magnification image showing the dimples and Rutile particles.

## 4.9 ANALYSIS OF THE RELATIONSHIP BETWEEN GRAIN SIZE AND HARDNESS

The correlation between the hardness and average grain size measured at the NZ of an AA6061-3% rutile composite welded using a TC tool is shown in Figure 4.35. The rotational speed and welding speed of the process have an impact on the grain size and hardness of the FS welded composite. Coarse grains are generated in NZ when the welding speed is low (60 mm/min) and the rotational speed is high (1250 rpm), leading to lower hardness in NZ. The hardness is also at its lowest when the rotating speed (750 rpm) and welding speed are both low. This results from the "annealing" (softening) effect (Xie et al. 2007). At the rotational speed of 1000 rpm and a tool traverse speed of 75 mm/min smaller grains and the highest hardness were obtained. The increase in hardness at NZ was caused by an enhancement in the fine-grain strengthening effect, which dominates the annealing effect. In every instance, the hardness increases due to the decrease in inter-particle spacing with decrease in the particle size.

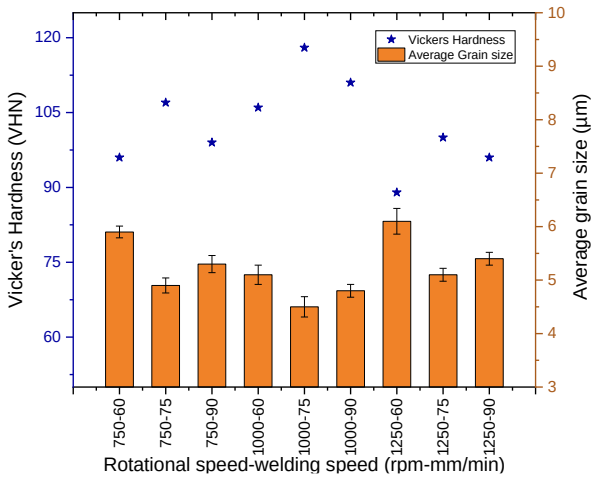


**Figure 4.35** Hardness and grain size variation at the NZ of the FS welded AA6061-3% Rutile composite joint, welded using TC tool

Figure 4.36 depicts the correlation between the hardness and grain size at the NZ of AA6061-3 (wt%) Rutile composite friction stir welded utilizing the CSTC tool. Figure 4.36 makes it clear that NZ's grain size and hardness are influenced by the process variables. As the rotating speed increases from 750 rpm to 1000 rpm, the grain size decreases as the hardness rises. The size of the grains increases with a further rise in rotational speed from 1000 rpm to 1250 rpm, while the hardness decreases. At a

rotational speed of 1250 rpm and a tool traverse speed of 60 mm/min, the minimum hardness with a coarse-grained structure is attained. Maximum hardness and small grain sizes are achieved at 1000 rpm rotational speed and 75 mm/min welding speed. The preceding section explained the cause of this. In comparison to the composite being welded with the TC and SQ tool, the composite being welded with the CSTC tool exhibits higher hardness.

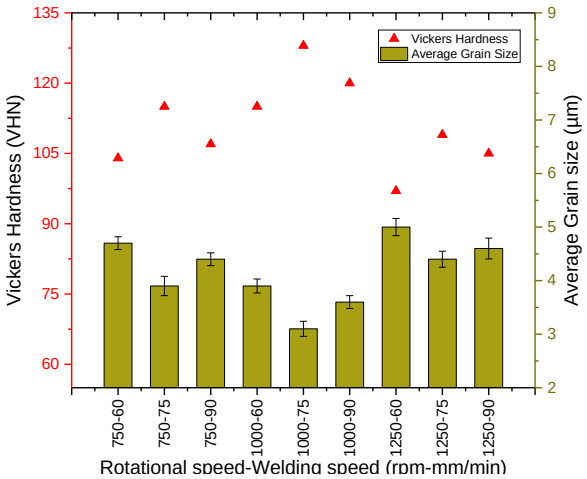


**Figure 4.36** Variation of hardness and grain size at the NZ of the FS welded AA6061-3% Rutile composite joint welded using the CSTC tool

Variation of grain size with the hardness of FS welded AA6061-3% Rutile composite samples employing the SQ tool is shown in Figure 4.37. The average grain size decreases while the hardness increases when the welding speed is raised from 60 to 75 mm/min with a constant rotational speed of 750 rpm.

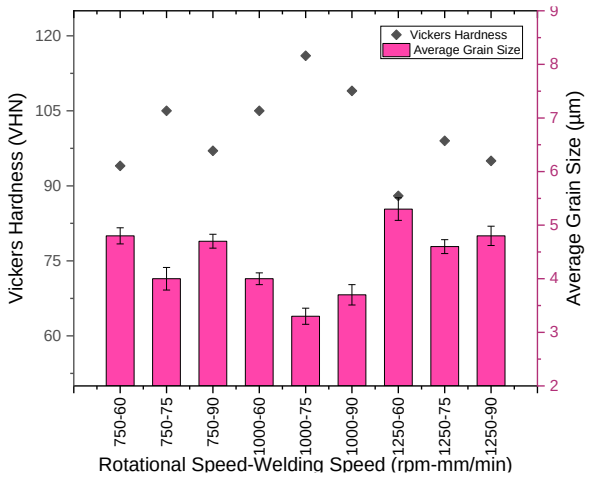


**Figure 4.37** Variation of hardness and grain size at the NZ of the FS welded AA6061-3% Rutile composite joint welded using the SQ tool

When the rotating speed is increased from 750 rpm to 1000 rpm, a reduction in the average grain size is seen. The hardness declines as welding speeds are further increased. The material softens as a result of the increased temperature created at the higher rotational speed of 1250 rpm compared to 1000 rpm. As a result, the grain structure was coarse. Thus, it became apparent that NZ's hardness had decreased. At a welding speed of 75 mm/min and a rotational speed of 1000 rpm, the finest grains with the highest hardness were produced.

## 4.10 RELATIONSHIP BETWEEN THE NZ HARDNESS AND UTS OF FS WELDED COMPOSITE

The relationship between the hardness and the UTS of FS welded AA6061-3% Rutile composite joint welded at different process variable combinations using the TC tool is shown in Figure 4.38. The relationship between hardness and UTS is direct as seen in Figure 4.38. Poor UTS and hardness were seen when welding at 750 and 1250 rpm while maintaining a constant 60 mm/min welding speed.

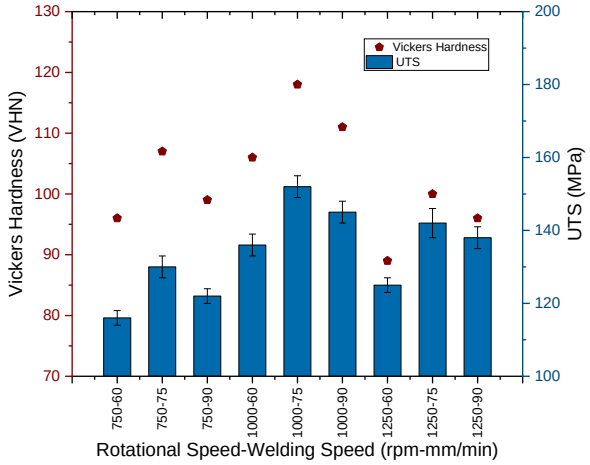


**Figure 4.38** Relationship between UTS and hardness of the NZ, FS welded AA6061-3(wt%) Rutile composite using TC tool

Rotational speed generates heat, whereas welding speed determines how much heat is applied to the material. Reduced heat supply results from decreased heat generation. To create a joint that has sufficient strength, enough heat is necessary. Reduced heat generation from lower rotational speeds leads to poor mixing, which lowers the UTS and joint hardness. Similar to slower cooling rates, slower welding speeds cause more heat to be supplied, while grain growth occurs from slower cooling rates. At 1000 rpm

of rotational speed and 75 mm/min of welding speed, it was discovered that the weld strength was quite near to the strength of the parent material.

The effect of tool traverse speed and rotational speed on the UTS and Hardness of the FS welded AA6061-3(wt%) Rutile composite employing the CSTC tool is shown in Figure 4.39. The image clearly shows that the UTS of the composite also rises as composite hardness rises. When a composite is welded using a CSTC tool, it has a higher hardness and UTS than when a composite is welded using a TC tool. According to Kunnathur Periyasamy et al. (2019), the probe profile and probe diameter have a direct impact on how much material is churned up during the welding process. The dynamic-to-static ratio will change if the probe profile changes. The dynamic-to-static ratio is higher with the CSTC tool. As a result, the UTS showed improvement.

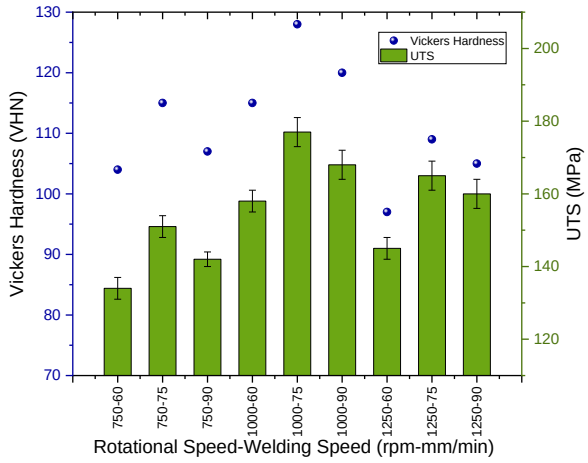


**Figure 4.39** Relationship between UTS and hardness at the NZ, FS welded AA6061-3(wt%) Rutile composite using CSTC tool

The change in UTS and hardness of the FS welded AA6061-3 (wt%) rutile composite using the SQ tool is shown in Figure 4.40 for various rotating and welding speeds. The composites being welded appear to have higher hardness and UTS values than the composites being welded with a TC tool, but lower than those of the CSTC tool. The dynamic-to-static ratio for square probe profiles is 1.57. As a result, during the welding process, it sweeps more material (Mahakur et al. 2021). According to Kumar and Raju (2012), the tool probe's square faces aid in creating a pulsing effect, which improves joint strength. For a tool traverse speed of 75 mm/min and a rotational speed of 1000 rpm, increased joint strength and hardness are obtained as shown in Figure 4.40. Proper

stirring of the material by the rotating tool and adequate heat generation led to an increase in joint strength. It was discovered that the CSTC tool produces joints with a higher strength than the TC and SQ tools when the joint strength of samples acquired using the three different pin profiles was analyzed. Uniform material flow directed by the threads and pulsing action of the square edges allow for improved heat generation, appropriate plasticization, stirring, and consolidation of the material in the weld zone. As a result, the joints made with CSTC tools have better mechanical characteristics.

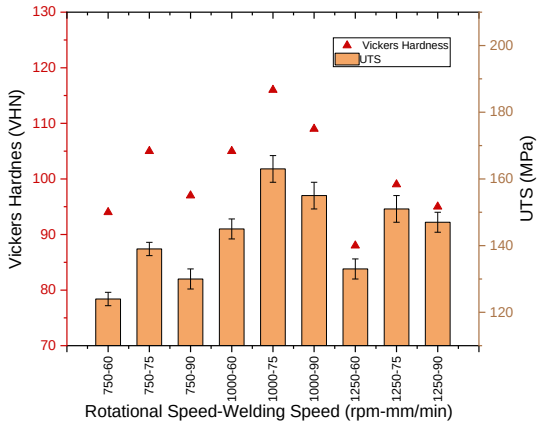


**Figure 4.40** Relationship between UTS and hardness of the NZ, FS welded AA6061-3(wt%) Rutile composite using SQ tool

## 4.11 TAGUCHI DESIGN OF EXPERIMENT

The impact of welding parameters on performance indicators such as yield strength, UTS, hardness, and percentage elongation is assessed. Table 4.16 contains a list of the input parameters and their corresponding levels employed for the current study. These criteria were chosen based on a review of the literature and preliminary research. To carry out the experiments in greater detail and examine the relevant process factors, an L9 Taguchi orthogonal array (OA) of experiments was used.

### 4.11.1 Experimental results:

Table 4.17 evaluates the process parameters' impact on the output characteristics and the corresponding S/N ratio values. All charts, designs, and analyses in the current study were included using Minitab software. The main purpose of measuring reactions is to produce goods and processes insensitive to noise effects (Cochran and Cox 1962). This usually allows for the identification of the predictable results of either a product or a

process when noise is present. The S/N ratio values with larger-the-better characteristics are used in the present study. The process variable that has a higher S/N ratio will produce the ideal result with the least amount of variance.

**Table 4.16** Experimental design using L9 orthogonal array

| Expt No. | Rotational speed (rpm) | Welding speed (mm/min) | Tool Geometry |
|---|---|---|---|
| 1 | 750 | 60 | 1 |
| 2 | 750 | 75 | 2 |
| 3 | 750 | 90 | 3 |
| 4 | 1000 | 60 | 2 |
| 5 | 1000 | 75 | 3 |
| 6 | 1000 | 90 | 1 |
| 7 | 1250 | 60 | 3 |
| 8 | 1250 | 75 | 1 |
| 9 | 1250 | 90 | 2 |

Tool Geometry: 1 - Threaded Cylindrical; 2 - Combined Square and threaded cylindrical; 3 – Square.

**Table 4.17** Experimental results for each response

| Expt. No. | YS (MPa) | | UTS (MPa) | | $H_v$ (VHN) | | % El | |
|---|---|---|---|---|---|---|---|---|
| | Expt. Value | S/N ratio | Expt. Value | S/N ratio | Expt. Value | S/N ratio | Expt. Value | S/N ratio |
| 1 | 80 | 38.06 | 116 | 41.29 | 96 | 39.6 | 8.2 | 18.28 |
| 2 | 106 | 40.51 | 151 | 43.58 | 115 | 41.2 | 7.7 | 17.73 |
| 3 | 93 | 39.37 | 130 | 42.28 | 97 | 39.7 | 7.0 | 16.90 |
| 4 | 110 | 40.83 | 158 | 43.97 | 115 | 41.2 | 7.5 | 17.50 |
| 5 | 117 | 41.36 | 163 | 44.24 | 116 | 41.3 | 6.9 | 16.78 |
| 6 | 101 | 40.09 | 145 | 43.23 | 110 | 40.8 | 7.1 | 17.03 |
| 7 | 95 | 39.55 | 133 | 42.48 | 88 | 38.9 | 7.8 | 17.84 |
| 8 | 99 | 39.91 | 142 | 43.05 | 100 | 40.0 | 8.0 | 18.06 |
| 9 | 110 | 40.83 | 160 | 44.08 | 105 | 40.4 | 7.5 | 17.50 |

YS: Yield Strength; UTS: Ultimate Tensile Strength; $H_v$: Hardness; El: Elongation

### 4.11.2 Effect of process parameters on output responses -ANOVA

The L9 OA, shown in Table 4.16, was used to analyze the effects of process variables on the responses such as hardness, yield strength, UTS, and % elongation. Using the Analysis of Variance (ANOVA) computational technique, the implications, the importance of the process parameters on the responses, and even the contribution percentage of the parameters on the responses were determined (Ross, 1996). ANOVA complies with the sum of squares, degrees of freedom, mean square, F-value, and P-value. Table 4.18 – 4.21 shows the Analysis of variance for friction stir welded composite material. It is clear from Tables 4.18 to 4.21 that the rotating speed, welding speed, and tool geometry are important variables and affect the output responses. Based on the P-value, the importance of the parameter is determined; if the P-value is less than 0.05, the parameter is considered significant. To determine the significant contribution made by the process parameters on the responses, the percentage of contribution for each process parameter is determined.

From Table 4.18, It is evident that rotational speed contributes the most to yield strength (40.53%), followed by tool geometry (35.70%), and welding speed (23.11%).

From Table 4.19, it can be observed that rotational speed has a major contribution of 40.47 % on UTS, followed by tool geometry of 38.03 % and welding speed of 20.48 %.

From Table 4.20, it can be observed that rotational speed has a major contribution of 50 % on hardness, followed by tool geometry of 27.94 % and welding speed of 21.48 %.

From Table 4.21, it can be observed that welding speed has the major contribution of 36.82 % on % elongation, followed by the rotational speed of 36.41 % and the tool geometry of 26.63 %.

**Table 4.18** Analysis of variance for Yield Strength (MPa)

| Source | DF | Seq SS | Adj SS | Adj Ms | F | P | % contribution |
|---|---|---|---|---|---|---|---|
| Rot. Speed (rpm) | 2 | 400.22 | 400.22 | 200.11 | 72.04 | 0.014 | 40.53 |
| Welding Speed (mm/min) | 2 | 228.22 | 228.22 | 114.11 | 41.08 | 0.024 | 23.11 |
| Tool Geometry | 2 | 353.56 | 353.56 | 176.78 | 63.64 | 0.015 | 35.80 |
| Residual error | 2 | 5.56 | 5.56 | 2.78 | | | 0.56 |
| Total | 8 | 987.56 | | | | | |

**Table 4.19** Analysis of variance for UTS (MPa)

| Source | DF | Seq SS | Adj SS | Adj Ms | F | P | % contribution |
|---|---|---|---|---|---|---|---|
| Rot. Speed (rpm) | 2 | 796.22 | 796.22 | 398.11 | 39.37 | 0.025 | 40.47 |
| Welding Speed (mm/min) | 2 | 402.89 | 402.89 | 201.44 | 19.92 | 0.048 | 20.48 |
| Tool Geometry | 2 | 748.22 | 748.22 | 374.11 | 37.00 | 0.026 | 38.03 |
| Residual error | 2 | 20.22 | 20.22 | 10.11 | | | 1.03 |
| Total | 8 | 1967.56 | | | | | |

**Table 4.20** Analysis of variance for Hardness (VHN)

| Source | DF | Seq SS | Adj SS | Adj Ms | F | P | % contribution |
|---|---|---|---|---|---|---|---|
| Rot. Speed (rpm) | 2 | 402.00 | 402.00 | 201.00 | 86.14 | 0.011 | 50.00 |
| Welding Speed (mm/min) | 2 | 172.67 | 172.67 | 86.33 | 37.00 | 0.026 | 21.48 |
| Tool Geometry | 2 | 224.67 | 224.67 | 112.33 | 48.14 | 0.02 | 27.94 |
| Residual error | 2 | 4.67 | 4.67 | 2.33 | | | 0.58 |
| Total | 8 | 804.00 | | | | | |

**Table 4.21** Analysis of variance for % Elongation

| Source | DF | Seq SS | Adj SS | Adj Ms | F | P | % contribution |
|---|---|---|---|---|---|---|---|
| Rot. Speed (rpm) | 2 | 0.60 | 0.60 | 0.30 | 268 | 0.004 | 36.41 |
| Welding Speed (mm/min) | 2 | 0.60 | 0.60 | 0.30 | 271 | 0.004 | 36.82 |
| Tool Geometry | 2 | 0.44 | 0.44 | 0.22 | 196 | 0.005 | 26.63 |
| Residual error | 2 | 0.00 | 0.00 | 0.00 | | | 0.14 |
| Total | 8 | 1.64 | | | | | |

From Table 4.18 – 4.21, it can be concluded that rotational has a major contribution to the output responses like yield strength, UTS, and hardness whereas % elongation was mainly affected by tool geometry followed by welding speed.

Figure 4.41 – 4.44 represents the main effect plots for yield strength, UTS, hardness, and %elongation of FS welded composite respectively. Tool rotational speed controls

the amount of heat developed at the weld zone whereas, the heat exposure time and rate of cooling are depended on welding speed. Optimum heat generation and cooling rate are necessary for proper plasticization and appropriate material flow in the weld zone thereby controlling the mechanical properties of the welded material. At lower rotational speed, the heat developed is insufficient whereas at higher rotational speed, higher heat input results in turbulent material flow. Higher strength was observed in the sample welded at 1000 rpm. The welding speed has a major impact on the hardness, as heat exposure time and cooling rate are dependent on it. Finer grains produce increased hardness, according to the Hall-Petch theory. Longer exposure time results in a reduced cooling rate thereby promoting the grain growth and formation of coarser grains. Similarly, reduced heat supply enables the formation of finer grains due to which the hardness of the workpiece increases.

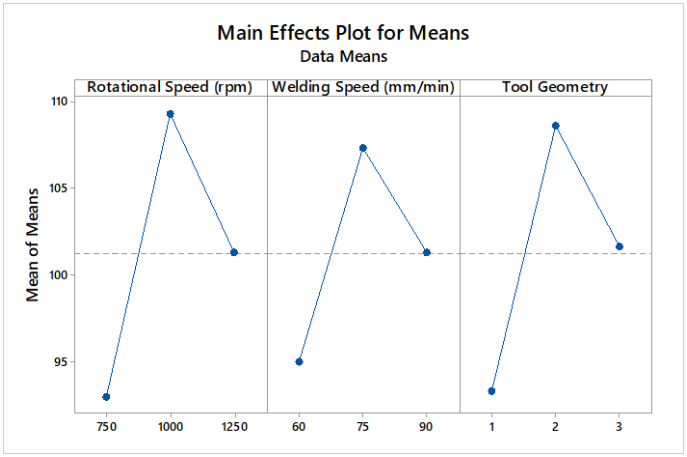


**Figure 4.41** Effect of process parameters on yield strength

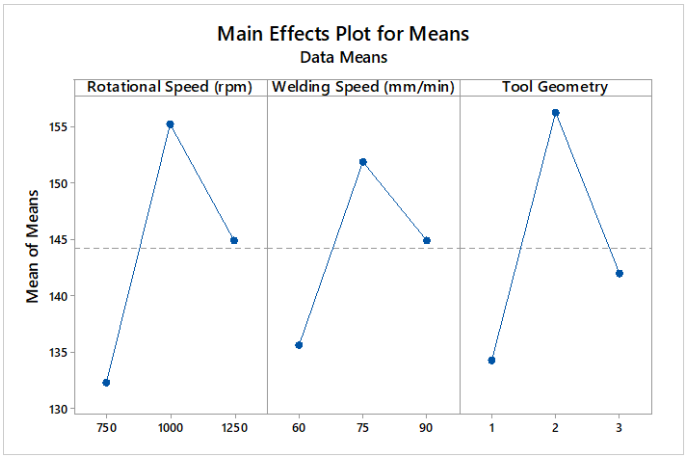


**Figure 4.42** Effect of process parameters on UTS

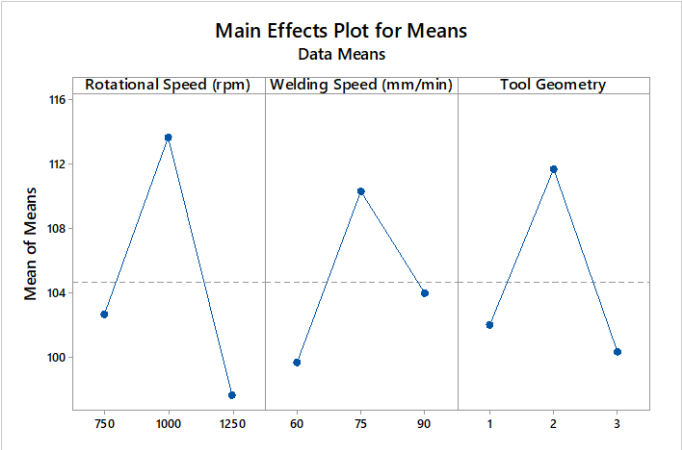


**Figure 4.43** Effect of process parameters on Hardness

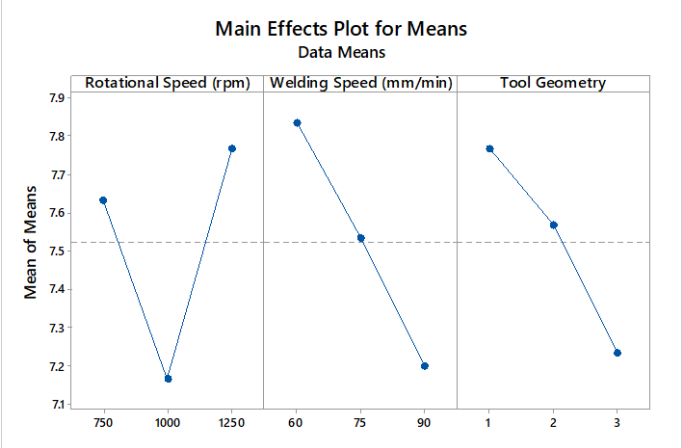


**Figure 4.44** Effect of process parameters on % elongation

## 4.12 RESPONSE SURFACE METHODOLOGY

### 4.12.1 RSM Modelling

The response prediction using RSM was implemented using the Central Composite Design (CCD). There were 20 trials performed, with an alpha value of 1, 8 cube points, 6 cube center points, and 6 axial points. Trials were performed to define the range of the process parameters to create joints without faults. The association between the process parameters and the FSW output responses is established in the current work using CCFCD. Analysis of variance (ANOVA) was utilized to validate the model's performance (Tables 4.22 – 4.25). Using this technique, the model's importance is determined. The model is significant if it meets the requirement that Prob>f is less than

0.0500. It may be said that all the proposed models are important because they all satisfy the requirement that Prob>f is less than 0.0500. The R2 correlation coefficient was used to determine whether the fitted regression model was adequate. R2 must be near unity in value. The "Pre-R-squared" values for each response are reasonably correlated with the "Adj R-Squared" values.

From the table, it is observed that each of the process parameters and interactions among themselves had a major influence on the process responses.

**Table 4.22** Analysis of Variance of Yield Strength (MPa)

| Source | DF | Adj SS | Adj MS | F-Value | P-Value |
|---|---|---|---|---|---|
| Model | 9 | 5323.64 | 591.52 | 135.79 | 0 |
| Linear | 3 | 532.9 | 177.63 | 40.78 | 0 |
| RS | 1 | 230.4 | 230.4 | 52.89 | 0 |
| WS | 1 | 108.9 | 108.9 | 25 | 0.001 |
| TG | 1 | 193.6 | 193.6 | 44.44 | 0 |
| Square | 3 | 4784.36 | 1594.79 | 366.1 | 0 |
| RS*RS | 1 | 455.05 | 455.05 | 104.46 | 0 |
| WS*WS | 1 | 295.36 | 295.36 | 67.8 | 0 |
| TG*TG | 1 | 455.05 | 455.05 | 104.46 | 0 |
| 2-Way Interaction | 3 | 6.38 | 2.13 | 0.49 | 0.698 |
| RS*WS | 1 | 3.13 | 3.13 | 0.72 | 0.417 |
| RS*TG | 1 | 0.13 | 0.13 | 0.03 | 0.869 |
| WS*TG | 1 | 3.13 | 3.13 | 0.72 | 0.417 |
| Error | 10 | 43.56 | 4.36 | | |
| Lack-of-Fit | 5 | 38.06 | 7.61 | 6.92 | 0.027 |
| Pure Error | 5 | 5.5 | 1.1 | | |
| Total | 19 | 5367.2 | | | |

**Table 4.23** Analysis of Variance of UTS (MPa)

| Source | DF | Adj SS | Adj MS | F-Value | P-Value |
|---|---|---|---|---|---|
| Model | 9 | 8664.92 | 962.77 | 888.65 | 0 |
| Linear | 3 | 856.2 | 285.4 | 263.43 | 0 |

| | | | | | |
|---|---|---|---|---|---|
| RS | 1 | 422.5 | 422.5 | 389.97 | 0 |
| WS | 1 | 240.1 | 240.1 | 221.62 | 0 |
| TG | 1 | 193.6 | 193.6 | 178.7 | 0 |
| RS*RS | 1 | 777.84 | 777.84 | 717.96 | 0 |
| WS*WS | 1 | 384.09 | 384.09 | 354.52 | 0 |
| TG*TG | 1 | 824.78 | 824.78 | 761.28 | 0 |
| 2-Way Interaction | 3 | 28.38 | 9.46 | 8.73 | 0.004 |
| RS*WS | 1 | 28.13 | 28.13 | 25.96 | 0 |
| RS*TG | 1 | 0.13 | 0.13 | 0.12 | 0.741 |
| WS*TG | 1 | 0.13 | 0.13 | 0.12 | 0.741 |
| Error | 10 | 10.83 | 1.08 | | |
| Lack-of-Fit | 5 | 5.33 | 1.07 | 0.97 | 0.513 |
| Pure Error | 5 | 5.5 | 1.1 | | |
| Total | 19 | 8675.75 | | | |

**Table 4.24** Analysis of Variance of Hardness

| Source | DF | Adj SS | Adj MS | F-Value | P-Value |
|---|---|---|---|---|---|
| Model | 9 | 4034.09 | 448.23 | 668.1 | 0 |
| Linear | 3 | 126.5 | 42.17 | 62.85 | 0 |
| RS | 1 | 57.6 | 57.6 | 85.85 | 0 |
| WS | 1 | 62.5 | 62.5 | 93.16 | 0 |
| TG | 1 | 6.4 | 6.4 | 9.54 | 0.011 |
| Square | 3 | 3899.09 | 1299.7 | 1937.22 | 0 |
| RS*RS | 1 | 563.78 | 563.78 | 840.32 | 0 |
| WS*WS | 1 | 213.84 | 213.84 | 318.73 | 0 |
| TG*TG | 1 | 238.78 | 238.78 | 355.9 | 0 |
| 2-Way Interaction | 3 | 8.5 | 2.83 | 4.22 | 0.036 |
| RS*WS | 1 | 8 | 8 | 11.92 | 0.006 |
| RS*TG | 1 | 0.5 | 0.5 | 0.75 | 0.408 |
| WS*TG | 1 | 0 | 0 | 0 | 1 |
| Error | 10 | 6.71 | 0.67 | | |

| | | | | | |
|---|---|---|---|---|---|
| Lack-of-Fit | 5 | 1.88 | 0.38 | 0.39 | 0.839 |
| Pure Error | 5 | 4.83 | 0.97 | | |
| Total | 19 | 4040.8 | | | |

**Table 4.25** Analysis of Variance of % Elongation

| Source | DF | Adj SS | Adj MS | F-Value | P-Value |
|---|---|---|---|---|---|
| Model | 9 | 2.94373 | 0.327081 | 50.89 | 0 |
| Linear | 3 | 1.646 | 0.548667 | 85.37 | 0 |
| RS | 1 | 0.009 | 0.009 | 1.4 | 0.264 |
| WS | 1 | 0.961 | 0.961 | 149.52 | 0 |
| TG | 1 | 0.676 | 0.676 | 105.18 | 0 |
| Square | 3 | 1.28273 | 0.427576 | 66.53 | 0 |
| RS*RS | 1 | 0.8046 | 0.804602 | 125.19 | 0 |
| WS*WS | 1 | 0.0046 | 0.004602 | 0.72 | 0.417 |
| TG*TG | 1 | 0.03273 | 0.032727 | 5.09 | 0.048 |
| RS*WS | 1 | 0.005 | 0.005 | 0.78 | 0.398 |
| RS*TG | 1 | 0.005 | 0.005 | 0.78 | 0.398 |
| WS*TG | 1 | 0.005 | 0.005 | 0.78 | 0.398 |
| Error | 10 | 0.06427 | 0.006427 | | |
| Lack-of-Fit | 5 | 0.02427 | 0.004855 | 0.61 | 0.702 |
| Pure Error | 5 | 0.04 | 0.008 | | |
| Total | 19 | 3.008 | | | |

### 4.12.2 Regression Analysis

To determine the relationship between the process parameters and the responses, regression analysis is chosen. The quadratic technique is utilized in the current study to fit the model and continue the analysis of the experimental data. The resulting regression equations are provided in equations 4.1 through 4.4.

*Z[YS_MPa] = 126.245+ 4.800*RS+ 3.300*WS+ 4.400*TG- 12.86*RS*RS- 10.36*WS* WS-12.86*TG*TG+ 0.625*RS*WS+ 0.125*RS*TG+ 0.625*WS*TG* *(4.1)*

*Z[UTS_MPa] = 175.227+ 6.500*RS+ 4.900*WS+ 4.400*TG- 16.818*RS*RS- 11.818* WS*WS- 17.318*TG*TG+ 1.875*RS*WS+ 0.125*RS*TG+ 0.125*WS*TG* *(4.2)*

*Z[Ha_VHN]=126.627- 2.400*RS+ 2.500*WS- 0.800*TG- 14.318*RS*RS- 8.818*WS* WS- 9.318*TG*TG+ 1.000*RS*WS+ 0.250*RS*TG+ 0.000*WS*TG* (4.3)

*Z[%El] = 7.2036+ 0.0300*RS- 0.3100*WS- 0.2600*TG+ 0.5409*RS*RS +0.0409*WS *WS- 0.1091*TG*TG- 0.0250*RS*WS+ 0.0250*RS*TG- 0.0250*WS*TG* (4.4)

Table 4.26 exhibits a Comparison of yield strength, UTS, Hardness, and % elongation predicted by the RSM Model, with the experimentally determined values for friction stir welded composites. The largest inaccuracy from the data in Table 4.26 was 3.0%, indicating that the RSM model with quadratic terms and interaction terms is capable of making accurate predictions.

**Table 4.26** Comparison of experimentally determined yield strength, UTS, hardness, and %elongation values with the predicted values by the RSM Model for friction stir welded AA6061/3wt% rutile composite

| Sl No. | Yield Strength (MPa) | | | UTS (MPa) | | | Hardness (VHN) | | | % Elongation | | |
|---|---|---|---|---|---|---|---|---|---|---|---|---|
| | Expt | Pr | Error | Expt | Pr | Error | Expt | Pr | Error | Expt | Pr | Error |
| 1 | 99 | 100.9 | -1.9% | 142 | 143.1 | -0.8% | 107 | 107.4 | -0.4% | 7.4 | 7.5 | -1.0% |
| 2 | 99 | 100.0 | -1.0% | 139 | 138.9 | 0.1% | 105 | 104.3 | 0.6% | 7.3 | 7.3 | -0.3% |
| 3 | 95 | 96.0 | -1.0% | 136 | 136.9 | -0.7% | 106 | 106.8 | -0.8% | 7.6 | 7.7 | -1.1% |
| 4 | 101 | 101.3 | -0.3% | 145 | 146.5 | -1.0% | 110 | 111.8 | -1.6% | 7.1 | 7.1 | -0.2% |
| 5 | 102 | 103.9 | -1.9% | 145 | 146.3 | -0.9% | 97 | 97.6 | -0.6% | 8.1 | 8.2 | -0.6% |
| 6 | 106 | 108.6 | -2.4% | 151 | 151.9 | -0.6% | 115 | 114.7 | 0.3% | 7.7 | 7.7 | -0.2% |

### 4.12.3 Summary

The joining of AA6061/3wt% rutile composites has been experimentally studied to determine the impact of FSW process parameters on output responses.

- The developed RSM model has generated very reasonable predictions for the output of FSW operation, which is supported by the validation experiments.
- The single response can be predicted using the RSM technique, which lessens the significance of the other responses. Therefore, if there are multiple responses, it is recommended to use multi-objective optimization.

Multi-objective optimization is the process of finding the most appropriate solution for multiple objective functions (deals with more than one objective function). The majority of optimization issues involve multiple objectives. Numerous objective functions that must be minimized or maximized make up a multi-objective function problem. All of the goals are significant; if one goal's solution is too extreme, it may be necessary to compromise on other goals. The optimum outcomes for the given problems within the restrictions can be achieved through the use of optimization. Here, a comparison of the GRA, Desirability Approach, and TLBO optimization techniques is made to determine the best optimization method.

## 4.13 GREY RELATIONAL ANALYSIS (GRA)

Deng (1989) proposed the Grey relational analysis, which is widely used to determine the degree of relationship between sequences via grey relational grading (Kuo et al. 2008a). Grey relation analysis is regarded as a "black-box" method that is typically used to pinpoint the core of a system that lacks information. To use this technique, information is divided into two categories: black for information that is lacking and white for abundant information. Grey simply refers to the information that is between these two categories of black and white. In other words, the information is considered to be grey since it is erratic and incomplete. As a result, the system with incomplete information is referred to as a grey system. The three terms that are particularly significant in the Grey phenomena are Grey System, Grey Number, and Grey Element. The element with only incomplete information is designated as Grey. The Grey number, according to the Grey system, is one with insufficient data. Similarly, the Grey relation is related to partial information. The term "black box" designates a system without inside information. In the case of discrete sequences, the Grey relation technique is typically applied to determine and examine the relational grade. The Grey relation analysis typically uses fewer data but analyses more variables, making it more advantageous than the statistical method.

### 4.13.1 Response Pre-processing

Since the unit and range of one response differ from the others, preprocessing of responses was necessary for GRA. When the scatter range of response is too large or

when the target direction of the response is different then also response preprocessing is to be carried out in GRA. Response preprocessing is a process of converting original responses into comparable values. Responses are to be normalized in the range of zero to one to make them comparable values using equation 4.5 (Kuo et al. 2008a; b). In the present study for all the responses namely Yield strength, UTS, hardness, and % elongation, the "larger the better" criteria were selected, as the quality of the weld was represented by higher values of these responses. The original values of responses were normalized as follows for the "larger the better" criteria and listed in Table 4.27.

$$p_i^*(k) = \frac{p_i(k) - min\, p_i(k)}{max\, p_i(k) - min\, p_i(k)} \qquad (4.5)$$

where, $p_i(k)$ and $p_i^*(k)$ are the values before and after response preprocessing, where i represents the experiment number and k represents the response. Further $\Delta_{oi}(k)$ represents the deviation of the normalized value $p_i^*(k)$, from the reference value $p_0^*(k)$. The calculation was done for all the experiments and responses as given in equation 4.6 (Kuo et al. 2008a; b).

$$\Delta_{oi}(k) = |p_0^*(k) - p_i^*(k)| \qquad (4.6)$$

### 4.13.2 Calculating Grey Relational Coefficient (GRC) and Grey Relational Grade (GRG)

A grey relational coefficient (GRC) was calculated using the values obtained after response preprocessing. GRC formulates the relationship between the actual normalized response values with the ideal values. The GRC can be calculated using equation 4.7.

$$\delta_i(k) = \frac{\Delta_{min} + \delta.\Delta_{max}}{\Delta_{0i}(k) + \delta.\Delta_{max}} \qquad (4.7)$$

Where $\Delta_{oi}(k)$ is the deviation of the normalized value $p_i^*(k)$, from the reference value $p_0^*(k)$, $\delta$ is a coefficient of identification (Kuo et al. 2008a). The value of $\delta$ is taken as 0.25 by considering the equal preference for all the variables. The GRC for each experiment was calculated and tabulated in Table 4.28.

After calculating GRC, Grey Relational Grade was obtained by taking the average of GRC corresponding to each experiment using equation 4.8 (Kuo et al.

2008a). The multiple response optimization of the process variables is based on the GRG.

$$\beta_i = \frac{1}{n}\sum_{k=1}^{n} \delta_i(k) \qquad (4.8)$$

Where $\delta_i(k)$ is the GRG for the ith experiment which varies from 1 to 9 and n is the number of responses. Table 4.28 lists the GRG for each experiment. The experiment which is nearer to the ideal normalized value shows a higher GRG.

**Table 4.27** Normalized Values of Responses

| Expt No. | Output Response | | | Normalized value | | |
|---|---|---|---|---|---|---|
| | YS (MPa) | UTS (MPa) | $H_v$ (VHN) | YS | UTS | $H_v$ |
| 1 | 80 | 116 | 96 | 0.0000 | 0.0000 | 0.2857 |
| 2 | 106 | 151 | 115 | 0.7027 | 0.7447 | 0.9643 |
| 3 | 93 | 130 | 97 | 0.3514 | 0.2979 | 0.3214 |
| 4 | 110 | 158 | 115 | 0.8108 | 0.8936 | 0.9643 |
| 5 | 117 | 163 | 116 | 1.0000 | 1.0000 | 1.0000 |
| 6 | 101 | 145 | 111 | 0.5676 | 0.6170 | 0.7857 |
| 7 | 95 | 133 | 88 | 0.4054 | 0.3617 | 0.0000 |
| 8 | 99 | 142 | 100 | 0.5135 | 0.5532 | 0.4286 |
| 9 | 110 | 160 | 105 | 0.8108 | 0.9362 | 0.6071 |

YS: Yield Strength; UTS: Ultimate Tensile Strength; $H_v$: Hardness

It was inferred from Table 4.28 that trial 5 yields a better multi-response value among the conducted trials since it possesses a higher GRG. It could be concluded from the present work that the multi-response optimization of FSW process variables of AMCs can be accomplished by transforming multi-responses into GRG.

The orthogonal experimental design helps to isolate the effect of each variable on the grey relational grade at various levels. For instance, the welding speed at three distinct levels was calculated by taking the mean of GRG for the trials [1,4,7], [2,5,8], and [3,6,9]. The impact of other parameters at various levels was computed and listed in

Table 4.29. A higher GRG implies that the product quality is closer to the best value. Therefore, for the best performance, a higher value of GRG was preferred.

**Table 4.28** Deviation Sequence, Grey Relational coefficient, Grey Relational Grade

| Expt No. | Deviation Sequence | | | Grey Relational Coefficient (GRC) | | | Grey Relational Grade (GRG) |
|---|---|---|---|---|---|---|---|
| | YS | UTS | $H_v$ | YS | UTS | $H_v$ | |
| 1 | 1.0000 | 1.0000 | 0.7143 | 0.2481 | 0.2481 | 0.3160 | 0.2707 |
| 2 | 0.2973 | 0.2553 | 0.0357 | 0.5261 | 0.5638 | 0.9023 | 0.6641 |
| 3 | 0.6486 | 0.7021 | 0.6786 | 0.3372 | 0.3197 | 0.3272 | 0.3280 |
| 4 | 0.1892 | 0.1064 | 0.0357 | 0.6356 | 0.7562 | 0.9023 | 0.7647 |
| 5 | 0.0000 | 0.0000 | 0.0000 | 1.0000 | 1.0000 | 1.0000 | 1.0000 |
| 6 | 0.4324 | 0.3830 | 0.2143 | 0.4328 | 0.4628 | 0.6063 | 0.5007 |
| 7 | 0.5946 | 0.6383 | 1.0000 | 0.3569 | 0.3408 | 0.2481 | 0.3153 |
| 8 | 0.4865 | 0.4468 | 0.5714 | 0.4042 | 0.4248 | 0.3661 | 0.3984 |
| 9 | 0.1892 | 0.0638 | 0.3929 | 0.6356 | 0.8379 | 0.4565 | 0.6434 |

YS: Yield Strength; UTS: Ultimate Tensile Strength; $H_v$: Hardness

**Table 4.29** Grey Relational Grade (GRG) Response Table

| Level | Rotational Speed | Welding Speed | Tool Geometry |
|---|---|---|---|
| 1 | 0.4210 | 0.4503 | 0.3899 |
| 2 | 0.7551* | 0.6875* | 0.6907* |
| 3 | 0.4523 | 0.4907 | 0.5478 |
| Delta | 0.3342 | 0.2372 | 0.3008 |
| Rank | 1 | 3 | 2 |

The total mean value of the GRG = 0.5428, * Optimum GRG levels.

The main effect plot of GRG for each process variable was depicted in Figure 4.45. Considering larger GRG, the optimal level of variables for better mechanical properties is rotational speed at level 2, welding speed at level 2, and tool geometry at level 2, i.e., 1000rpm, 75mm/min, and combined square and threaded cylindrical pin.

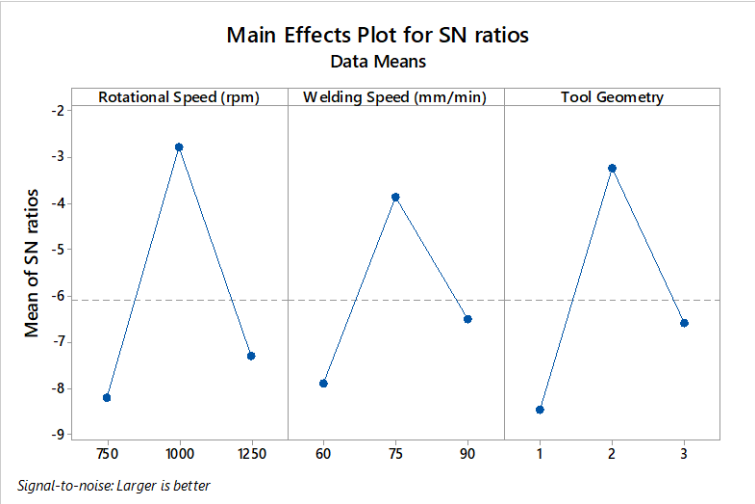


**Figure 4.45** Main effect plot for grey relational grade

### 4.13.3 Validation Test

To validate the improvement in the responses based on GRG results, a confirmation trial was performed using optimum levels of variables obtained from the TGRA. The output responses of the welded specimens were measured and tabulated. As shown in Table 4.30, a joint formed at the optimum value of the process parameter exhibits better mechanical properties than the specimen obtained at trial no.5 which had a higher GRG. This proves that TGRA can be effectively applied for the multi-response optimization of FSW of composites.

**Table 4.30** Response values of the joint at trial 5 and with optimal process variables

| Experiment No. | Rotational Speed(rpm) | Welding Speed (mm/min) | Tool Geometry | YS (MPa) | UTS (MPa) | $H_v$ (VHN) |
|---|---|---|---|---|---|---|
| 5 | 1000 | 75 | SQ | 117 | 163 | 116 |
| Optimum Value | 1000 | 75 | CSTC | 128 | 176 | 126 |

YS: Yield Strength; UTS: Ultimate Tensile Strength; $H_v$: Hardness

Related Article: Prabhu, S. R., Shettigar, A., Herbert, M. A., and Rao, S. S. (2022). "Optimization of FSW process parameters for maximum UTS of AA6061/rutile composites using Taguchi technique." *Sci. Iran.*, 29(2 B), 534–542.

### 4.13.4 Analysis of variance (ANOVA)

The effects of each process variable on welding behaviour were evaluated using ANOVA for the produced GRG data. The results are displayed in Table 4.31. It was found that the chosen process parameters welding speed exhibited the highest contribution to the responses followed by rotational speed and tool geometry respectively.

**Table 4.31** ANOVA of GRG

| Source | DF | Seq SS | Adj SS | Adj MS | F | P | % Contribution |
|---|---|---|---|---|---|---|---|
| Rotational Speed | 2 | 0.5956 | 0.5956 | 0.2978 | 268 | 0.004 | 36.41 |
| Welding Speed | 2 | 0.6022 | 0.6022 | 0.3011 | 271 | 0.004 | 36.82 |
| Tool Geometry | 2 | 0.4356 | 0.4356 | 0.2178 | 196 | 0.005 | 26.63 |
| Residual Error | 2 | 0.0022 | 0.0022 | 0.0011 | | | 0.14 |
| Total | 8 | 1.6356 | | | | | |

## 4.14 DESIRABILITY APPROACH FOR OPTIMIZATION

The optimization criteria must first be determined to do multi-characteristic optimization using the desirability approach. The main purpose of optimization is to maximize yield strength, ultimate tensile strength, and hardness. The input parameters rotational speed and welding speed are used in coded form by assigning values -1 to the minimum value and +1 to the maximum value. In the case of tool geometries, threaded cylindrical was assigned with -1, CSTC tool with zero, and square tool with value +1. Figure 4.46 shows the optimum values of process parameters and corresponding output responses. In the current study, it is observed that as the rotational speed increases the UTS increases initially, then it starts decreasing due to the turbulent material flow. The distribution of hardness in the various weld area regions is closely related to the UTS of the joint.

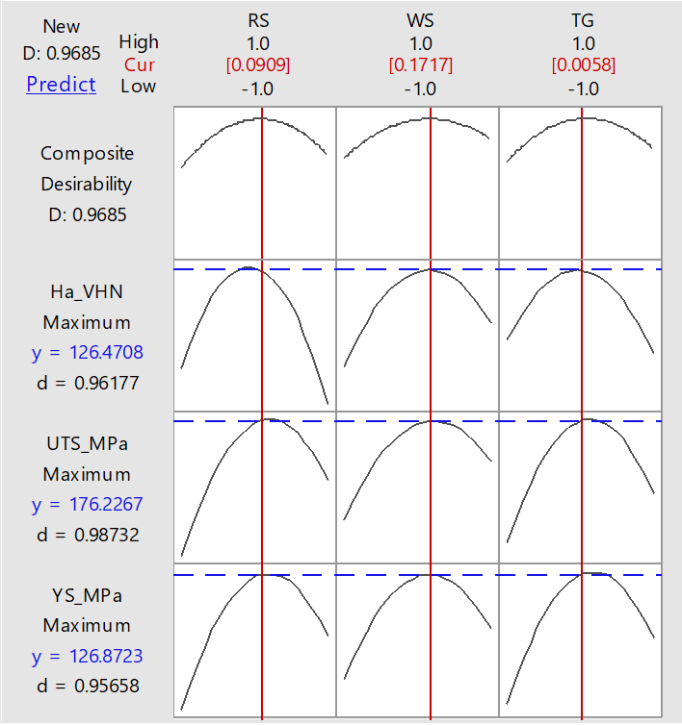


**Figure 4.46** Desirability optimization for FS welded AA6061/Rutile composite.

### 4.14.1 Validation Test

To validate the results of RSM, a confirmation trial was performed using optimum levels of variables obtained from the RSM. The output responses of the welded specimens were measured and tabulated. As shown in Table 4.32, a joint formed at the optimum value of the process parameter exhibits better mechanical properties than the specimen obtained by using the process parameter values suggested by TGRA. This proves that RSM can be effectively applied for the multi-response optimization of FSW of composites.

**Table 4.32** Response values of the joint at trial 5, joints using TGRA using DA

| Expt No. | Rotational Speed (rpm) | Welding Speed (mm/min) | Tool Geometry | YS (MPa) | UTS (MPa) | $H_v$ (VHN) |
|---|---|---|---|---|---|---|
| 5 | 1000 | 75 | SQ | 117 | 163 | 116 |
| Optimum Value | 1000 | 75 | CSTC | 126 | 175 | 125 |
| Optimum Value -DA | 1022.75 | 77.6 | CSTC | 126.9 | 176.2 | 126.5 |
| Experiment value | 1023 | 78 | CSTC | 127 | 176 | 126 |

YS: Yield Strength; UTS: Ultimate Tensile Strength; $H_v$: Hardness

### 4.15 TLBO

The present study considers both single-objective and multi-objective optimization of yield strength, hardness, and UTS. The TLBO algorithm employed the mathematical models created by RSM as a fitness function.

The second-order regression models for yield strength, UTS and hardness are obtained by using equations 4.1 to 4.3 respectively. These regression models are used for a single objective and multi-objective optimization using the TLBO as fitness functions.

MATLAB R2019b software was used to develop the TLBO algorithm. TLBO requires only the size of the population and the total number of iterations to develop the algorithm. The size of the population for the current study was fixed as 20 and the number of iterations as 50. The result of the TLBO is shown in Table 4.33.

**Table 4.33** TLBO algorithm predictions and the experimental values

| Response function optimized | TLBO algorithm estimations | | | | Experimental values | | | | Error % |
|---|---|---|---|---|---|---|---|---|---|
| | FSW process variables | | | Response value | FSW process variables | | | Response values | |
| | RS | WS | TG | | RS | WS | TG | | |
| YS(MPa) | 1047.9 | 77.6 | ~CSTC | 127.37 | 1050 | 78 | CSTC | 126 | 1.08 |
| UTS(MPa) | 1051.8 | 78.4 | ~CSTC | 176.73 | 1050 | 78 | CSTC | 174 | 1.54 |
| $H_v$(VHN) | 979.3 | 77 | ~CSTC | 126.92 | 980 | 78 | CSTC | 127 | 0.06 |

RS:Rotational Speed (rpm); WS: Welding Speed (mm/min); TG: Tool Geometry; YS: Yield Strength; UTS: Ultimate Tensile Strength; Hv: Hardness

**Related Article: Prabhu, S. R., Shettigar, A., Herbert, M. A., and Rao, S. S.** (2022). "Parameter investigation and optimization of friction stir welded AA6061/TiO2 composites through TLBO." *Weld. World*, 66(1), 93–103.

### 4.15.1 Validation

An optimal combination of FSW process variables was obtained from equations 4.1, 4.2, and 4.3 for output responses YS, UTS, and hardness respectively using the TLBO algorithm. Confirmation tests were performed to validate the results. Three friction stir weld samples were prepared using a close range of process variables obtained from the TLBO algorithm to validate its performance. Table 4.33 compares the output responses obtained from the TLBO algorithm with the response values obtained from the experiments. As three samples were prepared to have a close range of process parameters, the mean value of each of the output responses were considered for comparison with estimated response values. From the confirmation test, it can be confirmed that the developed models are acceptable to optimize the FSW process variable values to join AA6061/$TiO_2$ composite, using the TLBO algorithm.

### 4.15.2 Multi-objective optimization using TLBO

Here several objectives (either minimizing or maximizing) are optimized simultaneously satisfying a group of constraints. It is important to find a relative preference factor for multiple objectives based on which a composite fitness function is constructed as a weighted summation of normalized individual objectives. This converts a multi-objective optimization problem into an optimization problem with a single objective. Formulated combined fitness function is then optimized to obtain one trade-off solution.

The single-objective optimization results of the studied FSW process show that distinct parametric settings are obtained for various responses according to the use of algorithms. However, it is never conceivable for an operator to establish the FSW process parameters at various operating levels in a single FSW setup in a real-time welding environment.

Deriving a special combination of the process parameters is therefore usually advocated to simultaneously maximize all four responses. To do this, the following multi-objective optimization model is created, and the TLBO is then used to solve it.

In this investigation, single-objective functions are formulated as given in Eqs. 4.1 to 4.3. A multi-response optimization function is created by combining the single-objective functions mentioned above. The normalized multi-objective fitness function

was developed by giving each of these objectives equal weights as shown in Equation 4.9.

$$Maximize\ f(x) = [w1 * Y\ (Yield\ strength) / Yield\ strength\ (max)] + [w2 * Y\ (UTS) / UTS\ (max)] + [w3 * Y\ (Hardness) / Hardness\ (max)] + [w4 * Y\ (\%\ Elongation) / \%\ Elongation\ (max)] \quad (4.9)$$

where $w1$, $w2$, *and* $w3$ are the weights allotted to yield strength, UTS, and Hardness respectively. Yield strength (max), UTS (max), and Hardness (Max)) are the maximum value of the respective responses. These values are derived from the outcomes of the single-objective optimization of the responses. Equal weight is given to each response that is taken into account. Table 4.34 provides the solutions to this multi-objective optimization problem.

**Table 4.34** Comparison of Optimized process parameter and Output response values.

| Experiment Detail | Rotational Speed (rpm) | Welding Speed (mm/min) | Tool Geometry | YS (MPa) | UTS (MPa) | $H_v$ (VHN) |
|---|---|---|---|---|---|---|
| Optimum Value from L9 OA | 1000 | 75 | SQ | 117 | 163 | 116 |
| Optimum Value from GRA | 1000 | 75 | CSTC | 126 | 175 | 125 |
| Optimum Value from DA | 1022.75 | 77.6 | CSTC | 126.9 | 176.2 | 126.5 |
| Optimum Value from TLBO | 1024.15 | 77.6055 | ~CSTC | 126.9 | 176.3 | 126.5 |
| Experiment Value | 1025 | 78 | ~CSTC | 127 | 177 | 126 |

YS: Yield Strength; UTS: Ultimate Tensile Strength; $H_v$: Hardness

### 4.15.3 Summary of the optimization results

This part covered both conventional and novel optimization algorithms, including TLBO, desirability approach, and grey relational analysis. To compare the correlation between the input variables and output responses, the quadratic regression model has been designed. The TLBO method used the mathematical models created by the RSM

approach as a fitness function to optimize the welding parameters. The analysis leads to the following conclusions:

- Based on the TGRA, Desirability approach, and TLBO optimization technique, optimized process parameters were developed.
- It can be inferred from statistical (Desirability and GRA) and evolutionary (TLBO) optimization methodologies that the latter approach produces superior outcomes for the considered problem.

## 4.16 PREDICTION OF THE FSW PROCESS USING GA MLPNN

In this section, intelligent GA-MLPNN-based prediction algorithms for FSW operations are discussed. FSW is carried out at different rotational speeds, welding speeds, and tool geometries. 74% of the data gathered during experimentation are used to train the model, while the remaining data are utilized to test and validate it. The formulation of the GA-MLPNN model for prediction of yield strength, UTS, and Hardness of friction stir welded AA6061-3wt% rutile composite has been discussed in this chapter.

Linear regression plotting of the overall output of GA-MLPNN is shown in Figure 4.47. The small circles in the plot indicate the input data. The data has a decent fit and the co-efficient of Target is nearly equal to 1 which shows that this GA-MLPNN has excellent performance. The constant term in the y-axis of Figure 4.47 indicates it is the error or the residue. The error is added to scale the Target to keep it as close to the predicted output as possible. Ideally, it should be zero, here from Figure 4.47 the overall value of error is 0.65. This shows that the GA-MLPNN prediction is good. From Figure 4.48 it can be concluded that validation and test curve are remarkably similar hence they do not indicate any major problems with training. From Table 4.35 and Figures 4.49 to 4.52, it has been inferred that GA-MLPNN is better than MLPNN. From Tables 4.36 and 4.37, it has been observed that the average error in yield strength using MLPNN was 0.452 whereas GA-MLPNN was 0.111. Similarly, the prediction of UTS using MLPNN has an error of 0.644 whereas MLPNN-GA has 0.222. During the prediction of hardness, the error value in the case of MLPNN was 0.343 whereas the GA-MLPNN error was 0.010. Similarly, in the prediction of %elongation, the MLPNN error value was 0.057 whereas the GA-MLPNN error was 0.005. This shows that

combined prediction with GA-MLPNN is much better than prediction with MLPNN alone.

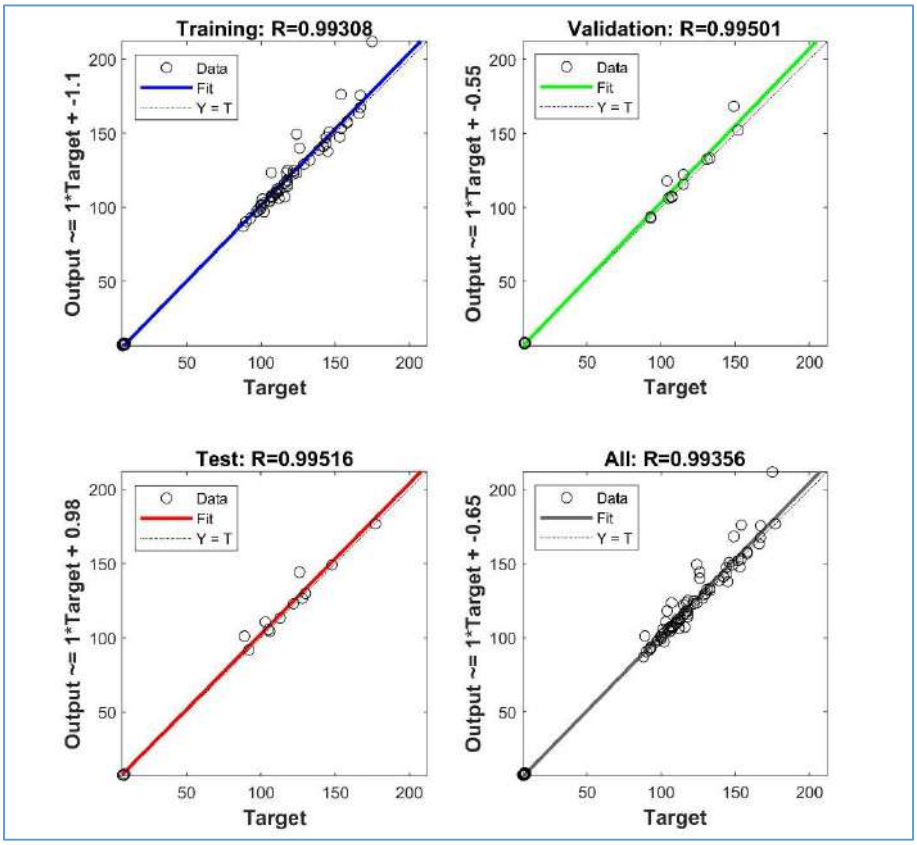


**Figure 4.47** Regression plot of GA-MLPNN

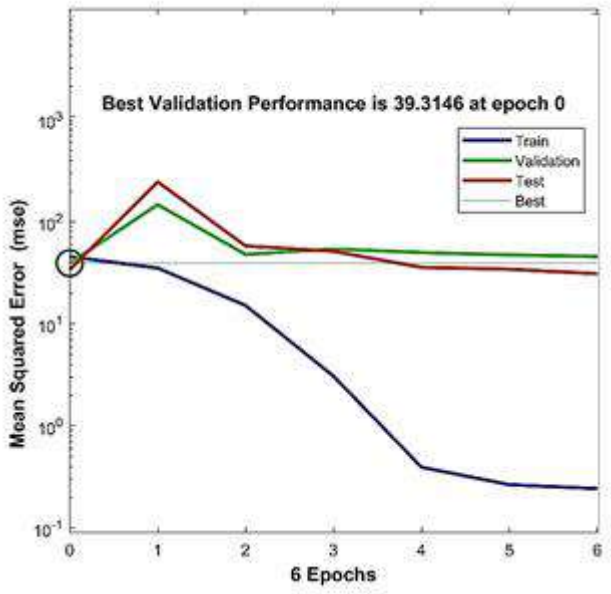


**Figure 4.48** MSE plot of train, test, and validation data.

**Table 4.35** Experimental Data

| Sl No | Rotational Speed (rpm) | Welding Speed (mm/min) | Tool Geometry | YS (MPa) | UTS (MPa) | $H_v$ (VHN) | % El. |
|---|---|---|---|---|---|---|---|
| 1 | 750 | 60 | TC | 80 | 116 | 96 | 8.2 |
| 2 | 750 | 75 | TC | 91 | 130 | 107 | 7.9 |
| 3 | 750 | 90 | TC | 84 | 122 | 99 | 7.7 |
| 4 | 1000 | 60 | TC | 95 | 136 | 106 | 7.6 |
| 5 | 1000 | 75 | TC | 106 | 152 | 118 | 7.3 |
| 6 | 1000 | 90 | TC | 101 | 145 | 110 | 7.1 |
| 7 | 1250 | 60 | TC | 88 | 125 | 89 | 8.3 |
| 8 | 1250 | 75 | TC | 99 | 142 | 100 | 8 |
| 9 | 1250 | 90 | TC | 94 | 138 | 96 | 7.6 |
| 10 | 750 | 60 | CSTC | 94 | 135 | 104 | 8.1 |
| 11 | 750 | 75 | CSTC | 106 | 151 | 115 | 7.7 |
| 12 | 750 | 90 | CSTC | 99 | 142 | 107 | 7.4 |
| 13 | 1000 | 60 | CSTC | 110 | 158 | 115 | 7.5 |
| 14 | 1000 | 75 | CSTC | 128 | 176 | 126 | 7.1 |
| 15 | 1000 | 90 | CSTC | 118 | 168 | 120 | 7 |
| 16 | 1250 | 60 | CSTC | 102 | 145 | 97 | 8.1 |
| 17 | 1250 | 75 | CSTC | 117 | 165 | 109 | 7.8 |
| 18 | 1250 | 90 | CSTC | 110 | 160 | 105 | 7.5 |
| 19 | 750 | 60 | SQ | 87 | 124 | 94 | 7.7 |
| 20 | 750 | 75 | SQ | 99 | 139 | 105 | 7.3 |
| 21 | 750 | 90 | SQ | 93 | 130 | 97 | 7 |
| 22 | 1000 | 60 | SQ | 102 | 145 | 105 | 7.2 |
| 23 | 1000 | 75 | SQ | 117 | 163 | 116 | 6.9 |
| 24 | 1000 | 90 | SQ | 110 | 155 | 109 | 6.7 |
| 25 | 1250 | 60 | SQ | 95 | 133 | 88 | 7.8 |
| 26 | 1250 | 75 | SQ | 108 | 151 | 99 | 7.3 |
| 27 | 1250 | 90 | SQ | 104 | 147 | 95 | 7.1 |

YS: Yield Strength; UTS: Ultimate Tensile Strength; $H_v$: Hardness; El: Elongation

**Table 4.36** Predicted values and corresponding Error from MLPNN

| YS (MPa) | Error | UTS (MPa) | Error | $H_v$ (VHN) | Error | % Elongation | Error |
|---|---|---|---|---|---|---|---|
| 81.45 | 1.82% | 116.54 | 0.47% | 97.25 | 1.30% | 8.44 | 2.95% |
| 91.46 | 0.51% | 131.59 | 1.22% | 108.36 | 1.27% | 7.81 | -1.12% |
| 85.12 | 1.33% | 124.29 | 1.88% | 99.27 | 0.27% | 7.62 | -1.01% |
| 95.13 | 0.14% | 135.35 | -0.48% | 105.14 | -0.82% | 7.55 | -0.67% |
| 108.05 | 1.94% | 152.05 | 0.03% | 116.68 | -1.12% | 7.40 | 1.36% |
| 100.20 | -0.79% | 146.68 | 1.16% | 111.05 | 0.96% | 7.28 | 2.60% |
| 88.47 | 0.53% | 125.17 | 0.14% | 90.19 | 1.34% | 8.27 | -0.33% |
| 98.82 | -0.18% | 142.36 | 0.25% | 99.40 | -0.60% | 8.00 | -0.05% |
| 95.79 | 1.91% | 137.46 | -0.39% | 96.50 | 0.52% | 7.62 | 0.31% |
| 95.38 | 1.47% | 137.77 | 2.05% | 103.49 | -0.49% | 8.28 | 2.19% |
| 107.38 | 1.31% | 151.12 | 0.08% | 116.03 | 0.90% | 8.07 | 4.77% |
| 98.85 | -0.15% | 141.76 | -0.17% | 107.59 | 0.55% | 7.52 | 1.61% |
| 109.43 | -0.51% | 157.41 | -0.38% | 114.54 | -0.40% | 7.44 | -0.83% |
| 129.00 | 0.78% | 175.27 | -0.42% | 127.28 | 1.02% | 7.21 | 1.53% |
| 117.60 | -0.34% | 168.93 | 0.55% | 119.35 | -0.54% | 7.00 | 0.06% |
| 103.12 | 1.10% | 146.16 | 0.80% | 97.38 | 0.39% | 8.06 | -0.47% |
| 116.78 | -0.19% | 165.45 | 0.27% | 108.03 | -0.89% | 7.94 | 1.78% |
| 110.78 | 0.71% | 161.29 | 0.81% | 105.45 | 0.43% | 7.46 | -0.59% |
| 86.30 | -0.81% | 123.88 | -0.10% | 94.95 | 1.01% | 7.82 | 1.51% |
| 98.96 | -0.04% | 140.93 | 1.39% | 105.77 | 0.73% | 7.03 | -3.66% |
| 94.53 | 1.64% | 132.33 | 1.79% | 96.41 | -0.60% | 6.84 | -2.22% |
| 101.80 | -0.19% | 145.59 | 0.41% | 106.08 | 1.03% | 7.21 | 0.18% |
| 116.91 | -0.07% | 163.20 | 0.12% | 116.37 | 0.32% | 6.88 | -0.29% |
| 110.42 | 0.38% | 155.81 | 0.52% | 110.42 | 1.31% | 6.76 | 0.84% |
| 94.85 | -0.16% | 133.10 | 0.07% | 87.76 | -0.27% | 8.06 | 3.36% |
| 108.73 | 0.68% | 151.63 | 0.42% | 99.20 | 0.20% | 7.60 | 4.05% |
| 103.46 | -0.52% | 146.12 | -0.60% | 95.50 | 0.53% | 7.21 | 1.51% |

YS: Yield Strength; UTS: Ultimate Tensile Strength; $H_v$: Hardness

**Table 4.37** Predicted values and corresponding Error from GA-MLPNN

| YS (Mpa) | Error | UTS (MPa) | Error | $H_v$ (VHN) | Error | % Elongation | Error |
|---|---|---|---|---|---|---|---|
| 79.53 | -0.58% | 115.22 | -0.67% | 95.48 | -0.54% | 8.27 | 0.85% |
| 90.72 | -0.31% | 129.00 | -0.77% | 108.11 | 1.04% | 7.84 | -0.78% |
| 85.14 | 1.36% | 123.06 | 0.87% | 98.46 | -0.55% | 7.68 | -0.29% |
| 93.90 | -1.16% | 134.56 | -1.06% | 107.54 | 1.45% | 7.68 | 1.08% |
| 107.54 | 1.45% | 152.61 | 0.40% | 116.44 | -1.32% | 7.33 | 0.48% |
| 100.01 | -0.98% | 146.21 | 0.83% | 112.43 | 2.21% | 7.05 | -0.66% |
| 86.54 | -1.66% | 123.59 | -1.13% | 90.63 | 1.83% | 8.26 | -0.53% |
| 99.99 | 1.00% | 143.30 | 0.91% | 99.66 | -0.34% | 7.99 | -0.08% |
| 94.73 | 0.77% | 138.37 | 0.27% | 96.69 | 0.72% | 7.65 | 0.64% |
| 93.31 | -0.74% | 133.47 | -1.13% | 102.70 | -1.25% | 8.09 | -0.13% |
| 105.35 | -0.62% | 150.76 | -0.16% | 117.02 | 1.76% | 7.76 | 0.76% |
| 100.75 | 1.76% | 143.49 | 1.05% | 107.56 | 0.53% | 7.47 | 1.00% |
| 110.29 | 0.27% | 157.59 | -0.26% | 114.37 | -0.55% | 7.53 | 0.43% |
| 127.92 | -0.06% | 175.26 | -0.42% | 125.66 | -0.27% | 7.09 | -0.15% |
| 117.06 | -0.80% | 168.52 | 0.31% | 120.29 | 0.24% | 6.91 | -1.25% |
| 100.58 | -1.39% | 144.56 | -0.30% | 97.05 | 0.05% | 8.14 | 0.51% |
| 116.91 | -0.07% | 163.53 | -0.89% | 109.35 | 0.33% | 7.78 | -0.21% |
| 111.68 | 1.53% | 162.56 | 1.60% | 102.40 | -2.48% | 7.49 | -0.14% |
| 88.11 | 1.28% | 126.27 | 1.83% | 95.38 | 1.47% | 7.66 | -0.46% |
| 98.82 | -0.18% | 140.36 | 0.98% | 106.04 | 0.99% | 7.24 | -0.82% |
| 91.22 | -1.91% | 132.46 | 1.89% | 97.92 | 0.95% | 7.06 | 0.91% |
| 103.73 | 1.70% | 146.98 | 1.36% | 107.34 | 2.23% | 7.10 | -1.42% |
| 116.05 | -0.82% | 162.53 | -0.29% | 110.82 | -4.46% | 6.94 | 0.60% |
| 110.63 | 0.58% | 153.70 | -0.84% | 107.67 | -1.22% | 6.76 | 0.96% |
| 97.00 | 2.11% | 134.71 | 1.28% | 87.54 | -0.52% | 7.78 | -0.20% |
| 107.68 | -0.30% | 151.55 | 0.37% | 99.50 | 0.51% | 7.32 | 0.27% |
| 104.93 | 0.89% | 144.07 | -1.99% | 93.30 | -1.79% | 7.13 | 0.36% |

YS: Yield Strength; UTS: Ultimate Tensile Strength; $H_v$: Hardness

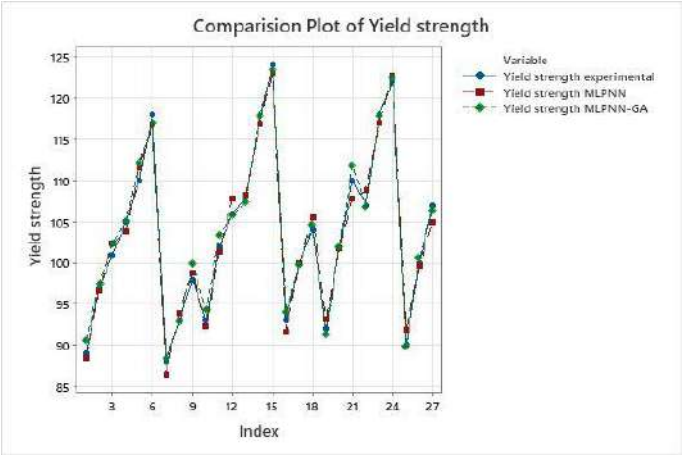


**Figure 4.49** Time Series Plot of Yield strength experimental, Yield strength MLPNN, Yield strength GA-MLPNN

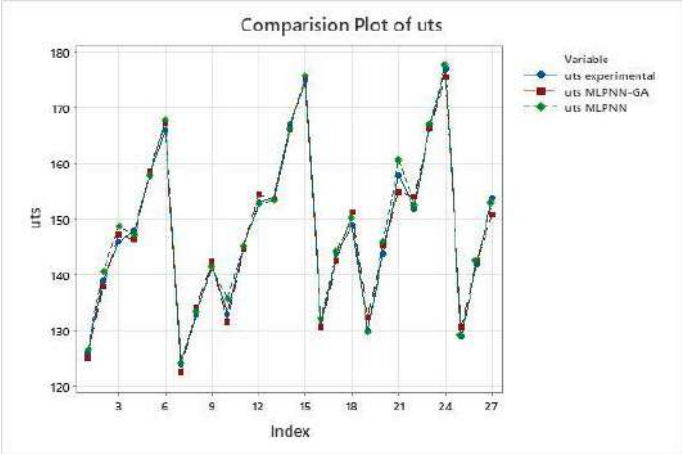


**Figure 4.50** Time Series Plot of UTS experimental, UTS MLPNN, UTS GA-MLPNN

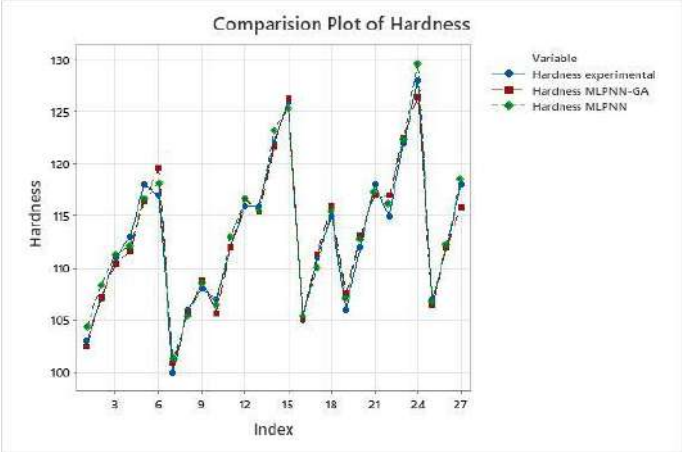


**Figure 4.51** Time Series Plot of Hardness experimental, Hardness MLPNN, Hardness GA-MLPNN

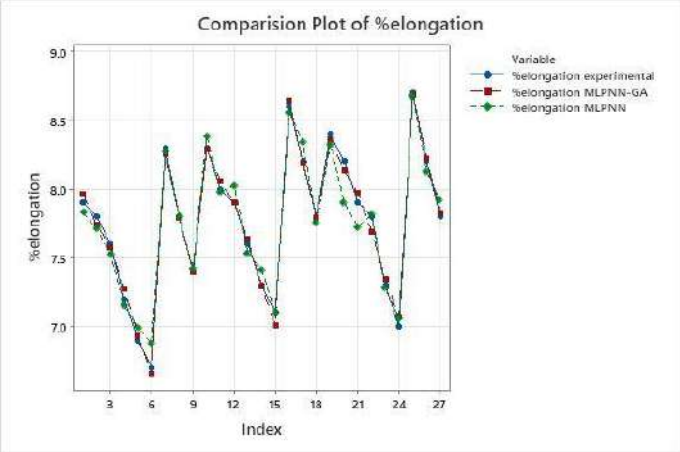


**Figure 4.52** Time Series Plot of %elongation experimental, % elongation MLPNN, % elongation GA-MLPNN

## 4.17 SUMMARY OF THE RESULTS

### 4.17.1 Characterization of as-cast AA6061-3(wt%) rutile composites

1. The X-Ray Diffraction (XRD) analysis of as-cast AA6061-3(wt%) rutile composites indicated the absence of peaks corresponding to intermetallic phases.
2. The SEM examination of as-cast AA6061-3 (wt%) rutile composite exhibited a dendrite structure. Measured mechanical properties of the as-cast composite were:- Vickers hardness value of 84±3 VHN, yield strength of 130 ± 4 MPa, Ultimate tensile strength is 190 ± 6 MPa, and percentage elongation of 9.5±0.2%.
3. Tear ridges were observed on the fracture surface of the AA6061-3 (wt%) rutile composite confirming ductile fracture.

### 4.17.2 Friction stir welding of AA6061 -3(wt%) rutile composites

Utilizing three different types of tools, friction stir welding of AA6061-3(wt%) rutile composite was done at various rotational and welding speed combinations. To analyze the impact of process parameters, the microstructure and mechanical characteristics of the welded specimens were examined. From this- the following conclusions are arrived.

**A. Macrostructural and Microstructural characterization of Friction Stir Welded AA6061-3 (wt%) Rutile composite:**

Based on the macro-structural analysis and micro-structural analysis, the effect of operational parameters on the joint qualities of AA6061-3 (wt%) Rutile composites during FSW has been explored.

1. Examining FS welded composite joints formed using threaded probe profiles revealed that defects were produced at rotational speeds greater than 1250 rpm and less than or equal to 500 rpm. Similar defects were seen when the tool traverse speed was more than 100 mm/min or less than 50 mm/min.
2. The investigation of the FS welded composites using a combined square and threaded probe profile has shown the ensuing outcomes: -
    a. Pinhole defects have been observed when the rotational speed is less than or equal to 500 rpm and the tool traverse speed is less than 50 mm/min. Wormholes were found when the rotating speed was less than 500 rpm and the tool traverse speed was greater than 100 mm/min.
    b. When the rotational speed is more than 1250 rpm and the welding speed is less than 50 mm/min and more than 100 mm/min, tunnel holes were seen in the weld zone. The process parameter window that gives defect-free welds was slightly narrower than the window obtained for the TC tool.
3. The results of the examination of the FS welded composites utilizing a square probe profile are displayed below: -
    a. For rotational speeds of less than 750 rpm and tool traverse speeds of less than 50 mm/min, pinhole defects were developed. Similarly, for a rotational speed of 750 rpm and a tool traverse speed of more than 100 mm/min wormhole defects were observed.
    b. When the rotational speed is more than 1250 rpm and the welding speed is less than 50 mm/min, pinhole, and wormhole defects are observed. When the rotational speed is more than 1250 rpm and the tool traverse speed exceeds 100 mm/min, tunnel holes, and wormholes were detected. The quality of the welds produced by the square profile probe is identical to that of the CSTC tool.

From the macro structural investigation, it can be concluded that the process parameter window to get defect-free weld during the FSW process is wider in the case of threaded cylindrical tools and narrower for tools with square pin. The parameter window for the combined square and threaded cylindrical pin was in between of square and threaded cylindrical pin. Presence of thread on the pin guides and assist the plasticized material to flow from front to back as well as from top to bottom of the pin. Proper material flow and consolidation of the material in the weld region reduces the weld defects, thereby widening the process parameter window to get quality weld.

4. The following results have been drawn from the microstructural characterization of the welded zone of the composite FS welded employing TC, SQ, and CSTC tools.:
    a. The microstructure of the FS Welded zone of the composite is divided into four distinct regions. Namely, i) Base material, ii) HAZ, iii) TMAZ, and vi) NZ.
    b. Fine recrystallized and equiaxed grains with a size range of 2 to 7 μm were observed in the NZ. The rutile particles were distributed uniformly in the NZ Due to the tool's stirring action and the collision of hard particles with one another, the size of the rutile particles was reduced.
    c. Extremely deformed, elongated grains were seen in the TMAZ region, along with the rutile particles which are distributed in parallel bands.
    d. At HAZ coarse grains were present due to the thermal cycle developed during the FSW process.
    e. In comparison to the Nugget zone's bottom part, the top region's grain size was larger.
    f. Smaller or finer grains were observed in the NZ of the FSW joint produced using the CSTC tool compared to the other tool profiles.

## B. Mechanical Properties of FS Welded AA6061-3 (wt%) Rutile Composites

### 1. Hardness

1. The cross-section of the welded junction revealed a W-shaped pattern of hardness distribution.

2. The highest hardness is attained at NZ regardless of tool rotational speed, tool traverse speed, and tool probe geometries.
3. Regardless of the tool probe geometries, the highest hardness at the Nugget Zone of FS welded composite was achieved at rotational speeds of 1000 rpm and a tool traverse speed of 75 mm/min. Similar to this, regardless of the tool probe geometries, the minimum hardness of the composites at the nugget zone was achieved at rotational speeds of 1250 rpm and a tool traverse speed of 60 mm/min. Below is a discussion of the hardness attained for various tool probe geometries.: -
    a. **TC tool :**

       The minimum and maximum hardness at the nugget zone of FS welded AA6061-3 (wt%) Rutile composite is 78 VHN and 118 VHN respectively.
    b. **CSTC tool :**

       The minimum and maximum hardness at the nugget zone of FS welded AA6061-3 (wt%) Rutile composite is 77 VHN and 128 VHN respectively.
    c. **SQ tool:**

       The minimum and maximum hardness at the nugget zone of FS welded AA6061-3 (wt%) Rutile composite is 76 VHN and 116 VHN respectively.
4. In the hardness distribution profile of the welded composite, the annealing effect causes the lowest hardness at HAZ.
5. Compared to the specimens welded with the SQ and TC tools, the CSTC tool demonstrated increased hardness.

**2. Tensile strength**

The Following conclusions were drawn from the result of the tensile test of FS welded AA6061-3 (wt%) rutile composites:

1. Regardless of tool rotational speed, tool traverse speed, and tool probe geometries, the tensile test of the FS welded composite, performed normal

to the weld axis revealed that fracture along the parent material/FSW zone interface, on the advancing side of the joint.

2. The ductile fracture was discovered through microscopic analysis of the fracture surfaces. It can be identified by the development of significant tear ridges and dimples on the fracture surface.
3. Regardless of the tool probe geometries, the maximum UTS has been achieved for a rotational speed and tool traverse speed of 1000 rpm and 75 mm/min respectively.
4. Small dimples were visible on the fractured surface of FSW composites that tested along the weld line and the rutile particles were observed at the bottom of these dimples

**i. TC tool**

1. An increase in the tensile strength is shown when the tool traverse speed is increased from 60 to 75 mm/min while maintaining a constant rotational speed. Tensile strength falls when the tool traverse speed rises to 90 mm/min.
2. Tensile strength is observed to be rising for a constant welding speed of 60, 75, or 90 mm/min and a raise in rotational speed to 1000 rpm from 750. Tensile strength begins to fall when rotational speed increases beyond 1000 rpm.
3. For a tool traverse speed of 75 mm/min and a rotational speed of 1000 rpm, FSW of AA6061-3(wt%) rutile composite produced a maximum joint efficiency of 75%
4. The joint efficiency rose by 15 % when the tensile test was carried out along the weld direction

**ii. CSTC tool**

1. An improvement in tensile strength is seen when the tool traverse speed is increased from 60 to 75 mm/min while maintaining a constant rotational speed. The tensile strength falls when the welding speed rises to 90 mm/min.
2. An improvement in tensile strength is noted with a constant tool traverse speed of 60, 75, or 90 mm/min and a rotational speed increase from 750

to 1000 rpm. Tensile strength falls when rotational speed rises to 1250 rpm.

3. The maximum joint efficiency of FS welded AA6061-3 (wt%) Rutile was 93 % for a rotational speed and welding speed of 1000 rpm and 90 mm/min respectively.
4. The joint efficiency increased by 20 % for an AA6061-3 (wt%) Rutile composite when the tensile test was carried out along the weld line.

**iii. SQ tool**

1. The UTS increases when the tool traverse speed is raised from 60 to 75 mm/min while the rotational speed stays constant. Tensile strength declines when the welding speed is raised to 90 mm/min.
2. The tensile strength improved when the welding speed was kept constant and the rotational speed was increased to 1000 rpm from 750 rpm. Tensile strength decreased as the rotating speed increased further.
3. The maximum joint efficiency of FS welded AA6061-3 (wt%) Rutile was 86 % for a tool traverse speed of 75 mm/min and a rotational speed of 1000 rpm.
4. The joint efficiency increased by 16 % for FS welded AA6061-3 (wt%) Rutile composite when the tensile test was performed along the weld line.
5. Smaller dimples were visible on the fracture surface of FS welded joints along the weld direction. Additionally, fragmented rutile particles were seen.

According to the results of the experimentation, a tool with a combined square and threaded cylindrical probe geometry, a rotational speed of 1000 rpm, tool traverse speed of 75 mm/min are the ideal conditions for obtaining the best joint strength when utilizing the FSW technique to join AA6061-3(wt%) rutile composite

### 4.17.3 Process parameter analysis utilizing the Taguchi design of experiments method

1. Taguchi design of the experimental method has been effectively applied to assessing the output of FS welded composite joints.

2. It is a reliable and effective way of figuring out the parameters of the welding process. It is implied that the weld joint strength is significantly influenced by the rotational speed, welding speed, and tool probe geometries.
3. The analysis of S/N ratios is used to determine the best set of process parameters for the highest UTS (rotational speed 1000 rpm, welding speed 75 mm/min, and CSTC tool).
4. The outcomes of the experiment support the validity test.

### 4.17.4 Process parameter optimization using Grey Relational Analysis (GRA), Desirability Approach (DA), and Teaching Learning Based Optimization (TLBO)

1. Based on the TGRA, Desirability approach, and TLBO optimization technique, optimized process parameters were developed.
2. Multi-response analysis through GRA enabled to ascertain an optimal solution. The process variable combination which resulted in maximum GRG was the rotational speed of 1000rpm, welding speed of 75 mm/min, and tool having CSTC pin. An enhancement of 9.5 % in YS, 8 % was achieved in UTS, and 9% in hardness in comparison with the best trial of the L9 array.
3. The findings of the ANOVA revealed that the joint properties are significantly influenced by the process variables welding speed and tool rotating speed. (with contributions of 37% and 36% respectively) followed by tool geometry with a contribution of 27%.
4. Both the desirability approach and TLBO technique can be successfully employed to optimize the FSW process parameters. It is clear from the statistical (Desirability and GRA) and evolutionary (TLBO) optimization methodologies that the desirability approach and TLBO produce the best results.
5. The computations show that for the problem under consideration, the TLBO technique is either on par with or outperforms the other optimization strategies.

### 4.17.5 Prediction of mechanical properties using GA-MLPNN model.

1. The developed GA-MLPNN model successfully predicted the yield strength, UTS, hardness and percentage elongation of friction stir welded AA6061-3 (wt%) rutile composite joints.
2. For hardness, the relative percentage inaccuracy varies from -2.1% to 1.91%, for UTS error ranges from -1.9% to 2%, for Hardness, the error ranges from -2.2 % to 4.5 %, and for % elongation, the error ranges from -1.1 % to 1.4 %.
3. The developed GA-MLPNN model successfully depicts the relationship between the mechanical properties and the FSW process parameters.

The distinguishing feature of the present study is the application of the TLBO technique to optimize the FSW process parameters, which yields more precise results than the Taguchi technique. And the development of the GA-MLPNN model to predict the process responses for the given set of process parameters with negligible or minimal error.

# Chapter 5

# CONCLUSIONS AND SCOPE FOR FUTURE WORK

The ceramic Reinforced Aluminium Matrix Composites have attracted a lot of interest in light of environmental considerations. But these composites' low weldability and machinability made welding them difficult. Being a solid-state welding, FSW is recognized as a competitive substitute for traditional welding. However, there is relatively little information available regarding the FSW of aluminium matrix composites reinforced with minerals. The current study clarifies the evolution of microstructure, examines the mechanical characteristics of composite joints, and examines the impact of process parameters on mechanical characteristics. Statistical techniques and evolutionary algorithms were used to optimize the welding parameters to get superior joint properties. For various process variable combinations, the GA-MLPNN model is developed and utilized to forecast the mechanical properties of the FSW composite. The main objective was to establish the relationship between mechanical and structural qualities and conduct a comparative investigation of both during the FSW process. The secondary goal was to produce defectless, sound FSW joints, utilizing various combinations of rotating speed, welding speed, and tool geometries. AA6061-3(wt%) rutile composites were prepared using bi stage stir casting process. These composites were welded using a CNC vertical machining machine equipped with the necessary FSW accessories.

## 5.1 CONCLUSIONS

1. Using the FSW tool with a concave shoulder, defect-free joints can be obtained. To improve stiffness, increase axial force, and ensure optimum frictional heat build-up at the tool-workpiece contact, the shoulder diameter was kept at three times the pin diameter. To properly consolidate the material behind the tool pin as the tool advances in the forward direction, the workpiece is slanted by a 2° angle. The joint strength of the base material is improved by increasing the dynamic-to-static volume ratio of the tool pin. The degree of defect-free welds in FS welded composites depends on the tool

pin profiles, rotating speed, and welding speed.

2. The grain size is influenced by the process variables such as rotational speed, welding speed, and tool pin profile. In contrast to the grain size attained for the as-cast composite, fine equiaxed grain structures were developed at the NZ because of dynamic recrystallization. Due to variations in the heat input condition, it was found that smaller grains were observed at the bottom of the nugget zone compared to the top portion of it. The stirring and abrasive activity of the tool caused numerous tiny rutile particles to be visible at the NZ

3. On the welded region, a variation in the hardness profile was seen. NZ exhibits the highest hardness as it possesses a fine grain structure and tiny rutile particles. Due to the thermal impact of welding, lesser hardness was attained at HAZ. All of the tensile specimens were seen to fracture near the HAZ, where the least hardness was found. Optimal joint strength was obtained in a joint, friction stir welded using a tool with a combined square and threaded cylindrical pin at a welding speed of 75 mm/min and rotational speed of 1000 rpm.

4. According to the Taguchi orthogonal array-based design, tool rotational speed is most significant for enhancing joint strength followed by tool pin geometries and welding speed respectively. Soft computing techniques namely RSM, Desirability approach, and TLBO were effectively formulated for optimization of the responses of FSW of AA6061-3(wt%) rutile composite, and a comparative study has been performed among these techniques. When it comes to optimization, the TLBO strategy is more successful and produces superior outcomes than the other approaches.

5. To predict the mechanical properties of FS welded AA6061-3(wt%) rutile composite joints, the developed GA-MLPNN model appears to be incredibly useful. The current work has demonstrated that the results of predictions made using GA-MLPNN are better than those made using statistical methods.

The unique aspect of the research is the use of a tool with a combined square and threaded cylindrical profiled pin. Presence of thread in the pin enables improved material flow in both direction, from top to bottom as well as around the pin. And the presence of a square profile helps in sweeping more material into the weld zone due to the higher dynamic to static volume ratio and assists in the formation of fine-grained

microstructure due to the pulsating effect. Due to these combined effects, the CSTC tool offers high-quality joints with improved mechanical properties.

The application of TLBO, a population-based, algorithm parameter-free optimization technique, to enhance the process parameters of FSW to create joints with higher mechanical properties.

To forecast the FSW responses for the specified set of input parameters, a novel GA (genetic algorithms) MLPNN technique is devised. The GA-MLPNN algorithm makes sure that the model avoids the possibility of becoming stuck in local minima and consistently conducts a global search and offers the optimum solution.

## 5.2 IMPLICATIONS AND PURPOSE OF INCLUDING DIFFERENT SOFT COMPUTING TECHNIQUES

| | **Techniques** | **Purpose** | **Outcome** |
|---|---|---|---|
| OPTIMIZATION | Grey Relation Analysis | A statistical optimization technique is used to optimize multi-responses by converting responses into grey relational grade. | Multi-response optimization. Weights are to be assigned to each response based on their significance. |
| | Desirability Approach | Multi-attribute optimization. Performs effectively within the given border parameters. | Moderate computational time. |
| | TLBO | Population-based, algorithm parameter-free optimization technique. | Provides accurate results, with minimal computational time. |
| PREDICTION | RSM | To assess the impact of the FSW process variables on output responsiveness. Outside the boundary, limits cannot be achieved. | Each response can be predicted separately from the developed equation. % Error is more. |
| | GA-MLPNN | To solve nonlinear data. | % Error is less than 5% Better computational speed and efficiency. |

## 5.3 DIRECTIONS FOR FUTURE RESEARCH

The results of the current study show that the FSW may be effectively adapted for linking ceramic reinforced metal matrix composites without impairing the composite's chemical homogenization. When compared to a traditional welding method, FSW generates less heat in the weld zone. As a result, it gets rid of solidification-related defects. The process parameters have a direct impact on the joint's strength. Consequently, DOE can produce optimal values. By using the TLBO approach, the process can be further optimized. The current study has sparked interest in the following areas for future research.

1. To evaluate the joint strength of various materials, the developed CSTC tool can be used. By varying the tool's hardness, the joint's quality can be investigated. It is possible to fine-tune the joint's performance by adjusting the shoulder-to-diameter ratio. The newly developed tool can be used to alter the metallographic features of the composite using the FSW technique for deeper levels of the surface.
2. Since the composite is age hardenable, a comparative study of its properties before and after age hardening can be studied.
3. The friction stir-treated composite's surface hardness can be predicted using the proposed GA-MLPNN model. Using the GA-MLPNN approach, online joint strength prediction can be accomplished by adding intelligence.
4. Further wear behavior and the damping properties of the welded composite can be evaluated.

# REFERENCES


Abioye, T. E., Zuhailawati, H., Anasyida, A. S., Yahaya, S. A., and Dhindaw, B. K. (2019). "Investigation of the microstructure , mechanical and wear properties of AA6061-T6 friction stir weldments with different particulate." *Integr. Med. Res.*, 8(5), 3917–3928.

Abraham, S. J., Dinaharan, I., Selvam, J. D. R., and Akinlabi, E. T. (2019). "Microstructural Characterization and Tensile Behavior of Rutile (TiO 2 )-Reinforced AA6063 Aluminum Matrix Composites Prepared by Friction Stir Processing." *Acta Metall. Sin. (English Lett.*, 32(1), 52–62.

Adamowski, J., Gambaro, C., Lertora, E., Ponte, M., and Szkodo, M. (2007). "Analysis of FSW welds made of aluminium alloy AW6082-T6." *Arch. Mater. Sci. Eng.*, 28(8), 453–460.

Ahmed, M. M. Z., Ataya, S., Seleman, M. M. E. S., Allam, T., Alsaleh, N. A., and Ahmed, E. (2021). "Grain structure, crystallographic texture, and hardening behavior of dissimilar friction stir welded aa5083-o and aa5754-h14." *Metals (Basel).*, 11(2), 1–17.

Aigbodion, V. S., and Hassan, S. B. (2007). "Effects of silicon carbide reinforcement on microstructure and properties of cast Al-Si-Fe/SiC particulate composites." *Mater. Sci. Eng. A*, 447(1–2), 355–360.

Anarghya, A., Harshith, D. N., Rao, N., Nayak, N. S., Gurumurthy, B. M., Abhishek, V. N., and Patil, I. G. S. (2018). "Thrust and torque force analysis in the drilling of aramid fibre-reinforced composite laminates using RSM and MLPNN-GA." *Heliyon*, 4(7), e00703.

Arbegast, W. J. (2008). "A flow-partitioned deformation zone model for defect formation during friction stir welding." *Scr. Mater.*, 58(5), 372–376.

Arora, a., De, a., and Debroy, T. (2011). "Toward optimum friction stir welding tool shoulder diameter." *Scr. Mater.*, 64(1), 9–12.

Arora, R., Kumar, S., Singh, G., and Pandey, O. P. (2015a). “Influence of particle size and temperature on the wear properties of rutile-reinforced aluminium metal matrix composite.” *J. Compos. Mater.*, 49(7), 843–852.

Arora, R., Kumar, S., Singh, G., and Pandey, O. P. (2015b). “Role of different range of particle size on wear characteristics of al-rutile composites.” *Part. Sci. Technol.*, 33(3), 229–233.

Ashok Kumar, B., and Murugan, N. (2014). “Optimization of friction stir welding process parameters to maximize tensile strength of stir cast AA6061-T6/AlNp composite.” *Mater. Des.*, 57, 383–393.

Aval, H. J., Serajzadeh, S., and Kokabi, A. H. (2011). “Theoretical and experimental investigation into friction stir welding of AA 5086.” 531–544.

Avettand-Fènoël, M. N., and Simar, A. (2016). “A review about Friction Stir Welding of metal matrix composites.” *Mater. Charact.*, 120, 1–17.

Barmouz, M., Besharati Givi, M. K., and Seyfi, J. (2011). “On the role of processing parameters in producing Cu/SiC metal matrix composites via friction stir processing: Investigating microstructure, microhardness, wear and tensile behavior.” *Mater. Charact.*, 62(1), 108–117.

Bassani, P., Capello, E., Colombo, D., Previtali, B., and Vedani, M. (2007). “Effect of process parameters on bead properties of A359/SiC MMCs welded by laser.” *Compos. Part A Appl. Sci. Manuf.*, 38(4), 1089–1098.

Bhandare, R. G., and Sonawane, P. M. (2013). “Preparation of Aluminium Matrix Composite by Using Stir Casting Method.” (2), 61–65.

Bharath, V., Ajawan, S. S., Nagaral, M., Auradi, V., and Kori, S. A. (2019). “Characterization and Mechanical Properties of 2014 Aluminum Alloy Reinforced with Al2O3p Composite Produced by Two-Stage Stir Casting Route.” *J. Inst. Eng. Ser. C*, 100(2), 277–282.

Bhushan, R. K., and Kumar, S. (2011). “Influence of SiC particles distribution and their weight percentage on 7075 Al alloy.” *J. Mater. Eng. Perform.*, 20(2), 317–323.

Bhushan, R. K., and Sharma, D. (2019). “Optimization of FSW parameters for maximum UTS of AA6082/SiC/10P composites.” *Adv. Compos. Lett.*, 28, 1–7.

BIST, A., SAINI, J. S., and SHARMA, B. (2016). “A review of tool wear prediction during friction stir welding of aluminium matrix composite.” *Trans. Nonferrous Met. Soc. China (English Ed.)*, 26(8), 2003–2018.

Bodaghi, M., and Dehghani, K. (2017). “Friction stir welding of AA5052: the effects of SiC nano-particles addition.” *Int. J. Adv. Manuf. Technol.*, 88(9–12), 2651–2660.

Boz, M., and Kurt, A. (2004). “The influence of stirrer geometry on bonding and mechanical properties in friction stir welding process.” *Mater. Des.*, 25(4), 343–347.

Bozkurt, Y., and Boumerzoug, Z. (2018). “Tool material effect on the friction stir butt welding of AA2124-T4 Alloy Matrix MMC.” *J. Mater. Res. Technol.*, 7(1), 29–38.

Buffa, G., Fratini, L., Pasta, S., and Shivpuri, R. (2008). “On the thermo-mechanical loads and the resultant residual stresses in friction stir processing operations.” *CIRP Ann. - Manuf. Technol.*, 57(1), 287–290.

Çam, G., and Mistikoglu, S. (2014). “Recent developments in friction stir welding of al-Alloys.” *J. Mater. Eng. Perform.*, 23(6), 1936–1953.

Cavaliere, P. (2013). “Friction stir welding of Al alloys: Analysis of processing parameters affecting mechanical behavior.” *Procedia CIRP*, 11, 139–144.

Cavaliere, P., Cerri, E., Leo, P., Marzoli, L., and Santos, J. Dos. (2004). “Friction Stir Welding of Ceramic Particle Reinforced Aluminium Based Metal Matrix Composites.” *Appl. Compos. Mater.*, 11(6), 399.

Ceschini, L., Boromei, I., Minak, G., Morri, a., and Tarterini, F. (2007a). “Effect of friction stir welding on microstructure, tensile and fatigue properties of the AA7005/10 vol.%Al2O3p composite.” *Compos. Sci. Technol.*, 67(3–4), 605–615.

Ceschini, L., Boromei, I., Minak, G., Morri, a., and Tarterini, F. (2007b). “Microstructure, tensile and fatigue properties of AA6061/20 vol.%Al2O3p friction stir welded joints.” *Compos. Part A Appl. Sci. Manuf.*, 38(4), 1200–1210.

Chaudhury, S. K., and Panigrahi, S. C. (2007). “Influence of TiO 2 particles on recrystallization kinetics of Al-2Mg-TiO 2 composites.” *J. Mater. Process. Technol.*, 182(1–3), 540–548.

CHEN, M., WU, C., & ZOU, Z. (2006). “Electron beam welding of SiCp / LD2 composite.” *Trans. Nonferrous Met. Soc. China*, 16(4), 818–823.

Chen, X. G., Silva, M. da, Gougeon, P., and St-Georges, L. (2009). “Microstructure and mechanical properties of friction stir welded AA6063-B4C metal matrix composites.” *Mater. Sci. Eng. A*, 518(1–2), 174–184.

Chen, Z. W., and Cui, S. (2008). “On the forming mechanism of banded structures in aluminium alloy friction stir welds.” *Scr. Mater.*, 58(5), 417–420.

Cioffi, F., Fernández, R., Gesto, D., Rey, P., Verdera, D., and González-Doncel, G. (2013). “Friction stir welding of thick plates of aluminum alloy matrix composite with a high volume fraction of ceramic reinforcement.” *Compos. Part A Appl. Sci. Manuf.*, 54, 117–123.

Colligan, K. (1999a). “Material flow behavior during friction stir welding of aluminum.” *Weld. J. (Miami, Fla)*, 78(7), 229-s.

Colligan, K. (1999b). “Material Flow Behavior during Friction Stir Welding of Aluminum.” (July), 229–237.

Dasgupta, R. (2012). “Aluminium Alloy-Based Metal Matrix Composites: A Potential Material for Wear Resistant Applications.” *ISRN Metall.*, 2012, 1–14.

DebRoy, T., De, a., Bhadeshia, H. K. D. H., Manvatkar, V. D., and Arora, a. (2012). “Tool durability maps for friction stir welding of an aluminium alloy.” *Proc. R. Soc. A Math. Phys. Eng. Sci.*, 468(2147), 3552–3570.

Delir Nazarlou, R., Nemati Akhgar, B., and Omidbakhsh, F. (2021). “Optimizations of friction stir welding parameters with Taguchi method for the maximum electrical conductivity in Al-1080 welded sections.” *Sci. Iran.*, 0(0), 0–0.

Devanathan, C., and Babu, a. S. (2014). “Friction Stir Welding of Metal Matrix Composite Using Coated Tool.” *Procedia Mater. Sci.*, 6(Icmpc), 1470–1475.

Dinaharan, I., Kalaiselvan, K., Vijay, S. J., and Raja, P. (2012). “Effect of material location and tool rotational speed on microstructure and tensile strength of dissimilar friction stir welded aluminum alloys.” *Arch. Civ. Mech. Eng.*, 12(4), 446–454.

Dinaharan, I., and Murugan, N. (2012a). “Effect of friction stir welding on microstructure, mechanical and wear properties of AA6061/ZrB 2 in situ cast composites.” *Mater. Sci. Eng. A*, 543, 257–266.

Dinaharan, I., and Murugan, N. (2012b). “Optimization of friction stir welding process to maximize tensile strength of AA6061/ZrB 2 in-situ composite butt joints.” *Met. Mater. Int.*, 18(1), 135–142.

Dong, P., Li, H., Sun, D., Gong, W., and Liu, J. (2013). “Effects of welding speed on the microstructure and hardness in friction stir welding joints of 6005A-T6 aluminum alloy.” *Mater. Des.*, 45, 524–531.

Elango, G., and Raghunath, B. K. (2013). “Tribological behavior of hybrid (LM25Al + SiC+ TiO2) metal matrix composites.” *Procedia Eng.*, 64, 671–680.

Elangovan, K., and Balasubramanian, V. (2007). “Influences of pin profile and rotational speed of the tool on the formation of friction stir processing zone in AA2219 aluminium alloy.” *Mater. Sci. Eng. A*, 459(1–2), 7–18.

Elangovan, K., and Balasubramanian, V. (2008a). “Influences of tool pin profile and welding speed on the formation of friction stir processing zone in AA2219 aluminium alloy.” *J. Mater. Process. Technol.*, 200(1–3), 163–175.

Elangovan, K., and Balasubramanian, V. (2008b). “Influences of post-weld heat treatment on tensile properties of friction stir-welded AA6061 aluminum alloy joints.” *Mater. Charact.*, 59(9), 1168–1177.

Falco, I. De, Cioppa, A. Della, and Tarantino, E. (2002). “Mutation-based genetic algorithm : performance evaluation.” 1, 285–299.

Feng, a. H., Xiao, B. L., and Ma, Z. Y. (2008a). “Effect of microstructural evolution on mechanical properties of friction stir welded AA2009/SiCp composite.” *Compos. Sci. Technol.*, 68(9), 2141–2148.

Feng, a, Xiao, B., and Ma, Z. (2008b). “Effect of microstructural evolution on mechanical properties of friction stir welded AA2009/SiCp composite.” *Compos. Sci. Technol.*, 68(9), 2141–2148.

Fernandez, G. J., and Murr, L. E. (2004). “Characterization of tool wear and weld optimization in the friction-stir welding of cast aluminum 359+20% SiC metal-matrix composite.” *Mater. Charact.*, 52(1), 65–75.

Fernández, R., Ibáñez, J., Cioffi, F., Verdera, D., and González-Doncel, G. (2017). “Friction stir welding of 25%SiC/2124Al composite with optimal mechanical properties and minimal tool wear.” *Sci. Technol. Weld. Join.*, 22(6), 526–535.

Fonda, R. W., Bingert, J. F., and Colligan, K. J. (2004). “Development of grain structure during friction stir welding.” *Scr. Mater.*, 51(3), 243–248.

GENG, P. hao, QIN, G. liang, ZHOU, J., and LI, C. an. (2019). “Parametric optimization and microstructural characterization of friction welded aeronautic aluminum alloy 2024.” *Trans. Nonferrous Met. Soc. China (English Ed.*, 29(12), 2483–2495.

Ghandvar, H., Farahany, S., and Idris, J. (2015). “Wettability enhancement of SiCp in cast A356/SiCp composite using semisolid process.” *Mater. Manuf. Process.*, 30(12), 1442–1449.

Ghetiya, N. D., Patel, K. M., and Kavar, A. J. (2016). “Multi-objective Optimization of FSW Process Parameters of Aluminium Alloy Using Taguchi-Based Grey Relational Analysis.” *Trans. Indian Inst. Met.*, 69(4), 917–923.

Gopalakrishnan, S., and Murugan, N. (2011). “Prediction of tensile strength of friction stir welded aluminium matrix TiCp particulate reinforced composite.” *Mater. Des.*, 32(1), 462–467.

Guerra, M., Schmidt, C., McClure, J. C., Murr, L. E., and Nunes, a. C. (2002). “Flow patterns during friction stir welding.” *Mater. Charact.*, 49(2), 95–101.

Guo, J., Gougeon, P., and Chen, X.-G. (2012a). “Study on laser welding of AA1100-16vol.% B4C metal–matrix composites.” *Compos. Part B Eng.*, 43(5), 2400–2408.

Guo, J., Gougeon, P., Nadeau, F., and Chen, X.-G. (2012b). “Joining of AA1100-16 vol.-%B<SUB>4</SUB>C metal matrix composite using laser welding and friction stir welding.” *Can. Metall. Q.*, 51(3), 277–283.

Guo, M. L. T., and Tsao, C. a. (2000). “Tribological behavior of self-lubricating aluminium / SiC / graphite hybrid composites synthesized by the semi-solid powder-densi ® cation method.” *Compos. Sci. Technol.*, 60, 65–74.

Gupta, R., Sharma, S., Nanda, T., and Pandey, O. P. (2019). “A comparative study of dry sliding wear behaviour of sillimanite and rutile reinforced LM27 aluminium alloy composites.” *Mater. Res. Express*, 7(1).

Haghshenas, M. (2016). “Metal–Matrix Composites.” *Ref. Modul. Mater. Sci. Mater. Eng.*, 1–28.

Hamilton, C., Dymek, S., and Sommers, a. (2008). “A thermal model of friction stir welding in aluminum alloys.” *Int. J. Mach. Tools Manuf.*, 48(10), 1120–1130.

Hashim, J., Looney, L., and Hashmi, M. S. J. (1999). “Metal matrix composites: production by the stir casting method.” *J. Mater. Process. Technol.*, 92–93, 1–7.

Hassan, A. M., Qasim, T., and Ghaithan, A. (2012). “Effect of Pin Profile on Friction Stir Welded Aluminum Matrix Composites.” *Mater. Manuf. Process.*, 27(12), 1397–1401.

Hattingh, D. G., Blignault, C., Niekerk, T. I. van, and James, M. N. (2008). “Characterization of the influences of FSW tool geometry on welding forces and weld strength using an instrumented tool.” *J. Mater. Process. Technol.*, 203(1–3), 46–57.

Heidarzadeh, A., Mironov, S., Kaibyshev, R., Çam, G., Simar, A., Gerlich, A., Khodabakhshi, F., Mostafaei, A., Field, D. P., Robson, J. D., Deschamps, A., and Withers, P. J. (2020). “Friction stir welding/processing of metals and alloys: A comprehensive review on microstructural evolution.” *Prog. Mater. Sci.*, 117(September 2020), 100752.

Herbert, M. A., Maiti, R., Mitra, R., and Chakraborty, M. (2008). “Wear behaviour of cast and mushy state rolled Al-4.5Cu alloy and in-situ Al4.5Cu-5TiB2 composite.” *Wear*, 265(11–12), 1606–1618.

Inegbenebor, A. O., Bolu, C. A., Babalola, P. O., Inegbenebor, A. I., and Fayomi, O. S. I. (2018). “Aluminum Silicon Carbide Particulate Metal Matrix Composite Development Via Stir Casting Processing.” *Silicon*, 10(2), 343–347.

Isaac, O., Jantan, A., and Esther, A. (2018). “State-of-the-art in arti fi cial neural network applications : A survey.” *Heliyon*, (June), e00938.

Jain, V. K. S., Varghese, J., and Muthukumaran, S. (2019). “Effect of First and Second Passes on Microstructure and Wear Properties of Titanium Dioxide-Reinforced Aluminum Surface Composite via Friction Stir Processing.” *Arab. J. Sci. Eng.*, 44(2), 949–957.

Jata, K. V., Sankaran, K. K., and Ruschau, J. J. (2000). “Friction-stir welding effects on microstructure and fatigue of aluminum alloy 7050-T7451.” *Metall. Mater. Trans. A*, 31(9), 2181–2192.

Jayaraman, M., Sivasubramanian, R., and Balasubramanian, V. (2009). “Effect of Process Parameters on Tensile Strength of Friction Stir Welded Cast LM6 Aluminium Alloy Joints.” *Journals Mater. Sci. Technol.*, 25(5), 655–664.

Jin, H., Kim, Y., Jin, Z., and Andreevna, A. (2022). “Optimization and analysis of bioenergy production using machine learning modeling : Multi-layer perceptron , Gaussian processes regression , K-nearest neighbors , and Artificial neural network models.” *Energy Reports*, 8, 13979–13996.

Kalaiselvan, K., Dinaharan, I., and Murugan, N. (2014a). “Characterization of friction stir welded boron carbide particulate reinforced AA6061 aluminum alloy stir cast composite.” *Mater. Des.*, 55, 176–182.

Kalaiselvan, K., Dinaharan, I., and Murugan, N. (2014b). “Characterization of friction stir welded boron carbide particulate reinforced AA6061 aluminum alloy stir cast composite.” *Mater. Des.*, 55, 176–182.

Kalaiselvan, K., and Murugan, N. (2012). “Optimizations of Friction Stir Welding Process Parameters for the Welding of Al-B4C Composite Plates using Generalized Reduced Gradient Method.” *Procedia Eng.*, 38, 49–55.

Kalaiselvan, K., and Murugan, N. (2013). “Role of friction stir welding parameters on tensile strength of AA6061-B4C composite joints.” *Trans. Nonferrous Met. Soc. China*, 23(3), 616–624.

Karbalaei Akbari, M., Rajabi, S., Shirvanimoghaddam, K., and Baharvandi, H. R. (2015). “Wear and friction behavior of nanosized TiB2 and TiO2 particle-reinforced casting A356 aluminum nanocomposites: A comparative study focusing on particle capture in matrix.” *J. Compos. Mater.*, 49(29), 3665–3681.

Karthikeyan, R., and Balasubramanian, V. (2010). “Predictions of the optimized friction stir spot welding process parameters for joining AA2024 aluminum alloy using RSM.” *Int. J. Adv. Manuf. Technol.*, 51(1–4), 173–183.

Kasman, Ş. (2013). “Multi-response optimization using the Taguchi-based grey relational analysis : a case study for dissimilar friction stir butt welding of AA6082-T6 / AA5754-H111.” 795–804.

Katoch, S., Chauhan, S. S., and Kumar, V. (2021). *A review on genetic algorithm : past , present , and future*. Multimedia Tools and Applications.

Khalilabad, M. M., Zedan, Y., Texier, D., and Bocher, P. (2022). “Effect of heat treatments on microstructural and mechanical characteristics of dissimilar friction stir welded 2198 / 2024 aluminum alloys.” *J. Adhes. Sci. Technol.*, 36(3), 221–239.

Krishna, G. G., Reddy, P. R., and Hussain, M. M. (2014). “Effect of Tool Tilt Angle on Aluminum 2014 Friction Stir Welds.” *Glob. J. Res. Eng.*, 14(7).

Kumar, a., and Raju, L. S. (2012). “Influence of Tool Pin Profiles on Friction Stir Welding of Copper.” *Mater. Manuf. Process.*, 27(12), 1414–1418.

Kumar, A., Mahapatra, M. M., Jha, P. K., Mandal, N. R., and Devuri, V. (2014a). “Influence of tool geometries and process variables on friction stir butt welding of Al-4.5%Cu/TiC in situ metal matrix composites.” *Mater. Des.*, 59, 406–414.

Kumar, A., Mahapatra, M. M., Jha, P. K., Mandal, N. R., and Devuri, V. (2014b). "Influence of tool geometries and process variables on friction stir butt welding of Al-4.5%Cu/TiC in situ metal matrix composites." *Mater. Des.*, 59, 406–414.

Kumar, A., Veeresh Nayak, C., Herbert, M. A., and Rao, S. S. (2014c). "Microstructure and hardness of friction stir welded aluminium–copper matrix-based composite reinforced with 10 wt-% SiCp." *Mater. Res. Innov.*, 18(sup6), S6-84-S6-89.

Kumar, B. A., and Murugan, N. (2014). "Optimization of friction stir welding process parameters to maximize tensile strength of stir cast AA6061-T6 / AlN p composite." *J. Mater.*, 57, 383–393.

Kumar, C. A. V., and Rajadurai, J. S. (2016). "Influence of rutile (TiO 2 ) content on wear and microhardness characteristics of aluminium-based hybrid composites synthesized by powder metallurgy." *Trans. Nonferrous Met. Soc. China (English Ed.*, 26(1), 63–73.

Kumar, K., and Kailas, S. V. (2008a). "The role of friction stir welding tool on material flow and weld formation." *Mater. Sci. Eng. A*, 485(1–2), 367–374.

Kumar, K., and Kailas, S. V. (2008b). "The role of friction stir welding tool on material flow and weld formation." *Mater. Sci. Eng. A*, 485(1–2), 367–374.

Kunnathur Periyasamy, Y., Perumal, A. V., and Kunnathur Periyasamy, B. (2019). "Optimization of process parameters on friction stir welding of AA7075-T651 and AA6061 joint using response surface methodology." *Mater. Res. Express*, 6(9), 096558.

Kuo, Y., Yang, T., and Huang, G. W. (2008a). "The use of a grey-based Taguchi method for optimizing multi-response simulation problems." *Eng. Optim.*, 40(6), 517–528.

Kuo, Y., Yang, T., and Huang, G. W. (2008b). "The use of grey relational analysis in solving multiple attribute decision-making problems." *Comput. Ind. Eng.*, 55(1), 80–93.

Kwon, Y., Saito, N., and Shigematsu, I. (2002). “Friction stir process as a new manufacturing technique of ultrafine grained aluminum alloy.” *J. Mater. Sci. Lett.*, 1473–1476.

Lakshminarayanan, a. K., and Balasubramanian, V. (2009). “Comparison of RSM with ANN in predicting tensile strength of friction stir welded AA7039 aluminium alloy joints.” *Trans. Nonferrous Met. Soc. China (English Ed.*, 19(1), 9–18.

Langari, J., and Kolahan, F. (2019). “The effect of friction stir welding parameters on the microstructure, defects, and mechanical properties of AA7075-T651 aluminium alloy joints.” *Sci. Iran.*, 26(4 B), 2418–2430.

Lei, Y. C., Wang, Z. W., and Chen, X. Z. (2011). “Effect of arc-ultrasound on microstructures and mechanical properties of plasma arc welded joints of SiCp/Al MMCs.” *Trans. Nonferrous Met. Soc. China (English Ed.*, 21(2), 272–277.

Leitão, C., Emílio, B., Chaparro, B. M., and Rodrigues, D. M. (2009). “Formability of similar and dissimilar friction stir welded AA 5182-H111 and AA 6016-T4 tailored blanks.” *Mater. Des.*, 30(8), 3235–3242.

Leitão, C., Louro, R., and Rodrigues, D. M. (2012). “Analysis of high temperature plastic behaviour and its relation with weldability in friction stir welding for aluminium alloys AA5083-H111 and AA6082-T6.” *Mater. Des.*, 37, 402–409.

Li, J. Q., and Liu, H. J. (2013). “Effects of tool rotation speed on microstructures and mechanical properties of AA2219-T6 welded by the external non-rotational shoulder assisted friction stir welding.” *Mater. Des.*, 43, 299–306.

Li, Y., Li, Q., Li, D., Liu, W., and Shu, G. (2016). “Fabrication and characterization of stir casting AA6061 − 31 % B 4 C composite.” 26, 2304–2312.

Li, Y., Murr, L. E., and McClure, J. C. (1999). “Solid-state flow visualization in the friction-stir welding of 2024 Al to 6061 Al.” *Scr. Mater.*, 40(9), 1041–1046.

Li, Y. Z., Wang, Q. Z., Xiao, B. L., and Ma, Z. Y. (2018). “Effect of welding parameters and $B_4C$ contents on the microstructure and mechanical properties of FS welded $B_4C$/6061Al joints.” *J. Mater. Process. Technol.*, 251(November 2016), 305–316.

Lin, P. T., Wu, C. S., Peng, C. H., Tsai, C. W., and Sato, Y. S. (2020). “Effects of rotational speed on the Al0.3CoCrCu0.3FeNi high-entropy alloy by friction stir welding.” *High Temp. Mater. Process.*, 39(1), 556–566.

Liu, H., Hu, Y., and Zhao, Y. (2015). “Microstructural characteristics and formation mechanism of friction stir welds of SiC particulates reinforced Al-Si matrix composites.” *Mater. Lett.*, 158, 136–139.

Liu, H. J., Zhang, H. J., and Yu, L. (2011). “Effect of welding speed on microstructures and mechanical properties of underwater friction stir welded 2219 aluminum alloy.” *Mater. Des.*, 32(3), 1548–1553.

Lloyd, D. J. (1994). “Particle reinforced aluminium and magnesium matrix composites.” *Int. Mater. Rev.*, 39(1), 1–23.

Lorrain, O., Favier, V., Zahrouni, H., and Lawrjaniec, D. (2010). “Understanding the material flow path of friction stir welding process using unthreaded tools.” *J. Mater. Process. Technol.*, 210(4), 603–609.

Ma, Z. Y., Feng, A. H., Chen, D. L., and Shen, J. (2018). “Recent Advances in Friction Stir Welding/Processing of Aluminum Alloys: Microstructural Evolution and Mechanical Properties.” *Crit. Rev. Solid State Mater. Sci.*, 43(4), 269–333.

Madhiarasan, M. (2022). “Analysis of Artificial Neural Network : Architecture , Types , and.” 2022(i).

Mahakur, V. K., Gouda, K., Patowari, P. K., and Bhowmik, S. (2021). “A Review on Advancement in Friction Stir Welding Considering the Tool and Material Parameters.” *Arab. J. Sci. Eng.*, 46(8), 7681–7697.

Mahmoud, E. R. I., Takahashi, M., Shibayanagi, T., and Ikeuchi, K. (2009). “Effect of friction stir processing tool probe on fabrication of SiC particle reinforced composite on aluminium surface.” 14(5), 413–425.

Mahoney, M. W., Rhodes, C. G., Flintoff, J. G., Bingel, W. H., and Spurling, R. a. (1998). “Properties of friction-stir-welded 7075 T651 aluminum.” *Metall. Mater. Trans. A*, 29(7), 1955–1964.

Mahto, R. P., Anishetty, S., Sarkar, A., Mypati, O., Pal, S. K., and Majumdar, J. D. (2019). "Interfacial Microstructural and Corrosion Characterizations of Friction Stir Welded AA6061-T6 and AISI304 Materials." *Met. Mater. Int.*, 25(3), 752–767.

Maity, P. C., Chakraborty, P. N., and Panigrahi, S. C. (1995). "Processing and properties of AlAl 2 O 3 (TiO 2 ) in situ particle composite." *J. Mater. Process. Tech.*, 53(3–4), 857–870.

Malopheyev, S., Vysotskiy, I., Kulitskiy, V., Mironov, S., and Kaibyshev, R. (2016). "Optimization of processing-microstructure-properties relationship in friction-stir welded 6061-T6 aluminum alloy." *Mater. Sci. Eng. A*, 662, 136–143.

Mao, Y., Ke, L., Chen, Y., Liu, F., and Xing, L. (2017). "Improving local and global mechanical properties of friction stir welded thick AA7075-T6 joints by optimizing pin-tip profile." *Int. J. Adv. Manuf. Technol.*, 88(5–8), 1863–1875.

Marzoli, L. M., Strombeck, a. V., Santos, J. F. Dos, Gambaro, C., and Volpone, L. M. (2006). "Friction stir welding of an AA6061/Al2O3/20p reinforced alloy." *Compos. Sci. Technol.*, 66(2), 363–371.

Mavhungu, S. T., Akinlabi, E. T., Onitiri, M. A., and Varachia, F. M. (2017). "Aluminum Matrix Composites for Industrial Use: Advances and Trends." *Procedia Manuf.*, 7, 178–182.

Mehta, K. P., and Badheka, V. J. (2016). "Effects of Tool Pin Design on Formation of Defects in Dissimilar Friction Stir Welding." *Procedia Technol.*, 23, 513–518.

Mehta, M., Arora, a., De, a., and Debroy, T. (2011a). "Tool geometry for friction stir welding - Optimum shoulder diameter." *Metall. Mater. Trans. A Phys. Metall. Mater. Sci.*, 42(9), 2716–2722.

Mehta, M., Arora, A., De, A., and Debroy, T. (2011b). "Tool geometry for friction stir welding - Optimum shoulder diameter." *Metall. Mater. Trans. A Phys. Metall. Mater. Sci.*, 42(9), 2716–2722.

Meng, C., Cui, H., Lu, F., and Tang, X. (2013). “Evolution behavior of TiB2 particles during laser welding on aluminum metal matrix composites reinforced with particles.” *Trans. Nonferrous Met. Soc. China*, 23(6), 1543–1548.

Meng, X., Huang, Y., Cao, J., Shen, J., and Santos, J. F. dos. (2021a). “Recent progress on control strategies for inherent issues in friction stir welding.” *Prog. Mater. Sci.*, 115, 100706.

Meng, X., Huang, Y., Cao, J., Shen, J., and Santos, J. F. dos. (2021b). “Recent progress on control strategies for inherent issues in friction stir welding.” *Prog. Mater. Sci.*, 115(December 2018), 100706.

Minak, G., Ceschini, L., Boromei, I., and Ponte, M. (2010). “Fatigue properties of friction stir welded particulate reinforced aluminium matrix composites.” *Int. J. Fatigue*, 32(1), 218–226.

Mishra, R. S., Ma, Z. Y., and Charit, I. (2003). “Friction stir processing: A novel technique for fabrication of surface composite.” *Mater. Sci. Eng. A*, 341(1–2), 307–310.

Mishra, R. S., Mahoney, M. W., Sato, Y., and Hovanski, Y. (2005). “Friction stir welding and processing.” *Mater. Sci. Eng. R*, 50, 1–78.

Mitra, R., Chiou, W. A., Fine, M. E., and Weertman, J. R. (1993). “Interfaces in as-extruded XD Al / TiC and Al / TiB2 metal matrix composites.”

Mohammadzadeh Jamalian, H., Farahani, M., Besharati Givi, M. K., and Aghaei Vafaei, M. (2016). “Study on the effects of friction stir welding process parameters on the microstructure and mechanical properties of 5086-H34 aluminum welded joints.” *Int. J. Adv. Manuf. Technol.*, 83(1–4), 611–621.

Moona, G., Walia, R. S., Rastogi, V., and Sharma, R. (2018). “Aluminium metal matrix composites: A retrospective investigation.” *Indian J. Pure Appl. Phys.*, 56(2), 164–175.

Moradi Faradonbeh, A., Shamanian, M., Edris, H., Paidar, M., and Bozkurt, Y. (2018). "Friction Stir Welding of Al-B4C Composite Fabricated by Accumulative Roll Bonding: Evaluation of Microstructure and Mechanical Behavior." *J. Mater. Eng. Perform.*, 27(2), 835–846.

Morisada, Y., Fujii, H., Nagaoka, T., and Fukusumi, M. (2006a). "MWCNTs/AZ31 surface composites fabricated by friction stir processing." *Mater. Sci. Eng. A*, 419(1–2), 344–348.

Morisada, Y., Fujii, H., Nagaoka, T., and Fukusumi, M. (2006b). "Effect of friction stir processing with SiC particles on microstructure and hardness of AZ31." *Mater. Sci. Eng. A*, 433(1–2), 50–54.

Moses, J. J., Dinaharan, I., and Sekhar, S. J. (2016). "Prediction of influence of process parameters on tensile strength of AA6061 / TiC aluminum matrix composites produced using stir casting." *Trans. Nonferrous Met. Soc. China*, 26(6), 1498–1511.

Mumali, F. (2022). "Artificial neural network-based decision support systems in manufacturing processes: A systematic literature review." *Comput. Ind. Eng.*, 165(October 2021), 107964.

Muñoz, a. C., Rückert, G., Huneau, B., Sauvage, X., and Marya, S. (2008). "Comparison of TIG welded and friction stir welded Al-4.5Mg-0.26Sc alloy." *J. Mater. Process. Technol.*, 197(1–3), 337–343.

Murugan, N., and Ashok Kumar, B. (2013). "Prediction of tensile strength of friction stir welded stir cast AA6061-T6/AlNp composite." *Mater. Des.*, 51, 998–1007.

Mustansar, C., Gupta, P., Engineering, M., Prakash, A., Shimla, G., and Pradesh, H. (2019). "Advance research progresses in aluminium matrix composites : manufacturing & applications." *Integr. Med. Res.*, 8(5), 4924–4939.

Nami, H., Adgi, H., Sharifitabar, M., and Shamabadi, H. (2011). "Microstructure and mechanical properties of friction stir welded Al/Mg2Si metal matrix cast composite." *Mater. Des.*, 32(2), 976–983.

Nandan, R., DebRoy, T., and Bhadeshia, H. K. D. H. (2008). “Recent advances in friction-stir welding - Process, weldment structure and properties.” *Prog. Mater. Sci.*, 53(6), 980–1023.

Ni, D. R., Chen, D. L., Wang, D., Xiao, B. L., and Ma, Z. Y. (2013). “Influence of microstructural evolution on tensile properties of friction stir welded joint of rolled SiCp/AA2009-T351 sheet.” *Mater. Des.*, 51, 199–205.

Nwobi-okoye, C. C., Quent, B., and Okiy, S. (2019). “Multi-objective optimization and modeling of age hardening process using ANN , ANFIS and genetic algorithm : Results from aluminum alloy A356 / cow horn particulate composite.” *Integr. Med. Res.*, 8(3), 3054–3075.

Okuyucu, H., Kurt, A., and Arcaklioglu, E. (2007). “Artificial neural network application to the friction stir welding of aluminum plates.” *Mater. Des.*, 28(1), 78–84.

Ozben, T., Kilickap, E., and Çakir, O. (2008). “Investigation of mechanical and machinability properties of SiC particle reinforced Al-MMC.” *J. Mater. Process. Technol.*, 198(1–3), 220–225.

Padhy, G. K., Wu, C. S., and Gao, S. (2018). “Friction stir based welding and processing technologies - processes, parameters, microstructures and applications: A review.” *J. Mater. Sci. Technol.*, 34(1), 1–38.

Padmanaban, G., and Balasubramanian, V. (2009). “Selection of FSW tool pin profile, shoulder diameter and material for joining AZ31B magnesium alloy - An experimental approach.” *Mater. Des.*, 30(7), 2647–2656.

Palanivel, R., Koshy Mathews, P., and Murugan, N. (2013). “Optimization of process parameters to maximize ultimate tensile strength of friction stir welded dissimilar aluminum alloys using response surface methodology.” *J. Cent. South Univ.*, 20(11), 2929–2938.

Palanivel, R., Koshy Mathews, P., Murugan, N., and Dinaharan, I. (2012). “Effect of tool rotational speed and pin profile on microstructure and tensile strength of dissimilar friction stir welded AA5083-H111 and AA6351-T6 aluminum alloys.” *Mater. Des.*, 40, 7–16.

Pandiyarajan, R., Maran, P., Murugan, N., Marimuthu, S., and Sornakumar, T. (2019). "Friction stir welding of hybrid AA 6061-ZrO2-C composites FSW process optimization using desirability approach." *Mater. Res. Express*, 6(6).

Parida, B., and Pal, S. (2015). "Fuzzy assisted grey Taguchi approach for optimisation of multiple weld quality properties in friction stir welding process." *Sci. Technol. Weld. Join.*, 20(1), 35–41.

Parikh, V. K., Badgujar, A. D., and Ghetiya, N. D. (2019). "Joining of metal matrix composites using friction stir welding: a review." *Mater. Manuf. Process.*, 34(2), 123–146.

Pawar, P. J., and Rao, R. V. (2013). "Parameter optimization of machining processes using teaching-learning-based optimization algorithm." *Int. J. Adv. Manuf. Technol.*, 67(5–8), 995–1006.

Pazhouhanfar, Y., and Eghbali, B. (2018). "Microstructural characterization and mechanical properties of TiB2 reinforced Al6061 matrix composites produced using stir casting process." *Mater. Sci. Eng. A*, 710(November 2017), 172–180.

Peddavarapu, S., Raghuraman, S., Bharathi, R. J., Sunil, G. V. S., and Manikanta, D. B. N. S. (2017). "Micro Structural Investigation On Friction Stir Welded Al–4.5Cu–5TiB2Composite." *Trans. Indian Inst. Met.*, 70(3), 703–708.

Periyasamy, P., Mohan, B., Balasubramanian, V., Rajakumar, S., and Venugopal, S. (2013). "Multi-objective optimization of friction stir welding parameters using desirability approach to join Al/SiCp metal matrix composites." *Trans. Nonferrous Met. Soc. China (English Ed.)*, 23(4), 942–955.

Prabhu, S. R., Shettigar, A., Herbert, M., and Rao, S. (2018). "Multi Response Optimization of Friction Stir Welding Process Variables using TOPSIS approach." *IOP Conf. Ser. Mater. Sci. Eng.*, 376(1).

PRABHU, S. R., SHETTIGAR, A. K., HERBERT, M. A., and RAO, S. S. (2019). "Microstructure and mechanical properties of rutile-reinforced AA6061 matrix composites produced via stir casting process." *Trans. Nonferrous Met. Soc. China (English Ed.)*, 29(11), 2229–2236.

Prabhu, S., Shettigar, A. K., Rao, K., Rao, S., and Herbert, M. (2016). “Influence of Welding Process Parameters on Microstructure and Mechanical Properties of Friction Stir Welded Aluminium Matrix Composite.” *Mater. Sci. Forum*, 880, 50–53.

Prado, R., Murr, L., Soto, K., and McClure, J. (2003). “Self-optimization in tool wear for friction-stir welding of Al 6061+ 20% Al 2 O 3 MMC.” *Mater. Sci. …*, 349, 156–165.

Prasad, R., Kumar, H., Kumar, P., Tewari, S. P., and Singh, J. K. (2021). “Microstructural, Mechanical and Tribological Characterization of Friction Stir Welded A7075/ZrB2 In Situ Composites.” *J. Mater. Eng. Perform.*, 30(6), 4194–4205.

Prasanth, R. S. S., and Hans Raj, K. (2018). “Determination of Optimal Process Parameters of Friction Stir Welding to Join Dissimilar Aluminum Alloys Using Artificial Bee Colony Algorithm.” *Trans. Indian Inst. Met.*, 71(2), 453–462.

Pratap, V., Kumar, S., Ranjan, A., and Kuriachen, B. (2020). “Recent research progress in solid state friction-stir welding of aluminium – magnesium alloys : a critical review.” *Integr. Med. Res.*, (x x), 1–40.

Rai, R., De, a, Bhadeshia, H. K. D. H., and DebRoy, T. (2011). “Review: friction stir welding tools.” *Sci. Technol. Weld. Join.*, 16(4), 325–342.

Rajakumar, S., Muralidharan, C., and Balasubramanian, V. (2010a). “Establishing empirical relationships to predict grain size and tensile strength of friction stir welded AA 6061-T6 aluminium alloy joints.” *Trans. Nonferrous Met. Soc. China (English Ed.*, 20(10), 1863–1872.

Rajakumar, S., Muralidharan, C., and Balasubramanian, V. (2010b). “Optimization of the friction-stir-welding process and tool parameters to attain a maximum tensile strength of AA7075-T6 aluminium alloy.” *Proc. Inst. Mech. Eng. Part B J. Eng. Manuf.*, 224(8), 1175–1191.

Rajakumar, S., Muralidharan, C., and Balasubramanian, V. (2011). “Predicting tensile strength, hardness and corrosion rate of friction stir welded AA6061-T6 aluminium alloy joints.” *Mater. Des.*, 32(5), 2878–2890.

Rajesh, G. L., Auradi, V., and Kori, S. A. (2016). “Mechanical Behaviour and Dry Sliding Wear Properties of Ceramic Boron Carbide Particulate Reinforced Al6061 Matrix Composites.” *Trans. Indian Ceram. Soc.*, 75(2), 112–119.

Ramesh, C. S., Khan, A. R. A., Ravikumar, N., and Savanprabhu, P. (2005). “Prediction of wear coefficient of Al6061-TiO2 composites.” *Wear*, 259(1–6), 602–608.

Ramnath, B. V., Elanchezhian, C., Annamalai, R. M., .Aravind, S., Atreya, T. S. A., Vignesh, V., and Subramanian, C. (2014). “Aluminium metal matrix composites - A review.” *Rev. Adv. Mater. Sci.*, 38(1), 55–60.

Rao, R. V., and Patel, V. (2013). “An improved teaching-learning-based optimization algorithm for solving unconstrained optimization problems.” *Sci. Iran.*, 20(3), 710–720.

Rao, R. V., Savsani, V. J., and Vakharia, D. P. (2011). “Teaching-learning-based optimization: A novel method for constrained mechanical design optimization problems.” *CAD Comput. Aided Des.*, 43(3), 303–315.

Raturi, M., Garg, A., and Bhattacharya, A. (2019). “Joint strength and failure studies of dissimilar AA6061-AA7075 friction stir welds: Effects of tool pin, process parameters and preheating.” *Eng. Fail. Anal.*, 96(August 2018), 570–588.

Ravichandran, M., Sait, A. N., and Anandakrishnan, V. (2015). “Workability studies on Al+2.5%TiO2+Gr powder metallurgy composites during cold upsetting.” *Mater. Res.*, 17(6), 1489–1496.

Ravindiran, C., Pravinkumar, P., and Vinoth, L. (2016). “A Characteristics Study of Aluminum Metal Matrix In Friction Stir Welding Process.” 2(22), 187–205.

Reynolds, a. P. (2000). “Visualisation of material flow in autogenous friction stir welds.” *Sci. Technol. Weld. Join.*, 5(2), 120–124.

Rezaei, H., Mirbeik, M. H., and Bisadi, H. (2011). “Effect of rotational speeds on microstructure and mechanical properties of friction stir-welded 7075-T6 aluminium alloy.” *Proc. Inst. Mech. Eng. Part C J. Mech. Eng. Sci.*, 225(8), 1761–1773.

Rowe, C. E. D., and Wayne, T. (2006). “Advances in Tooling Materials for Friction.” *TWI Cedar Met. Ltd*, 1–11.

Sachin, B., Narendranath, S., and Chakradhar, D. (2018). “Experimental evaluation of diamond burnishing for sustainable manufacturing.” *Mater. Res. Express*, 5(10).

Sajjadi, S. A., Ezatpour, H. R., and Torabi Parizi, M. (2012). “Comparison of microstructure and mechanical properties of A356 aluminum alloy/Al2O3 composites fabricated by stir and compo-casting processes.” *Mater. Des.*, 34, 106–111.

Salazar, D., and Barrena, M. I. (2003). “Dissimilar fusion welding of AA7020 / MMC reinforced with Al 2 O 3 particles . Microstructure and mechanical properties.” 352, 162–168.

Salih, O. S., Ou, H., Sun, W., and McCartney, D. G. (2015). “A review of friction stir welding of aluminium matrix composites.” *Mater. Des.*, 86, 61–71.

Salih, O. S., Ou, H., Wei, X., and Sun, W. (2019). “Microstructure and mechanical properties of friction stir welded AA6092/SiC metal matrix composite.” *Mater. Sci. Eng. A*, 742(August 2018), 78–88.

Sato, Y. S., Urata, M., Kokawa, H., and Ikeda, K. (2003). “Hall-Petch relationship in friction stir welds of equal channel angular-pressed aluminium alloys.” *Mater. Sci. Eng. A*, 354(1–2), 298–305.

Schneider, J., Beshears, R., and Nunes, A. C. (2006). “Interfacial sticking and slipping in the friction stir welding process.” *Mater. Sci. Eng. A*, 435–436, 297–304.

Schubert, E., Klassen, M., Zerner, I., Walz, C., and Sepold, G. (2001). “Light-weight structures produced by laser beam joining for future applications in automobile and aerospace industry.” *J. Mater. Process. Technol.*, 115(1), 2–8.

Seidel, T. U., and Reynolds, a. P. (2001). “Visualization of the material flow in AA2195 friction-stir welds using a marker insert technique.” *Metall. Mater. Trans. A*, 32(11), 2879–2884.

Sharkawy, A. (2020). “Principle of Neural Network and Its Main Types : Review.” *J. Adv. Appl. Comput. Math.*, 7, 8–19.

Sharma, P., Sharma, S., and Khanduja, D. (2015). “Production and some properties of Si 3 N 4 reinforced aluminium alloy composites.” *J. Asian Ceram. Soc.*, 3(3), 352–359.

Shettigar, a K., Salian, G., Herbert, M., and Rao, S. (2013). “Microstructural Characterization and Hardness Evaluation of Friction Stir Welded Composite AA6061-4 . 5Cu-5SiC ( Wt .%).” 63(4), 429–434.

Shin, J. H., Choi, H. J., and Bae, D. H. (2014). “The structure and properties of 2024 aluminum composites reinforced with TiO2 nanoparticles.” *Mater. Sci. Eng. A*, 607, 605–610.

Shindo, D. J., Rivera, a R., and Murr, L. E. (2002). “Shape optimization for tool wear in the friction-stir welding of cast AI359-20 % SiC MMC.” *J. Mater. Sci.*, 7(23), 4999–5005.

Shojaeefard, M. H., Behnagh, R. A., Akbari, M., Givi, M. K. B., and Farhani, F. (2013). “Modelling and pareto optimization of mechanical properties of friction stir welded AA7075/AA5083 butt joints using neural network and particle swarm algorithm.” *Mater. Des.*, 44, 190–198.

Singh, G., Singh, K., and Singh, J. (2011). “Effect of process parameters on microstructure and mechanical properties in friction stir welding of aluminum alloy.” *Trans. Indian Inst. Met.*, 64(4–5), 325–330.

Singh, S., Singh, I., and Dvivedi, A. (2017). “Design and development of novel cost effective casting route for production of metal matrix composites (MMCs).” *Int. J. Cast Met. Res.*, 30(6), 356–364.

Sinha, P., Muthukumaran, S., and Mukherjee, S. K. (2008). “Analysis of first mode of metal transfer in friction stir welded plates by image processing technique.” *J. Mater. Process. Technol.*, 197(1–3), 17–21.

Sivaprasad, K., and Muthupandi, V. (2020). *Recent Advances in Materials and Manufacturing Engineering (IMME19). Trans. Indian Inst. Met.*

Sivasankaran, S., and Alaboodi, A. S. (2016). “Structural Characterization and Mechanical Behavior of Al 6061 Nanostructured Matrix Reinforced with TiO2 Nanoparticles for Automotive Applications.” *Funct. Nanomater.*, (December).

Sivasankaran, S., Sivaprasad, K., and Narayanasamy, R. (2011). “Microstructure, cold workability and strain hardening behavior of trimodaled AA 6061-TiO2 nanocomposite prepared by mechanical alloying.” *Mater. Sci. Eng. A*, 528(22–23), 6776–6787.

Soltani, S., Azari Khosroshahi, R., Taherzadeh Mousavian, R., Jiang, Z. Y., Fadavi Boostani, A., and Brabazon, D. (2017). “Stir casting process for manufacture of Al–SiC composites.” *Rare Met.*, 36(7), 581–590.

Soni, N., Chandrashekhar, S., Kumar, A., and Chary, V. R. (2017). “Defects Formation during Friction Stir Welding: A Review.” *Int. J. Eng. Manag. Res. Page Number*, 7(3), 121–125.

Sreenivasan, K. S., Satish Kumar, S., and Katiravan, J. (2019). “Genetic algorithm based optimization of friction welding process parameters on AA7075-SiC composite.” *Eng. Sci. Technol. an Int. J.*, 22(4), 1136–1148.

Steuwer, a., Peel, M. J., and Withers, P. J. (2006). “Dissimilar friction stir welds in AA5083-AA6082: The effect of process parameters on residual stress.” *Mater. Sci. Eng. A*, 441(1–2), 187–196.

Storjohann, D., Barabash, O. M., Babu, S. S., David, S. A., Sklad, P. S., and Bloom, E. E. (2005). “Fusion and friction stir welding of aluminum-metal-matrix composites.” *Metall. Mater. Trans. A Phys. Metall. Mater. Sci.*, 36(11), 3237–3247.

Sued, M. K., Pons, D., Lavroff, J., and Wong, E. H. (2014). “Design features for bobbin friction stir welding tools: Development of a conceptual model linking the underlying physics to the production process.” *Mater. Des.*, 54, 632–643.

Surappa, M. K. (2003). “Aluminium matrix composites: Challenges and opportunities.” *Sadhana*, 28(1–2), 319–334.

Suthar, J., and Patel, K. M. (2018). “Processing issues, machining, and applications of aluminum metal matrix composites.” *Mater. Manuf. Process.*, 33(5), 499–527.

Tarasov, S. Y., Rubtsov, V. E., and Kolubaev, E. a. (2014). “A proposed diffusion-controlled wear mechanism of alloy steel friction stir welding (FSW) tools used on an aluminum alloy.” *Wear*, 318(1–2), 130–134.

Taylor, P., Yigezu, B. S., Jha, P. K., and Mahapatra, M. M. (2013). “The Key Attributes of Synthesizing Ceramic Particulate Reinforced Al-Based Matrix Composites through Stir Casting Process : A Review.” *Mater. Manuf. Process.*, 28(September), 37–41.

Thiagarajan, R., Chandrasekharendra, S., and Viswa, S. (2015). “Experimental Study on fabrication of hybrid ( Al + Tio 2 + Gr ) metal matrix composites.” 37(November), 3–7.

Thomas, W. ., and Nicholas, E. . (1997). “Friction stir welding for the transportation industries.” *Mater. Des.*, 18(4–6), 269–273.

Thomas, W. M., Johnson, K. I., and Wiesner, C. S. (2003). “Friction stir welding-recent developments in tool and process technologies.” *Adv. Eng. Mater.*, 5(7), 485–490.

Thomas, W. M., Staines, D. J., Watts, E. R., and Norris, I. M. (2005). “The simultaneous use of two or more friction stir welding tools.” *Weld. Inst.*, (3), 2–7.

Threadgill, P. L. (2007). “Terminology in friction stir welding.” *Sci. Technol. Weld. Join.*, 12(4), 357–360.

Threadgilll, P. L., Leonard, A. J., Shercliff, H. R., and Withers, P. J. (2009). “Friction stir welding of aluminium alloys.” *Int. Mater. Rev.*, 54(2), 49–93.

Ureña, a, Escalera, M. ., and Gil, L. (2000). “Influence of interface reactions on fracture mechanisms in TIG arc-welded aluminium matrix composites.” *Compos. Sci. Technol.*, 60(4), 613–622.

Uzun, H. (2007). “Friction stir welding of SiC particulate reinforced AA2124 aluminium alloy matrix composite.” *Mater. Des.*, 28(5), 1440–1446.

Venkateshkannan, M., Rajkumar, V., Sadeesh, P., Arivazhagan, N., Narayanan, S., and Devendranath, R. K. (2014). “Influences of tool geometry on metallurgical and mechanical properties of friction stir welded dissimilar AA 2024 and AA 5052.” *Procedia Eng.*, 75, 154–158.

Vijay, S. J., and Murugan, N. (2010). “Influence of tool pin profile on the metallurgical and mechanical properties of friction stir welded Al-10wt.% TiB2 metal matrix composite.” *Mater. Des.*, 31(7), 3585–3589.

Vijayavel, P., Balasubramanian, V., and Sundaram, S. (2014). “Effect of shoulder diameter to pin diameter (D/d) ratio on tensile strength and ductility of friction stir processed LM25AA-5% SiCp metal matrix composites.” *Mater. Des.*, 57, 1–9.

Vilaça, P., Quintino, L., Santos, J. F. dos, Zettler, R., and Sheikhi, S. (2007). “Quality assessment of friction stir welding joints via an analytical thermal model, iSTIR.” *Mater. Sci. Eng. A*, 445–446, 501–508.

Wang, D., Xiao, B. L., Wang, Q. Z., and Ma, Z. Y. (2014). “Evolution of the Microstructure and Strength in the Nugget Zone of Friction Stir Welded SiCp/Al-Cu-Mg Composite.” *J. Mater. Sci. Technol.*, 30(1), 54–60.

Wang, H. M., Chen, Y. L., and Yu, L. G. (2000). “‘ In-situ ’ weld-alloying / laser beam welding of SiCp / 6061Al MMC.” 293, 1–6.

Wang, J., Yuan, W., Mishra, R. S., and Charit, I. (2013). “Microstructure and mechanical properties of friction stir welded oxide dispersion strengthened alloy.” *J. Nucl. Mater.*, 432(1–3), 274–280.

Woo, W., Choo, H., Brown, D. W., Feng, Z., and Liaw, P. K. (2006). “Angular distortion and through-thickness residual stress distribution in the friction-stir processed 6061-T6 aluminum alloy.” *Mater. Sci. Eng. A*, 437(1), 64–69.

Xi-he, W., Ji-tai, N., Shao-kang, G., Le-jun, W., and Dong-feng, C. (2009). “Investigation on TIG welding of SiCp-reinforced aluminum-matrix composite using mixed shielding gas and Al-Si filler.” *Mater. Sci. Eng. A*, 499(1–2), 106–110.

Xie, G. M., Ma, Z. Y., and Geng, L. (2007). “Development of a fine-grained microstructure and the properties of a nugget zone in friction stir welded pure copper.” *Scr. Mater.*, 57(2), 73–76.

Xu, W., Liu, J., Luan, G., and Dong, C. (2009). “Microstructure and mechanical properties of friction stir welded joints in 2219-T6 aluminum alloy.” *Mater. Des.*, 30(9), 3460–3467.

Yang, X., Li, W., Xu, Y., Wen, Q., Feng, W., and Wang, Y. (2019). “Effect of welding speed on microstructures and mechanical properties of Al/Cu bimetal composite tubes by a novel friction-based welding process.” *Weld. World*, 63(1), 127–136.

Yigezu, B. S., Jha, P. K., and Mahapatra, M. M. (2013). “The key attributes of synthesizing ceramic particulate reinforced Al-based matrix composites through stir casting process: A review.” *Mater. Manuf. Process.*, 28(9), 969–979.

Yigezu, B. S., Venkateswarlu, D., Mahapatra, M. M., Jha, P. K., and Mandal, N. R. (2014). “On friction stir butt welding of Al+12Si/10wt%TiC in situ composite.” *Mater. Des.*, 54, 1019–1027.

Yoganandam, K., Raja, K., and Lingadurai, K. (2016). “Mechanical and micro structural characterization of Al6082-$TiO_2$ metal matrix composites produced via compo casting method.” *Indian J. Sci. Technol.*, 9(41), 7–10.

Yousif, Y. K., Daws, K. M., and Kazem, B. I. (2008). “Prediction of Friction Stir Welding Characteristic Using Neural Network.” 2(3), 151–155.

Zeng, W. M., Wu, H. L., and Zhang, J. (2006). “Effect of tool wear on microstructure, mechanical properties and acoustic emission of friction stir welded 6061 Al alloy.” *Acta Metall. Sin. (English Lett.*, 19(1), 9–19.

Zettler, R., and Vugrin, T. (2003). *Effects and defects of friction stir welds*. *Frict. stir Weld.*, Woodhead Publishing Limited.

Zhang, H. W., Zhang, Z., and Chen, J. T. (2005). “The finite element simulation of the friction stir welding process.” *Mater. Sci. Eng. A*, 403(1–2), 340–348.

Zhang, X.-P., Ye, L., Mai, Y.-W., Quan, G.-F., and Wei, W. (1999a). “Investigation on diffusion bonding characteristics of SiC particulate reinforced aluminium metal matrix composites (Al/SiCp-MMC).” *Compos. Part A Appl. Sci. Manuf.*, 30(12), 1415–1421.

Zhang, X. P., Quan, G. F., and Wei, W. (1999b). “Preliminary investigation on joining performance of SiC p -reinforced aluminium metal matrix composite ( Al / SiC p – MMC ) by vacuum brazing.” 30, 823–827.

Zhang, Y. N., Cao, X., Larose, S., and Wanjara, P. (2012a). “Review of tools for friction stir welding and processing.” *Can. Metall. Q.*, 51(3), 250–261.

Zhang, Y. N., Cao, X., Larose, S., and Wanjara, P. (2012b). “Review of tools for friction stir welding and processing.” 51(3), 250–261.

# APPENDIX

## TLBO – MATLAB CODE

### 1. Code for equation entry

function Z[YS_MPa] or Z[UTS_MPa] or Z[Ha_VHN ] or Z[%El] or Maximize f(x) = fun(variable)
no_of_variable = 3;

Z[YS_MPa]= 126.245+ 4.800*variable (1)+ 3.300*variable (2)+ 4.400*variable (3)- 12.86*variable (1)*variable (1)- 10.36*variable (2)* variable (2)-12.86*variable (3)*variable (3)+ 0.625*variable (1)*variable (2)+ 0.125*variable (1)*variable (3)+ 0.625*variable (2)*variable (3)

OR

Z[UTS_MPa]= 175.227+ 6.500*variable (1)+ 4.900*variable (2)+ 4.400*variable (3)- 16.818*variable (1)*variable (1)- 11.818* variable (2)*variable (2)- 17.318*variable (3)*variable (3)+ 1.875*variable (1)*variable (2)+ 0.125*variable (1)*variable (3)+ 0.125*variable (2)*variable (3)

OR

Z[Ha_VHN]=126.627- 2.400*variable (1)+ 2.500*variable (2)- 0.800*variable (3)- 14.318*variable (1)*variable (1)- 8.818*variable (2)* variable (2)- 9.318*variable (3)*variable (3)+ 1.000*variable (1)*variable (2)+ 0.250*variable (1)*variable (3)+ 0.000*variable (2)*variable (3)

OR

Z[%El] = 7.2036+ 0.0300*variable (1)- 0.3100*variable (2)- 0.2600*variable (3)+ 0.5409*variable (1)*variable (1) +0.0409*variable (2) *variable (2)- 0.1091*variable (3)*variable (3)- 0.0250*variable (1)*variable (2)+ 0.0250*variable (1)*variable (3)- 0.0250*variable (2)*variable (3)

OR

Maximize f(x) = [w1 * Z[YS_MPa] / Yield strength (max)] + [w2 * Z[UTS_MPa]/ UTS (max)] + [w3 * Z[Ha_VHN]) / Hardness (max)] + [w4 * Z[%El] / % Elongation (max)]

end

**2. Code for parameter setting**

```
clear all
clc
no_of_run = 100;
no_of_student = 50; %specify population size
no_of_iteration = 100; %specify number of iterations
        tf = 1;
        for i = 1:no_of_run
        [bvf bvx]=mainline(no_of_student, no_of_iteration, tf);
        bvf1(i,:)=bvf;
        bvx1(i,:)=bvx;
end
bvf = bvf1(:,1);
[bvfmin,k0]=min(bvf)
bvxmin = bvx1(k0,:)
bvfmin = bvf1(k0,:)
```

**3. Code for fixing the range for process variables**

```
function [bvf bvx]=mainline(no_of_student, no_of_iteration, tf)
no_of_variable = 3; % specify number of variables
lowerlimitofa = -1; % specify the lower bound (750rpm)
upperlimitofa = 1; % specify the upper bound (1250 rpm)
lowerlimitofb = -1; specify the lower bound (60 mm/min)
upperlimitofb = 1; specify the lower bound (90 mm/min)
lowerlimitofc = 1; specify the lower bound (TC tool)
upperlimitofc = 3; specify the lower bound (SQ tool)
        for i = 1:no_of_student
        % initialization of the variables
                a = lowerlimitofa + rand *(upperlimitofa-lowerlimitofa);
                b = lowerlimitofb + rand *(upperlimitofb-lowerlimitofb);
                c = lowerlimitofc + rand *(upperlimitofc-lowerlimitofc);
        x(i,:)=[a b c];
end

%limit array
limit=[lowerlimitofa;upperlimitofa;lowerlimitofb;upperlimitofb;lowerlimitofc;upperli
mitofc];
        parameter=[no_of_student;no_of_iteration;tf;no_of_variable];
        [bvf,bvx]=tlbo1(limit,x,parameter);
```

**4. Main program for TLBO optimization.**

```
function [bvf,bvx]=tlbo1(limit,x,parameter)
no_of_student = parameter(1);
no_of_iteration = parameter(2);
tf = parameter(3);
no_of_variable = parameter(4);
        for i = 1:no_of_student
                variable = x(i,:);%arrange variable row wise for 100
                [funxz]=fun(variable);
                fxx(i,1)=funxz;%arrange columnwise function value
end
for ng1 = 1:no_of_iteration;
m = mean(x);%calculate mean of each design variable
[sfx,k0]=min(fxx);%getting the min function value
bt = x(k0,:);
        for i = 1:no_of_student
                k = 1;
                for j = 1:no_of_variable
                        xs(i,j)=x(i,j)+rand *(bt(1,j)-tf*m(1,j));
                        if xs(i,j)<limit(k) || xs(i,j)>limit(k + 1)
                        x1(i,j)=x(i,j);
                else
                        x1(i,j)=xs(i,j);
                end
        k = j + 2;
        end
        variable = x1(i,:);%best function variable
end
        for i = 1:no_of_student
                variable = x1(i,:);
                [funxz]=fun(variable);
                fxx1(i,1)=funxz;
        end
        for i = 1:no_of_student
                if fxx1(i,1)>fxx(i,1)
                fxx1(i,:)=fxx(i,:);
                x1(i,:)=x(i,:);
        end
```

```
end
[sfx1,k1]=min(fxx1);
bs = x1(k1,:);
        for i = 1:no_of_student
        k = 1;
                for j = 1:no_of_variable
                        xs(i,j)=x1(i,j)+rand *(bs(1,j)-x1(i,j));
                        if xs(i,j)<limit(k) || xs(i,j)>limit(k + 1)
                        x(i,j)=x1(i,j);
                else
                        x(i,j)=xs(i,j);
                end
        k = j + 2;
        end
variable = x(i,:);
end
        for i = 1:no_of_student
                variable = x(i,:);
                [funxz]=fun(variable);
                fxx(i,1)=funxz;
        end
        for i = 1:no_of_student
                        if fxx(i,1)>fxx1(i,1)
                        fxx(i,:)=fxx1(i,:);
                        x(i,:)=x1(i,:);
                end
        end
end

[bvff,k2]=min(fxx);
bvf(1,:)=fxx(k2,:);
bvx = x(k2,:);
```

## LIST OF PUBLICATIONS BASED ON Ph.D. WORK

***International Journal Publications:***


1. Prabhu, S. R., Shettigar, A., Herbert, M. A., and Rao, S. S. (2022). "Influence of machine variables on the microstructure and mechanical properties of AA6061/$TiO_2$ friction stir welds." *Adv. Mater. Process. Technol.*, 9(2), 441–456.
2. Prabhu, S. R., Shettigar, A., Herbert, M. A., and Rao, S. S. (2022). "Parameter investigation and optimization of friction stir welded AA6061/$TiO_2$ composites through TLBO." *Weld. World*, 66(1), 93–103.
3. Prabhu, S. R., Shettigar, A., Herbert, M. A., and Rao, S. S. (2022). "Optimization of FSW process parameters for maximum UTS of AA6061/rutile composites using Taguchi technique." *Sci. Iran.*, 29(2 B), 534–542.
4. Prabhu, S. R., Shettigar, A., Herbert, M. A., and Rao, S. S. (2021). "Experimental assessment of FSW process to join AA6061/Rutile composite and parametric optimization using TGRA." *Eng. Res. Express*, 3(3), 035035.
5. PRABHU, S. R., SHETTIGAR, A. K., HERBERT, M. A., and RAO, S. S. (2019). "Microstructure and mechanical properties of rutile-reinforced AA6061 matrix composites produced via stir casting process." *Trans. Nonferrous Met. Soc. China (English Ed.*, 29(11), 2229–2236.
6. Prabhu, S. R. B., Shettigar, A. K., Herbert, M. A., and Rao, S. S. (2019). "Microstructure evolution and mechanical properties of friction stir welded AA6061/rutile composite." *Mater. Res. Express*, 6(8). 0865i7.

***International Conference Proceedings:***

1. Subramanya, P., Amar, M., Arun, S., Mervin, H., and Shrikantha, R. (2018). “Friction stir welding of Aluminium matrix composites - A Review.” *MATEC Web Conf.*, 144, 03002

## BIODATA

The author Subramanya R Prabhu B was born on 8th March 1982 at Bellampalli, Udupi, Karnataka. He obtained his primary education in Jai Hind AHPS Bellampalli, Karnataka. He completed his secondary education in SVHS Bellampalli, Karnataka. He secured his Bachelor's degree in Mechanical Engineering from MIT, Manipal, in the year of 2003 with Distinction. He worked with M/s BPL Ltd Automation Division, Bangalore for three years as Asst. Manager QA and BOSCH India Ltd for two years as Senior Engineer – Process Planning. He obtained his Master's degree in Mechatronics Engineering from NITK University in the year 2010, securing First Class with Distinction. Then he joined as an Assistant Professor in the Department of Mechanical and Manufacturing Engineering of MIT Manipal, Karnataka, in the year 2010. Currently, he is working in the same college as an Assistant Professor, Selection Grade, in the Department of Mechatronics. He is pursuing his PhD at NITK, Surathkal in the Department of Mechanical Engineering.

The author has published a part of his research work in the form of papers in six International Journal and in the international conference. The author is a member of ISTE and IE Mechatronics.

His research interests include Friction stir welding of composites, Soft Computing and Optimization.

**Address for Communication**

Subramanya R Prabhu B
Prabhu Nivas
Post Bellampalli
Via Perdoor – Udupi 576124
Email: subramanya.prabhu@gmail.com
subramanya.prabhu@manipal.edu
Ph: 9448240151